**Alma Mater Studiorum - Università di Bologna**

**DOTTORATO DI RICERCA IN**
**ASTRONOMIA**

**Ciclo XXIX**

**Settore Concorsuale di afferenza:**
02/C1 - Astronomia, Astrofisica, Fisica della Terra e dei Pianeti

**Settore Scientifico disciplinare:**
FIS/05 - Astronomia e Astrofisica

# "Starbursting to Quenching: the role of X-ray emission in Active Galactic Nuclei feedback processes"

**Presentata da:** MICHELE PERNA

Relatore:
Dott.ssa
Marcella Brusa

Coordinatore Dottorato:
Francesco Ferraro

**Esame finale anno 2016**

The work described in this thesis was undertaken between October 2013 and October 2016 under the supervision of Dr. Marcella Brusa, at the Department of Physics and Astronomy, Alma Mater Studiorum - Università di Bologna. The research has been funded by the FP7/CIG grant, *"eEASY": 'SMBH evolution through cosmic time: from current surveys to eROSITA and Euclid AGN Synergies'* (No 321913).

Portions of this work have appeared (or are to appear) in the following papers:

- Brusa M., Bongiorno A., Cresci G., **Perna M.** et al., 2015a, MNRAS, 446, 2394; *X-shooter reveals powerful outflows in* $z\sim1.5$ *X-ray selected obscured QSOs*

- **Perna M.**, Brusa M. et al., 2015, A&A, 574, 82; *Galaxy wide outflows in* $z\sim1.5$ *luminous obscured QSOs revealed through NIR slit-resolved spectroscopy*

- ○ Cresci G., Mainieri V., Brusa M., Marconi A., **Perna M.** et al., 2015, ApJ, 799, 81; *Blowin' in the wind: both 'negative' and 'positive' feedback in an obscured high-z QSO*

- **Perna M.**, Brusa M. et al., 2015, A&A, 583, A77; *SINFONI spectra of heavily obscured AGNs in COSMOS: evidence of outflows in a MIR/O target at* $z\sim2.5$

- Brusa M., **Perna M.** et al., 2016, A&A, 588A, 58; *A fast ionised wind in a star-forming quasar system at* $z \sim 1.5$ *resolved through adaptive optics assisted near-infrared data*

- Brusa M., Feruglio C., Cresci G., Mainieri V., Sargert M.T., **Perna M.** et al., 2015, A&A, 578, 11; *Evidence for feedback in action from the molecular gas content in the* $z \sim 1.6$ *outflowing QSO XID2028*

- **Perna M.**, et al. 2016, to be submitted, *An X-ray/SDSS sample: outflowing gas Electron Temperature and Density*

In addition to the work presented in this thesis, the author has also contributed to the following papers during the period of its PhD:

- ○ Lanzuisi G., **Perna M.** et al., 2015, A&A, 578, 120; *The most obscured AGN in the COSMOS field*

- ○ Lanzuisi G., **Perna M.** et al., 2016, A&A, 590, A72; *NuSTAR reveals the extreme properties of the super-Eddington accreting SMBH in PG 1247+267*

- ○ Trevese D., **Perna M.** et al., 2015, A&A, 795, 164; *CIV and CIII] reverberation mapping of the luminous quasar PG 1247+267*

- ○ Saturni F.G., Trevese D., Vagnetti F., **Perna M.**, Dadina M., 2016, A&A, 587, 43; *A multi-epoch spectroscopic study of the BAL quasar APM 08279+5255 II. Emission- and absorption-line variability time lags*

- ○ Trevese D., Saturni F.G., Vagnetti F., **Perna M.**, et al., 2013, A&A, 557, 91; *A multi-epoch spectroscopic study of the BAL quasar APM 08279+5255. I. C IV absorption variability*

- ○ Trevese D., Saturni F.G., Vagnetti F., Paris D., **Perna M.**, 2012, ASPC, 460,1007; *Multi-epoch Observation of CIV Absorption Variability in APM 08279+5255*

- **Perna M.**, Trevese D., Vagnetti F., Saturni F.G., 2014, AdSpR, 54, 1429P (COSPAR award); *Reverberation time lags in the high luminosity quasar PG 1247+267*
- Saturni F.G., Trevese D., Vagnetti F., **Perna M.**, 2014, AdSpR, 54, 1434; *A multi-epoch study of the C IV absorption variability in the broad absorption line quasar APM 08279+5255*

# Contents

# Abstract

One of the most debated topics of modern extragalactic astrophysics is the co-evolution between the supermassive black holes (SMBHs) sitting in the nuclei of the galaxies and their hosts. According to the most popular models of Active Galactic Nuclei (AGN) and galaxies co-evolution, starburst galaxies, unobscured quasars and inactive (and quenched) galaxies represent the different phases of an evolutionary sequence reproducing the most massive galaxies observed in the Universe. In this context, gas flows in the form of energetic outflows are postulated to play a pivotal role in this process, given that they regulate both accretion and ejection of material onto and from the SMBH and can propagate momentum and energy over a wide spatial scale, acting on the fuel from which new stars form and stopping the host galaxy growth.

In order to validate this binding nature between the central SMBH and the host galaxy, we investigate the kinematic and physical properties of ionized and atomic gas components of the interstellar medium of well selected AGN-galaxy systems, obtained from ultraviolet, optical, near-infrared spectroscopic analysis, to unveil the presence of outflows. In particular, we propose and test different selection criteria to isolate sources at $z \sim 2$ in the predicted feedback phase, starting from multiwavelength information collected in the COSMOS field. As a complementary approach, we also collect a large sample of X-ray selected AGNs at $z < 0.8$ from the SDSS database to unveil the incidence of outflows and prove the crucial role of X-ray observations for the investigation of the feedback phase.

The dynamical conditions of the ionized outflows for the high-z samples, for which slit-resolved spectroscopy and/or integral Field spectroscopic (IFS) data are available, are studied in detail through the combination of multicomponent and non-parametric line fitting algorithms. We report the unambiguous presence of fast, massive outflows in 4 obscured QSO, extending up to 10 kpc in the host galaxy and with profound effects on the host galaxy.

We carefully discuss the uncertainties related to the assumption of the plasma conditions in the estimate of the outflows properties and we report, for the first time, the plasma electron density and temperature in a mid-size sample of AGN.

Finally, we combine the ionized/neutral gas kinematic and physical conditions with SMBH accretion and host galaxy properties, recovered from multiwavelength spectral energy distribution analysis and X-ray spectroscopic investigation, to infer the general conditions regulating the feedback processes. We also discuss our results in the context of the more recent observational and theoretical returns.

CHAPTER 1

# Introduction

## 1.1 Active Galactic Nuclei across the electromagnetic spectrum

### 1.1.1 Discovery and key spectral signatures

The term “active galactic nucleus” (AGN) refers to the existence of energetic phenomena in the nuclei of galaxies that distinguish these sources from the majority of galaxies. AGNs are, in fact, among the most luminous objects in the sky at every wavelength at which they have been observed, from radio frequencies to hard X-ray and $\gamma$ ray bands.

The earlier observations of AGNs started with Carl Seyfert, who reported the properties of few peculiar galaxies showing a luminous “stellar” nucleus surrounded by a faint, nebulous envelope (Seyfert 1943). Such nuclear luminosity, containing a large percentage of the light of the system, and the presence of emission lines in the nuclear spectra covering a wide range of ionization states, are the most important characteristics of these sources, named *Seyfert* galaxies in honour of their discoverer. At the beginning of the 1960s, other peculiar galaxies were discovered: few extremely bright radio sources were associated with optical counterparts totally indistinguishable from stars, i.e. without any outer nebulous envelope (Matthews and Sandage 1963). These “quasi-stellar radio sources”, or *quasars*, turned out to be more distant than any known object at that time, and to have luminosities higher than an ordinary galaxy even by a factor of 100 or more (Greenstein 1963; Schmidt 1963, 1965). Detailed observational efforts were required to probe the connection between quasars and Seyfert galaxies (Khachikian and Weedman 1977; Lynden-Bell 1971); in addition, two populations comprising bright radio sources (“radio loud”) and radio faint (“radio quiet”) quasi-stellar galaxies (e.g., Sandage 1965) were identified[1]. We now consider quasars (QSOs) and Seyferts as two subclasses of AGNs, with quasars being the most luminous and rarest versions of Seyferts.

In the 1960-1970s, the first AGN surveys provided the observational material needed to define the typical properties of these sources (see Weedman 1977 for an earlier review). Seyfert galaxies were classified in two types, on the basis of the differences in their optical-ultraviolet (UV) spectra, following an observational scheme first proposed by Khachikyan and Weedman

---

[1] This thesis mostly focus on the optical and X-ray observational characterization of AGNs. We will briefly outline radio quiet and radio loud sources in the next sections, in the context of our analysis results. We defer the reader to recent reviews for more detailed description of AGN radio properties (e.g., Heckman and Best 2014; Padovani 2016).

(1971, 1974) and still used today. Seyfert 1 galaxies are those with very broad permitted emission lines, such as those of the hydrogen Balmer series H$\alpha$ and/or H$\beta$[2], characterized by profiles with full-widths at half-maximum (FWHM) of the order of $1-5\times10^3$ km/s. Their forbidden features, such as [O III]$\lambda\lambda$4959,5007 and [NII]$\lambda\lambda$6548,6583 emission lines, are instead characterized by FWHM of the order of few hundred of km/s. In Seyfert 2 galaxies, on the contrary, both permitted and forbidden lines have the same widths (a few 100 km/s).

The broad permitted emission lines and the wide range of ionization provide, however, just some indication of the activity that distinguishes active galaxies. Most AGNs also show a featureless power-law continuum in the optical-UV region (Weedman 1977). Moreover, many AGNs are variable in brightness, with optical continuum fluctuations at $0.3-0.5$ magnitude level on time scales of few days. These changes have been used to set upper limits to the size of the nuclear emitting region applying coherence arguments: the entire emitting region, if causally connected, must have a maximum size related to light-travel time (Peterson 2001). It turned out, hence, that the emitting nuclear region, capable to radiate as much energy as an entire galaxy, is comparable in size to the Solar System. A tiny, unresolved object within the nucleus had to be at the origin of the energy distinctive of AGNs.

### 1.1.2 Theory of accretion

Accretion onto compact objects has been proposed as the mechanism for producing the high energy radiation observed in nuclei of active galaxies. The most accepted physical picture requires a 'central engine' that consists of a hot accretion disk around a massive black hole (Salpeter 1964; Zel'dovich and Novikov 1964), thanks to which the gravitational energy of accreting material is transformed into radiation. Assuming that the AGN luminosity is the result of accretion of matter, this luminosity can be expressed as

$$L = \eta \dot{M} c^2 \tag{1.1}$$

where $\dot{M}$ is the mass accretion rate, $c$ is the light velocity and $\eta$ is the efficiency of the mass-to-energy conversion. Very basic physical arguments suggest that $\eta \approx 0.1$ (Peterson 1997), i.e. an order of magnitude more efficient than fusion of hydrogen to helium, which sustains the nuclear processes during most of a star's life.

A fundamental quantity related to accretion processes is the Eddington luminosity (Eddington 1916). This luminosity is defined as a theoretical upper limit on the luminosity that can be obtained assuming accretion of spherically symmetric, completely ionized hydrogen gas onto a black hole (BH) of mass $M_{BH}$. This upper limit is obtained assuming a balance between the inward gravitational force, acting on gas protons, and the outward radiation force, acting on gas electrons, so it is required that

$$L \leq L_{Edd} = \frac{4\pi G M_{BH} m_p c}{\sigma_T} \approx 1.3\times10^{38}\left(\frac{M_{BH}}{M_\odot}\right)\ erg/s \tag{1.2}$$

where $m_p$ is the proton mass, $G$ is the gravitational constant, $\sigma_T$ is the Thomson cross-section for an electron and $M_{BH}$ is the BH mass. Because of the assumptions in this derivation, the Eddington limit should be taken as a rough estimate of the maximum luminosity achievable by

---

[2] Detailed discussion about the nature of forbidden and permitted emission features, together with the physical conditions at the origin of such lines, is provided in Appendix A. The nomenclature used in the text refers to a single emission line when the species is followed by the proper rest-frame wavelength (e.g., He I$\lambda$4686) and to a doublet emission line in the case it is followed by a pair of rest-frame wavelengths (e.g., [O III]$\lambda\lambda$4959,5007). Square brackets around the species note forbidden line transitions.

an accreting AGN (see, e.g., Fabian et al. 2008, who discussed the role of dust in deriving the Eddington luminosity).

The ratio of the accretion luminosity $L$ to the Eddington luminosity, $\lambda_{Edd} = L/L_{Edd}$ (hereafter, the Eddington ratio), can be a useful measure of the accretion rate onto the central black hole. As a rough estimate, we can infer the mass of a black hole comparing Eqs. 1.1 and 1.2: an AGN accreting at an Eddington luminosity of $10^{45}$ erg/s, i.e. with an $\lambda_{Edd} = 1$, requires a black hole of $\sim 10^7$ $\mathrm{M}_\odot$. Typical black hole masses in AGNs are found in the range $10^6 - 10^9$ $\mathrm{M}_\odot$ (e.g., Shen et al. 2011).

The simplest model of accretion onto a compact object takes into account a geometrically thin, optically thick accretion disk (Shakura and Sunyaev 1973). It predicts a monochromatic luminosity per unit frequency of the disk roughly consistent with observations over a limited range of frequency, with a spectrum

$$L_\nu \propto \nu^{1/3}, \tag{1.3}$$

i.e., reproducing the featureless power-law continuum observed in the optical-UV region. The accretion rate and the black hole mass determine the coefficient of proportionality in Eq. 1.3, while the range of frequency is fixed assuming the physical boundaries of the disk, i.e. its inner and outer radii (Netzer 2013)[3]. This part of the spectral energy distribution (SED) of the AGN is referred as the thermal big blue bump (BBB), one of the various physical components that are thought to make up the very broad SED of AGNs (see Fig. 1.1).

### 1.1.3 Reprocessed radiation

Typical disk emission, therefore, did not account for the full wide band emission observed in AGNs. For example, in a typical Seyfert 1 galaxy, X-rays provide about $10 - 20\%$ (e.g., Lusso et al. 2012) of the total (bolometric) AGN luminosity, $L_{bol}$, defined as the integrated AGN emission over the entire SED. An optically thin corona around the accretion disk is thought to be at the origin of the observed X-ray emission (Fig. 1.1). According to this scenario, the photons produced at the accretion disk undergo inverse-Compton scattering of hot relativistic electrons in the medium to produce the X-ray power-law spectra that are observed in AGNs, in particular in type 1 sources. Type 2 are instead generally associated with faint sources in the soft X-ray ($0.5 - 2$ keV energy band), and stronger emitters in the hard ($2 - 10$ keV) X-ray (Osterbrock and Ferland 2006). The simplest interpretation suggests the presence of high column density of neutral gas ($N_H$) which absorbs the low-energy photons. We will see that this obscuration occurs in a toroidal structure which blocks our view of the central engine.

This structure would be also responsible for the infrared (IR) emission observed in both type 1 and type 2 in the $5 - 25$ $\mu$m range (Fig. 1.1). This emission is due to thermal radiation produced by dust grains heated (from 100 up to 2000 K) by the AGN radiation field. The sub-mm/far-IR frequency range, instead, presents a minimal contribution from the AGN and is generally associated with the thermal emission of cooler dust heated by young stars in the host galaxy (e.g., Mullaney et al. 2011; see Lutz 2014 for a review; but see also Symeonidis et al. 2016). The SEDs of AGNs at radio frequencies may display a several orders of magnitude difference in the luminosities from radio-loud compared to radio-quiet AGN (e.g., Elvis et al. 1994; Fig. 1.1). The radio emission in radio-loud AGNs originates from point-like radio cores or from relativistic jets, which are launched close to the optical-UV and X-ray continuum source (Fig. 1.5, right inset). In radio-quiet AGNs the radio emission is often spread across the host galaxy and is more presumably associated with star formation (SF) activity (Padovani 2016

---

[3] Typical extensions of accretion disks are of the order of $10^{-3} - 10^{-2}$ pc (e.g., from microlensing variability; see Morgan et al. 2010).

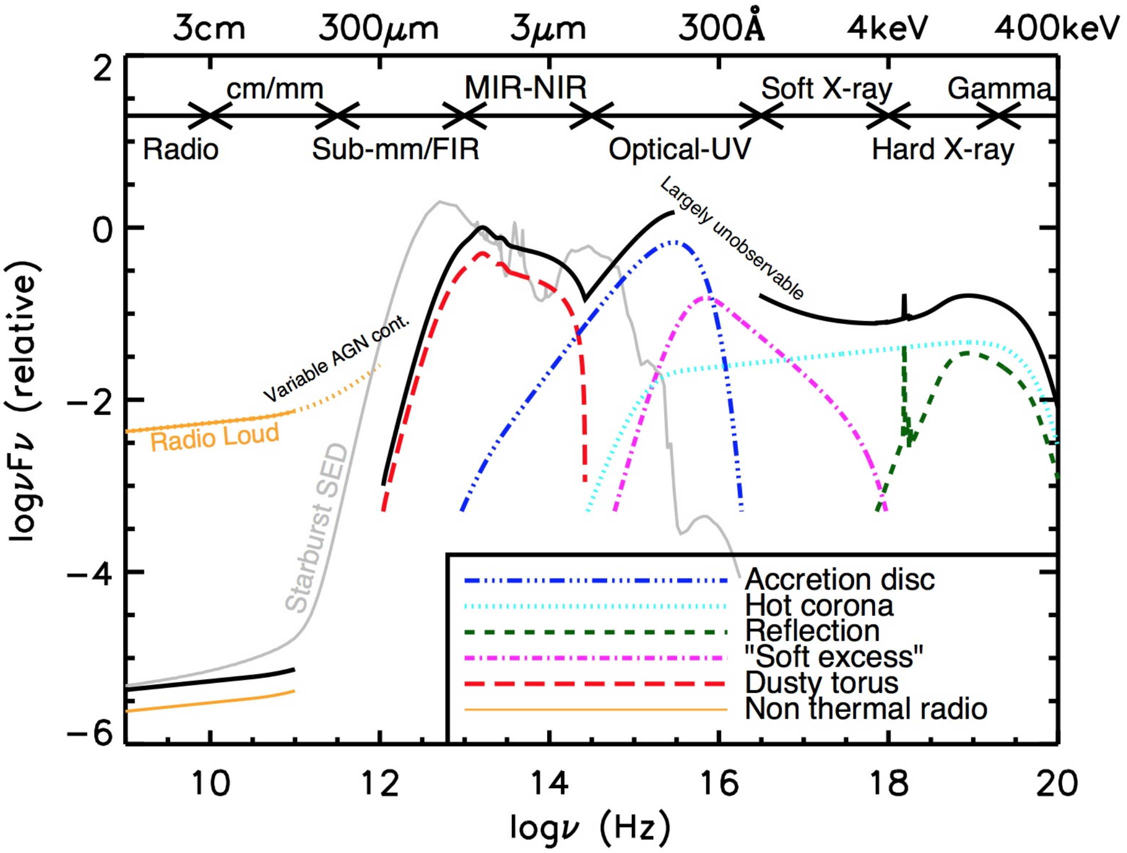

Figure 1.1: Schematic representation of a multiwavelength AGN SED, from radio to X-rays. The physical components introduced in Sect. 1.1.3 are highlighted with different colours; the solid black curve marks the observable AGN SED. As a comparison, the grey curve shows a typical spectrum of a starburst galaxy (M82 SED, from Silva et al. 1998). Taken from C. Harrison's webpage: `http://astro.dur.ac.uk/~cpnc25/research.html`.

and references therein), although significant compact emission, often variable and/or associated with weak jets linked to the central AGN has been observed in local sources for which high resolution imaging is achievable (e.g., Panessa and Giroletti 2013 and references therein).

## 1.2 Optical spectra

The sample of peculiar galaxies originally studied in 1943 by Carl Seyfert did not increase significantly for 25 years, until the Markarian and Zwicky surveys (e.g., Markarian 1967, 1969; Sargent 1970). From these early surveys of few hundred galaxies, it turned out that approximately 10% of sources are found to meet the Seyfert definition. In the past decade, large surveys such as the Sloan Digital Sky Survey (SDSS; York et al. 2000) have obtained spectra for large portions of the sky, constructing samples of hundreds of thousands of AGNs publicly available for large-scale analysis, pointing to the understanding of their collective properties. Figure 1.2 shows typical spectra extracted from the SDSS database for normal inactive and active galaxies. Narrow emission lines observed in AGNs are much the same as those observed in SF-galaxies, with H II region like spectra (upper panel), except that AGN lines show a considerably wider range of ionization states: [O II]$\lambda\lambda$3726,3729, [O III]$\lambda\lambda$4959,5007 and [N II]$\lambda\lambda$6548,6583 are usually observed together with low stage of ionization lines, such as [O I]$\lambda$6300, [S II]$\lambda\lambda$6716,6731 (middle panel), which are much stronger than in H II galaxies; sometimes, also [Ne V]$\lambda$3426,

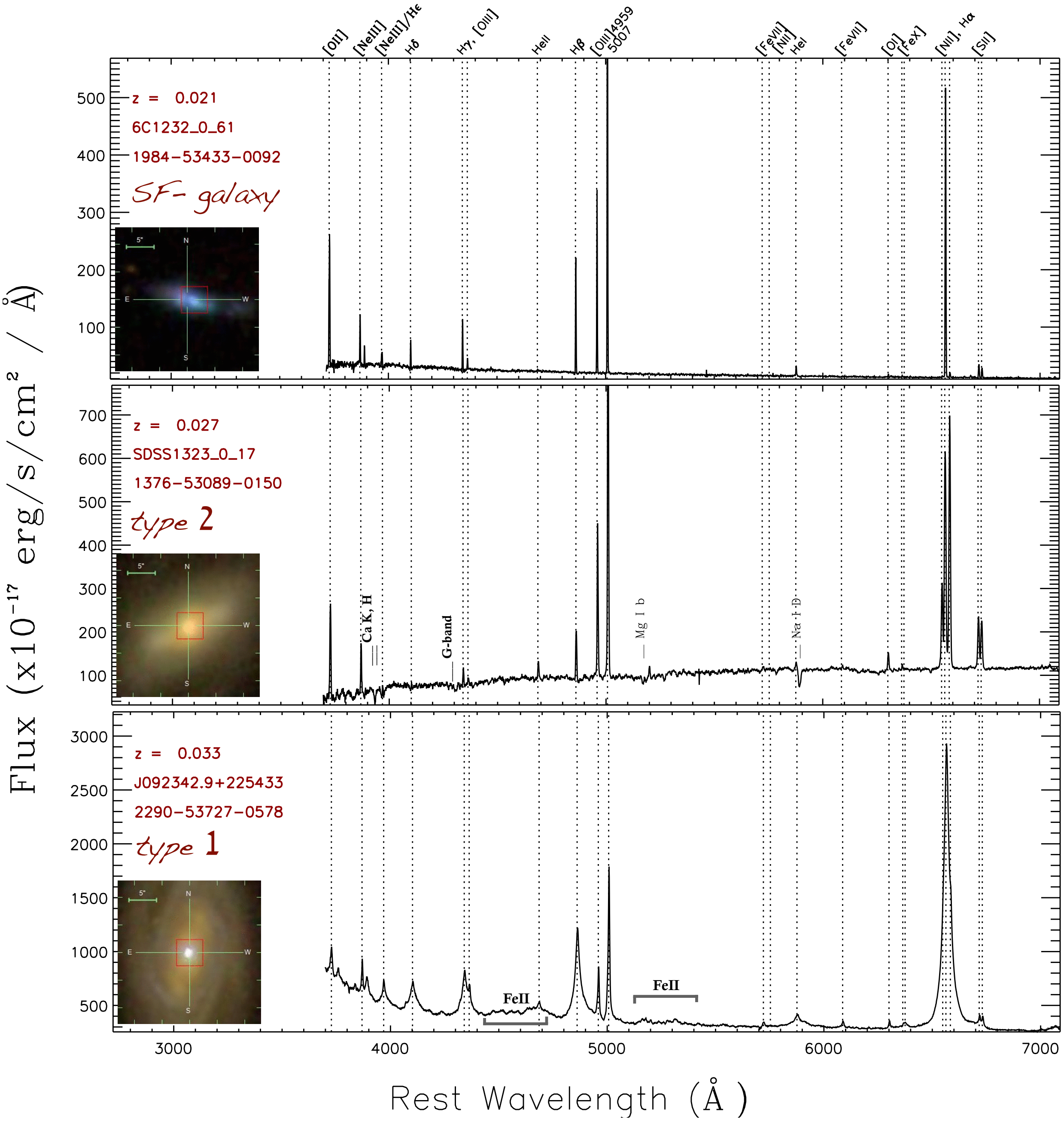

Figure 1.2: Rest-frame optical spectra extracted from the SDSS database. In each panel the redshift and the name of the source are labelled, in addition to the MJD, the plate and the fibre numbers which uniquely identifies the SDSS spectrum. The spectral classification is also showed, according to the observational scheme described in the text. The dashed vertical lines mark the location of the most prominent emission lines, besides some features crucial for the analysis presented in this thesis. The inset on the right corner of each panel shows the SDSS colour-composite cut-out of the source, with a red square marking the spatial region from which the 3″ diameter spectra has been obtained. *top panel:* Optical spectrum of a H II-like galaxy. *central panel:* Optical spectrum of a type 2 AGN, with typical stellar continuum and absorption lines (highlighted in the panel), as well as prominent AGN ionized [O III] and [N II] doublets. *bottom panel:* Optical spectrum of a type 1 AGN, with very broad Balmer lines (H$\alpha$, H$\beta$, H$\gamma$, H$\delta$), in addition to large HeI and HeII features. Permitted Fe II multiplets are labelled. A power-law continuum is also noticeable. For display purposes, the [O III]$\lambda$5007 line in the first two panels shows an intensity cut.

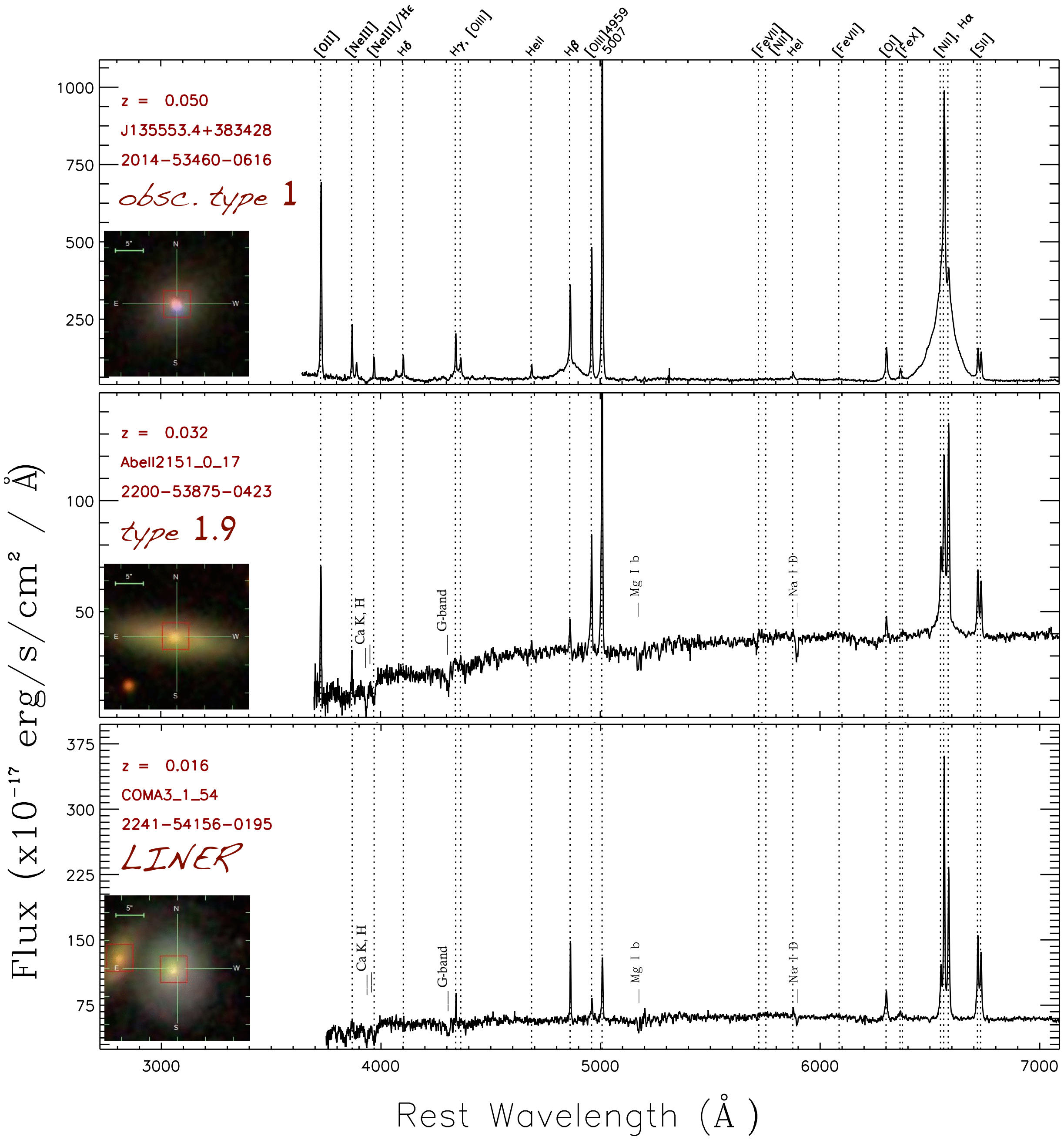

Figure 1.3: Three other examples of rest-frame optical spectra extracted from the SDSS database. See previous figure for expansive description. *top panel:* Obscured type 1 AGN spectrum, characterized by the presence of broad Balmer lines and a very flat, non-stellar continuum. *central panel*: Optical spectrum of a type 1.9 AGN, in which the broad H$\beta$ line is not detected and the continuum is dominated by starlight emission. *bottom panel:* Typical spectrum of a LINER source, with faint [O III] lines and strong low ionization [O I] and [S II] lines.

[Fe VII]$\lambda\lambda$5720,6086 and [Fe X]$\lambda$6374 are found (see Table A.1 for a list of most prominent lines in the optical-near UV region). In addition, permitted lines of Balmer series, mostly H$\alpha$ and H$\beta$, as well as He I$\lambda$5876 and He II$\lambda$4686 in the optical regime, and CIV$\lambda$1549, Mg II$\lambda$2798 in UV regime, are moderately strong. Figure 1.2 (central and bottom panels) shows typical differences between Seyfert 1 and Seyfert 2. Beyond the above mentioned broad permitted lines, many Seyfert 1 spectra show highest ionization state lines (i.e., [FeVII] , [Fe X]; see Table A.1) and broad permitted Fe II emission lines in the $4000-5500\mathring{A}$ wavelength range (Fig. 1.2, bottom panel). These emission lines come from several multiplets overlapping in two 'broad bands' near 4570 and 5200$\mathring{A}$ (Kovačević et al. 2010; see Chapter 5).

Another class of active galaxies is represented by low-ionization AGNs, or low-ionization nuclear emission line regions (LINERs; Heckman et al. 1980). These sources are usually associated with the lowest luminosity AGNs. The spectra of LINERs are dominated by low-ionization lines like [N II]$\lambda\lambda$6548,6583 and [OI]$\lambda$6300, while higher ionization lines (e.g., [OIII]$\lambda$5007) are considerably weaker than in other AGNs (see e.g., Fig. 1.3, bottom panel). Like other AGNs, LINERs can be classified into type 1 and type 2 sources, although the great majority of the discovered LINERs are type 2 (Netzer 2013).

As seen in Sect. 1.1.1, in addition to the emission lines, a power-law continuum emission is observed in most AGNs (e.g., Weedman 1977). Such emission is very strong in Seyfert 1 (Fig. 1.2, bottom panel), and most probably comes from the thermal emission originated within the accretion disk (Salpeter 1964; Zel'dovich and Novikov 1964). In type 2 AGNs the non-stellar continuum is much fainter, and in most cases can be detected only after the subtraction of the dominant stellar continuum emission (Osterbrock and Ferland 2006). In Fig. 1.2 (central panel) and Fig. 1.3 (central and bottom panels), a stellar continuum with typical absorption line features (calcium K and H, G-band, Mg I$\lambda$5175 and Na I D$\lambda$5893) together with AGN emission features can be easily identified.

The spectra of type 1 and type 2 AGNs shown in Fig. 1.2 (central and bottom panels) clearly illustrate relevant differences in emission line widths and nuclear continua. However, the division between such two classes may definitely depend on observational limitations. Low-luminosity type 1 AGNs may be easily mistaken for type 2 when stronger stellar continua hide weak broad permitted lines wings (e.g., Oh et al. 2015). If so, high spatial-resolution observations are required to avoid the extended starlight emission of the host galaxy and unveil the broad wings. Indeed, AGN emission may be dimmed due to extinction by dust. Such attenuation, taking the simple form of a power-law extinction law ($\propto \lambda^{-1}$) in the optical regime (Gaskell and Benker 2007), reddens the nuclear spectrum and fades the emission lines at lower wavelengths (Glikman et al. 2012; Netzer 2013). Emblematic examples are represented by the spectra in Fig. 1.3. The top panel shows a reddened type 1 AGN, in which broad permitted lines are associated with a very flat non-stellar nuclear continuum. The central panel shows an AGN whose continuum is dominated by starlight emission, with a broad H$\alpha$ line and basically no broad H$\beta$. Sources characterized by this peculiarity are usually referred in literature as type 1.9 AGNs, and define a subclass of type 1 AGNs. The presence of substantial attenuation by dust can be inferred thanks to Balmer decrement arguments, which relate deviations from a fixed flux ratio between H$\alpha$ and H$\beta$ ($f(H\alpha)/f(H\beta) \approx 3.1$) with the presence of extinction (see Appendix A.4). Typical extinctions observed in type 1.9 AGNs are of the order of a few visual magnitudes (Netzer 2015). The classification of such subclass of type 1 AGNs may be particularly challenging, because the detection of broad emission lines is restricted to the H$\alpha$ profile only (i.e., in the case of SDSS spectra such classification is missed at z $> 0.4$).

To summarize, high S/N and spatially resolved observations covering large wavelength range, are required to mitigate the effects of stellar light and dust attenuation and obtain correct AGN classifications (see, e.g. Sect. 2.4). For the reasons stated above, it is evident that additional indications, such as the presence of a non-stellar continuum, of emission lines typical of type 1 sources such as Fe II or other high ionization lines play an important role in such classification.

### 1.2.1 Diagnostics and Physics in Narrow-Line and Broad-line gas

The emission lines observed in optical-UV spectra contain a large amount of information about the physical conditions in the line emitting gas: the level of ionization, the electron temperature and density, the chemical composition. Such information can be derived by borrowing nebular diagnostic methods, because the emission lines observed and the abundances of elements in AGNs are much the same as in H II regions (except for the above mentioned characteristics). The study of physical conditions derived for narrow-line and broad-line gas pointed to the fact that these emission lines arise from different environments, and are characterized by proper physical and kinematic conditions. Narrow emission lines were associated with the so-called narrow line region (NLR), extended on kpc-scales, whose emission is due to interstellar gas exposed to the AGN radiation field, while broad-line gas were related with high velocity gas under the direct gravitational influence of the SMBH (at sub-pc scales), in the so-called broad line region (BLR).

The principal diagnostic methods historically used to place observational constraints on the AGN structure and the relative outcomes are briefly mentioned in this Section. Detailed discussions are reported in Appendix A.

#### Line ratio diagnostic diagrams

After the line profile classification was adopted, other criteria were proposed to distinguish between inactive and active galaxies, as well as between Seyfert and LINER galaxies. The narrow component of Balmer line to forbidden line intensity ratios were found to well correlate with AGN classes above mentioned (e.g., Adams and Weedman 1975). The diagnostic diagrams proposed by Baldwin, Phillips & Terlevich in 1981 (known as BPT diagrams) are the most widely used methods in literature. BPT are constructed on the basis of the comparison between pairs of observed line flux ratios, such as [O III]$\lambda$5007/H$\beta$ vs. [N II]$\lambda$6583/H$\alpha$, and [O III]$\lambda$5007/H$\beta$ vs. [S II]$\lambda\lambda$6716,6731/H$\alpha$. A detailed characterization of these (and other) diagnostic diagrams can be found in Appendix A.5. Here, we briefly mention that such diagnostics take into account the mean level of ionization ([O III]/H$\beta$) and the shape of the spectrum of the ionizing source (through [N II]/H$\alpha$, and [S II]/H$\alpha$ ratios). Both these physical characteristics enable the best separation between different classes of sources on the basis of the measurement of emission line fluxes (Kewley et al. 2013, 2001).

#### Ionized gas density

Electron density in the gas producing the narrow line emission can be derived through standard nebular diagnostic methods that quantify the effects of collisional de-excitation. Estimates of electron density ($N_e$) are usually obtained from the flux ratio of the [S II] doublet, $R_{SII} = f(\lambda 6717)/f(\lambda 6731)$ (see Appendix A.3 for detailed discussions). Densities of $300 - 3000$ cm$^{-3}$ have been derived for few local sources (Koski 1978; Osterbrock and Ferland 2006) and, with the advent of SDSS survey, for larger samples (Vaona et al. 2012; D. Xu et al. 2007; Z. T. Zhang et al. 2013). These authors found average $N_e$ of the order of $\sim 250 - 400$ cm$^{-3}$. Because of the unknown degree of structure within the narrow-line gas, several arguments may suggest that such diagnostic gets to underestimate of the electron density. Probably, much of the

[S II] emission arises in a less highly ionized region than other emission lines such as [O III] (Osterbrock and Ferland 2006). Therefore, the mean electron density derived from this ratio could not be representative of the entire ionized volume.

The electron density of BLR gas cannot be derived from diagnostic line ratios, but simple arguments suggest that should be associated with denser regions with respect to NLR. Such conclusions are based on the study of the critical density of forbidden [O III] (semiforbidden C III]$\lambda$1909) emission lines showing differences (similarities) in the FWHM with those of the permitted lines responsible of the BLR emission. More details are found in Appendix A, here we just state that an electron density of $10^9$ cm$^{-3}$ could be a rough estimate for the electron density of the broad-line gas.

### Ionized gas Temperature

The [O III]$\lambda$5007 line (hereafter [O III]) is seen in the spectrum of almost all AGNs. The combination with [OIII]$\lambda$4363 can be used to determine temperatures in low-density gas (i.e., $N_e < 10^4$ cm$^{-3}$; see Appendix A.2.2). Temperatures of $1.2 - 2.5 \times 10^4$ K have been derived for few local sources (Koski 1978; Osterbrock and Ferland 2006). With the advent of SDSS survey, such values have been confirmed also for larger samples (Vaona et al. 2012; D. Xu et al. 2007; Z. T. Zhang et al. 2013), with average electron temperature of $\sim 1.5 \times 10^4$ K.

There is no direct information on the temperature in the broad-line gas: no straightforward temperature diagnostics are found from permitted lines. However, an upper limit can be set thanks to the observed Fe II emission lines, which indicate $T_e < 3.5 \times 10^4$ K. In fact, assuming an electron density of $10^9$ cm$^{-3}$, the Saha equation predict that the iron would be completely collisionally ionized to Fe III for higher temperatures (Osterbrock and Ferland 2006).

These temperatures give strong observational evidence that the main source of energy input is by photo-ionization. The only other plausible energy input mechanism is the shock wave heating that, requiring much higher temperatures ($T_e > 5 \times 10^5$ K; Osterbrock and Ferland 2006), is ruled out.

### Ionized gas Mass and Size

Typical mass and size of emitting gas regions can be computed measuring the luminosity of prominent emission lines (basically, H$\beta$ and the [OIII]$\lambda$5007; Osterbrock and Ferland 2006; see Appendix B). Through the equations

$$M_{ion} \approx 2.8 \times 10^8 \left(\frac{L_{H\beta}}{10^{43}\ erg/s}\right)\left(\frac{N_e}{1000cm^{-3}}\right)^{-1} M_\odot,$$

we may estimate for the NLR, assuming typical plasma properties (i.e., $N_e$ and $T_e$) and an H$\beta$ luminosity typical for a Seyfert 1 galaxy, $L(H\beta) \approx 10^{41}$ erg/s, a ionized gas mass of $\approx 10^7$ M$_\odot$ and, assuming a spherical configuration ($V = 4\pi/3R^3$), a kpc-scale spread. Such NLR extensions have been confirmed by long-slit spectroscopy, high-resolution imaging and integral field unit studies (e.g., Hainline et al. 2014; McElroy et al. 2015; see also Fig. 1.5). This gas can not be under the gravitational influence of the central black hole and is therefore associated with host galaxy interstellar medium (ISM) photo-ionized by the AGN field. The velocity widths of such emission lines are, in fact, similar to those of the stellar absorption lines (e.g., Greene and Ho 2005).

We can estimate the mass and size of broad-line gas in a manner similar to that of the narrow-line gas, simply adopting a typical luminosity for BLR H$\beta$ is $10^{42}$ erg/s and a density of $10^9$ cm$^{-3}$: the total mass of broad line gas becomes $M_{ion} \approx 40 M_\odot$, while the size becomes $R \approx 0.07 pc$ (therefore, unresolvable with modern telescopes). The BLR velocities are of the order of those expected for rotation in the gravitational field of a black hole of $M_{BH} \approx 10^8$ M$_\odot$: an average rotational velocity of 2500 km/s at an average radius (i.e., $\approx$ 0.035 pc) corresponds to a mass

$$M_{BH} = \frac{rV^2}{G} \approx 10^8 M_\odot. \tag{1.4}$$

This significant rotational component within the broad-line gas suggests for the structure of the BLR a disk conformation, though there are recent evidences favouring both disk and symmetrical configurations (e.g., Pancoast et al. 2014, 2015). Equation 1.4, usually referred to as *virial equation*, is derived under the hypothesis of virialized orbits in the BLR and provides the only direct way to estimate the black hole mass beyond the local Universe. The $M_{BH}$ can be derived after knowing the BLR distance from the SMBH, determining the time lag between changes in the continuum emission and the corresponding variations in the broad line flux (Blandford and McKee 1982). Such technique is known as Reverberation Mapping (RM) and, in the last two decades, provided the black hole mass of $\sim$ 50 AGNs (Bentz et al. 2009; Kaspi et al. 2000). Reverberation results suggested also a dependence between the luminosity and the dimension of broad-emission gas environment, with more extended BLR in more luminous objects (Bentz et al. 2013; Kaspi et al. 2005; Saturni et al. 2016). Such $R_{BLR} - L$ relation has been used to estimate the SMBH mass from single-epoch AGN spectra, simply measuring the AGN luminosity and the BLR line width (see Appendix B for more details), unveiling the build-up of massive black holes over cosmic time (e.g., Merloni et al. 2010; Schulze et al. 2015).

All the differences in electron density, velocity regimes, extensions and gas masses prove that NLR and BLR are associated with distinct regions with different physical and kinematic conditions.

## 1.3 X-ray spectra

AGNs are the most powerful type of X-ray sources yet discovered. The primary emission observed in X-ray spectra is well represented by a single power-law of the type $L_\nu \propto \nu^{-\alpha_X}$ on the energy range $0.2 - 10$ keV, with $\alpha_X \sim 1$. Such power-law is usually expressed using the "photon index" $\Gamma$ instead of $\alpha_X$ (with $\Gamma = \alpha_X + 1$). An average spectral slope $< \Gamma >= 1.9$ has been found for large samples of Seyfert and bright quasars (Nandra and K. Pounds 1994; Piconcelli et al. 2005), with dispersions $\sigma_\Gamma \sim 0.2 - 0.3$ (Mateos et al. 2005). This index is defined such that $N(E) \propto E^{-\Gamma}$, where N(E) is the number of emitted photons per unit time and energy. Such emission is thought to originate in a corona surrounding the accretion disk where optical and ultraviolet photons from the disk are inverse-Compton scattered to higher energies (Haardt and Maraschi 1993). X-ray spectra are however characterized by additional components whose origin has been related with different processes involving the interaction of the primary power-law emission with the medium. An X-ray photon that is injected from the corona into the medium can pass directly into our line of sight, and therefore being responsible of the power-law emission observed, or be absorbed, or undergo one or more Compton scatterings with the inner side of the obscuring torus and the gas in the accretion disk. The role of such physical processes is related to the amount of obscuring material.

We have mentioned above that the distinction between type 1 and type 2 AGNs reflects also in X-ray spectra, and that an absorbing medium along the line of sight is invoked to explain such separation. X-ray astronomers prefer the use of the terms unobscured and obscured AGN instead of type 1 and type 2.

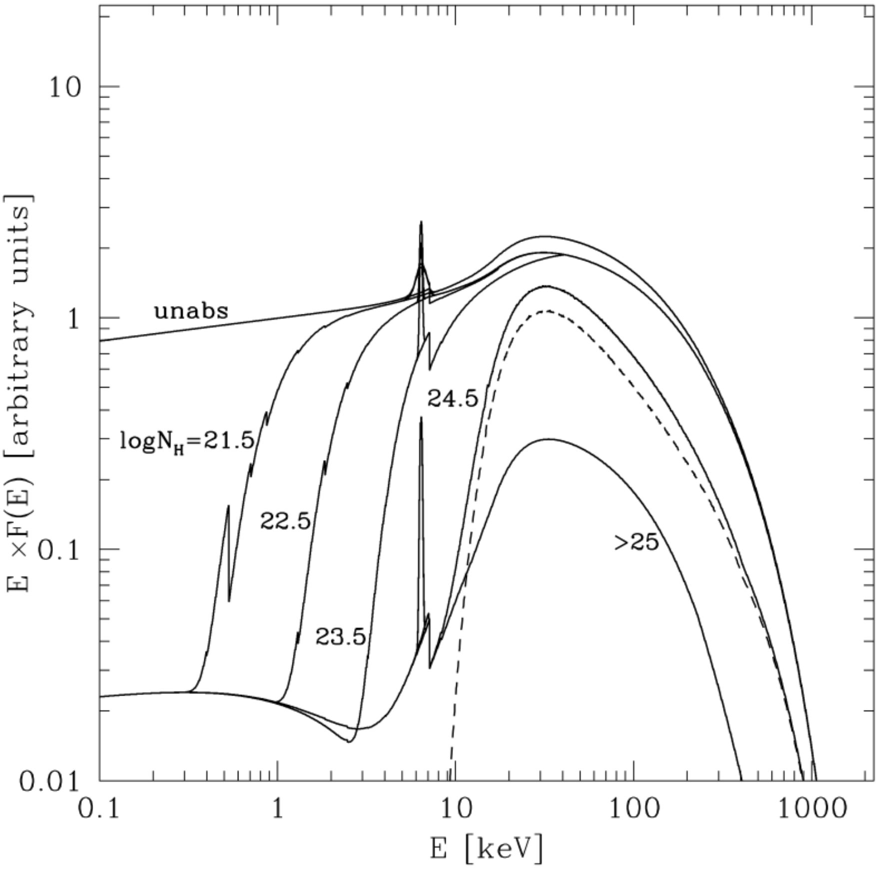

Figure 1.4: AGN X-ray spectra for different absorptions as derived from the model presented by Gilli et al. (2007). Solid lines from top to bottom mark the results obtained for an unabsorbed AGN, and for increasing column densities. In each spectrum, a 6.4 keV iron emission line is also visible.

### Unobscured AGNs

In addiction to the primary power-law, a hardening of the spectrum at $\gtrsim$ 10 keV, coupled with an iron emission line at 6.4 keV, K$\alpha$, is seen in AGN of Seyfert-like luminosity but not in bright quasars (Nandra et al. 1997; Page et al. 2005). The equivalent width (EW[4]) of K$\alpha$ is of the order of 100 eV. Both iron and additional weak continuum emission are ascribed to reprocessing by the gas in the accretion disk of the power-law photons emitted by the corona. The latter is usually referred as disk reflection component. A steepening of the spectrum is also observed at much lower energies ($\lesssim$1-2 keV; Perola et al. 2002; Piconcelli et al. 2005; Porquet et al. 2004), usually referred as "soft excess". This has been interpreted either as the exponential tail of the thermal emission from the accretion disk (Czerny and Elvis 1987) or as due to a large number of spectral features (Guainazzi and Bianchi 2007).

### Obscured AGNs

Seyfert 2 weakness in soft X-ray band is due to the photoelectric absorption cut-off related to the presence of the torus on the line of sight (LOS; Maiolino 2001). Column density typically well in excess of $N_H \sim 10^{22}$ cm$^{-2}$ are required to reproduce the observed spectra of obscured

---

[4] The equivalent width is defined as $\int(1 - f_{line}/f_{con})d\lambda$, where the $f_{line}$ and $f_{con}$ indicate the line and the continuum flux respectively. The EW is defined for absorption line systems and is therefore negative for emission features. Through the Thesis, we will implicitly refer to its absolute value.

AGNs (see Fig. 1.4). Moreover, in some cases, the hard X-ray spectrum of obscured AGNs is characterized by the presence of a well defined disk reflection component and a very strong Fe K$\alpha$, with EW$\gtrsim$>500 eV, in addiction to the absorbed ("transmitted") power-law emission. Such features can only be explained by assuming that the direct power-law radiation of the corona is totally absorbed by a Compton thick medium (i.e., $N_H = 1.2 \times \sigma_T \approx 10^{24}$ cm$^{-2}$) and that the observed (weak) continuum is instead due to reflection component. The absence of a strong continuum explains also the prominent iron emission line. A soft excess is observed also in these sources.

## 1.4 The Unified Model

Figure 1.1 shows a schematic representation of the several physical emission components described in the previous sections. The unification model for AGNs, introduced by Antonucci (1993) (see also Urry and Padovani 1995) has been able to combine the emitting/absorbing nuclear components into a general picture and to explain the multiwavelength heterogeneity in the great majority of the AGN population. The model postulates that all the observed differences between type 1 and type 2 are only due to orientation effects relative to an obscuring medium which hides the view of the inner engine (Antonucci 1993). The obscurer, historically referred to as the central torus, is also able to explain the near-IR and mid-IR thermal emission.

The first unification models were constructed following the results of various polarization experiments in the mid-1980s showing that Seyfert and LINER galaxies exhibit typical Seyfert 1 continuum and line emission in their polarized light (Antonucci and Miller 1985). This suggested that an absorber able to fully obscure the power-law continuum and the BLR but also to scatter towards us some of this buried radiation may be present in the circum-nuclear region of AGNs. More confirmation of unified models comes from X-ray observations, for which unabsorbed and absorbed X-ray AGNs are associated with optical Seyfert 1 and 2, respectively (Awaki et al. 1991).

The key ingredients of this unified model are a supermassive black hole surrounded by an optically thin accretion disk, and a geometrically (and optically) thick dusty toroidal structure[5]. Figure 1.5 shows these two key elements, as well as the previously defined NLR and BLR; it clearly illustrates how the inclination of the system to the observer's line of sight determines the observable properties. The dusty torus absorbs the photons emitted from the inner regions, i.e. the accretion disk, the hot corona and the broad line emitting gas, making all of them unobservable along some line of sight: when the view is close to the perpendicular of the torus axis, the observer recognises the source as an obscured type 2 AGN. Contrary, when the observer's view is closer to the axis of the torus, the broad lines, the accretion disk and X-ray emission are directly visible, and the observer is able to see an unobscured type 1 AGN. Whereas the innermost parts of AGNs are still unresolved and the information about their geometrical structure is just inferred by spectroscopy (e.g., with RM technique), remarkable results have been obtained in the last decades and the Unified model is nowadays supported by observations at all wavelengths. The panel in the right corner of Fig. 1.5 shows the core of NGC 4261, a galaxy hosting a type 2 LINER, observed with HST (Ferrarese et al. 1996). A dark, dusty structure whose axis is aligned with a pair of jets[6] (in the radio image) is observed.

---

[5] Ongoing research suggests a more complex geometrical distribution, with dust distributed in clumps instead of homogeneously filling the torus volume (e.g., Hönig et al. 2006; Mor et al. 2009).

[6] The unified model is also capable to explain the differences between radio loud AGNs and "high-excitation radio galaxies" (Fig. 1.5, upper part in the cartoon), characterized by high-excitation lines and radio emission typical of AGNs, but without BLR emission.

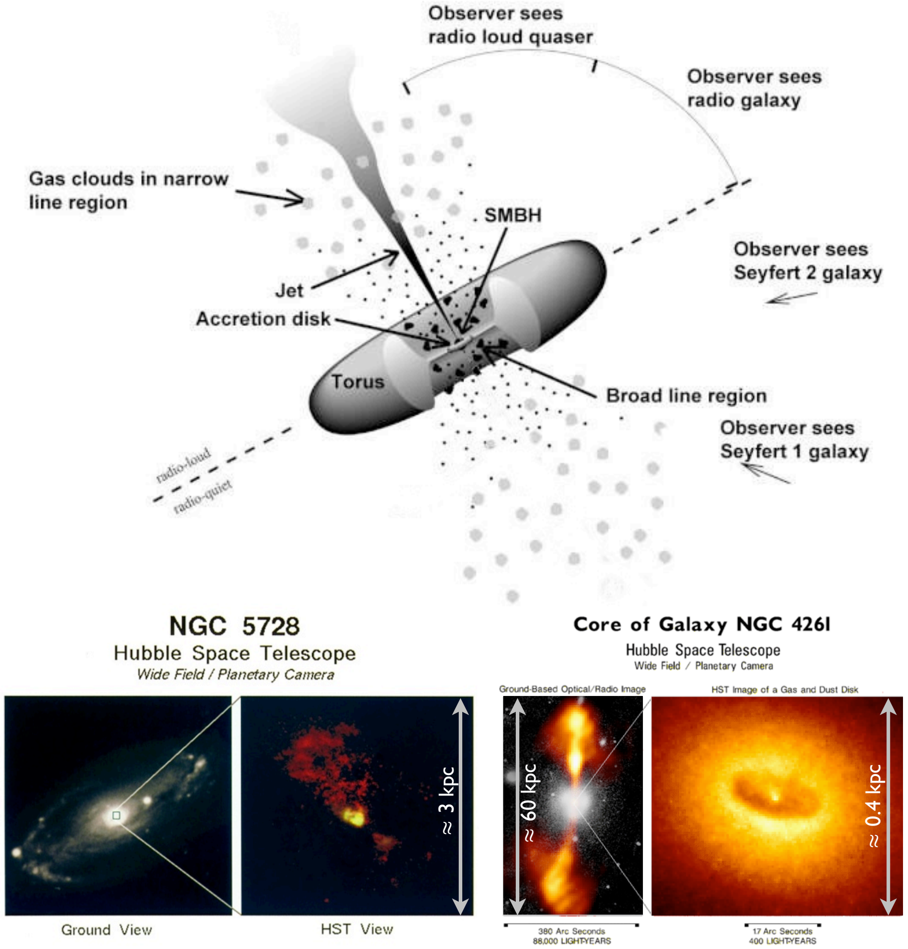

Figure 1.5: Schematic representation of an AGN, adapted from Urry and Padovani 1995. The image shows the main ingredients of the unification scheme and how the viewing angle of the torus determines the type of AGN, for both radio loud (upper part of the cartoon, showing the radio jet) and radio quiet AGNs (lower part). The lower inset on the left shows the nuclear regions of NGC 5728, in which the bi-conical structure delineating the NLR is traced by the [O III] emission (figure from http://hubblesite.org/newscenter/archive/releases/1993/15/image/a/). The lower inset on the right displays the core of NGC 4261, in which a circum-nuclear dusty structure is visible (Ferrarese et al. 1996).

Indeed, the typical size of the toroidal absorbers is found to be large enough to obscure the BLR, with typical size of the inner wall of the order of $0.1 - 1$ pc (Burtscher et al. 2013), hence standing an important observational test of the unification scheme. The presence of a torus can also easily explain the (bi-)conical morphology of NLR, as the ionizing radiation escapes along the polar axis of the obscuring structure. Bi-conical structures are usually observed with high-resolution, narrow band imaging of HST in many nearby AGN (see Fig. 1.5, inset on the left; Fig. 1.6).

### 1.4.1 Beyond the the Unified Model

Although this simple unified model can account for several observational properties of AGNs, some open issues point to the need of more complex/different AGN structures. High-resolution observations of many nearby ($z < 0.05$) AGN (e.g., Fischer et al. 2013; Müller-Sánchez et al. 2011) show that the axis of the ionization cones of the NLR is often not aligned with that of the gaseous disk of the host galaxy, meaning that the toroidal absorber orientation may not necessarily depend on that of the host disk (see, e.g., Fig. 1.6). This scenario opens to possible misunderstanding in the structure of complex systems: it is difficult to discriminate between a galaxy-scale absorber and the presence of a torus, which can be both as well responsible for AGN signatures typical of type 1.9 and type 2 sources. In fact, type 1.9 AGNs are thought to be reddened by galactic scale dust or by the external part of the torus, while highly inclined galaxies may determine a galactic extinction so large that it can completely obscure the central AGN emission at optical wavelength (Goulding & Alexander 2009). The cut-outs associated with the spectra shown in Figs. 1.2 and 1.3 clearly manifest this ambiguity.

Other open questions on the unified model are still to be answered: a large number of Seyfert 2 galaxies lack the broad emission lines in their optical polarized spectra (but see Antonucci 2012); it is not clear how the internal structure involving accretion disk, BLR and NLR, torus, change with the AGN accretion properties. Important clues regards also observational results clearly in disagreement with the unification model: the measurements of black hole mass from near-IR spectra of Seyfert 2 reveal that these objects have, on average, lower masses than type 1 objects (Onori et al. 2016). Moreover, strong differences in the clustering properties of Type-1 and Type-2 AGNs suggest that the AGN type is in some way dependent on the presence of neighbours (e.g., Villarroel and Korn 2014). Finally, the X-ray spectra of a large number ($\sim 30\%$) of type 2 AGN do not indicate large column densities of absorbing gas, as would be expected if the AGN were surrounded by an obscuring torus (Merloni et al. 2014). Altogether, these findings suggest that the single unified model based solely on orientation arguments is not sufficient and that an evolutionary link between the two major AGN types might exist.

## 1.5 SmBH-galaxy co-evolution

Almost every massive galaxy host a supermassive black hole ($M_{BH} = 10^6 - 10^9$ $M_\odot$) at its centre (Magorrian et al. 1998, Kormendy and Ho 2013 an references therein), presumably a relic of previous AGN or quasar activity (Soltan 1982). At the present time, there are several theoretical results that suggest that galaxies and their black holes growths might be intimately connected. The mutual dependence of galaxy star formation and AGN activity on the availability of cold gas has been indicated as the possible source of such connection (Madau and Dickinson 2014; Vito et al. 2014), although the vastly different spatial scales at which SF (kpc) and SMBH (sub-pc) operate make the scenario challenging. Recent observational

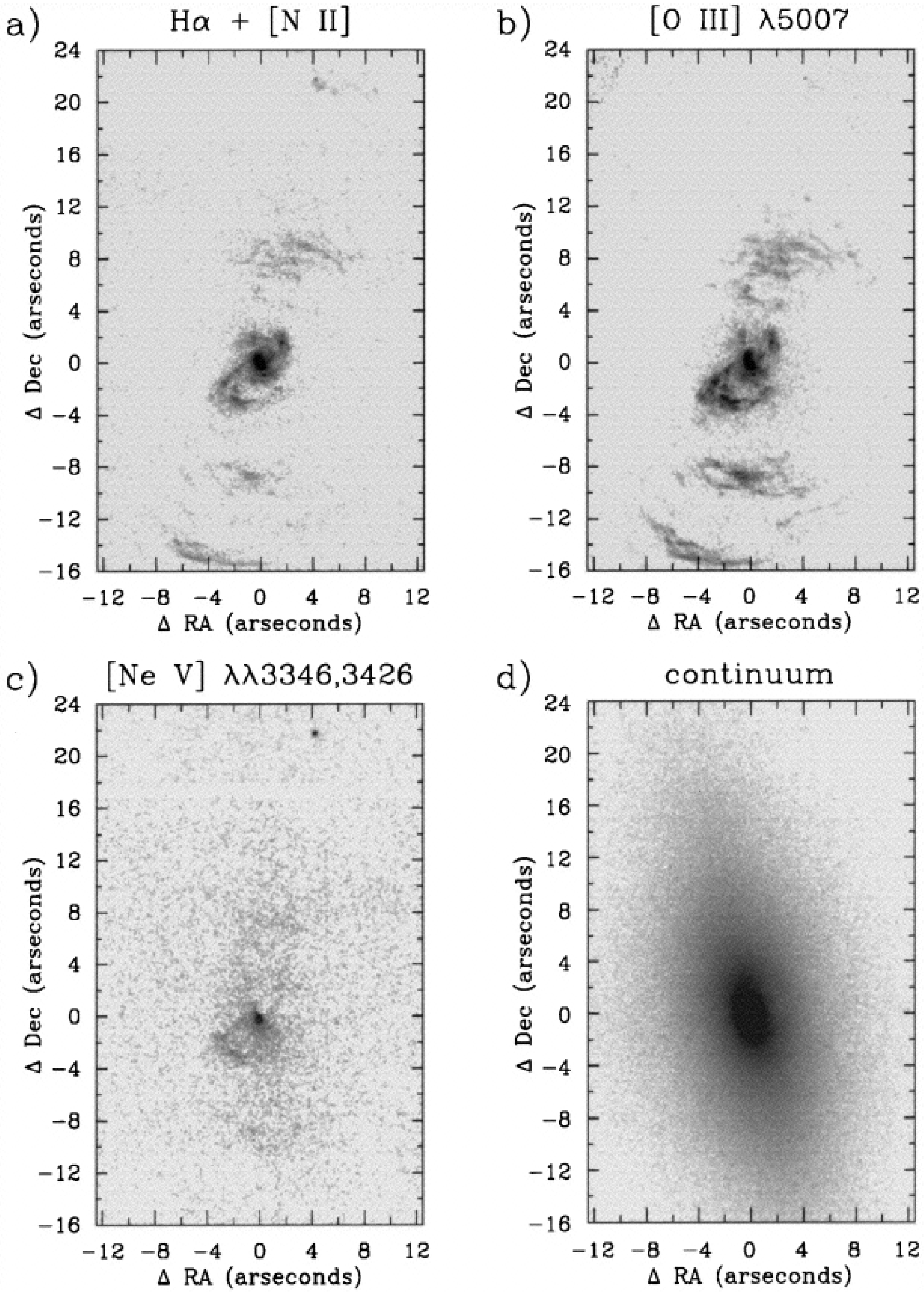

Figure 1.6: HST images of NGC 5252 in different narrow-band filters. NLR emission in a bi-conical morphology extending out to ∼ 5 kpc from the central SMBH is observed in low and high-ionization state lines. The emission form the higher ionization line [Ne V] is instead more compact (∼ 1 kpc). Continuum emission is also shown (d); the galaxy major axis seems quite close to the NLR bi-conical axis. Figure from Morse et al. (1998).

progresses have revealed several strong pieces of evidence suggesting that galaxies and SMBHs indeed co-evolve by regulating each other's growth.

This section summarizes some observational and theoretical evidences that support such a co-evolutionary scenario. Feedback phenomena will be then introduced as the key actors that could have established a long-lasting link between hosts and BH.

**Scaling relations:** The seminal discovery (almost 20 years ago) by Magorrian et al. coupled with the identification of a tight correlation between the black hole mass and the mass of the host bulge, with the BH mass being about a few thousandths of the mass of the spheroidal bulge (then confirmed by several authors: e.g., Marconi and Hunt 2003, Kormendy and Ho 2013 and reference therein). Such reciprocity was then followed by other similar correlations, between $M_{BH}$ and the stellar velocity dispersion ($\sigma_*$) of the bulge component of the host galaxy (Ferrarese and Merritt 2000; Gebhardt et al. 2000; Heckman et al. 2004), and with bulge luminosity (see Kormendy and Ho 2013 for a review).

**Cosmic BH and star formation accretion history:** The cosmic mass accretion history of massive black holes can be inferred using the “Soltan argument” (Soltan 1982), which posits that most galaxies went through phases of AGN activity in the past, the remnants of which are the quiescent SMBH in z = 0 galactic nuclei. It permits to relate the quasar bolometric luminosity density to the rate at which mass accumulates into black holes. In Fig. 1.7, several recent determinations of the massive black hole mass growth rate are compared with the SFR density (Madau and Dickinson 2014). Both star formation and black hole accretion history follow similar general trends and peak around z ∼ 1-2 and then decline rapidly towards the present day. Moreover, the cosmic star formation history and the black hole accretion history preserve roughly a ratio of 1:1000, which notably corresponds to the $M_{BH} - M_{bulge}$ relation, whose existence is also often invoked as evidence for co-evolution. Although speculative, this result could be interpreted as evidence that, in a volume-averaged sense, BHs and galaxies have been synchronized, remaining on the local black hole to bulge relationships over the last ∼ 11 Gyrs (e.g., Mullaney et al. 2012). However, these results do not tell us what sets this relation. Cosmic downsizing observed both in SMBH and galaxies (see, e.g., Delvecchio et al. 2014; La Franca et al. 2005), adds another observational argument suggesting such connection.

**Galaxy mass function:** The observed stellar mass function is very different to the halo dark matter mass function predicted by $\Lambda-$CDM (grey line in Fig. 1.8). In particular, observations show a steep decline of the stellar mass function at low and high masses. Even though semi-analytical models have shown that stellar feedback from supernovae can reproduce the inefficient star-formation at low luminosity regimes, removing large amounts of gas (Bolatto et al. 2013; Cicone et al. 2014; Sakamoto et al. 2014), such processes on their own cannot reproduce the break at high galaxy luminosities ($L \gtrsim 10^{12}$ $L_\odot$), without adding an additional source of energy (Benson et al. 2003; Gabor et al. 2011).

The answer to all these issues requires some sort of long-lasting self-regulation mechanism acting between the SMBH and its host galaxy. More recently, the review of Kormendy and Ho (2013) showed that the scaling relations do not affect galaxies with pseudo-bulges, and are instead specific of elliptical and classical bulges galaxies[7]. Theoretical and numerical arguments demonstrate that bulges and elliptical galaxies formed in the same way, when dynamical violence

---

[7] Observationally, pseudo-bulges can be distinguished from classical bulges and ellipticals as having a disc-like morphology, flatter surface brightness profiles and being more rotationally supported (Kormendy and Ho 2013)

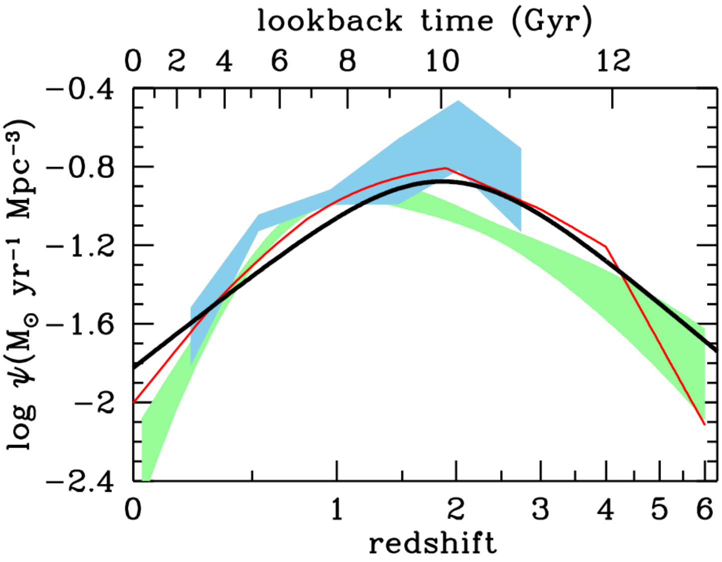

Figure 1.7: Comparison of star formation history derived by Madau and Dickinson (2014) (thick solid curve) with the massive black hole accretion history, both from X-ray observations, from Shankar et al. 2009 (red curve) and Aird et al. 2010 (light green area), and infrared data, from Delvecchio et al. (2014) (light blue area). The shading regions indicate the $1\sigma$ uncertainty range on the total bolometric luminosity density. The comoving rates of black hole accretion is scaled by a factor of 3300 for display purposes. Figure from Madau and Dickinson (2014).

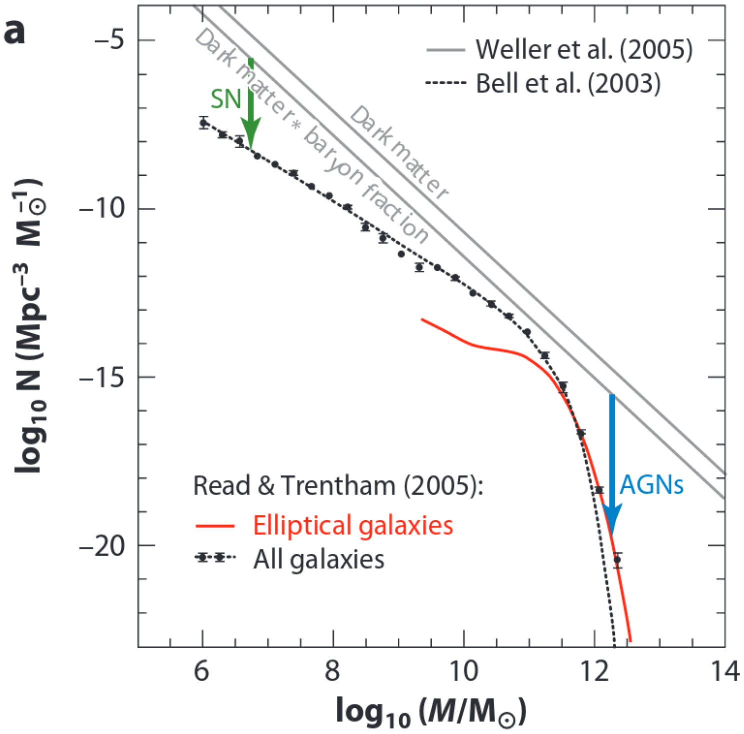

Figure 1.8: Galaxy baryonic mass function (black points; from Read & Trentham 2005) fitted with a Schechter (1976) function, compared to the mass spectrum of cold dark matter halos from numerical simulations scaled with the cosmological baryonic fraction $f_g = 0.163$ (Planck Collaboration et al. 2014). Green and blue arrows represent the effects of stellar and AGN feedback processes in semi-analytical models required to reproduce the observed stellar mass function, respectively. Figure from Kormendy and Ho (2013).

of major galaxy mergers scrambles disks into ellipsoids, while pseudo bulges are due to slow secular processes within disc galaxies (Kormendy and Kennicutt 2004). Wet galaxy mergers can easily account co-eval rapid black hole and bulge growth. In fact, during the initial phases of the merger, a large amount of gas is funnelled into the nuclear regions, favouring both AGN and SF activity. During these stages, a strong physical coupling (generally termed "feedback") could have established, emerging in the nowadays observed link between the SMBH and the host galaxy.

## 1.6 The feedback process

In order to drive the observed SMBH-galaxy scaling relations, it is expected that the black hole communicates its presence to the host galaxy. The sphere of influence of the SMBH is significantly smaller than the bulge ($\sim 3$ order of magnitude; A. King and K. Pounds 2015); this argument rules out the possibility that the source of this connection is gravitational.
The Soltan argument has led to the development of models where large-scale feedback processes self-regulate both the AGN activity and the bulge growth when the SMBH has reached a critical mass (e.g., Di Matteo et al. 2005; A. King 2003; Silk and Rees 1998). The basic argument is as follows: if the BH is accreting near the Eddington limit, then the accretion luminosity $L \propto M_{BH}$ (see Eq. 1.2) and the energy released is

$$E_{BH} \approx \eta M_{BH} c^2 \sim 2 \times 10^{61} M_8 \; erg \tag{1.5}$$

(where $M_8$ is the black hole mass in units of $10^8$ M$_\odot$). The binding energy[8] of the bulge can be derived assuming that the black hole is close to the $M_{BH} - M_{bulge}$ relation, $M_{bulge} \sim 10^3 M_{BH}$:

$$E_{bulge} \sim M_{bulge} \sigma_*^2 \sim 8 \times 10^{58} M_8 \sigma_{200}^2 \; erg, \tag{1.6}$$

with $\sigma_{200} = \sigma_*/200$ km/s. From this equation, using the gas fraction, $E_{gas} = f_g E_{bulge}$, with $f_g = 0.162$ (the cosmological mean value; Planck Collaboration et al. 2014), we obtain the gas binding energy,

$$E_{BH} \sim 10^3 E_{gas}, \tag{1.7}$$

with an implicit factor $\propto 1/\sigma_{200}^2$. Thefore, if some fraction (a few percent) of the AGN radiant energy can couple to the surrounding material, it will be comparable to the gas binding energy.

These simple arguments suggest that when the SMBH reaches some critical limit at about $10^{-3}$ M$_{bulge}$, the AGN energy can have noticeable effects on the host heating up and/or ejecting the gas from the galaxy, terminating the growth of both SMBH and galaxy. Large-scale AGN-driven outflows observed in AGNs (see next Section) provide the most compelling indication of the existence of effects in the host ISM due to the AGN activity. However, the overall picture in terms of relative coupling between the released energy and the ISM, of the long-lasting effects of these outflows on the host galaxy, is vague. Moreover, different mechanisms have been proposed to explain feedback processes. At least two major modes have been identified: the first is the *radiative mode*, also known as the quasar or wind mode, which operates in a typical bulge when the accreting black hole is close to the Eddington limit. It is associated with wide-angle outflows, driven by the radiative output of the AGN, which can expel most of the gas in the host galaxy (e.g., A. King and K. Pounds 2015). The second mode is the *kinetic mode*, also known as the radio, or maintenance mode. This typically operates in more

---

[8] The relation is derived combining the binding energy of a spherical distribution $E = GM_{bulge}^2/r$ with the escape velocity $v = \sqrt{2GM/r}$.

massive galaxies with hot halos (or in galaxies at the centre of a group or cluster of galaxies) and the accreting black hole has powerful jets. It tends to occur at a lower Eddington fraction and is mostly concerned with efficiently suppressing the cooling of hot gas, resulting in the regulation of SF and SMBH growth (e.g., R. J. Dunn and Fabian 2006, 2008; Schindler et al. 2001; Wagner and Bicknell 2011 for both theoretical and observational results). Figure 1.9 shows three different examples of outflow phenomena observed by high resolution imaging, displaying major differences between radiative and radio mode. We note that the presence of powerful jets can be both associated with radiative and kinetic modes, with the solid differences in the accreting ratios and the physical scales explained above. Through this thesis we focus on the study of radiative mode outflows, which occur in late-type galaxies and can be therefore associated with the initial phases of the co-evolution, when the scaling relations are established.

## 1.7 The "evolutionary sequence"

"AGN feedback" nowadays features in many theoretical, numerical, and semi-analytic simulations of galaxy growth and evolution (e.g., Ciotti et al. 2010; Croton et al. 2006; Di Matteo et al. 2005; Granato et al. 2004; Hopkins et al. 2006; Kauffmann and Haehnelt 2000; Scannapieco et al. 2012; Sijacki et al. 2015; Springel et al. 2005) and gives rise to the observed scaling between SMBH mass and stellar velocity dispersion found in bulges and elliptical galaxies. Simulations follow the assembling of a massive galaxy, starting from major gas-rich mergers[9]. Fig. 1.10 shows one representation, among many similar others, of the evolutionary sequence postulated by simulations. After the early stages of the merger, represented in Fig. 1.10 by $a$, $b$ and $c$ panels, the system is characterized by a rapid and efficient ($\lambda_{Edd} > 0.1$) accretion onto the SMBH ($d$ panel). This short-lasting ($\sim 10^8$ yr, e.g. Hopkins et al. 2008) phase is also characterized by the presence of powerful star formation enshrouded in dense dusty environments and fuelled by huge amounts of gas and dust. These systems are commonly identified as sub-millimeter galaxies (SMGs) and Ultra Luminous InfraRed Galaxies (ULIRGs; Sanders and Mirabel 1996); observations often show disturbed morphologies consistent with galaxy mergers, both in local and high-redshift sources (Alexander et al. 2005; Engel et al. 2010; Laird et al. 2010; Tacconi et al. 2008; Urrutia et al. 2009). Moreover, the majority of them are frequently associated with luminous, often obscured quasars, overall supporting a coherent SMBH−SF growth (Sanders et al. 1988).

When the accreting black hole reaches its critical mass, the system crosses a very short-lasting ($\sim 10^7 - 10^8$ yr) "blow-out" phase (Fig. 1.10; panel $e$), during which the energy output of the SMBH couples to the different phases of the ISM. As a consequence, such galaxy-wide outflows are expected to quench the galaxy SF, by reheating the gas or pushing it out of the galactic potential well. At this point the accretion on the SMBH is expected to be at its maximum and, from an observational point of view, should be revealed as a blue unabsorbed type 1 AGN or an obscured type 2 AGN (Fig. 1.10; panel $f$), depending on the line of sight through the torus. When the accretion stops, the galaxy evolves passively to the massive early type systems we observe today in local galaxies, with a central quiescent SMBH (Fig. 1.10; panel $h$).

In the evolutionary scenario, the nuclear obscuration changes dramatically with time during the SMBH active phases (see, e.g., Hopkins et al. 2005, fig. 2). Reddened AGNs are associated with early-stage merging systems, during which large amount of gas is channelled in the central

---

[9] Galaxy merger is considered to play an important role in triggering ULIRGs and quasars, but bar-driven and minor merger interaction-driven fuelling mechanisms could be at the origin of nuclear activity in Seyfert and low-luminosity AGNs.

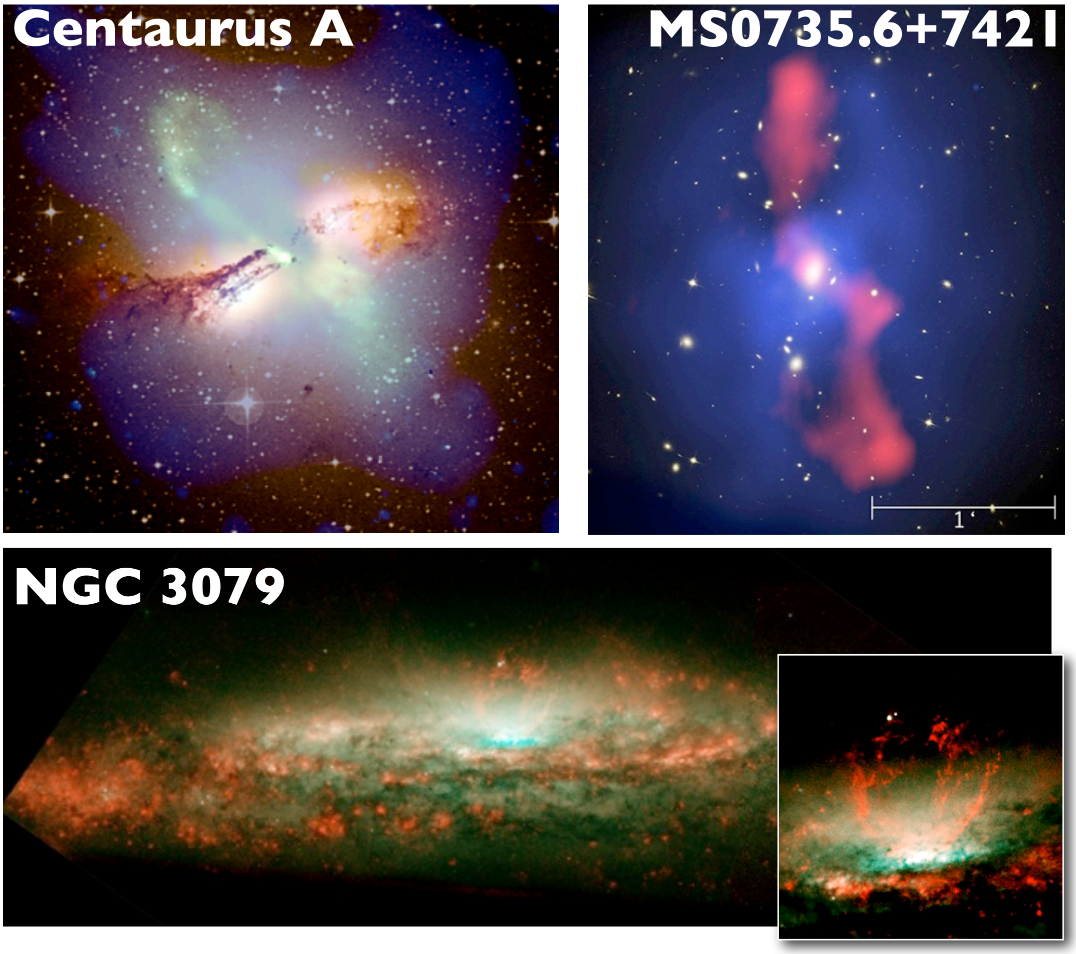

Figure 1.9: High resolution images of nearby galaxies hosting SMBH powering wide-scale outflows, by both *kinetic mode* (MS0735.6+7421) and *radiative mode* (Centaurus A and NGC 3079). (*top left:*) Centaurus A galaxy hosting a radio loud AGN. The composite image is obtained combining Chandra X-ray (blue), SDSS optical (yellow and orange), NRAO VLA radio [green, for continuum emission; pink for 21-cm emission] observations. A central radio core within the extended dust disk as well as two radio jets are distinguishable. Image for `http://chandra.harvard.edu/photo/2002/0157`. (*top right:*) Inner $\sim$ 200 arcsec (700 kpc) of the MS0735.6+7421 cluster at z=0.22, presented by McNamara et al. (2009) and obtained combining the Chandra X-ray (blue), HST/ACS I-band (white), and VLA radio wavelengths (red). Large pair of X-ray cavities are filled with radio emission. The X-ray cavities produced by AGN jets (as shown in the panel) are at the origin of the feedback process in the kinetic mode. (*Bottom panel:*) Composite HST image of NGC 3079, a radio faint Seyfert 2 galaxy at z=0.004. [N II]$\lambda$6583+H$\alpha$ emission lines (red) and I-band (green) trace the high-ionized regions and starlight, respectively. The inset shows a zoom in the nuclear region. Narrow ionized outflowing filaments rise above the galaxy disk forming a V-shaped pattern. The same configuration has been found also in X-ray and radio emission (Cecil et al. 2001; Veilleux et al. 2005). NGC 3079 has both nuclear starburst and intense AGN activity and it is still not clear if the observed outflow is starburst or AGN-driven (see Shafi+2015). Figures from `http://chandra.harvard.edu/photo/2003/ngc3079/more.html`.

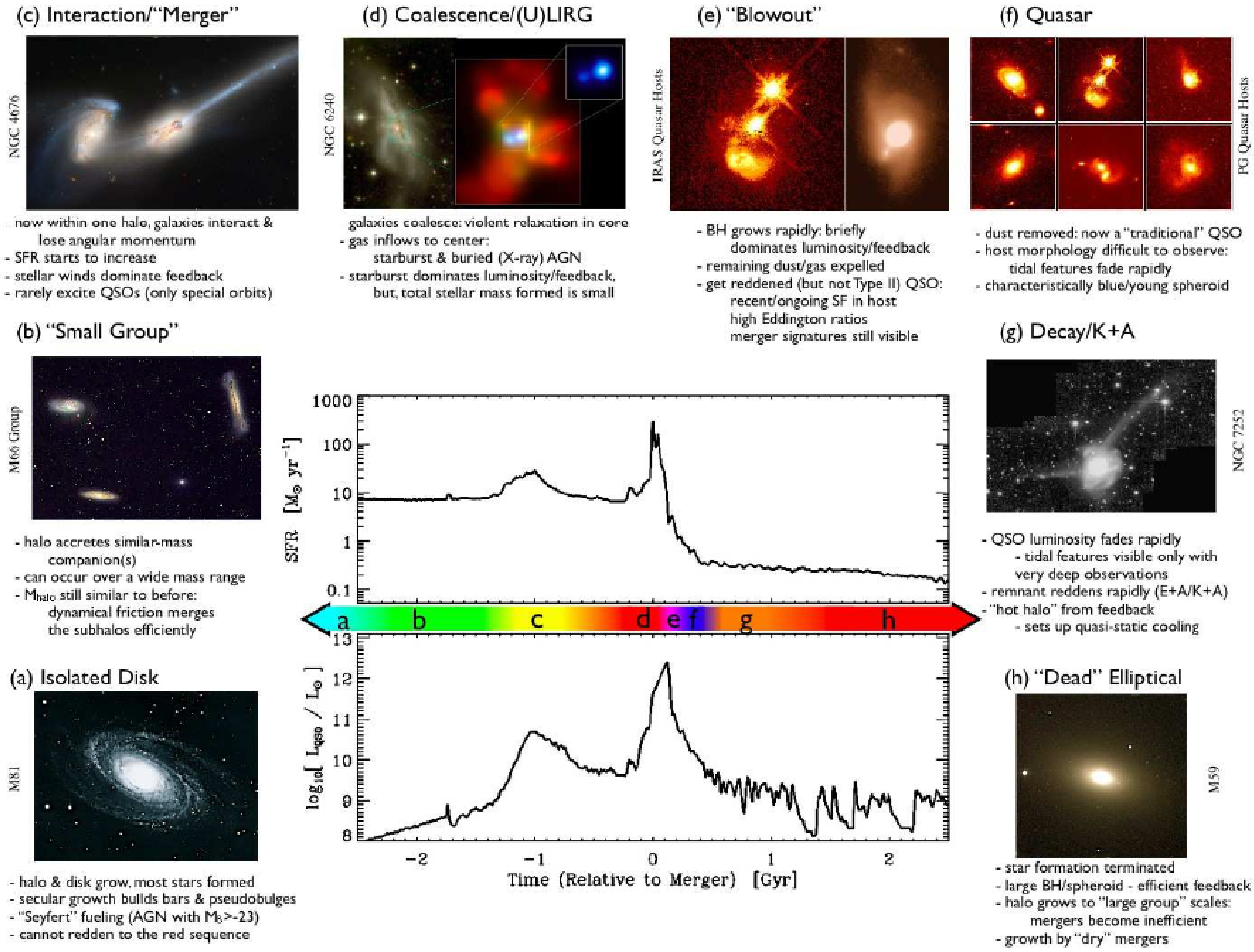

Figure 1.10: Schematic outline of the phases of growth in a "typical" massive galaxy undergoing a gas-rich major merger. From an isolated disk galaxy, the sequence shows how close approach galaxy-galaxy passages ($c$ phase) induce SF and BH activities, as displayed in the central panel, where the SFR and AGN bolometric luminosity are plotted as function of time. The sequence then shows how the system evolve through the coalescence/ULIRG ($d$) phase, during which larger amount of gas is channelled in the central regions and the released energy is dominated by star forming processes while the BH is buried by high column densities, the blow-out ($e$) phase, associated with the presence of large scale outflows expelling the gas reservoirs, and the unobscured QSO ($f$) phases, until the final stages resulting in a dead elliptical galaxy. Figure from Hopkins et al. 2008

regions and the observed extinction is hence due to large-scale dust environments. During these stages, it is supposed that even the presence of a well defined torus may be questionable, because of the perturbed phases after a merging event (Netzer 2015). Then, after the blow-out phase, the absorbing material is not extended over the entire host galaxy any more and, we can actually observe an AGN as type 1 or a type 2 depending on the inclination of the torus with respect to the LOS. This scenario is able to explain the differences between type 2 and type 1 black hole masses and clustering properties (see Sect. 1.4.1). However, it is clear that a detailed physical assessment of the dust distribution, the total gas reservoir of the system, the black hole and bulge masses, is crucial to our understanding and to discriminate between the two scenarios, i.e. between obscuration due to LOS intercepting a torus or due to the perturbed early-stages of a merger.

Though it is today well established that the evolution of active SMBHs is connected to the evolution of their hosts, the underlying mechanisms explaining their mutual connection and some key features common to most models are still poorly constrained. Differences in the details of the physical conditions in the system, coupled with different model assumptions (such as the time-scale of the processes, the fraction of the energy released and the physical mechanisms that can link such energy with ISM, the lag between SF and AGN activity) translate into the fact that the host properties of QSOs experiencing the outflow phase may indeed scatter substantially in the different models (see e.g. Hickox et al. 2014; Lamastra et al. 2013).

## 1.8 Outflows

According to radiative mode predictions (see above), powerful winds are expected in the blow-out phase (see A. King and K. Pounds 2015 and Fabian 2012 for recent reviews). These winds can expel most of the gas in the host galaxy, which is therefore not available any more to sustain SF and the BH growth, explaining the termination of the two processes. Powerful outflows sustained by relativistic and collimated jets in the hosts of luminous radio galaxies have been commonly observed out to z $\sim$ 4 (see e.g., Fu and Stockton 2009; Nesvadba et al. 2011, 2008). Outflowing winds in radio-quiet objects, which are more representative of the AGN population, are instead less commonly observed. Only very recently spatially resolved optical, far-infrared (FIR) and millimetre spectroscopic studies convincingly showed evidences for the existence of energetic outflows, both in the local Universe (e.g., Cicone et al. 2014; Feruglio et al. 2010; Fischer et al. 2013; Harrison et al. 2014; McElroy et al. 2015; Rodríguez Zaurín et al. 2013; Rupke and Veilleux 2011; Villar-Martín et al. 2011; Westmoquette et al. 2012; K. Zhang et al. 2011), and at higher redshift (e.g Carniani et al. 2015; Collet et al. 2016; Harrison et al. 2012, 2016; Kakkad et al. 2016; Maiolino et al. 2012).

These winds are detected via observations of line features showing complex shapes, resulting from the combination of a distinct, prominent Gaussian profile (in emission or in absorption, according to the nature of the species transition) and heavy asymmetric wings, widely extending at bluer and (occasionally) redder wavelengths. Given that these line broadening can hardly be ascribed to gravitational motions (see Appendix A.2.1), they are interpreted as tracing the kinematics of large-scale energetic gas flows. In these gas flows, the blue asymmetry is interpreted as fast material moving towards our line of sight, while the receding gas expected in the case the ejected material is receding from us is responsible of the red asymmetry. As an example, we show in Fig. 1.11 the powerful outflow observed by Nesvadba et al. (2008) in a radio loud AGN at z = 2.44, MRC0404 − 244. The spatially integrated spectrum in the lower panel shows asymmetric profiles in [O III], historically associated with outflows (e.g., Aoki et al. 2005; Zamanov et al. 2002), with a FWHM of 1350 km/s. Integral Field Unit

(IFU) spectroscopic analysis reveals how these features are associated with the presence of complicated kinematics over kpc-scales, with line splitting and velocity offsets of the order of several hundreds of km/s (see the inset in the lower panel). The velocity maps in the upper panels show a bipolar emission with velocity offsets (left) and FWHM (right) of the order of $1000 - 1200$ km/s and extended out to $\sim$ 10 kpc from the nucleus. Such ionized material is probably launched by the collimated jets, as suggested by the fact that [O III] emission is perfectly tracing the observed radio emission (black contours in the velocity maps).

These results represent a clear evidence of the existence of a connection between ISM conditions and AGN activity. The characterization of such outflows, the study of their effects on the host galaxy, the determination of the main properties of AGN and host galaxy experiencing the feedback phase, are imperative to improve our knowledge of the main processes responsible for the AGN-galaxy co-evolution.

## 1.9 Thesis overview

In this Introduction Chapter we have discussed the physical and observational properties of AGN, including different useful diagnostics. In order to understand the role of outflows in shaping galaxies, the first crucial point is to select AGNs in the blow-out phase, possibly at the epoch of peak of galaxy and SMBH assembly, when major mergers play a significant role (e.g., Hopkins et al. 2006). Prototypes of sources carefully selected as candidate targets in the blow-out phase have been studied in the last years, both locally and at high redshift (see Chapter 2 for a short review). However, earlier works biased the analysed samples towards particular properties and, chiefly, also the characterization of the outflows; to test co-evolutionary models, we need to select and isolate different populations of active galaxies in the different phases of the AGN-galaxy co-evolution, starting from their predicted conditions (Sect. 1.7). Given that the sources in the feedback phase are expected to be dusty and reddened (either by the host galaxy or the torus), the study of obscured AGNs represents a good starting point.

We test distinct selection criteria combining flux ratios, colours and line strengths to search for objects in different phases of the AGN-galaxy sequence, from highly obscured, starburst/quasar phase to the almost unobscured QSO stage associated with likely completely suppressed star formation activity (Fig.1.10). The first three criteria take advantage from multiwavelength information collected in the COSMOS field. In fact, the large body of XMM-COSMOS state-of-the-art multiwavelength information allowed us to devise robust methods to isolate candidate objects transitioning from being starburst dominated to AGN dominated, i.e. exactly in the phase when powerful outflows driven by the SMBH are expected (Chapter 2, **??**) or in the prelude of this phase (Chapter 4). The fourth criterion is instead based solely on X-ray detection and exploit the SDSS spectroscopic database.

In Chapter 2 we show the VLT/X-shooter follow-up observations of 10 objects, representative of the entire population of luminous, obscured QSOs at z $\sim$ 1.5. These sources are selected adopting the criterion introduced by Brusa et al. (2010) and based on the observed red colours and high X-ray-to-optical and mid-infrared-to-optical flux ratios. We unveil the presence of ionized outflowing material in 6 out of 8 targets, confirming the efficiency of this selection criterion. Slit resolved spectroscopic analysis is also presented for the two brightest AGNs in this sample, XID 2028 and XID 5321. This technique allows us to probe the ISM conditions handling sufficiently the nuclear contamination and to study the complex emission and absorption line kinematics associated with the presence of spatially extended outflows.

In Chapter **??** we propose a new selection criterion to isolate sources in the blow-out phase. It is based on X-ray detection coupled to extreme [O II]$\lambda\lambda$3726,3729 equivalent widths, probing the AGN accretion activity and the ongoing SF in the AGN-galaxy system. We present the high-resolution adaptive optics (AO) data obtained with Subaru/IRCS and VLT/SINFONI of a prototypical target selected as the most extreme object of this selection criterion, XID 5395. Our analysis reveals kinematic complexities and asymmetries in and around the nuclear regions associated with a powerful, wide angle outflow. All the nuclear and host galaxy properties we derive from our analysis fit with the transition phase of feedback in the AGN-galaxy co-evolutionary path.

In Chapter 4 we report new VLT/SINFONI AO-assisted observations of 4 highly obscured/CT QSOs, selected as extreme mid-infrated-to-optical objects from the 24$\mu$m Spitzer MIPS survey. Such criterion, introduced by Fiore et al. (2008), should be able to detect buried AGNs in the prelude of the blow-out phase. We combine SINFONI observations with ancillary multi-wavelength data to probe the highly obscured nature of these sources, discuss their physical properties and, in particular, to unveil the presence of ionised outflowing gas in dust enshrouded environments. The constraints we obtained from our targets and from other comparative samples from the literature suggest that optically faint, luminous infrared galaxies hosting obscured AGNs, may represent a brief evolutionary phase between the post-merger starburst and the unobscured QSO phase. In only one target, MIRO 20581, we clearly resolved a fast (1600 km/s) and extended ($\sim$ 5 kpc) outflow.

In Chapter 5 we present a large sample of X-ray selected AGNs at $z < 0.8$ from the SDSS database. The incidence of ionized and atomic outflows are derived and related to the AGN type, distinguishing between type 1 and type 2 AGNs, and different AGN power tracers. We also derive average values for the plasma properties of outflowing gas.

Finally, in Chapter 6 we discuss our results in the context of recent observational and theoretical issues.

* * *

This Introduction Chapter is mostly based on the text books by Osterbrock and Ferland (2006) and Netzer (2013).

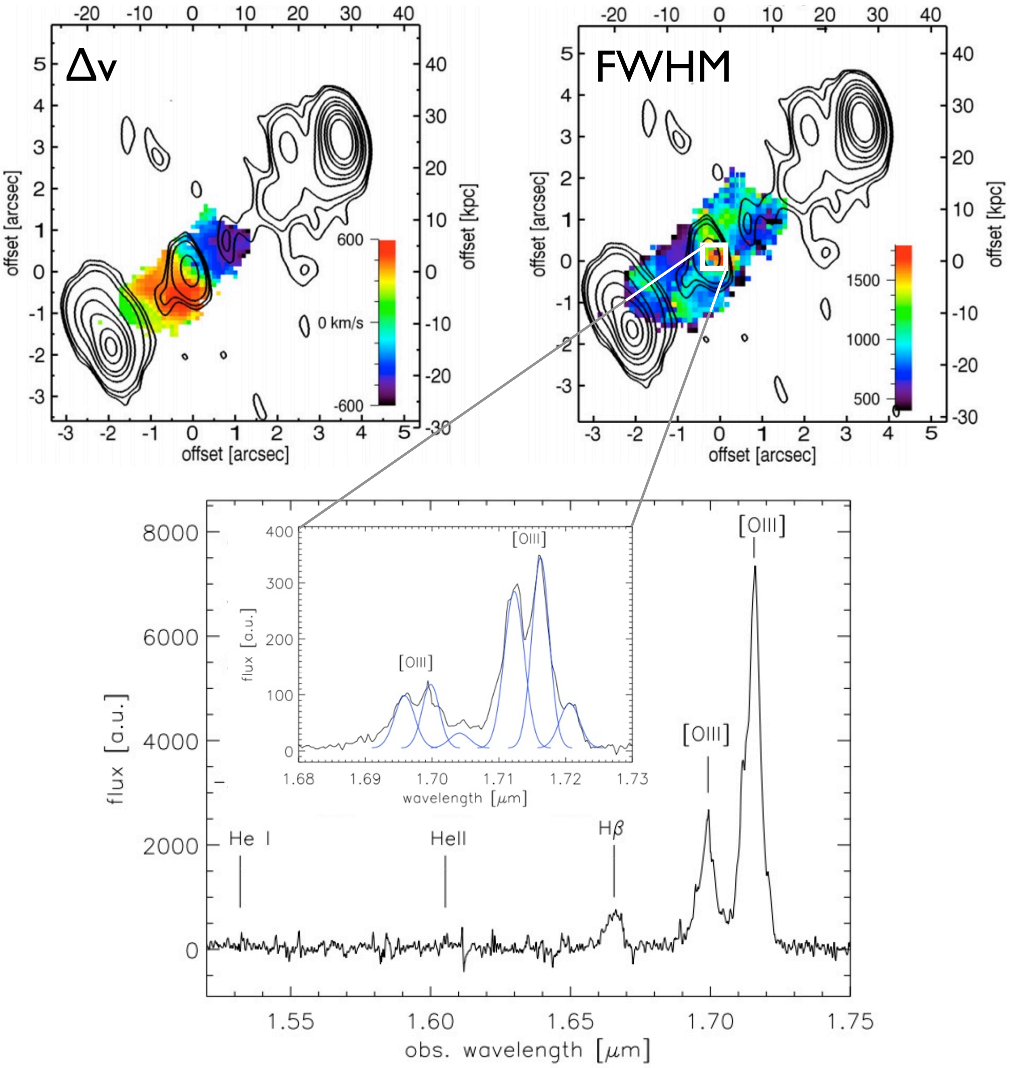

Figure 1.11: (*top panels:*) [O III] emission line velocity maps of MRC0404 − 244 for both velocity offsets (left) and FWHM (right). Colour bars show the velocity in km/s; contours indicate the 1.4 GHz flux, tracing the nuclear and the extended jet emission. (bottom panel:) Nuclear [OIII] doublet emission of MRC0404 − 244, showing line splitting for both the doublet components. Blue Gaussian profiles mark three separate kinematic components required to reproduce the total profiles. Figures from Nesvadba et al. (2008).

## Chapter 2

# Powerful outflows in z $\sim$ 1.5 X-ray selected obscured quasi-stellar objects

## Abstract

According to the most popular AGN-galaxy co-evolutionary models, the transitioning phase from starburst to AGN dominated systems is associated with a powerful, obscured and dust-enshrouded accreting supermassive black hole. The selection criteria introduced by Brusa et al. (2010), based on X-ray detection at bright fluxes ($L_X \gtrsim 10^{44}$ erg/s) coupled to red optical-to-near-infrared and optical-to-mid-infrared colours, are designed to isolate z $\sim$ 1.5 quasi-stellar objects (QSOs) with such characteristics. We present X-shooter observations of a sample of 10 luminous, X-ray obscured quasars from the XMM-COSMOS survey, selected on the basis of the above mentioned criteria. X-shooter spectroscopic information confirm the obscured nature of the sample, including type 2 and moderately reddened type 1 (and 1.9) AGNs. We report the detection of significant emission in [O III]$\lambda$5007 line wings, resulting in sharply asymmetric profiles, for six out of eight sources with this feature observable in regions free from strong atmospheric absorptions. The full width at half-maximum (FWHM) associated with the wings components are in the range $900 - 1600$ km/s, comparable to those observed for QSO/ULIRG systems for which the presence of kpc-scale outflows has been revealed through integral field unit (IFU) spectroscopy. The prototypical X-ray bright, obscured quasar, XID 2028, as well as a second bright quasar showing similar properties, XID 5321, have been studied with slit-resolved spectroscopic analysis. This technique allows us to unveil the spatial extension of the outflow emission out to $\sim$ 10 kpc from the central black hole. Interestingly, we also detect kpc scale outflows in the [O II]$\lambda\lambda$3726,3729 emission lines and in the neutral gas component, traced by the sodium I D and magnesium absorption lines in the UV/optical regime, confirming that a substantial amount of the outflowing mass is in the form of neutral gas. We infer the gas outflow velocities and kinetic powers, under reasonable assumptions on the geometry and physical properties, for the entire sample of sources experiencing outflows. Overall, the high outflow velocities ($V_{out} > 1000$ km/s) and the presence of strong winds also in objects undetected in the far-infrared, suggest they are due to AGN accreting energy and not to stellar processes.

.

## 2.1 Introduction

We have seen in the Introduction Chapter that, according to the most popular AGN-galaxies co-evolutionary models, the first phases of the QSOs life are associated to rapid SMBH growth and efficient SF in a dust-enshrouded, dense environment. These initial stages are followed by the "blow-out" or "feedback" phase during which the SMBH releases radiative and kinetic energy in the form of powerful winds, before becoming a "normal" unobscured AGN once the obscuring material has been cleared out (see, e.g., Fig. 1.10). In this framework, AGN feedback should be revealed through the presence of outflowing material driven by energetic winds (see, e.g., Fabian 2012; Zubovas and A. King 2012). However, these outflows could also be powered by SF activity (e.g., Heckman et al. 1990; Veilleux et al. 2005) and it is not fully understood the relative dominance of the two different mechanisms involved. Regardless of their nature, during the peak of star formation ($z \sim 1.5-3$; Fig. 1.7) outflows are believed to play a pivotal role in shaping galaxies, and much effort, both observational and theoretical, is underway to quantify the relative dominance of the different mechanisms involved.

Several well-defined classes of objects have been proposed in the recent past as prototype of candidate sources in the outflowing phase. For example, Lípari and Terlevich (2006) first proposed that broad absorption line quasars (BAL QSOs; e.g. J. P. Dunn et al. 2010) may be objects in the transition phase between the ULIRGs and unobscured QSO phase, where the outflowing wind in the ionized component is seen directly in optical-ultraviolet (UV) spectra (e.g. de Kool et al. 2001; Hamann et al. 2002). Recent works also suggest that about 40 % of infrared (IR) selected and Sloan Digital Sky Survey (SDSS) QSOs are BAL QSOs, pointing towards the fact that they are quite common (J. T. Allen et al. 2011; Dai et al. 2008) and that the outflow and unobscured phases may be of comparable length, in agreement with the Hopkins et al. scenario (see also Glikman et al. 2012). Moreover, from the analysis of [O III] luminosity matched obscured and unobscured samples of QSOs at $z \sim 0.5$ presented in Liu et al. (2013) and Liu et al. (2014), it has been proposed that high luminosities ($L[O\ III] > 10^{43}$ erg/s) are characteristic of the peak of quasar feedback phase (see also Chapter 5). Given that the sources in the feedback phase are expected to be dusty and reddened (either by the host galaxy or the torus), another class of objects proposed to be in the transition phase are the 'red QSOs', selected from large area, bright IR surveys such as Two Micron All Sky Survey (2MASS) or UKIRT Infrared Deep Sky Survey (UKIDSS), on the basis of a red colour in the near-infrared (NIR) band (e.g. $J - K \gtrsim 2$) indicative of a steep spectral energy distribution (SED) due to obscured AGN (Banerji et al. 2012; Glikman et al. 2012; Urrutia et al. 2009). Detailed high-resolution imaging, spectroscopy or morphological follow-up of carefully selected prototypes of this class of sources at various redshifts convincingly favour such an interpretation (e.g. Banerji et al. 2014; Urrutia et al. 2012). Finally, another well-studied class of objects are the SMGs associated with ULIRGs and luminous QSOs mentioned above. Only recently, with the advent of high resolution and sensitive NIR spectrographs, it has been possible to break the $z > 1$ barrier and characterize the neutral and ionized kinematic components of luminous high-z quasars and SMGs by sampling the redshifted optical lines in the NIR band (e.g. Alexander et al. 2010; Cano-Díaz et al. 2012; Carniani et al. 2015; Collet et al. 2016; Cresci et al. 2015a; Harrison et al. 2012, 2016; Kakkad et al. 2016; Perna et al. 2015b).

Luminous X-ray selected obscured AGNs with red colours also represent optimal targets for objects where feedback from the AGN is expected to halt SF and to start cleaning out gas from the galaxy. Indeed, in the AGN evolutionary framework described above, the obscured phase of a quasar corresponds to a time when the SMBH is accreting mass very rapidly and at the Eddington limit (Hopkins et al. 2005), implying that the black hole should manifest itself as a

X-ray quasar. In this respect, while most if not all of the studies at z > 1 have been performed on QSO/ULIRGs and objects undergoing intense SF, a selection based on the X-ray emission offers the advantage of being independent of the SF properties, which, in principle, cannot be predicted a priori for the QSOs in the feedback phase (see Sect. 1.7).

In a previous work based on XMM-Newton observations of the Cosmic Evolution Survey (COSMOS) field (Scoville et al. 2007b), Brusa et al. proposed a criterion to isolate such very rare objects, on the basis of their observed red colours and high X-ray to optical and/or mid-infrared (MIR) to optical flux ratios (Brusa et al. 2010). The combined analysis of a high-resolution Keck spectrum, morphology from Hubble Space Telescope (HST)/Advanced Camera for Surveys (ACS) data and an accurate SED fitting of the prototype of this class of sources (XID 2028) convincingly showed that the proposed criteria appear robust in selecting promising objects in the blowout phase (see section 9 in Brusa et al. 2010).

In this Chapter we present the data reduction and analysis of X-shooter observations at the Very Large Telescope (VLT) of the 10 brightest obscured QSOs at z ∼ 1.5 in the XMM-COSMOS survey, focusing on the detection of the broad and shifted components in [O III] lines. For the two brightest sources, XID 2028 and XID 5321, we present also slit resolved analysis. A more detailed investigation of both atomic and ionized features in the UV/optical wavelength range is exposed. The results enabled a comprehensive understanding of the winds physics, in terms of spatial location, ionization level and energetics involved in both the gas components.

The Chapter is organized as follows: Section 2.2 presents the sample selection, Section 2.3 the AGN and host galaxy properties. Section 2.4.1 introduce the X-shooter observations and the fitting prescriptions used through this Thesis. In Sect. 2.4.2 and 2.4.3 we show the spectroscopic analysis results and compare our results with literature. Section 2.5 present the multiwavelength data analysis and the slit-resolved spectroscopic investigation for the two brightest, representative targets, XID 2028 and XID 5321. Finally, in Sect. 2.6 we discuss the main results and their implications.

## 2.2 Sample selection

The XMM-COSMOS survey (Cappelluti et al. 2009; Hasinger et al. 2007) consists of ∼1800 X-ray AGN selected over the entire 2 deg$^2$ COSMOS field, with complete multiwavelength data from radio to UV, including spectroscopic and photometric redshifts, as well as morphological classification, accurate estimates of stellar masses, star formation rate (SFR) and IR luminosities (see B10; Bongiorno et al. 2012; Lusso et al. 2012; Rosario et al. 2012; Salvato et al. 2011; Santini et al. 2012). In particular, the XMM-COSMOS survey has the combination of area and depth necessary to sample with the adequate statistics rare objects (such as those expected in the feedback phase discussed above) otherwise missed in pencil-beam surveys such as the Chandra Deep Fields (see e.g. Alexander and Hickox 2012 for a review). In addition, the XMM-COSMOS survey sample obscured objects at lower intrinsic luminosity ($L_{bol} \sim 10^{45} - 10^{46.5}$ erg/s), more representative of the entire luminous QSO population than the 'monsters' accessible from larger area IR surveys, such as, e.g., the Wide-field Infrared Survey Explorer (WISE) targets, with $L_{bol} > 10^{47}$ erg/s (Weedman et al. 2012; see also Banerji et al. 2012). In Brusa et al. (2010) it was presented a sample of about 150 candidate obscured AGNs isolated from the entire XMM-COSMOS sample, on the basis of their observed-frame X-ray (X-ray to optical flux ratio X/O> 10), mid-infrared (24 $\mu$m/O > 1000), near-infrared (R - K > 5 or R - [3.6] > 4) and optical properties (following Brusa et al. 2005; Fiore et al. 2003, 2009; Mignoli et al. 2004). In Fig. 2.1 are plotted the selection regions in the two diagnostics described above that we used to select our X-shooter targets. The small empty circles in this plot

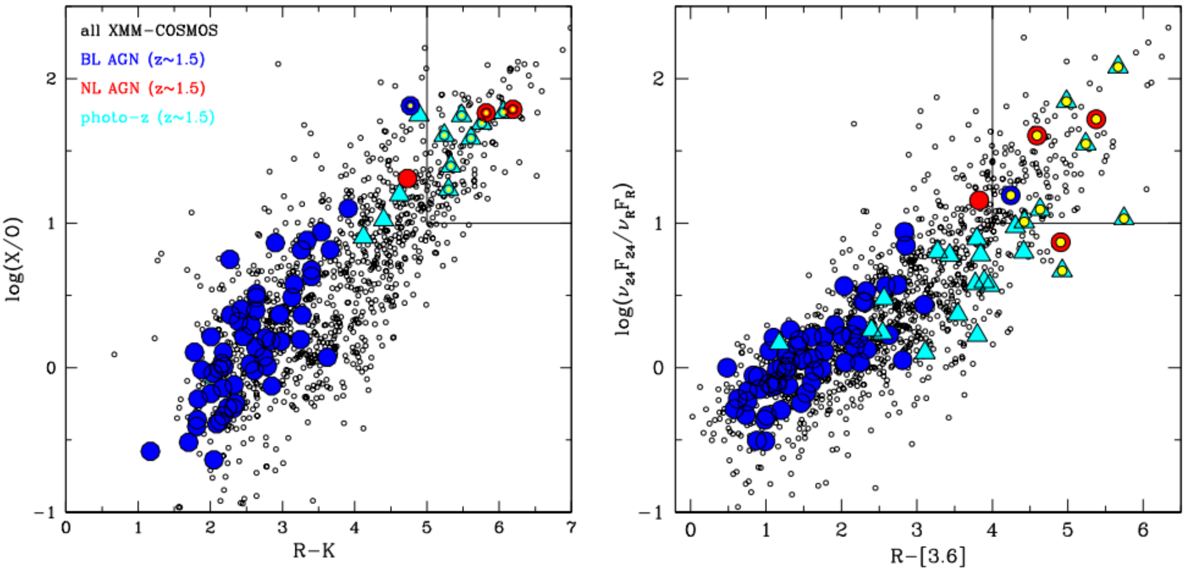

Figure 2.1: Selection region for the X-shooter targets. (a) X-ray to optical flux ratio versus R - K (Vega) colour and (b) 24 $\mu$m to optical flux ratio versus R - [3.6] colour for all the XMM-COSMOS sources (small empty circles) and for those with redshift in the range z = 1.25-1.72, K $<$ 19 and $f_{2-10,rest} > 5 \times 10^{-15}$ erg/cm$^2$/s (large symbols). Blue circles denote spectroscopically confirmed BL AGN, red circles spectroscopically confirmed NL AGN and cyan triangles objects with only photometric redshifts. The yellow circles are the obscured AGN candidates proposed for the X-shooter observations, e.g. sources with photometric redshifts which satisfy one (R - K $>$ 4.5 and X/O $>$10) or the other (log($\nu_{24} f F_{24}/\nu_R f_R > 1$ and R - [3.6] $>$ 4) selection criterion.

represent the full XMM-COSMOS population; from this original sample, were selected all the sources with K magnitude lower than 19, de-absorbed rest frame $f_{2-10} > 5 \times 10^{-15}$ erg/cm$^2$/s, and redshifts in the range $1.25 - 1.72$, such that their H$\alpha$ and [O III] lines are expected to lie in regions free from strong atmospheric absorptions. This sums up to a total of 12 objects proposed for X-shooter observations, of which 10 were then observed (see Brusa et al. 2015). The 10 targets comprise: three spectroscopically confirmed type 2 obscured AGNs (XID 2028, XID 60053, XID 5053) selected on the basis of the lack of broad emission lines (C IV, Mg II) in the available optical spectra, one type 1 AGN (XID 18), and six objects with only photometric redshifts. In Fig. 2.1, objects marked with large symbols are those satisfying the conditions above mentioned: blue circles denote spectroscopically confirmed broad-line AGNs, red circles spectroscopically confirmed narrow-line AGNs and cyan triangles objects with only photometric redshifts. The yellow circles are the obscured AGN candidates observed by X-shooter.

Our sample is similar in size, but more homogeneous in the selection, with respect to the sample presented in Harrison et al. 2012 (10 objects), which represented, at the time of publication, one of the most recent analysis and study of [O III] profiles in high-z (z $\sim$ 2) SMG/AGN systems. The sample is also similar in size to the sample of heavily reddened quasars at z $\sim$ 2 selected from the UKIDSS Large Area Survey (ULAS; Banerji et al. 2012; 12 objects). We note that, although our sources on average show lower/bluer near-IR colour than the colour cut used in Banerji et al. 2012 ($J - K > 2.5$), they actually populate the same region of other color-magnitude diagnostics (e.g., $I - K$ versus $I$-band, see Banerji et al. 2012, fig. 2), extending to faint magnitudes given the deeper limiting fluxes of COSMOS with respect to ULAS. In fact, our prototype source (XID 2028) is also selected as a red quasar from ULAS (ULAS J1002+0137) and is part of the Banerji et al. sample. The most important properties

Table 2.1: Main accretion and hosts galaxies properties for our 10 X-shooter targets.

| (1) | (2) | (3) | (4) | (5) | (6) | (7) | (8) | (9) | (10) | (11) |
|---|---|---|---|---|---|---|---|---|---|---|
| XID | RA | DEC | z | lg($L_X$) | lg($N_H$) | lg($M_*$) | SFR | $S_{1.4GHz}$ | lg($L_{AGN}$) | L/$L_{Edd}$ |
|  | hms | dms |  | erg/s | $cm^{-2}$ | $M_\odot$ | $M_\odot$/yr | $\mu$Jy | erg/s |  |
| 18 | 10:00:31.93 | 02:18:11.8 | 1.598 | 44.9 | 22.5 | 11.39 | 4.9 | $< 80$ | 46.2 | 0.5 |
| 60053 | 10:01:09.25 | 02:22:54.7 | 1.582 | $> 43.5$† | [**] | 11.17 | 740* | 718 | 46.1 | 1.0 |
| 175 | 09:58:52.97 | 02:20:56.4 | $1.55^p$ | 44.7 | 21.4 | 11.55 | 1.4 | $< 80$ | 45.6 | 0.10 |
| 2028 | 10:02:11.27 | 01:37:06.6 | 1.592 | 45.3 | 21.9 | 11.67 | 275* | 102 | 46.3 | 0.05 |
| 5321 | 10:03:08.83 | 02:09:03.5 | $1.27^p$ | 45.7 | 21.6 | 11.56 | 230* | 180 | 46.3 | 0.01 |
| 5053 | 10:01:29.03 | 01:57:11.6 | 1.374 | 44.3 | 23.2 | 11.03 | $< 1$ | $< 80$ | 45.3 | – |
| 5325 | 10:02:18.83 | 02:46:04.3 | $1.43^p$ | 43.1 | 20.0 | 11.19 | 28.8 | $< 80$ | $44.6^a$ | 1.0 |
| 5573 | 09:58:07.15 | 01:47:08.5 | $1.66^p$ | 44.4 | 22.2 | 10.91 | 16.5 | $< 80$ | 45.1 | – |
| 54466 | 10:02:25.34 | 02:26:14.1 | $1.47^p$ | 43.8† | 23.2 | 10.93 | 107* | 191 | 45.2 | – |
| 31357 | 10:01:34.97 | 02:38:07.3 | $1.71^p$ | 44.5 | 23.2 | 11.24 | $< 1$ | $< 80$ | 45.3 | – |

Notes and column description: (1) XID from Brusa et al. 2010; (2,3) optical coordinates (J2000); (4) redshift available before the X-shooter run ($^p$ marks photometric redshifts); (5,6) X-ray luminosities ($L_X$, unobscured) and column densities are in the $0.5 - 10$ keV rest frame range and are obtained from proper spectral analysis if available (Mainieri et al. 2011) or from rest frame flux corrected from absorption as inferred from the hardness ratio (sources marked with †, following Merloni et al. 2014). The source marked with a double asterisks (**) is a candidate Compton Thick AGN. (7) Stellar masses are from Bongiorno et al. (2014; first 3 sources) or Bongiorno et al. (2012; last 5 sources), computed from SED fitting and assuming a Chabrier IMF. XID 2028 and XID 5321 stellar masses are from Perna et al. (2015a) (see Sect. 2.5); (8) SFR are from Bongiorno et al. (2012) or Bongiorno et al. (2014). Sources marked with an asterisk (*) are those with detection in PEP. (9) The 1.4 GHz flux is taken from the VLA survey of COSMOS Schinnerer et al. 2010. (10) Bolometric luminosity from SED fitting as derived from Lusso et al. (2012); for the source marked with $^a$, $L_{bol}$ is derived from $L_X$ and a $k_{bol} \sim 20$; (11) Eddington ratio. The first 5 sources above the horizontal line are those with BH masses measurements presented in Bongiorno et al. (2014).

of the targets are reported in Table 2.1, and discussed in detail in the next section.

## 2.3 Host galaxy and AGN properties

For all the targets, host galaxies stellar masses ($M_*$) and SFR based on galaxy and AGN decomposition were taken from Bongiorno et al. (2014, 2012), or re-obtained following the same prescriptions for those sources for which we could provide new spectroscopic redshifts. All our targets have $M_*$ in the range $10^{11} - 10^{12}$ $M_\odot$. The SFR and stellar mass properties of our targets are shown in Fig. 2.2, where we plot the 'starburstiness' RSB = sSFR/sSFRMS of the host galaxies versus $M_*$. The specific star formation rate (sSFR = SFR/$M_*$) of our targets is normalized assuming the best-fit of the galaxy main sequence (MS) as a function of redshift obtained by Whitaker et al. (2012). Four of the targets (XID 5321, XID 2028, XID 60053 and XID 54466) are detected in the PACS Evolutionary Probe (PEP) survey by Herschel/Photodetector Array Camera and Spectrometer (PACS) in at least one band (Lutz et al. 2011; Santini et al. 2012). For these objects, the SFR was re-obtained by fitting PACS fluxes (see Brusa et al. 2015). Our targets are marked in Fig. 2.2 by blue symbols; those detected in the PEP survey have been highlighted by a red star. From this figure it is possible to see that, with the exception of XID 60053 which is above the MS, our targets lie in or below the MS of star-forming galaxies at z $\sim$ 1.5 as defined by the black line (Whitaker et al. 2012). For the six PEP undetected sources, we report in Fig. 2.2 two values of RSB (paired by solid lines): the lower one is obtained using the SFR obtained from SED fitting while the upper one is plotted assuming a SFR $\sim$ 70 $M_\odot$/yr, corresponding to the PEP stacked signal detected at $\sim 3\sigma$ level. Even if the SFR from SED fitting were severely underestimated, the PEP stacked signal confirms that these systems are not above the MS. In particular, the four objects with SFR $< 10$ $M_\odot$/yr ($\log(RSB) < -1$; see Table 2.1), may be in their way to be quenched (see also Mainieri et al. 2011; Mignoli et al. 2004). In contrast, the SMG/ULIRG sample presented in Harrison et al. (2012) is on average above the MS of star-forming galaxies at the same redshift ($z \sim 2.2$; see red shaded area in Fig. 2.2). In the same plot we also show the loci occupied by two other samples we will use in the following as comparison: the green area marks the locus occupied by the eight massive star-forming galaxies presented in Förster Schreiber et al. (2014), while the black area marks the mass range of MS star-forming galaxies presented in Kashino et al. (2013). Differently from Harrison et al. (2012), for which a radio detection was imposed to conduct the integral field unit (IFU) follow-up, only 40 % of our objects (all those detected also in PACS) are detected in the radio band at 1.4 GHz in the Very Large Array (VLA) observations of the COSMOS field (Schinnerer et al. 2010). The radio powers observed in our sample place these objects below the radio-loud class; moreover they are also one order of magnitude fainter than the high-z radio galaxies and the SMG/ULIRGs discussed in Harrison et al. (2012) (see their fig. 1b). In particular, the low level of radio emission (apart from XID 60053) assures little or marginal contribution from radio jets in the energetic of the systems.

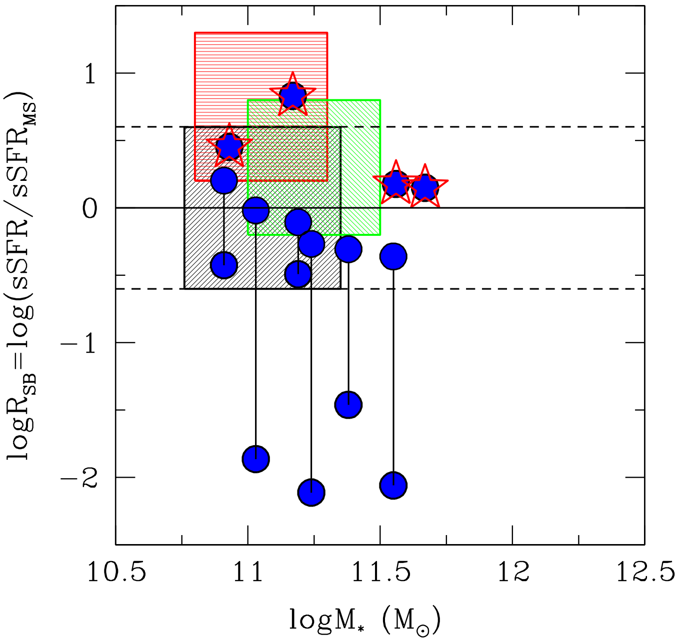

Figure 2.2: Ratio between the Specific Star Formation Rates (sSFR=SFR/$M_*$) of our targets[1] with respect to those expected for Main Sequence galaxies ($sSFR_{MS}$) at a given stellar mass, versus the host stellar mass $M_*$). The ratio $R_{SB}$=sSFR/$sSFR_{MS}$ is plotted in logarithmic scale. The sSFR values are normalized assuming the best fit of the galaxy main sequence as a function of redshift obtained by Whitaker et al. 2012. The dashed horizontal lines mark the region of MS galaxies. Starred symbols mark objects for which the SFR is derived from PACS photometry. For the 6 sources undetected in PEP, we report as blue circles the value corresponding to the SFR derived from the SED fitting decomposition (lower paired points), and the $R_{SB}$ value computed assuming a SFR$\sim$ 70 $M_\odot$/yr as derived from stacking of the PACS fluxes (upper paired points; see text for details). The shaded areas mark the loci occupied by the $z \sim 2$ SMG/ULIRGs presented in Harrison et al. (2012) (red), the 8 massive star forming galaxies presented in Förster Schreiber et al. 2014 (green) and the MS galaxies presented in Kashino et al. 2013 (black).

The morphology of our targets is shown in Fig. 2.3, through HST/ACS $I_{848}$-band cut-outs. XID 5321 is the only source which lies outside the HST COSMOS area; for this target the UltraVista J-band cut-out is shown in Fig. 2.13. Point-like nucleus, likely responsible for the X-ray emission, as well as residual diffuse or patchy components and/or close companions, which may trace the host galaxy, extending on scales comparable to or even larger than the slits apertures (∼8 kpc, see next section) are present in the majority of sources.

Rest-frame, absorption corrected X-ray luminosities in the $0.5-10$ keV band ($L_{\rm X}$) and absorbing column densities (NH) have been obtained from proper spectral analysis for objects with enough counting statistics ($>150$ counts; Mainieri et al. 2011). For the objects with low counting statistics, the $N_{\rm H}$ is inferred from the observed hardness ratio[2] and it is used to K-correct the rest frame flux to derive the unobscured luminosity (see Merloni et al. 2014). Most of our sources have $L_{\rm X} > 10^{44}$ erg/s and moderate to large obscuring column densities ($N_{\rm H} > 10^{21} cm^{-2}$). We note that the $N_{\rm H}$ measured are based on relatively low counts data that cannot disentangle the complexity of the spectra and different components. In particular, the multiwavelength analysis of XID 60053 suggests that for this source the column density is heavily underestimated (and therefore the unobscured $L_{\rm X}$) and this object is a candidate Compton Thick (CT) AGN (see Bongiorno et al. 2014).

The AGN bolometric luminosities ($L_{\rm bol}$) have been evaluated from SED fitting decomposition of the galaxy, torus and SF components, by integrating the torus component only for Type 2 AGN or from the combined constraints from the disk and torus emission for Type 1 AGN (see Lusso et al. 2012, 2013). Overall, our targets have total AGN luminosities in the range $L_{\rm bol} = 10^{45} - 10^{46.5}$ erg/s, with median value $L_{\rm bol} = 10^{46}$ erg/s. When comparing the X-ray and the bolometric AGN luminosities, we note that these sources have bolometric corrections in the range $k_{\rm bol} = L_{\rm bol}/L_{\rm X} \approx 4-20$, lower than the value generally assumed for X-ray (and optically) selected samples ($k_{\rm bol} \approx 30-100$; see discussion in Lusso et al. 2012). Finally, the BH masses measured from the X-shooter data for 6 out of 10 of our targets have been published by Bongiorno et al. (2014) and Brusa et al. (2015). From the comparison between $L_{\rm bol}$ and the Eddington luminosity associated with the measured $M_{BH}$, it is possible to infer also the Eddington ratios ($\lambda_{Edd} = L_{\rm bol}/L_{Edd}$) for these 6 sources, in the range $0.01-1$ (see Table 2.1).

## 2.4 X-shooter observations and spectral analysis

The XMM-COSMOS obscured QSOs targets have been observed with the X-shooter spectrograph (D'Odorico et al. 2006; Vernet et al. 2011) on the ESO VLT-UT2 (Kueyen) during the nights of February 8-10, 2013, as part of programme 090.A-0830(A). Due to scheduling constraints, only 10 targets have been observed. The exposure times range from 1hr to 2hrs. We used the 0.9″ width slit (corresponding to a spectral resolution R∼5100 in the NIR and R∼8800 in the VIS). Observing conditions were reported to be photometric, and seeing condition was $0.5-1.0$" (FWHM). Further details about the observing strategy and the data reduction can be found in Brusa et al. (2015). Figure 2.4 shows the 10 X-shooter VIS+NIR spectra of our XMM-COSMOS targets, sorted by increasing (spectroscopic) redshift. The shaded areas in each spectrum mark the regions of the H$\beta$+[O III] (left) and H$\alpha$+[N II] (right) lines. A first visual inspection allows us to notice the wrong first spectral classification: H$\alpha$ broad-line emission is detected in all AGNs initially classified as type 2 sources on the basis of the absence of broad profiles in near-UV emission lines (see also Fig. 2.5). Such wrong classification is

---

[2] The hardness ratio is defined as (H - S)/(H + S), where H and S are the counts in the hard and soft bands, respectively.

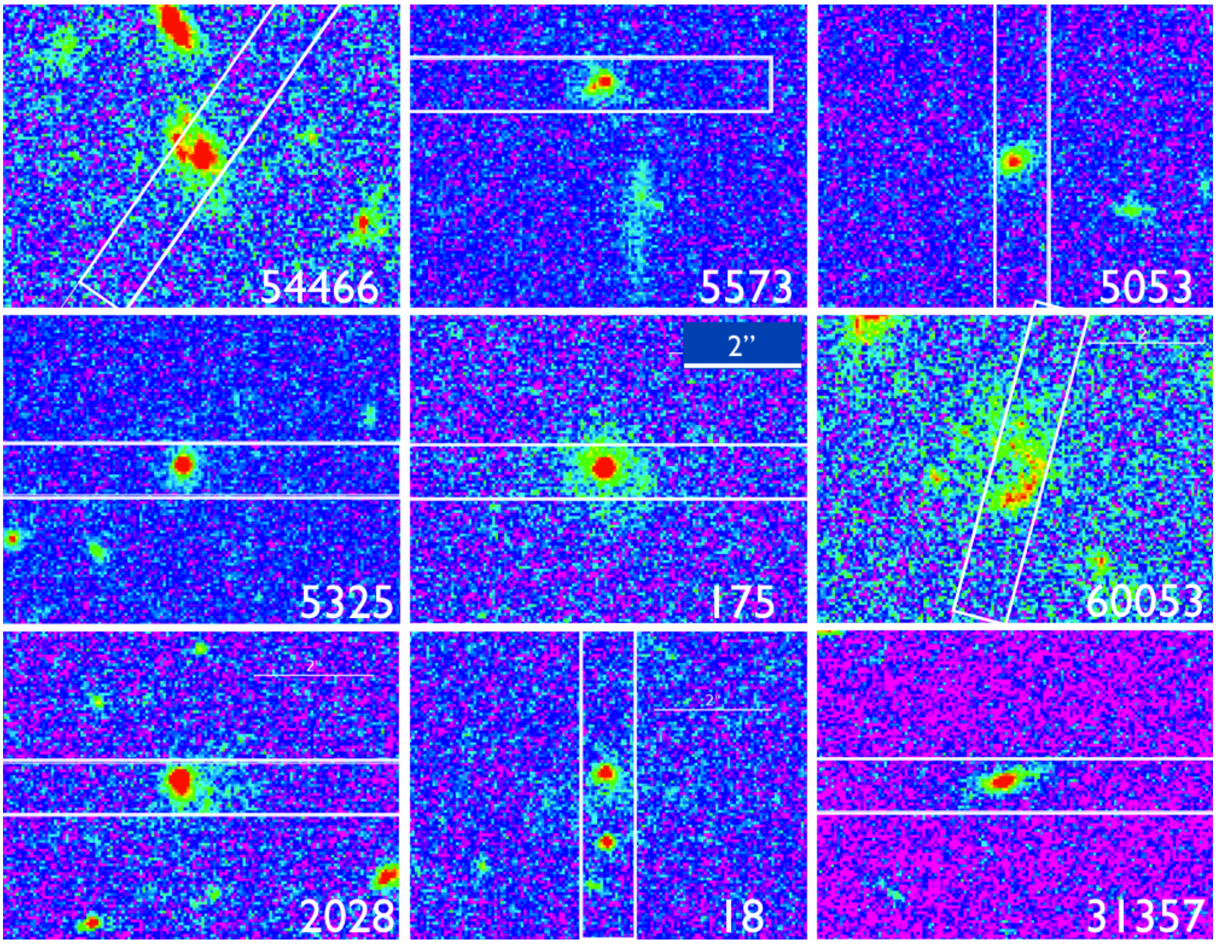

Figure 2.3: $I_{814}$ band cutouts around the 9 targets with HST/ACS data (all but XID 5321 which lies outside the HST COSMOS area), ordered by increasing redshifts (same as figure 2.4). The labels indicate the XID. In the central panel we report also the $2''$ scale ($\sim$ 17 kpc at z $\sim$ 1.5) common to all the figures, and the $0.9'' \times 11''$ slit used in the X-shooter observations is marked in each panel. The intensity level of the images is logarithmic, with blue/purple marking the background level and red marking the peak emission, with an aveage contrast of about a factor of 10.

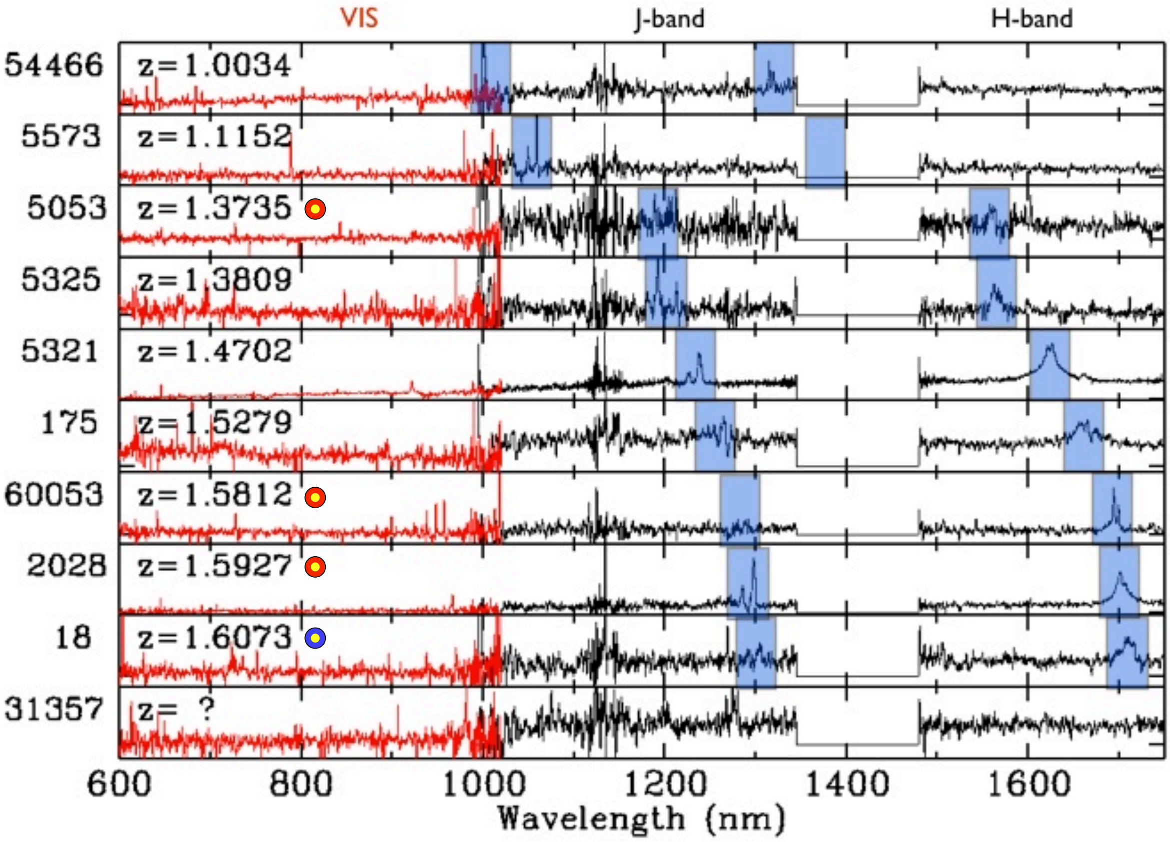

Figure 2.4: X-shooter spectra of the 10 XMM-COSMOS targets, sorted by increasing spectroscopic redshift. The region defining the limits between the J and H filters is masked out because characterized by low atmospheric transmission. The blue shaded areas in each spectrum mark the wavelengths ranges of the redshifted [O III] (left) and H$\alpha$ (right) lines. Zoom of these regions can be found in Brusa et al. (2015), fig. 6. The NIR ($1 - 1.75\mu$m) and VIS ($0.6 - 1\mu$m) spectra are shown in black and red, respectively. The fluxes are all flux calibrated in erg cm$^{-2}$ s$^{-1}$$\AA^{-1}$, but the scale is not shown on the y-axis. The XID and redshifts of the sources are given on the left of each panel. Blue and red circles within some panels indicate type 1 and type 2 AGNs, as defined on the basis of a first spectral classification prior to the X-shooter observations.

actually expected whenever the source is buried by dust environments.

Figure 2.5 shows, for each source, a zoom in the regions around the [O III] and H$\alpha$ lines. The upper panels display the X-shooter 2D spectra from which we extract the 1D spectra (central panels), using 1″ apertures as labelled with black solid lines. Red to blue/purple colours represent increasing fluxes. By way of explanation, we consider the 2D spectrum of XID 5321, around the H$\alpha$ complex. Strong emission is detected in the entire wavelength range 1560 − 1680 nm, with intensity peaks at the position of the redshifted H$\alpha$, [NII]$\lambda$6583 (indicated by purplish colours) and [S II] doublet lines (greenish colours). Such emission cover $\approx 1''$ along the y-axis, which roughly corresponds to a physical size of 8 kpc for the emitting source. In addition, narrow, vertical structures are detected along the entire wavelength range (magenta colours indicate negative fluxes). These systems delineate strong sky subtraction residuals and, unlikely the target emission, cover the entire y-axis extension. This behaviour allows a useful diagnostic to distinguish between narrow emission lines and bad sky residuals, in particular in those sources whose emission features are detected at lower S/N (see, e.g., the XID 175 2D spectrum around 1675 nm). Such kind of information is also taken into account in the modelling of the 1D spectra displayed in Fig. 2.5, whose guidelines are described in the next sections.

### 2.4.1 Rest-frame optical spectral analysis

To determine the kinematic and physical condition of the ionized gas, and in particular to unveil and characterize the possible presence of outflows in NLR emission, we proceed using two interdependent approaches: a multi-component, simultaneous line fitting and a non-parametric analysis. Through simultaneous line fitting technique we distinguish between unperturbed gas components, or Narrow component (NC), associated with emitting gas under the influence of the gravitational potential of the galaxy, and Outflow components (OC), most probably associated with outflowing gas emission. Therefore, such modelling allows a good estimate of the unperturbed and outflowing gas fluxes separately. When the spectral fit requires OC to reproduce the line profiles, the non-parametric analysis is used to infer more accurate outflow velocity measurements on the basis of the best-fit results obtained with the former approach.

The fitting prescription and the non-parametric approach exposed below are the ones used to analyse rest-frame optical spectra that appeared in several works published within the framework of this Thesis (Brusa et al. 2015, 2016; Perna et al. 2015a,b) and that are also reported in Chapters 4,**??** (see also Lanzuisi et al. 2015a, whose results are not presented in this Thesis). To avoid recurrences through the Chapters, we describe in the next two sections such prescriptions in the most generic manner.

#### Simultaneous modelling the H$\beta$+[O III] and H$\alpha$+[N II] line complexes

We simultaneously fitted each of the most prominent emission lines, from the He II$\lambda$4686 to [S II] doublet with four (at maximum) sets of Gaussian profiles:

BC – one (two) Broad component(s): three Gaussian (or Lorentzian) functions for the He II, H$\beta$ and H$\alpha$ BLR emission lines, with a FWHM greater than 1000 km/s. A second BC is added when H$\alpha$ and H$\beta$ BLR cannot be modelled with a single broad gaussian profile (see e.g. Shen and Kelly 2012; Chapter 5);

NC – a Narrow component: nine Gaussian lines, one for each emission line in the two regions of interest (i.e. He II, H$\beta$, [O III] doublet, H$\alpha$, [N II] and [S II] doublets) to account for the presence of unperturbed systemic emission (from the NLR or the host galaxy). The width of this kinematic component is set to be $\lesssim 550-600$ km/s;

OC – one (two, in an handful of cases) Outflow component(s): eight Gaussian lines, one for each emission line (with the exclusion of the He II, which is usually faint and never well constrained) to account for the presence of outflowing ionised gas. No upper limits have been fixed for the width of this kinematic component. We introduce OC component(s) when high residuals in the [O III] region are found.

In addition, we used theoretical model templates of Kovačević et al. (2010) to reproduce FeII emission when it is detected (Chapter 5). Prior to the modelling of the emission lines, we estimated the local continuum by fitting a power-law to the spectra at both sides of the regions using those wavelength ranges that are not affected by prominent features and or bad sky-subtraction residuals (e.g. $4000-4050$ and $5600-5650$ for the H$\beta$ region). For each sets of Gaussian profiles, the wavelength separation between emission line within a given set of Gaussian is constrained in accordance with atomic physics. This mean that the velocity offset of the OC from the systemic components are constrained to be the same for each emission line. Moreover, the relative flux of the two [N II] and [O III] components is fixed to 2.99; [S II] flux ratio was required to be within the range $0.44 < f(\lambda6716)/f(\lambda6731) < 1.42$ (Osterbrock and Ferland 2006).

The different ionization potentials and critical densities of NLR line features suggest a gas stratification with respect to the central SMBH (De Robertis and Osterbrock 1986). In order to account such effect, the fitting procedure would consider a different line width for each emission feature within a given set of Gaussian lines. Our fitting procedure has proved to well reproduce all the analysed emission lines with the constraints above mentioned, from low ionization emission lines, such as [S II doublet (with IP = 10.4 eV; see Table A.1), to high ionization lines (i.e. [O III], with IP = 35 eV). Indeed, we note that even when different line widths have been derived from low-to-median wavelength resolution data, their values were always consistent within the errors of the Gaussian fit (see De Robertis and Osterbrock 1986; Wang and D. W. Xu 2015). We therefore conclude that the spectral resolution of the spectra we analysed do not permit to unveil a possible NLR stratification.

### Non-parametric analysis

In order to obtain best representative velocity of the outflowing gas, we compute the non-parametric measurements. These do not strongly depend on the specific fitting procedure and on the physical interpretation of any of the parameters of the individual Gaussian profile, but take advantage of the noiseless best-fit approximation of the overall shape of the emission line profile derived from the fitting procedures. We used the non-parametric analysis for the only [O III]$\lambda$5007 (or [O II] doublet) emission line(s) to derive the kinematic conditions of the ionized gas within the AGN NLRs.

Non-parametric measurements (e.g., Liu et al. 2013; Rupke and Veilleux 2013; Zakamska and Greene 2014) are obtained by measuring velocity $v$ at which a given fraction of the line flux is collected, using the cumulative flux function $F(v) = \int_{-\infty}^{v} F_v(v')\,dv'$. The position of $v = 0$ of the cumulative flux is determined using the systemic redshifts derived from the NC of the simultaneous best-fit results. Following the prescription indicated by Zakamska and Greene (2014), we estimate for the total emission line best-fit profiles the following parameters:

(i) The velocity peak, $v_p$, the velocity of the peak flux density in the overall emission-line profile. Generally, this traces the brightest narrow emission-line component;

(ii) The line width $W80$, the width comprising 80% of the flux, that for a Gaussian profile is very close to the FWHM value. It is defined as the difference between the velocity at 90% ($v90$) and 10% ($v10$) of the cumulative flux, respectively;

(iii) The velocity offset of the broad underlying wings, $\Delta V$, measured as $(v05 + v95)/2$, with $v95$ and $v05$ defined as above;

(iv) A maximum velocity parameter $V_{max}$, defined as $v02$ when blue prominent broad wings are present, or as $v98$ when red ones are, on the contrary, present.

In contrast to $V_{max}$ and $v_{peak}$, values of $W80$ and $\Delta V$ include only differences between velocities and do not depend on the accurate determination of the systemic velocity. A possible residual error in the determination of the systemic velocity, however, may produce a variation of at most few tens of km/s in the $v_{max}$ value, corresponding to variation of a few % (see below).

Generally, the best-fit line profile used to derive non-parametric estimates is taken from the simultaneous fitting procedure results. Such approach is, in fact, less dependent on particular poor S/N conditions in the vicinity of the emission line: the low S/N regions around an individual emission feature, if fitted independently, may be wrongly interpreted as extended wings and modelled with a faint and broad Gaussian profile. However, when high wavelength resolution and very good S/N emission lines are detected, an independent fit could allow a better modelling of the line profile and more accurate velocity measurements. The downside, in such cases, is represented by the severe increasing in the degeneracy between the Gaussian components reproducing the total complex profile of the emission line. This means that, in contrast to the simultaneous fit, we are no more able to distinguish between unperturbed and outflowing gas emission.

#### Fitting routines

We fit the Gaussian profiles using a fortran code implementing the Minuit package (James and Roos 1975). In order to estimate errors associated with our measurements, we use Monte Carlo simulations. For each modelled spectrum, we collect the fit results of 1000 mock spectra obtained from the best-fit final models (red curves in Fig. 2.5; see also Figs. 2.14 and 2.16), and adding Gaussian random noise (based on the standard deviation of the corresponding local continuum). When Fe II features were fitted, prior to the MC simulations, we subtracted our best-fit Fe II template in order to minimise the degeneracy in the errors estimation. The errors are calculated by taking the range that contains 68.3% of values evaluated from the obtained distributions for each Gaussian parameter/non-parametric measurement. Finally, we note that since line profiles generally are non-Gaussian and much broader than the spectral resolution (see Section 2.5.4), we did not correct the observed profiles for instrumental effects and report all values as measured.

### 2.4.2 Results: Incidence of ionized outflows in [O III] lines

The best fit solutions of the simultaneous modelling of the X-shooter sample in the regions of the [O III] and H$\alpha$ are shown as a red curve in Fig. 2.5 (central panels), for each source. The best-fit Gaussian components needed to fit the full line profiles are also superimposed with arbitrary normalization in order to ease the visualization: the NC, as solid/blue, the OC as dashed/blue, the BC in solid/green. The bottom panel shows the residuals [(data-model)/error, where the error is estimated in the local continuum] that, added in quadrature, determine the $\chi^2$. Table 2.2 summarizes the parameters obtained for the NC and OC components for the [O III]$\lambda$5007 line, as well as the $v_{max}$ velocities obtained from the non-parametric approach. The reduced minimum $\chi^2_{red}$ values obtained for the proposed best fit solutions are reported in the second to last column.

Before discussing about the outflow signatures found in our sample, we note that the FWHM and fluxes of the BC associated with the BLR are in agreement with those presented in Bongiorno et al. (2014), despite the different modelling of the narrow components, and we refer to that paper for the estimate of the BH masses. We also note that in most of the sources where the broad H$\alpha$ is detected (XID 5321, XID 2028, XID 18, XID 175, XID 60053 and XID 5325), the H$\beta$ is considerably extincted (with R(H$\alpha$/H$\beta$) ∼5-10). This is consistent with the buried nature of the objects and with the moderate obscuration measured in the X–ray spectra

Table 2.2

Fit to the [O III]$\lambda$5007 line in XMM-COSMOS obscured QSOs

| XID | $\lambda$,NC nm | FWHM$_{NC}$ km/s | Flux(NC) ($10^{-20}$) | $\lambda$,OC nm | FWHM$_{OC}$ km/s | Flux(OC) ($10^{-20}$) | $\Delta$v km/s | $\chi^2_{\rm red}$ | $V_{max}$ km/s |
|---|---|---|---|---|---|---|---|---|---|
| 18 | (1305.52) | (404 ±85) | (from H$\alpha$ fit) | 1304.28 | 1065 ± 409 | 4883 ± 1875 | -287 | 0.75 | 1230 |
| ‡60053 | 1292.35 | 272 ± 11 | 782 ± 65 | – | – | – | – | 0.74 | – |
| 175 | 1266.44 | 513 ± 46 | 8167 ± 301 | 1263.53 | 1652 ± 150 | 7541 ± 685 | -688 | 0.50 | 1800 |
| 2028 | 1298.24 | 520 ± 17 | 29188 ± 658 | 1296.45 | 913 ± 37 | 17127 ± 694 | -413 | 0.99 | 1350 |
| 5321 | 1236.80 | 272 ± 14 | 5556 ± 149 | 1238.31 | 1306 ± 14 | 74664 ± 800 | 366 | 1.10 | 1730 |
| 5053 | (1188.48) | (538 ± 24) | (from H$\alpha$ fit) | 1187.96 | 1372 ± 616 | 3655 ± 1641 | -131 | 1.74 | 1500 |
| 5325 | 1191.85 | 403 ± 12 | 4448 ± 52 | 1194.45 | 1050 ± 210 | 3313 ± 662 | 653 | 1.76 | 1660 |
| 5573 | 1059.14 | 233 ± 10 | 7982 ± 93 | – | – | – | – | 1.02 | – |

Notes: Fluxes are in units of $10^{-20}$ erg cm$^{-2}$ s$^{-1}$. $\lambda$(NC), FWHM$_{NC}$ and Flux(NC) denote the best fit parameters and errors for the narrow component; $\lambda$(OC), FWHM$_{OC}$ and Flux(OC) instead refer to the outflow component. $\Delta$v is measured from the difference in centroids of the 2 measured components (OC-NC). Values in parenthesis refer to measurements constrained from the H$\alpha$ region fit. ‡: 2 components fit not significant. Narrow component consistent with only narrow lines seen in the H$\alpha$ region.

($N_{\rm H} \sim 10^{21-22}$ cm$^{-2}$) [3].

Four out of 8 sources (XID 2028, XID 5321, XID 175, and XID 5325) need all three sets of Gaussians to reproduce simultaneously the H$\beta$+[O III] and H$\alpha$+[N II] line profiles. The fit with a single set of gaussian lines to model the NLR emission, even without imposing an upper limit on the FWHM, produced a significantly larger $\chi^2$. This is particularly true for our highest S/N sources (XID 5321 and XID 2028), where the [O III] emission is clearly asymmetric and a single component therefore cannot reproduce the observed emission. In all cases, the Gaussian amplitudes of the NC and OC needed to fit the [O III] profiles were not consistent with zero (while these may be the case for other lines of the same components at lower S/N, e.g. [S II]). In 4 cases, the OC component shows a significant shift ($|\Delta v| > 300$ km s$^{-1}$) from the systemic redshift of the galaxy: XID 2028 and XID 175 reveal a blueshift component, while XID 5321 and XID 5325 show a redshifted component. We note that the velocity shift measured for the [O III] line Gaussian decomposition for XID 2028 ($\Delta$v$\sim -370$ km s$^{-1}$) is consistent with the value reported in Brusa et al. (2010) and measured from the shift of the Mg II absorption lines in the Keck spectrum ($\Delta$v$\sim -300$ km s$^{-1}$). A similar fraction of NC+OC to NC line modelling has been found in Harrison et al. (2012): 4 out of the 8 targets presented in that work needed a multiple component fit to reproduce the NLR emission (see their fig. 3).

For the remaining 4 targets, in 2 cases (XID 18 and XID 5053) the quality of the spectra was not such to allow a 2 Gaussian decomposition below the [O III] lines and the fit has been limited to a single, blueshifted OC component[4], whose centroid has been constrained from the combined fit on the H$\alpha$ region. The detection of the broad component for these two sources is significant at the 2-3$\sigma$ confidence level. For XID 5573, the best fit of the [O III] line has been obtained with only a narrow component (FWHM$_{NC} \sim 230$ km/s). Finally, for XID 60053 only narrow components are detected in the H$\alpha$ region, in correspondence with two peaks observed also in the [O III] lines (as labelled in Fig. 2.5). The observed H$\alpha$ flux, if ascribed entirely to SF, translates into a SFR$\sim 10$ M$_\odot$ yr$^{-1}$ (Kennicutt 1998). From the comparison of the SFR

---

[3] $N_H$ determines to which wavelengths the medium is opaque and to which wavelengths the medium is transparent: A medium with $N_H > 10^{21} cm^{-2}$ will obscure the UV emission, a medium with $N_H > 10^{22}$ will obscure the broad H$\alpha$ line and the 3 $\mu$m emission, and a medium with $N_H > 10^{23}$ will obscure the 10 $\mu$m emission. All the numbers assume a Galactic dust composition and dust to gas ratio.

[4] In this case the definition of NC and OC is superseded, but we report these values in the column "OC" in Table 2.2

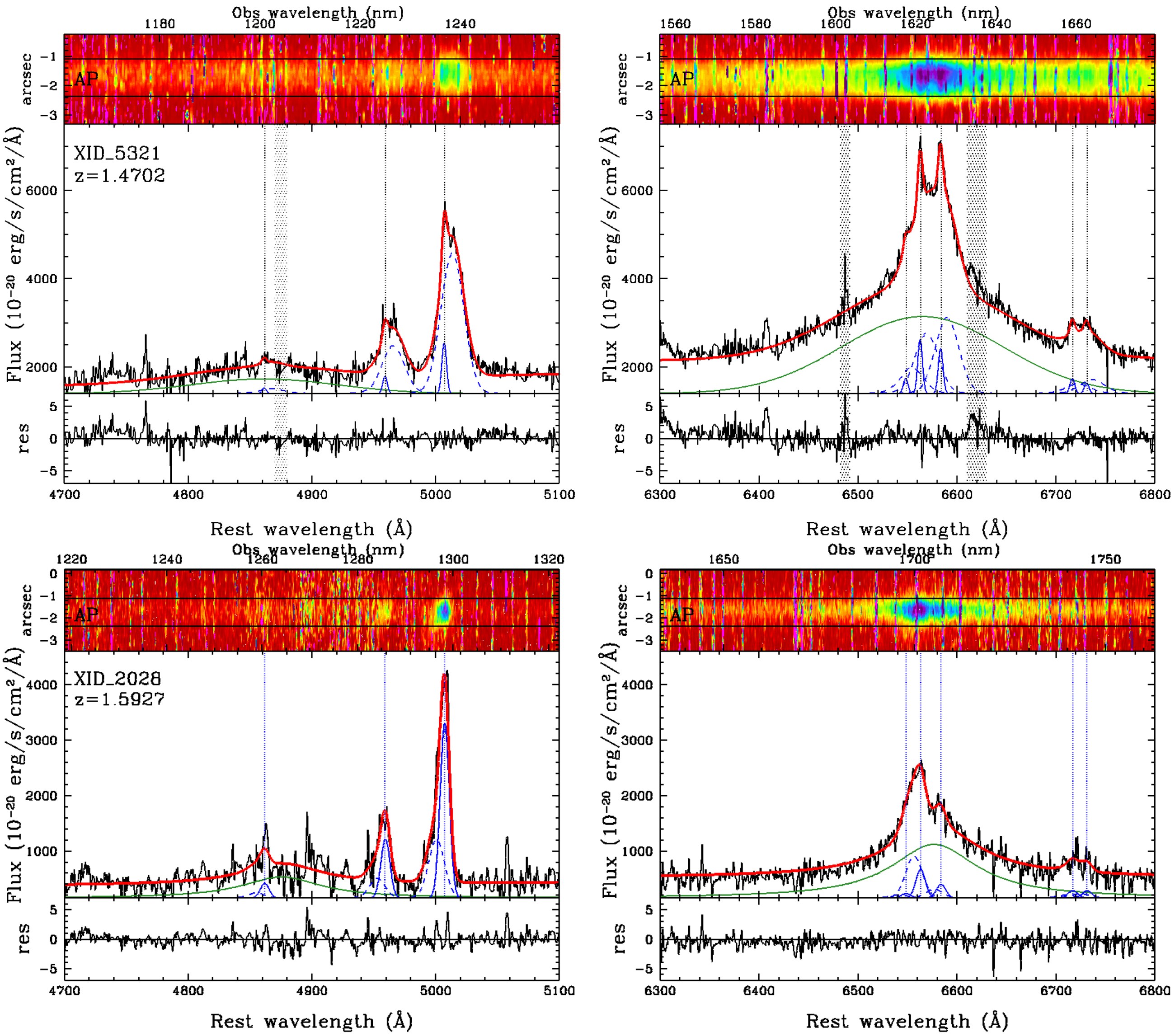

Figure 2.5: Zoom in the regions of [O III] (left) and H$\alpha$ (right) lines for the 9 sources for which we could determine the redshifts. For each spectrum and each region, the upper panel shows the observed X-shooter 2D spectrum with the 1″ aperture used to extract the 1D X-shooter spectrum labeled. The central panel shows in black the rest-frame spectrum (smoothed for plotting purposes with a binning factor of 3 to 11, depending on the spectrum). The flux scale has been multiplied by (1+z) in order to conserve the observed integrated flux in the rest-frame fit and is maintained the same for each source to ease the comparison of the relative strength of the emission lines. The dotted lines mark the wavelengths of H$\beta$, [O III]$\lambda$4959, [O III]$\lambda$5007 (left) and [NII]$\lambda$6548, H$\alpha$,[N II]$\lambda$6581, and the [S II] doublet (right), from left to right, respectively. The regions excluded from the simultaneous fit corresponding to the most intense sky lines are highlighted as shaded areas. Superimposed on the spectra are the best fit components presented in Section 2.4.1, with arbitrary normalization in order to ease the visualization: solid (blue) curves represent the systemic narrow components (“NC”); dashed (blue) curves the outflow components (“OC”). The solid (green) curves below H$\beta$ and H$\alpha$ with FWHM$\gtrsim$ 2000 km s$^{-1}$ represent the BLR component (“BC”). The red solid curve shows the best-fit sum of all components (including the power-law). When only one component is needed, the fit is shown as red curve only. In the bottom panel of each fit the residuals with respect to the best fit are shown. XID 5321 and XID 2028 are shown here.

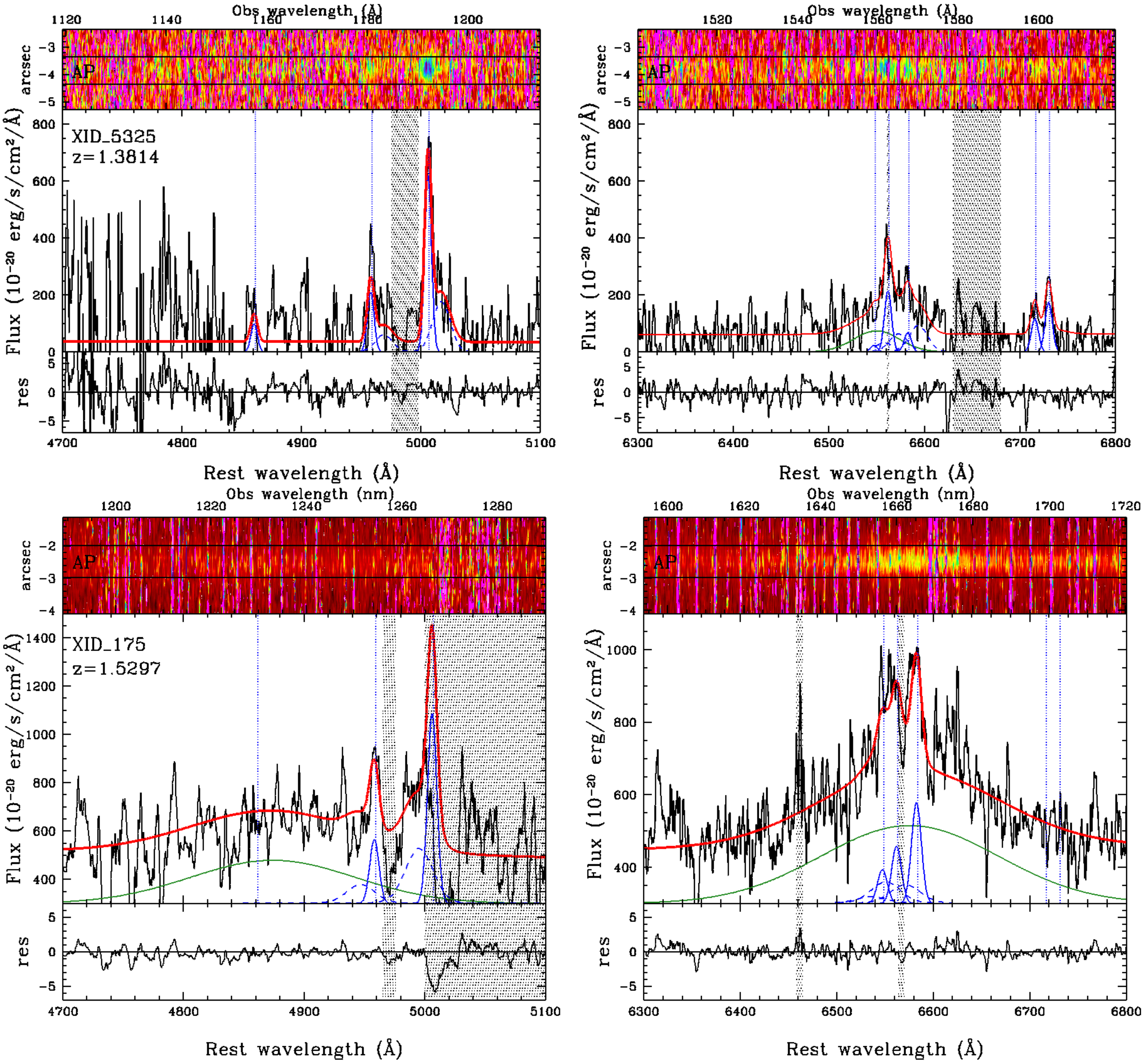

Figure 2.6: – Zoom in the regions of the [O III] (left) and H$\alpha$ (right) for XID 5325 and XID 175. See previous page for description.

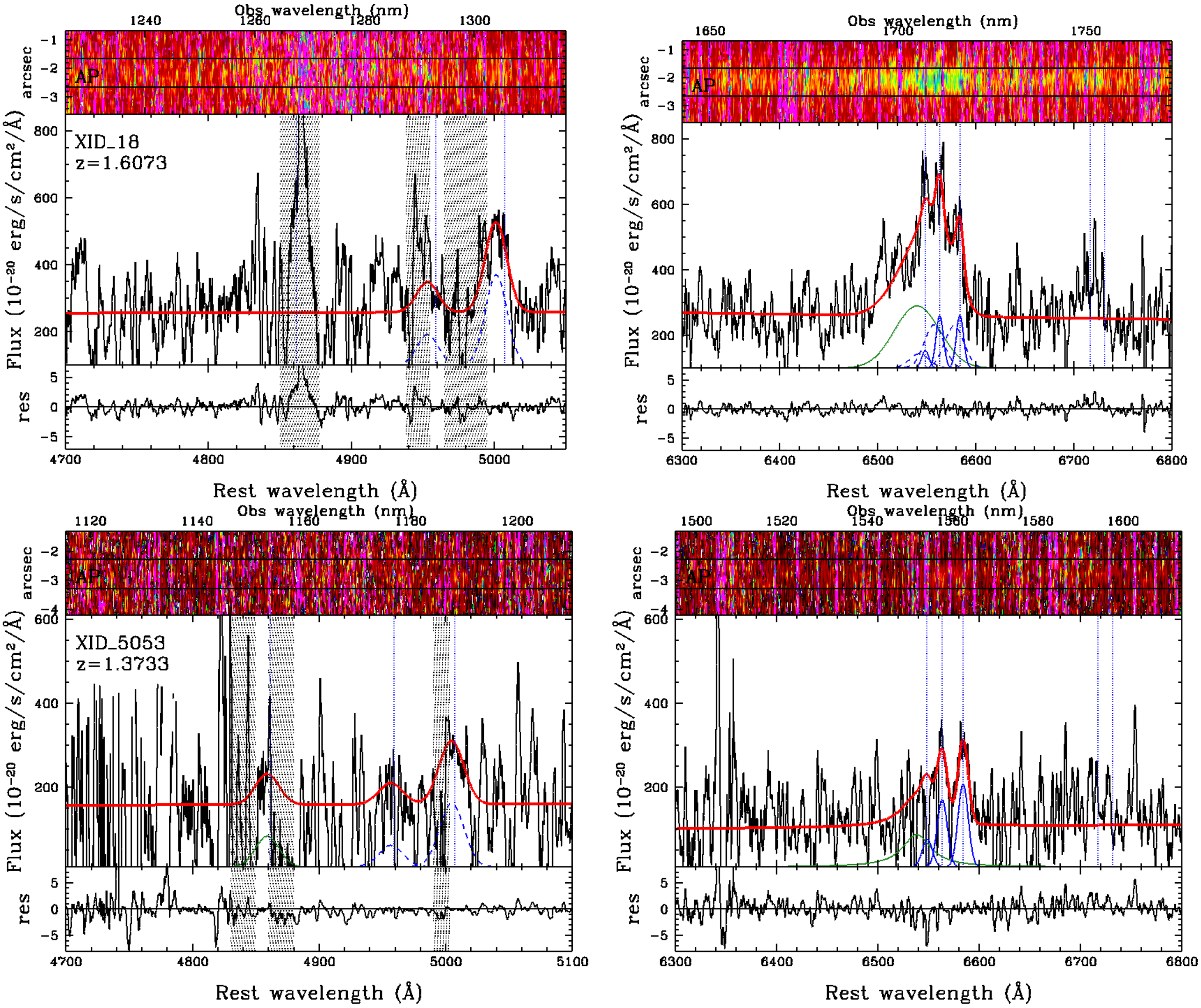

Figure 2.7: – Zoom in the regions of the [O III] (left) and H$\alpha$ (right) for XID 18 and XID 5053. See previous page for description.

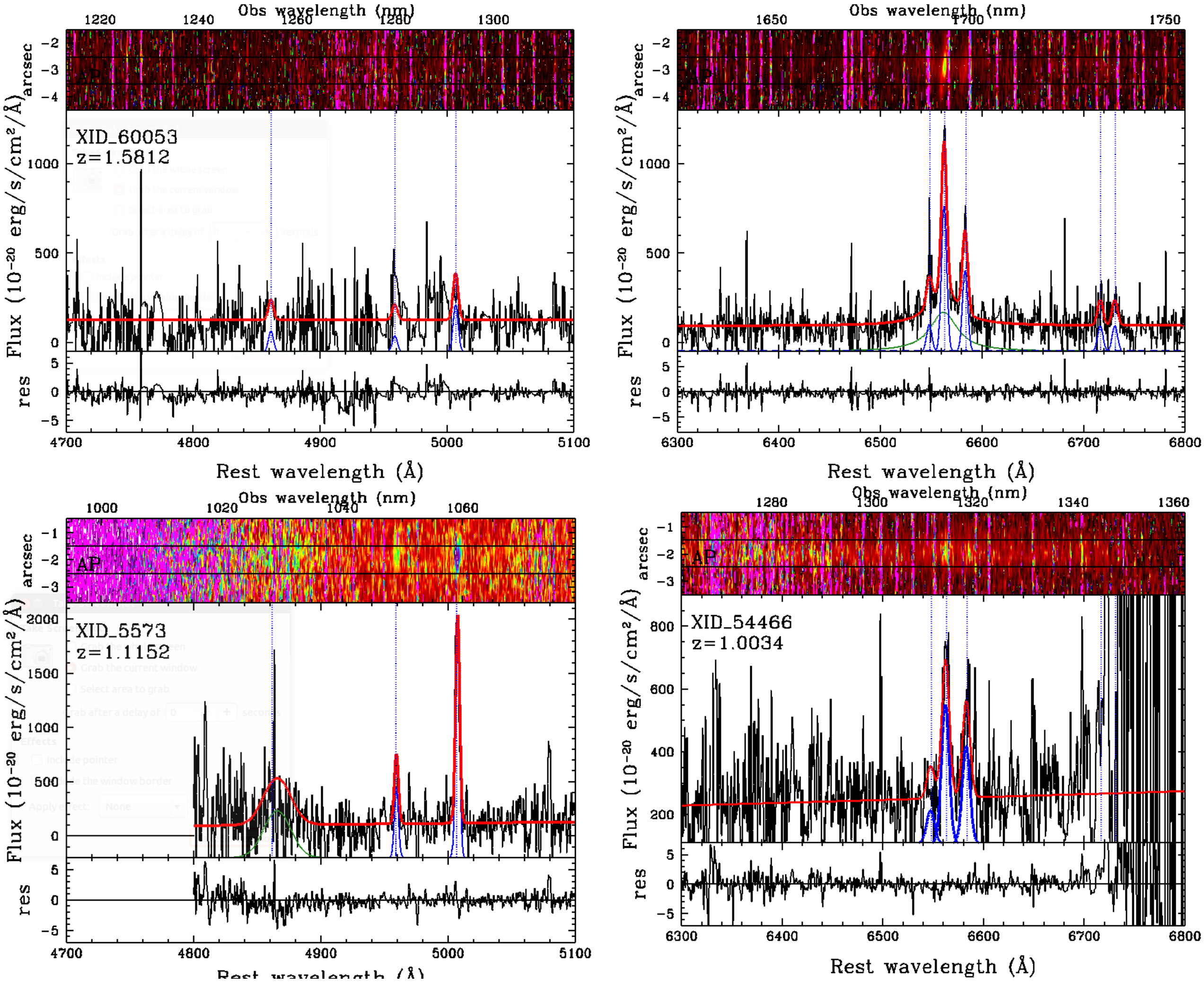

Figure 2.8: – Zoom in the regions of the [O III] (left) and Hα (right) for XID 60053 (first row). In the second row we show the [O III] region for XID 5573 (left) and the Hα region for XID 54466 (right). See previous page for description

from the FIR and the H$\alpha$, we infer a lower limit to the extinction of $A_V \sim 6$ mag. Such a high extinction would also suppress most of the [O III] flux which indeed is only barely detected in the X-shooter spectrum.

For four out six sources, the non-parametric measurements are obtained from the [O III] best-fit solution of the simultaneous fits. For the remaining 2 targets, XID 2028 and XID 5321, the high S/N and the peculiar, well defined profiles of the emission lines, allow us a supplementary, independent fit only for the doubly ionized oxygen doublet. For both the sources, the fit required three Gaussian profiles to reproduce the doublet (see the spectra in Fig. 2.14, *b* panels).

Summarizing, for 6 out of 8 targets we report the presence of outflow components with $\mathrm{FWHM}_{OC}$ and $V_{max}$ in the range $900-1800$ km/s (4/6 with high significance, while the remaining 2 at a $\sim 2-3\sigma$ confidence level), while in the remaining 2 sources only narrow components (FWHM$\sim$ 250 km/s) are revealed in the [O III] lines, therefore proving the efficiency of the selection criteria we used to isolate our X-Shooter sample.

### 2.4.3 Observational constraints on the OC from literature

A trend between the outflow velocity and the bolometric AGN luminosity is expected from some co-evolutionary models (e.g., Menci et al. 2008). In Fig. 2.9, following Harrison et al. (2012), we plot the FWHM of the outflow component (NC in the case of single Gaussian fits) in our measurements with the total [O III] luminosity, not corrected for extinction, and we compare them with different literature samples, both local and at high redshift. Our sources (blue circles) are compared with different samples of ULIRGs and SMGs in which outflows have been detected (e.g., Harrison et al. 2012; Rodríguez Zaurín et al. 2013; Westmoquette et al. 2012; see the caption for more details). Overall, these studies showed that *1)* FWHMs larger than 1000 km/s can be safely used to advocate the presence of kpc-scale outflows, on the basis of IFU follow-up data (see, e.g., Harrison et al. 2012; Westmoquette et al. 2012); *2)* in nearly complete sample of ULIRGs, those associated with Seyfert nuclei show evidence of outflows on scale of $\sim 5$ kpc, while those without Seyfert nuclei do not show such complex line profiles and spatial extensions (Rodríguez Zaurín et al. 2013; see also similar results in the molecular gas outflow properties of AGN ULIRGs versus non-AGN ULIRGs presented in Cicone et al. 2014).

In Fig. 2.9, we also compare our results with those reported in the literature for objects selected on the basis of a purely AGN classification. We report the contour levels extracted for the type 2 AGN only, obtained by Mullaney et al. (2013) from a multicomponent analysis of the [O III] lines in the SDSS. The [O III] width derived from the stacked spectrum of all XMM-COSMOS type 2 AGN at $z = 0.5-0.9$ from which [O III] is visible in the zCOSMOS sample is consistent with the average value of the broadest component observed in SDSS sample at comparable luminosities (pinkish square). We also plot the results for 15 type 2 QSOs studied in Greene et al. (2011, 2009) and other 10 type 2 from Liu et al. (2013) (in this case we use their $W80$ non-parametric measure of the line width). Finally, we add the $\approx 50$ X-ray AGNs at $z = 1.1-1.7$ from a more recent work, Harrison et al. (2016).

Overall, the comparison of the results obtained in our sample and the other samples discussed above may be seen as an indication that the colour selection applied to our X-ray sample is effective in picking up objects with FWHM larger than the average values. A further indication come from the results we derive from our own analysis on the sample presented in Urrutia et al. (2012). The authors presented a sample of 13 dust-reddened QSOs at $z = 0.5-1$, selected solely on the basis of a red J-K colour. The intrinsic E(B-V) $\sim 0.5$ of these targets is similar to what is observed in our targets. We have analysed 11 out of 13 objects from the

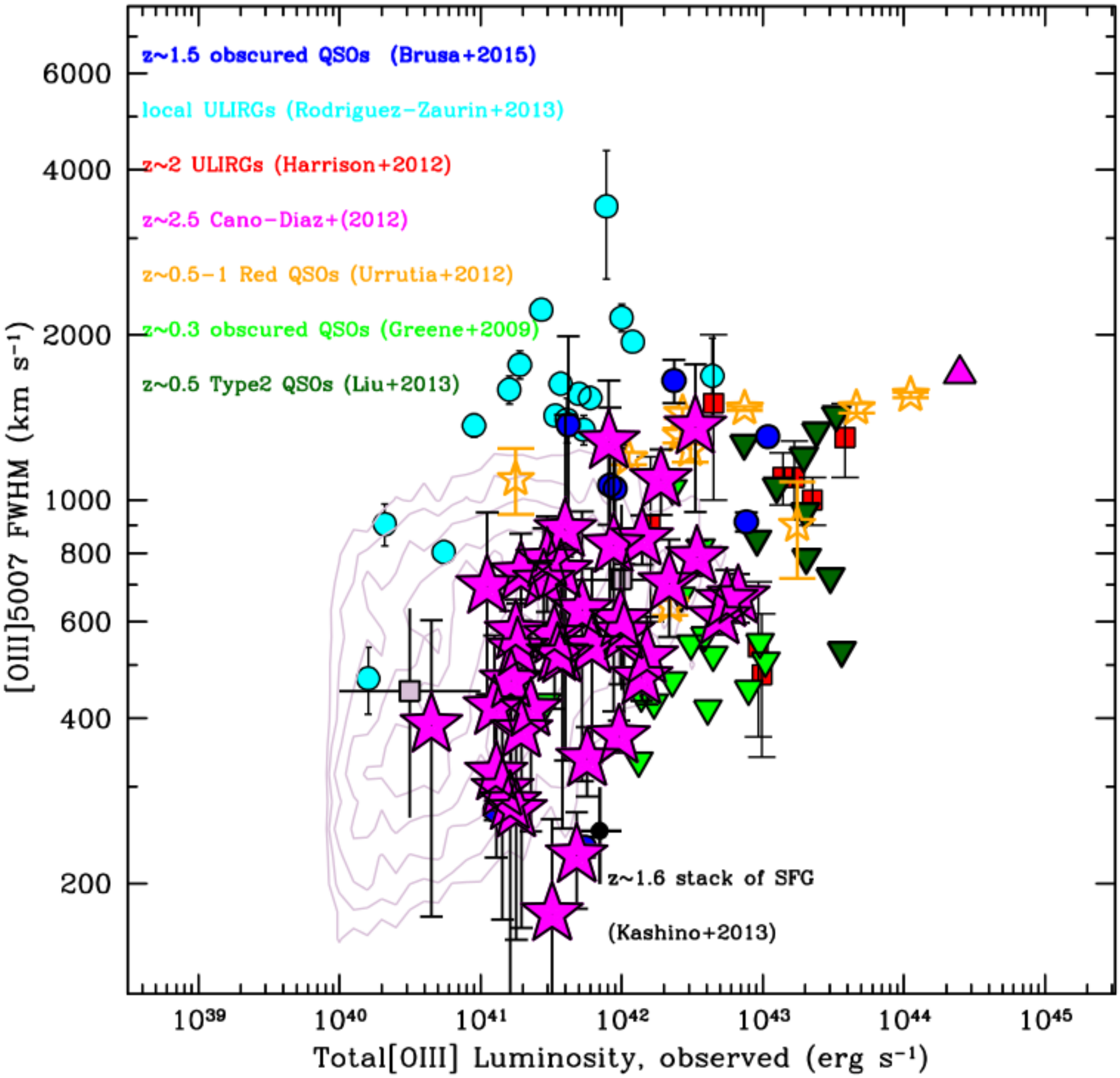

Figure 2.9: FWHM (broad component) of the $\lambda$5007 line against the total [O III]$\lambda$5007 luminosity. The [O III] luminosity is not corrected for extinction. In both panels our X-shooter targets are marked with blue circles. For completeness, we also plot the 2 sources (XID 5573 and XID 60053), fitted by only a narrow component in the [O III] lines, by using the FWHM of the NC. Our results are compared with known literature samples of Star forming systems (both ULIRGs and MS) and Seyfert 2 and Type 2 QSOs, as labelled. The black filled circle in the represents the average for a population of 30 massive star forming galaxies at z $\sim$ 1.6 (Kashino et al. 2013, see text for details). Following Harrison et al. (2012), in this plot in case of fits with multiple Gaussian components, the FWHM from the OC is plotted. Otherwise, the FWHM derived from a single component fit is adopted. For the objects in the sample of Liu et al. (2013) we use the velocity widths containing 80% of the flux ($W80$). Finally, magenta stars mark the $W80$ vs. [O III] luminosity for the QSO sources recently studied by Harrison et al. (2016). The [O III] luminosity is derived from the total [O III] flux for all samples.

Urrutia et al. (2012) sample using the spectra provided by Glikman et al. (2012) and applying a model similar to that described in the previous Sect. 2.4.1, limited only to the H$\beta$+[O III] region but including a proper modelling of the Fe II lines. The details of the fits and the results are reported in Brusa et al. (2015), and the FWHMs associated with the broad component are shown as orange stars in the lower panel Figure 2.9. In the hypothesis that the broad components can be ascribed to outflowing winds (see above), the high incidence of outflow components in ours and the Urrutia et al. (2012) sample (13/19 have FWHM$_{OC}$ > 1000 km/s) in such dust reddened QSOs may be an additional evidence that the blow-out phase is indeed heavily obscured.

The study of the small sample of sources isolated through the Brusa et al. (2010) selection criteria has revealed the efficiency in the selection of targets with emission line profiles severely affected by non-gravitational broadening. We find complex [O III] profiles in $\approx$ 70% of our sample. Such fraction is very high, but it is also consistent with very recent results we obtain studying z < 0.8 SDSS X-ray AGNs (see Chapter 5), and those at $= 1.1 - 1.7$ in Harrison et al. (2016): the most luminous sources have $\gtrsim$ 2 higher incidence of high velocities. Moreover, Harrison et al. 2016 find no evidence that the highest ionised gas velocities are preferentially associated with X-ray obscured AGNs. Such results, however, are derived for small samples ($\lesssim$ 10 sources with X-ray luminosities comparable to those of our sources) and a strong conclusion is still neglected.

## 2.5 XID 2028 and XID 5321 as prototype of obscured QSOs

In the next sections we focus our analysis on the two brightest X–ray targets, XID 2028 and XID 5321, in order to exploit the high S/N of our data and constrain at best the multi-wavelength properties of the population of obscured quasars. These are the two sources detected at the highest S/N in X-shooter NIR spectra. In addition, they are also extreme in the host galaxies properties: they have stellar masses of the order of $5 \times 10^{11}$ M$_\odot$ and exhibit substantial SFRs (SFR$\sim$250 M$_\odot$/yr), as inferred from the Herschel PACS detection (Brusa et al. 2015). These SFRs are consistent with those observed for the normal population of star forming galaxies at z $\sim$ 1.5 and place the targets on the main sequence (see Fig. 2.2). Finally, they have BH masses of the order of $10^9 - 10^{10}$ $M_\odot$, obtained as H$\alpha$ single-epoch virial estimates, typical of the population of QSOs at z $\sim$ 1.5 (Bongiorno et al. 2014). Morphology and radio emission properties are approximately consistent with those of the entire sample of 10 X-ray selected QSOs (see Table 2.1). Figure 2.10 shows the CFHT/WIRCam cutouts of the H band image of the two targets, in which complexities and asymmetries are noticeable (see also Fig. 2.3).

### 2.5.1 Spectral energy distribution in obscured (type 1) QSOs

The rest-frame SEDs of the two targets are shown in Figure 2.11, from far-IR wavelengths to X-ray soft and hard energy bands (black points). Such energy distributions differ from the one presented in the Introduction Chapter (Fig. 1.1). This is mostly due to the fact that in obscured AGNs the optical-UV nuclear emission is absorbed by the dusty material which hides the view of the central region and is then reprocessed in the IR. As a consequence, the contribution of the AGN is maximum at MIR wavelengths (around 12 $\mu$m, Gandhi et al. 2009), while most of the emission at longer wavelengths can be mostly ascribed to star formation (the BBB emission is strongly attenuated). The data points from far-infrared to the UV band of

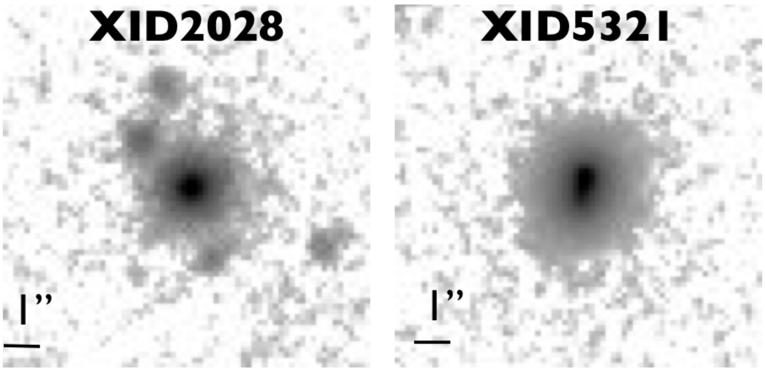

Figure 2.10: Cosmos CFHT/WIRCam H band images ($10'' \times 10''$) of XID 2028 (left) and XID 5321 (right). Images are oriented with north up and east to the left.

XID 2028 and XID 5321 are therefore fitted using the SED-fitting code presented in Lusso et al. (2013), with a combination of four elements: *1)* a BBB component for the AGN accretion disk thermal emission (blue curves); *2)* a stellar component, to account for the host galaxy contribution (green curves); *3)* a torus component to consider the reprocessed AGN emission in the MIR (brown curves); *4)* a starburst component for the on-going star formation (grey curves). The red lines represent the best-fit SEDs. We notice that, given the quality of the data points (e.g., dense sampling, bright fluxes and small errors) and the distinctive shape of the SEDs, the decomposition in the different components is basically independent from the details of the fitting code, both in terms of templates used, and minimization procedure. In particular, we verified that all the physical parameters of interest (e.g., AGN luminosities, SFR, extinction) are solid and do vary only marginally (within 10-20%) when other SED fitting codes developed in COSMOS are used instead (e.g., Bongiorno et al. 2012; Delvecchio et al. 2014). The only parameter which vary significantly (a factor of 2) is the stellar mass, contingent on the presence of the reddened accretion disk component in these targets. From these fits we infer reddening values E(B-V)=0.95 and 1.0 for the AGN components in XID 5321 and XID 2028, respectively. The extinctions are obtained by reddening the BBB template according to the Small Magellanic Clouds (SMC) law (Prevot et al. 1984). Overall, the AGN contribution to the bolometric output (in the range 1-1000 $\mu$m) is $\sim$ 60% for XID 2028 and $\sim$ 80% for XID 5321. Accounting for the extinctions and the best-fitting model SEDs, we infer total a bolometric luminosity of $L_{bol} \sim 2 \times 10^{46}$ erg/s for both the sources. Using the BH masses already mentioned, we obtain Eddington ratios of $L_{bol}/L_{Edd}$ of few %.

Composite SEDs for a sample of Type 2 AGN in XMM-COSMOS are presented in Lusso et al. 2011 for different bins of redshifts and luminosities. In each panel of Figure 2.11 we have plotted the composite SED constructed in a similar range of luminosity of our targets (log $L_{8\mu\mathrm{m}} \sim 44.3 - 45.7$, which roughly corresponds to log $L_{\mathrm{bol}} \sim 45.3 - 46.7$). From the comparison of the SED of our targets and the average SED of X–ray selected sources at the same luminosity, we note that the X–ray data-points of XID 2028 and XID 5321 are above the average SED by $\sim 0.5$ dex. This confirms that these 2 targets are X–ray loud (as per their selection on the basis of the high X/O ratio) but optically weak (without a clear view of the accretion disc emission). Indeed, the flat shape between 1-10 $\mu$m and the presence of BLR lines in the NIR X-shooter spectra, are all consistent with a transition from type 2 to type 1 through a reddened type 1 phase.

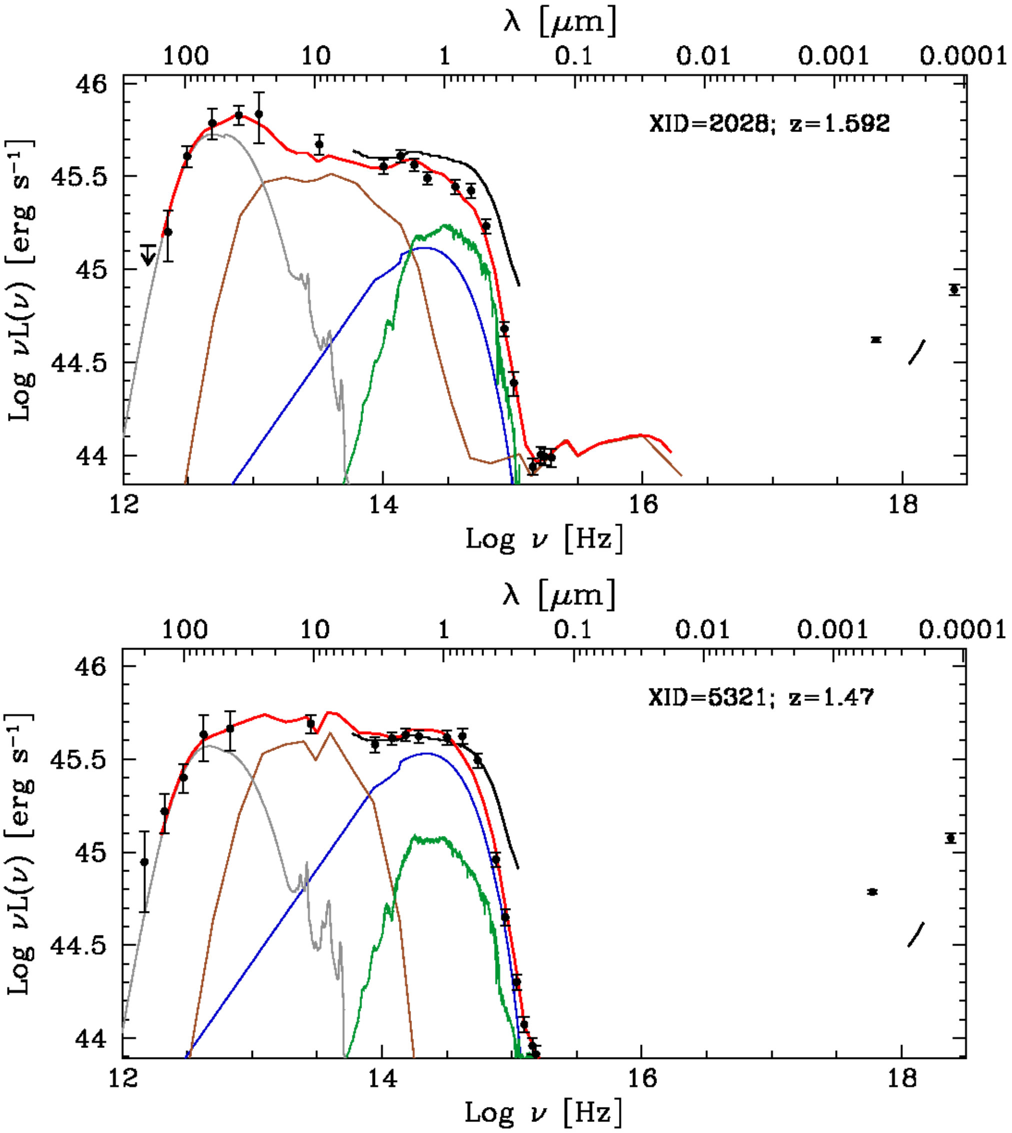

Figure 2.11: SED fits of XID 2028 and XID 5321. Black circles are the observed photometry data. The grey, brown, blue and green lines correspond to the starburst, AGN torus and disk, and host-galaxy best-fit templates obtained using the the SED-fitting code by Lusso et al. (2013). The red lines show the best-fit SEDs. As a comparison, the black lines represent the mean SED computed by Lusso et al. (2011) for obscured AGN in the XMM-COSMOS survey at redshift z= 1.5 and with similar bolometric luminosity.

### 2.5.2 X–ray spectra and absorber environments

For both sources medium-deep X–ray spectra are available from the XMM-COSMOS survey (Mainieri et al. 2011). XMM-Newton pn and mos spectra were extracted using standard techniques and calibration files, following the procedures described in details in Mainieri et al. (2011) and Lanzuisi et al. (2014).

The best-fit model for XMM spectra are presented in Figure 2.12 (left panel). An absorbed power law provides a good fit over the $\sim 0.3$–8 keV energy range. For both sources the best-fit intrinsic slope and absorption column density are similar: $\Gamma \simeq 1.84{\pm}0.12$, $N_H \sim 7.1{\pm}0.2{\times}\ 10^{21}$ cm$^{-2}$ for XID 2028, and $\Gamma \simeq 1.78 \pm 0.12$, $N_H \sim 5.8 \pm 0.2{\times}\ 10^{21}$ cm$^{-2}$ for XID 5321. The $N_H$ versus $\Gamma$ confidence contours (68, 90 and 99%) are shown in Figure 2.12 (right panels). There is no evidence of iron K$\alpha$ emission with 90% upper limits of 100 eV and 250 eV (rest–frame) in XID 2028 and XID 5321, respectively. The addition of a Compton reflection component subtending a $2\pi$ angle at the continuum source marginally improves the fits ($\Delta\chi^2$ $\sim$2). The intrinsic spectral slope gets steeper $\Gamma \sim 1.93$–1.99 and the intrinsic absorption higher $N_H \sim$ 7–8 $\times$ $10^{21}$ cm$^{-2}$ respectively. The moderate, but significant intrinsic X–ray absorption argues against a pure Type 1 nature, while it is fully consistent with the reddened spectra obtained by the near infrared X-shooter instrument (Fig. 2.4). The moderate obscuration observed in the X–rays, coupled with the Eddington ratio ($\lambda_{\rm Edd} \sim 1-5\%$) places these objects in the region of "short-lived clouds" presented in Raimundo et al. (2010), where outflows or transient absorption are expected to happen. However, the observed intrinsic absorption could be consistent with material in the host galaxy, or with some circum-nuclear material such as a low column density torus or the outer parts of a thicker one. Current observations at X-ray and infrared bands do not allow such discrimination (but see Netzer 2015; Schneider et al. 2015). While the so far collected information point to the interpretation of QSOs caught in the transition phase, we still need to prove that the observed attenuation is actually due to a galaxy-wide absorption material, as expected in the initial phases of a merger (e.g., Hopkins et al. 2008), and not to a toroidal absorber. We anticipate that the rest-frame optical spectroscopic analysis will allow an important step in the direction of the former scenario.

### 2.5.3 NIR slit-resolved spectroscopy analysis

As presented above, the XID 2028 and XID 5321 spectral analysis revealed the presence of outflowing components in their nuclear spectra (extracted from an aperture of $\sim 1''$), associated with the most prominent NLR emission lines in the H$\beta$-[O III] and H$\alpha$-[N II regions, with velocity shifts $V_S$ with respect to the systemic features, on the order of $|V_S| \sim 350-450$ km/s, and $V_{max} \sim 1500$ km/s, . XID 2028 shows a blueshifted component, while XID 5321 shows a less common redshifted component (see also Bae and Woo 2014; Harrison et al. 2012; Villar-Martín et al. 2011 for other examples of [O III] lines with redshifted broad wings).

Here we analyze in more detail the X-shooter spectra of these two sources, with the aim of determining more accurate estimates of the key parameters related to the outflowing winds, namely spatial extension, outflow velocity and amount of material involved in such phenomena.

The analysis presented here is based on the spectra extracted from three different spatial positions along the slit ($a$, $b$, $c$; see Figure 2.13), taking into account the seeing conditions during the observations. For both the sources, the ($b$) region is centred on the nucleus, as determined from the peak of the spatial profile of the continuum emission. Such nuclear region covers a projected area of $0.85 \times 0.90''$ (i.e. $\sim 7.3 \times 7.7$ kpc). The ($a$) and ($c$) apertures, instead, consider the emission from two regions offset from the nucleus. The slit position used in the X-shooter observations and the spatial location of each aperture are shown in the upper panels

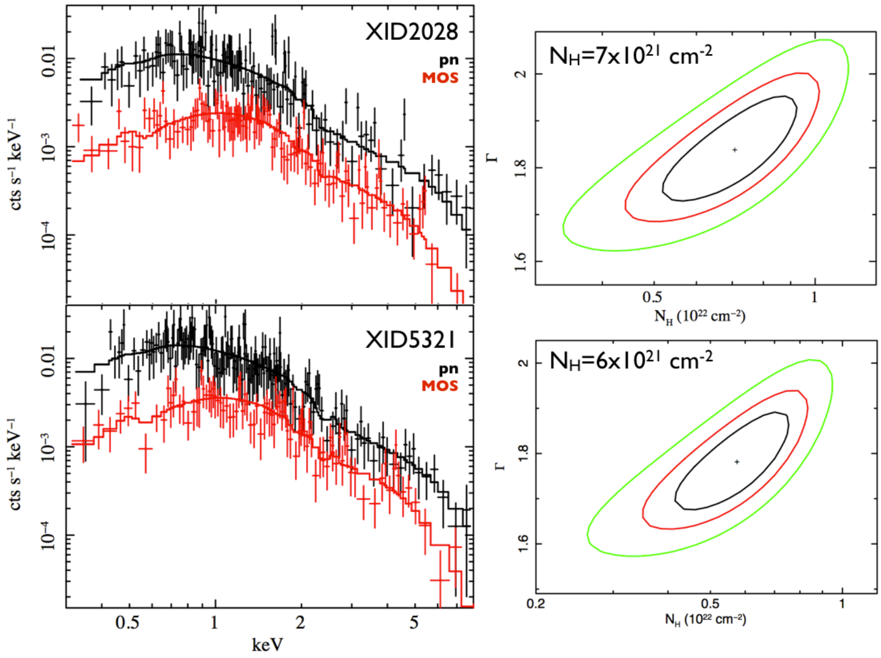

Figure 2.12: X–ray spectra of XID 2028 (top, left) and XID 5321 (bottom, left). The different datasets used (XMM pn and MOS), are labelled in different colours. The best-fit model is also shown as a solid line for each dataset. The total number of net counts used in the spectral fitting sums up to $\sim 1500$ for both sources. On the right are shown the combined constraints on N$_H$ and the spectral slope, with confidence contours at 68, 95 and 99% level.

of Figure 2.13.

### Evidences of wide-scale outflows

The spatial profiles obtained from the 2D spectra are shown in Figure 2.13 (bottom panels). The *solid curves* show the spatial profile of the continuum flux, obtained by averaging profiles extracted at many line-free regions along the entire dispersion axis; the *dashed curves* show the spatial profile of the emission in the [O III]λ5007 line. The vertical dotted lines mark the regions indicating the location of the three apertures described above, as labelled. For XID 2028, such spatial profiles display the first evidence that complex kinematics may be in place. In the ($a$) aperture, we observe an enhancement in the ionized gas emission with respect to the continuum profile, more presumably associated with host galaxy stellar emission. A possible interpretation is that the projected spatial distribution of the ionized gas is more extended than the host galaxy, and that oxygen emission is tracing outflowing material unleashed from the system. In XID 5321 we observe only a small displacement between the two spatial profiles, most probably due to the observed slight tilt in the 2D spectrum along the dispersion axis.

Figure 2.14 shows the spectra around the [O III]λ5007 line, extracted from each region, indicated with letters ($a$, $b$, $c$; detailed description for the best-fit models showed with coloured lines are given below). For both sources, significant signal is detected not only in the central region (covering $\approx 4-5$ kpc), but also in the off-nuclear aperture (aperture ($a$) for XID 2028, ($c$) for XID 5321). The 2D spectra shown in the lower panels clearly display the broadening of the emission lines at bluer (XID 2028) and redder (XID 5321) wavelengths, responsible of the asymmetric and broad wings in the 1D spectra, as well as an extended line emissions, which are fully resolved ($\gtrsim 2 \times$ seeing), out to a distance of R $\approx 10-12$ kpc, therefore extending considerably over the host galaxy.

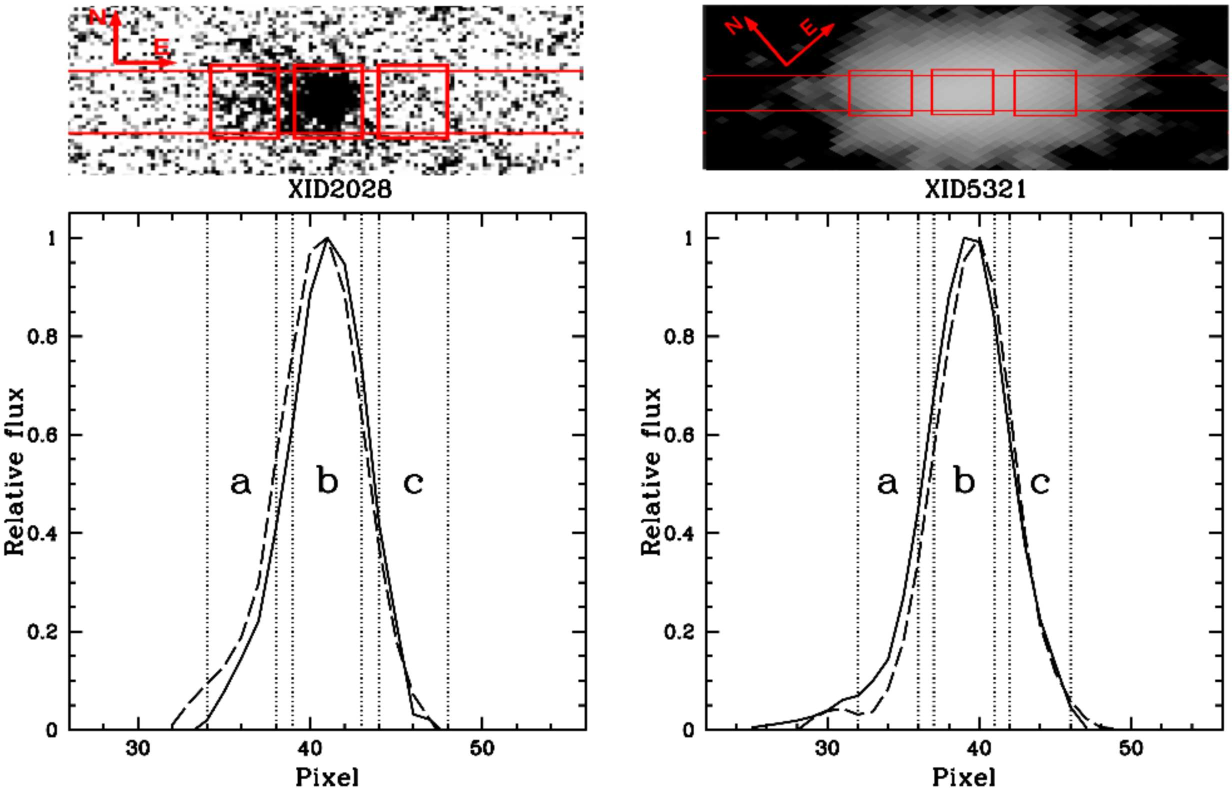

Figure 2.13: (*lower panels*) Spatial profiles of the 2D spectrum of XID 2028 (left) and XID 5321 (right) of the continuum flux (solid curves) and in the proximity of [O III]$\lambda$5007 emission line (long dashed curves). Both continuum and [O III]$\lambda$5007 wavelength range profiles are normalized to unity. The dotted lines shows the demarcations of the three regions from which the apertures were extracted (denoted with $a$, $b$, and $c$). (*upper panels*) HST/ACS F814 image of XID 2028 (left) and J-band UltraVista image of XID 5321 (right) showing the position and orientation of the 0.9" slit and the spatial locations of the three apertures.

A comparison with the results we obtain from SINFONI follow-up for XID 2028, published in Cresci et al. (2015a), are shown in Fig. 2.15: the extended emission in the right panel maps the [O III] blue wing, in the range $1294 < \lambda < 1296$ nm, while the circular shape in the left panel correspond to the core of the emission line ($1296 < \lambda < 1300$ nm). The elongated shape tracing the outflowing gas is covered by X-shooter slit, whose position angle was chosen ad hoc to follow the patchy morphology displayed in Fig. 2.3. This means that the slit resolved analysis is actually able to map such outflowing ionized material. Indeed, the same physical projected extension we estimate from 2D spectra ($\approx 10$ kpc) is confirmed in SINFONI data.

In order to constrain at best the properties of the ionized outflow component, we performed both non-parametric analysis and simultaneous fit of the emission lines. The non-parametric measurements of the emission lines allow better constraints on the velocity properties (Section 2.4.1), while the simultaneous fitting allowed us to quantify the relative outflow luminosities at different radii and to disentangle the contribution of the outflow fluxes from those of the unperturbed gas in the central apertures (Sect. 2.4.1).

### Multicomponent simultaneous fit

In the nuclear regions, we apply the simultaneous modelling, as described in Sect. 2.4.1. In the off-nuclear apertures, where we do not expect to see BLR emission lines, and the S/N is low,

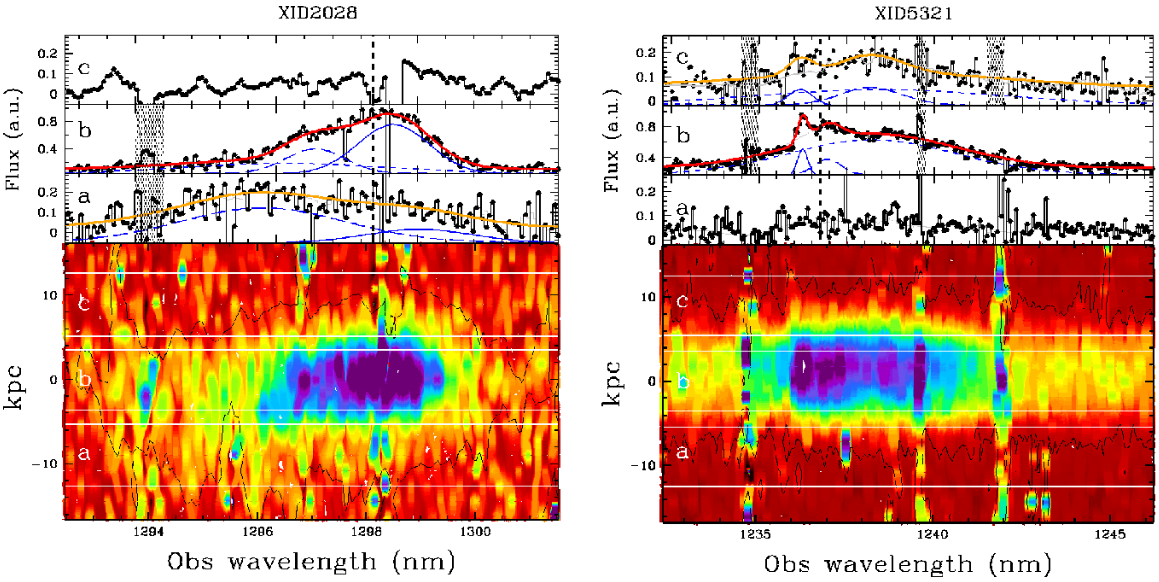

Figure 2.14: XID 2028 (left) and XID 5321 (right) X-Shooter spectra of the regions $a$, $b$, $c$, centred on [O III]$\lambda$5007. The red and orange lines indicate the best-fit solutions that reproduce the line profiles according to the non-parametric approach (see Section 2.4.1). The Gaussian components are shown with arbitrary normalization in order to ease the visualization. The dotted lines mark the wavelength of [O III]$\lambda$5007 at the systemic redshift determined by B14. The lower panels show the 2D spectra, indicating the apertures used to extract the 1D spectra seen in the upper panels. Red to blue colours represent increasing flux. Extended vertical structures, like the one at $\sim$ 1242 nm (right), delineate strong sky features and are indicated in the 1D spectra as shaded areas.

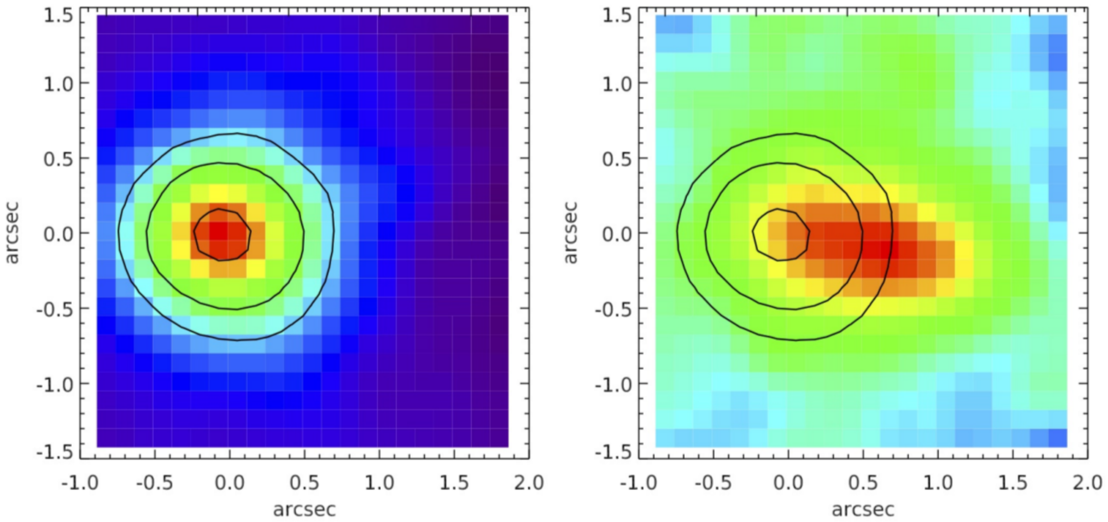

Figure 2.15: SINFONI [O III]$\lambda$5007 channel maps obtained integrating the continuum subtracted SINFONI datacube on the line core ($1296 < \lambda < 1300$ nm, *left*) and on the blue wing ($1294 < \lambda < 1296$ nm, *right*). The contours on the line core (levels 0.3, 0.5, 0.9 relative to the peak), marking the position of the central QSO, are shown in black in both panels. The fully resolved, extended blue wing due to the outflow is extended up to 1.5”, i.e. $\approx$ 13 projected kpc from the QSO position. North is up and East is left, 1” corresponds to 8.5 kpc. Figure form Cresci et al. (2015a)

only one set of Gaussian profiles is used, with no limit to the FWHM.

Figure 2.16 shows the best-fit solution of our spectra, as in Fig. 2.5, for the apertures (*a*) and (*b*) for XID 2028 and (*b*) and (*c*) for XID 5321. It turns out, especially for the [O III] emission lines, that the profiles of the nuclear regions (red curves in the figure) are broad and asymmetric. The same effect cannot be recognised in the other emission lines, namely H$\alpha$, H$\beta$ and the forbidden [N II] and [S II], because they are blended with the BLR component and/or of lower S/N (but see the decomposition in Fig. 2.5; see also the type 2 AGN spectra shown in Chapter 5). Using all the constraints due to the atomic physics, and therefore minimizing the degeneracy (especially in the [N II]+H$\alpha$ profile), this approach allows us to unveil, in the nuclear regions, the presence of one component associated with overall narrow profiles (FWHM $\sim$ 300-500 km s$^{-1}$), likely associated with the unperturbed gas within the NLR, and of another component with FWHM $\sim 1300 - 1600$ km/s and shifted with respect to the narrower ones ($V_S \sim 340$ km s$^{-1}$), associated with outflowing emitting gas. Moreover, it allows us to study the physical conditions of the ionizing gas of these two components using the line flux ratios (see Section 2.5.5). The profiles in the off-nuclear regions (orange curves in Figure 2.16) appear broader and shifted with respect to those determined in the nuclear regions (see Section 2.4.2), and are likely associated with outflowing emitting gas.

### Non-parametric velocity estimates

In order to reproduce at the best the nuclear and off-nuclear [O III] profiles and perform non-parametric analysis, we realize an independent fit for the oxygen doublet only. The best-fit solutions for the XID 2028 and XID 5321 [O III] lines are shown in Figure 2.14 for the different apertures along the slits. Gaussian components with widths up to $\sim$ 1000 km s$^{-1}$ are required, especially in the off-nuclear apertures. In particular, the [O III] line of the nuclear aperture of XID 5321 presents a peculiar profile, with different peaks. Two out of the three Gaussian lines that reproduce the total profile have width smaller than 500 km/s, and could be attributed to emitting gas within NLR and star forming regions characterized by different kinematic conditions. Alternatively, they can be originated in two distinct systems (e.g., merging galaxies) not resolved by our imaging data[5] (see Fig. 2.10). Such complexity is not revealed in other emission lines. This suggests a third possible explanation: a simple bad sky feature residual could be responsible of the peculiar shape (as also seems to be confirmed by follow-up SINFONI observations; Cresci et al. in prep).

Figure 2.17 shows the comparison between [O III] velocity profiles for the nuclear (upper panels, red curves) and the off-nuclear regions (lower panels), with the non-parametric measurements of the best-fit labelled. The profiles in the lateral apertures appear broad and shifted with respect to the systemic velocity determined in the nuclear regions. In particular, $V_{max}$ increases by $\sim$ 200 km s$^{-1}$ going from the nuclear to the off-nuclear apertures, for both sources. The [O III] of XID 5321 shows, in both apertures, also a blueshifted wing, although it is much less extended than the red wing.

In Table 2.3 we quote the $V_{max}$, the line widths $W80$ and the velocity shifts $\Delta V$ as obtained from the non-parametric analysis, and the FWHM of the outflow components and the velocity shift $V_S$ from the simultaneous fitting, all values which are used as estimator of velocity of the outflow in the literature (e.g., Cano-Díaz et al. 2012; Cresci et al. 2015a; Harrison et al. 2012, 2014, 2016; Westmoquette et al. 2012). We underline that simultaneous fit results, i.e. the first three columns, regard all the emission lines and not only the [O III] emission.

---

[5] Although the COSMOS field has been imaged by HST/ACS with a mosaic over 1.7 deg$^2$ (Koekemoer et al. 2007), XID 5321 lies outside such area and therefore the highest resolution imaging data are limited at 0.7".

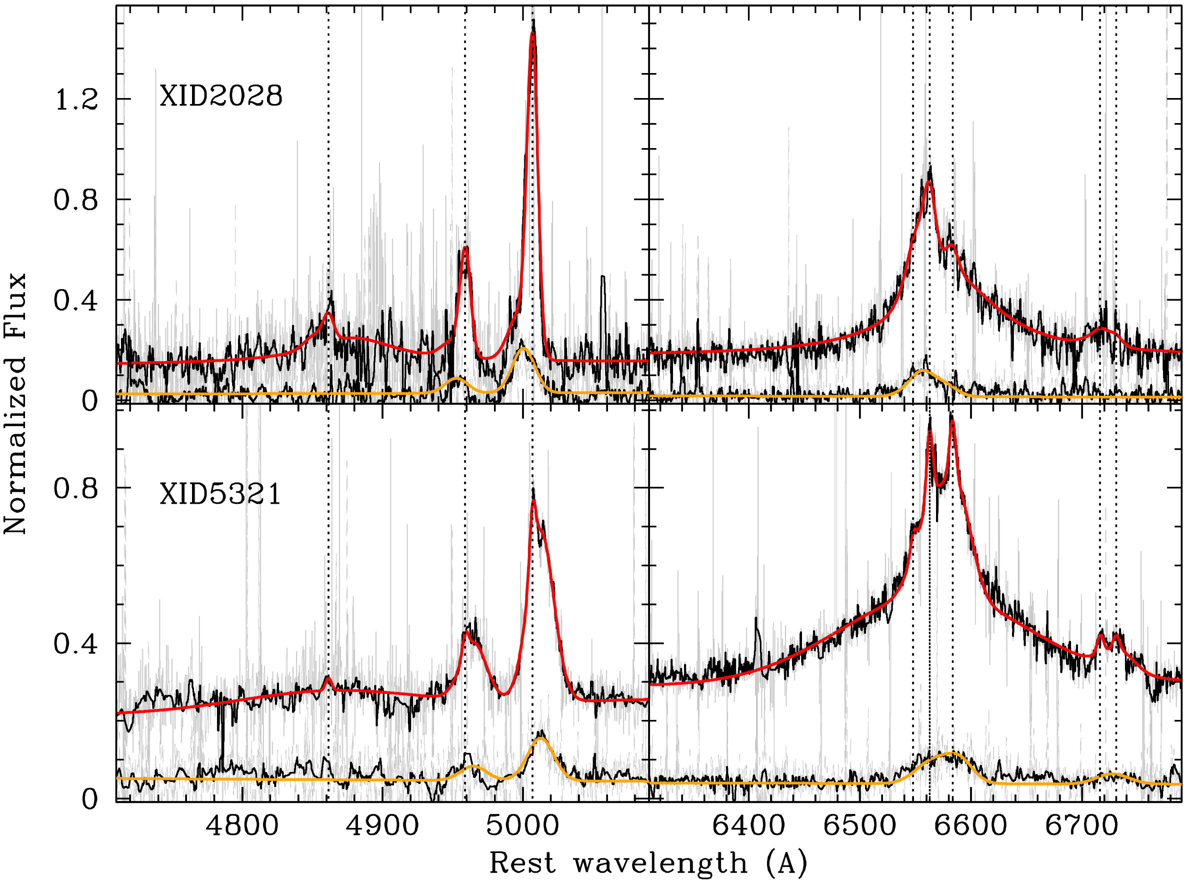

Figure 2.16: Spectra of the two quasars normalised so that the intensity of the strongest emission line of the nuclear aperture is unity. For clarity, in the figure the nuclear spectrum of XID 2028 is shifted vertically in order to facilitate a visual inspection of the apertures. The grey and black lines indicate the original and the cleaned (of cosmic ray hits, bad pixels and telluric lines) spectra. The red and orange lines indicate the best-fit solutions that reproduce the line profiles of the central and the lateral apertures according to the simultaneous fit approach. The dotted lines mark the wavelengths of H$\beta$, [O III]$\lambda$4959, [O III]$\lambda$5007 (left) and [N II]$\lambda$6548, H$\alpha$, [N II]$\lambda$6581, and the [S II] doublet (right), from left to right, at the systemic velocity.

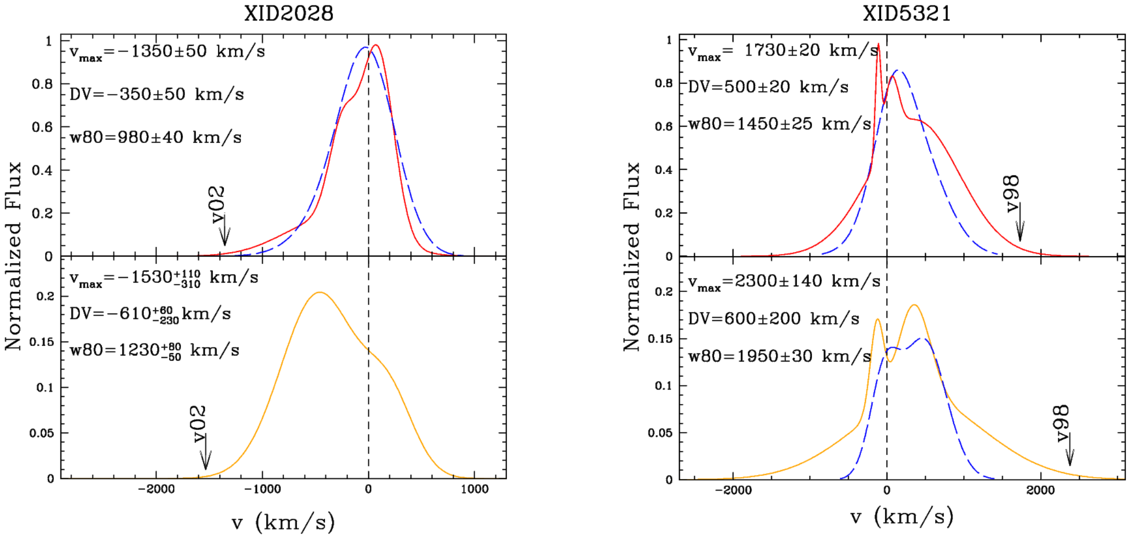

Figure 2.17: Comparison between [O III]$\lambda$5007 velocity profiles: red curves for the nuclear apertures in the upper panels, orange curves for the off-nuclear apertures retaining the outflow emission in the lower panel. The non parametric measurements of the [O III] fit are labeled. We also overplot in long-dashed blue the results for [O II] emission lines fit (see Section 2.5.4). The [O II] profiles are renormalized in order to facilitate a comparison with the [O III]. The dashed lines mark the positions chosen as zero velocity (the systemics for [O III], and the mean wavelength of the [O II] doublet), the arrows mark the 98th and 2th percentiles indicating the $V_{max}$ velocities.

The velocity estimators obtained in the off-nuclear regions have all very high values ($V_{max} \gtrsim$ 1500 km/s). Overall, all the velocity estimators are greater in the lateral apertures by up to 45%. Differences between the velocity offsets $V_S$ and the non-parametric $\Delta V$ estimators are due to the fact that $\Delta V$ depends strongly on the relative flux contributions of different components of the line profile.

## 2.5.4 Additional evidences of outflow

### [O II] emission lines

Zakamska and Greene (2014) found that [O II]$\lambda\lambda$3726,3729 also show outflow signatures, in some cases consistent with extremely broad features as seen in [O III]. At the redshift of our targets, the [O II] lines are redshifted in the 9200-9600 Å range, sampled by the VIS arm of the X-shooter instrument.

In this instance, we do not need to infer the flux emission from both unperturbed and perturbed gas, our purpose is to obtain the non-parametric velocity measurements described previously and, possibly, to infer the presence of outflowing gas also in these low-ionization lines. In fact, given the lower S/N of [O II] with respect to the previously analysed lines, and the wavelength separation between the doublet lines (comparable with the resolution), we are required to treat the doublet as a single Gaussian line. This means that in such a case it is not either possible to distinguish between NC and OC as in the previous fits. The [O II] emission line non-parametric velocity measurements are collected in Table 2.3.

The XID 2028 [O II] emission lines are at the edge of the spectral range covered by the VIS arm, where the total transmission is very low. For this reason, we re-analysed the available Keck/DEIMOS spectrum (presented byBrusa et al. 2010, fig. 13). Such spectrum of XID 2028, obtained with DEIMOS (in MOS mode) at Keck-II telescope (Faber et al. 2003) on 2008

Table 2.3: Velocity measurements

| | | $FWHM_{NC}$ | $FWHM_{OC}$ | $V_S$ | $\Delta V$ | $V_{max}$ | $W80$ |
|---|---|---|---|---|---|---|---|
| | | (km s$^{-1}$) | | | | | |
| XID 5321 | | | | | | | |
| $[OIII]$ | a | - | - | - | - | - | - |
| $[OII]$ | | - | - | - | $256 \pm 15$ | $950 \pm 70$ | $1040 \pm 55$ |
| $[OIII]$ | b | $310 \pm 15$ | $1320 \pm 10$ | $350 \pm 10$ | $500 \pm 20$ | $1730 \pm 20$ | $1450 \pm 25$ |
| $[OII]$ | | - | - | - | $280 \pm 20$ | $1050 \pm 25$ | $1060^{+60}_{-20}$ |
| $[OIII]$ | c | - | $1650 \pm 50$ | $330 \pm 20$ | $600 \pm 200$ | $1950 \pm 30$ | $2300 \pm 140$ |
| $[OII]$ | | - | - | - | $225 \pm 65$ | $1350^{+110}_{-60}$ | $1230^{+200}_{-100}$ |
| XID 2028 | | | | | | | |
| $[OIII]$ | a | - | $1300 \pm 45$ | $-385 \pm 15$ | $-610^{+60}_{-230}$ | $-1530^{+110}_{-310}$ | $1230^{+80}_{-50}$ |
| $[OIII]$ | b | $510 \pm 13$ | $1310 \pm 65$ | $-340 \pm 30$ | $-350 \pm 50$ | $-1350 \pm 50$ | $980 \pm 40$ |
| $[OIII]$ | c | - | - | - | - | - | - |
| $[OII]$ | Keck | - | - | - | $-100 \pm 15$ | $810 \pm 20$ | $-900 \pm 100$ |

Notes and column description. The values in the first three columns, corresponding to the simultaneous fit results, regard all the emission lines and not only the [O III] emission. $FWHM_{NC}$ and $FWHM_{OC}$ refer to narrow and outflow components described in Section 2.4.1.

January 8, with mildly lower resolution (2.5$\mathring{A}$; seeing $\sim 1''$), was flux-recalibrated in order to re-normalize it to the X-shooter spectra by multiplying the spectrum by a constant factor. The best-fit solutions are shown in Figure 2.18: two Gaussian lines, one of them blueshifted with respect to the systemic velocity, are required to reproduce the shape of the emission line. As mentioned above, we have not tried to deblend the doublet, but a hint of the peaks could be in the vicinity of the dashed vertical lines. The [O II] velocity offset of XID 2028 is lower (∼30%) than the [O III] one, but still statistically significant, supporting the presence of outflowing ionizing gas also in this lower (but comparable to the [S II]; see Table A.1) ionization phase.

As for the NIR, we extracted the XID 5321 VIS spectra from the same three regions along the slit. The [O II] emission lines of XID 5321 are detected in all the three apertures (see Figure 2.19), i.e. show a greater spatial extension with respect to the [O III] emission line. The best fitting models are shown in Figure 2.19 and include two components for the nuclear (*b*) and off-nuclear (*c*) X-shooter spectra, and one component for the off-nuclear (*a*) spectrum. The wavelengths of the [O II] doublet are indicated with dashed vertical lines; here, again, a hint of peaks is in the vicinity of the systemic [O II] lines. Nevertheless, we stress that we are interested in the measure of outflow velocity and that in the non-parametric approach we just need to reproduce the entire profile, without associate particular interpretation to the individual Gaussian profiles shown in the figure. Even in this case, the [O II] velocity offsets of XID 5321 are lower (∼40%) than the [O III] one, but still significant.

The comparison between the [O III]$\lambda$5007 and [O II] doublets are shown in Figure 2.17: [O II] velocity profiles are narrower than [O III], but also shows almost the same asymmetries and shifts, in agreement with the results of Zakamska and Greene (2014).

Summarizing, although at lower S/N, these emission lines confirm the presence of outflowing gas in both targets, and in one case (XID 5321) with a greater spatial extension than in the [O III] emission.

### Absorption Lines

Kpc-scale outflows are observed in both the neutral and ionized gas phases (e.g., Rupke and Veilleux 2013, 2011). Sodium Na I D$\lambda\lambda$5890,5896 and magnesium Mg II$\lambda\lambda$2796,2803, Mg I$\lambda$2853

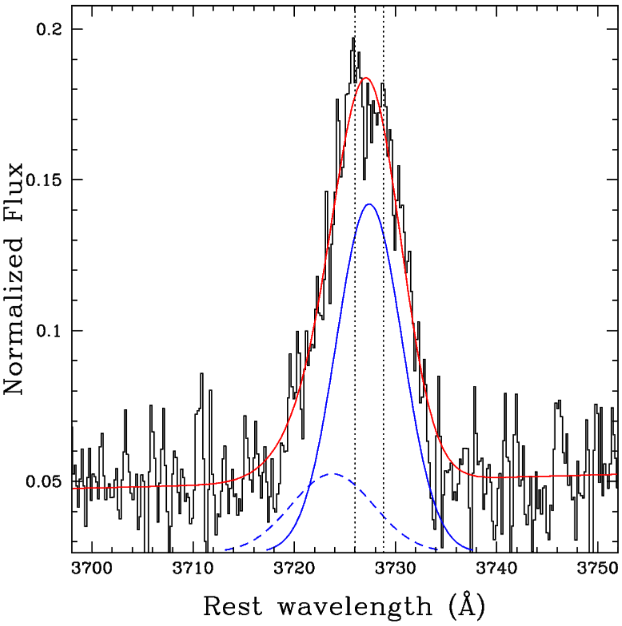

Figure 2.18: Keck/DEIMOS spectrum around the [O II]$\lambda\lambda$3726,3729 region of XID 2028. The spectrum is normalised so that the intensity of the strongest emission line (in the VIS+NIR wavelength range) of the nuclear aperture is unity. Superimposed on the spectrum are the best-fit non-parametric analysis components (solid and dashed blue curves, with arbitrary normalization in order to ease the visualization). The red solid curves represent the sum of all components, including the power-law. Dotted lines mark the wavelengths of the [O II] emission lines.

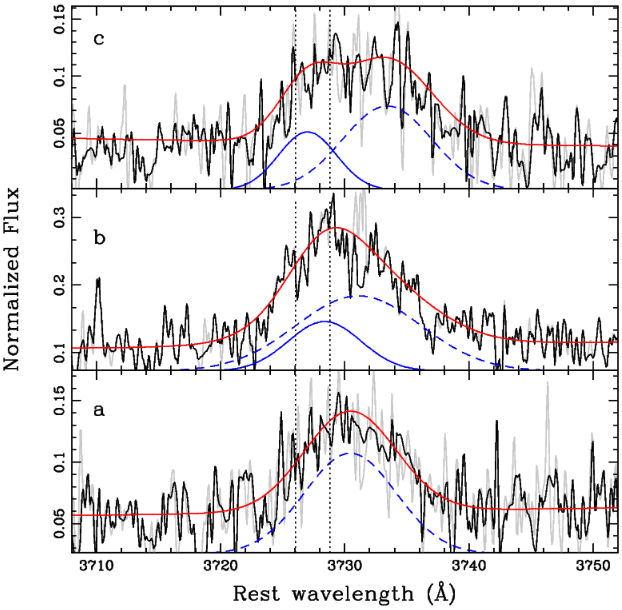

Figure 2.19: X-shooter spectra around the [O II]$\lambda\lambda$3726,3729 region of XID 5321. Grey and black lines indicate the original and the cleaned (as above) spectra. All the regions $(a, b, c)$ are shown. See previous figure for description.

absorption lines are detected in our spectra. Figure 2.20 shows the XID 2028 Keck/DEIMOS spectrum (on the right) and the XID 5321 X-shooter VIS spectrum (on the left) with the

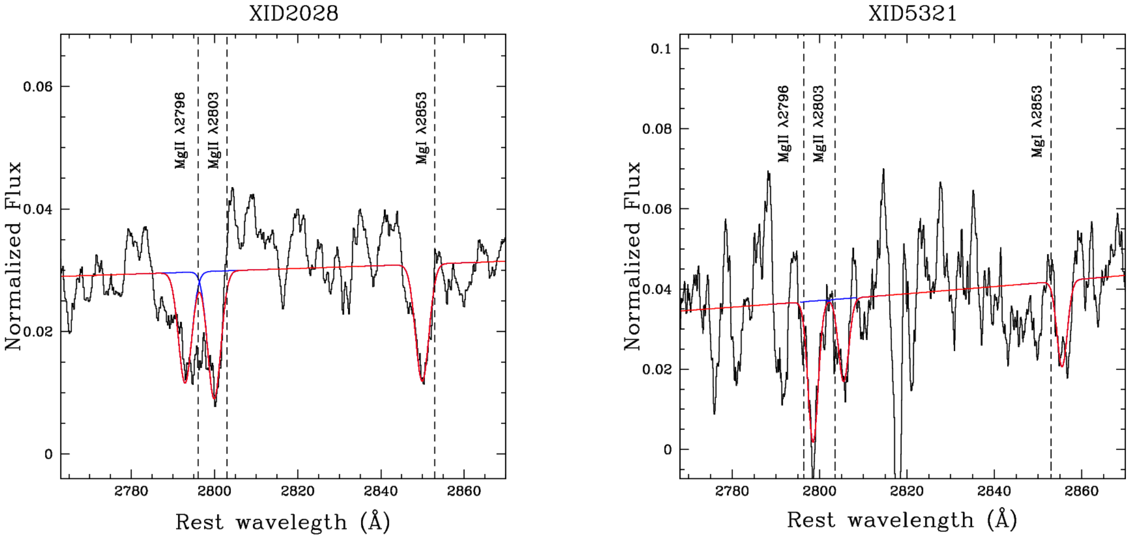

Figure 2.20: XID 2028 smoothed Keck/DEIMOS spectrum (left) and XID 5321 smoothed X-shooter spectrum (right) with the magnesium absorption lines marked. The dashed lines in the spectra mark the rest-frame wavelengths of Mg II and Mg I, as determined from the systemic redshift. Superimposed on the spectra are the best-fit components indicated as solid blue Gaussian curves. The red solid curves represent the sum of the Gaussian components.

magnesium absorption lines labelled. The Keck spectrum was preferred to the X-shooter one due to its higher S/N. Given the low S/N, only the central aperture of XID 5321 has been analysed.

Each of the magnesium absorption lines of XID 2028 were fit with one set of Gaussian profiles, as shown in Figure 2.20 (left). A velocity shift $V_S \approx$ -330 km s$^{-1}$ with respect to the systemic velocity was found. The sodium profiles, although affected by numerous sky features, seem to be reproduced with the same velocity component of the magnesium profiles.

Each of the magnesium lines of XID 5321 were fit with one Gaussian component too, as shown in Figure 2.20 (right). The corresponding velocity shift is $V_S \approx 260$ km s$^{-1}$. Even for this source, the sodium profiles were reproduced with the same velocity component of the magnesium profiles.

We stress that for both sources, the sodium regions are strongly affected by sky features; the estimated continua and the Gaussian components did not allow us to study the properties of the absorbing gas, and are presented uniquely as proof of the constrained magnesium components, themselves characterized by low S/N.

The estimated shifts VIS-NIR of a few tens of km s$^{-1}$ between magnesium and sodium lines of XID 2028 and XID 5321 respectively, are greater than the accuracy of the wavelength calibration ($\sim$ 10 km s$^{-1}$; $\Delta z = 0.0004$) checked with the position of known sky lines in both VIS and NIR spectra (see Brusa et al. 2015, sect. 4.1). However, given that all our absorption lines suffer of low S/N, they could be fully explained by an imperfect determination of the centre of the fitted Gaussian profiles and interpreted as residual error of the (greater) velocity shift $V_S$ values observed.

The XID 2028 absorption lines can be ascribed to an outflowing neutral/low-ionization component on the line of sight, with roughly the same velocity shift of the emission lines. The XID 5321 absorption lines show a velocity shift of the same magnitude of the emission lines too; possible interpretations are discussed in Section 2.5.6 and 2.6.

Table 2.4: Balmer decrements

| | BC | | NC | | OC | |
|---|---|---|---|---|---|---|
| | $f(H\alpha)/f(H\beta)$ | $A_V$[a] | $f(H\alpha)/f(H\beta)$ | $A_V$ | $f(H\alpha)/f(H\beta)$ | $A_V$ |
| XID 2028 | | | | | | |
| nuclear (b) | $4.4 \pm 0.3$ | $0.9 \pm 0.4$ | $3.2 \pm 0.6$ | $0.1 \pm 1.1$ | $6.2 \pm 0.5$ | $1.8 \pm 0.5$ |
| off-nuclear (a) | - | - | - | - | $> 1.7$ | - |
| XID 5321 | | | | | | |
| nuclear (b) | $6.4 \pm 0.5$ | $1.9 \pm 0.5$ | $> 3.8$ | $> 0.6$ | $> 3.7$ | $> 0.5$ |
| off-nuclear (c) | - | - | - | - | $> 1$ | - |

---

[a] Assuming Case B ratio of 3.1 and SMC extinction curve.

## 2.5.5 Emission line diagnostics

As mentioned in the Introduction, most previously reported studies which showed convincing evidence of the existence of large scale outflows have been conducted on AGN-ULIRGs systems. Given the concomitant presence of on-going SF and BH activity, it is not obvious to determine which is the main driver of the observed outflowing wind. Our targets are not ULIRGs but are however interested by strong SF activity (SFR $\approx$ 250 $M_\odot$/yr). In order to distinguish between AGN-driven and SF-driven outflows, we need to determine the ionization source of the observed emission lines. Furthermore, in order to unveil the mass and energy involved in the outflow components (Sect. 2.5.6; Appendix B), we need to derive the exact luminosity emitted by perturbed gas, i.e. we need to estimate the exact amount of extinction in the observed emission lines. These two important quantities can be derived from emission line diagnostics (see Appendix A).

### Estimates of extinction

We used line ratios to estimate the reddening of the sources. This is crucial to derive the corrected [O III] luminosity used later to estimate the outflow power. We used the Balmer decrements $f(H\alpha)/f(H\beta)$, as measured in our simultaneous fits described in Sect. 2.4.1, where $f$ represents the line flux. These can be determined for each set of Gaussian component of the simultaneous fit. In particular, for the nuclear apertures, we computed the ratios for the BLR (BC) components, the systemic NC, and for the OC. For the off-nuclear apertures, only one ratio can be estimated (see Sect. 2.4.1). When no H$\beta$ NC or/and OC were detected, we used the standard deviation of the continuum regions (in the vicinity of the emission line) and the FWHM of that set of Gaussian profiles to derive a 3$\sigma$ upper limit on the flux. Balmer decrements are reported in Table 2.4.

The $f(H\alpha)/f(H\beta)$ Case B ratio (Gaskell and Ferland 1984) is mostly used to determine the amount of extinction for low-density, such as that of the NLR, and for BLR gas (Dong et al. 2008; see Appendix A.4). We assumed the same ratio also for the outflow components. Therefore, assuming Case B ratio of 3.1 and the SMC dust-reddening law, the relation between the emission line colour excess and the Balmer decrements gives us, for XID 2028, a V-band extinction $A_V$ in the range 0.1-1.8, where the first value is evaluated for the NLR component and 1.8 for the outflow component. For XID 5321, we obtain an extinction $A_V$ in the range 0.5-1.9, where the first value is a lower limit evaluated for the outflow component, and 1.9 is obtained for the BLR region. Ratios from the off-nuclear apertures are smaller than 3.1, and no $A_V$ can be derived. Lower limits on the extinction follow from the use of upper limits on the flux of undetected H$\beta$ emission lines. Such lower limits imply the presence of significant

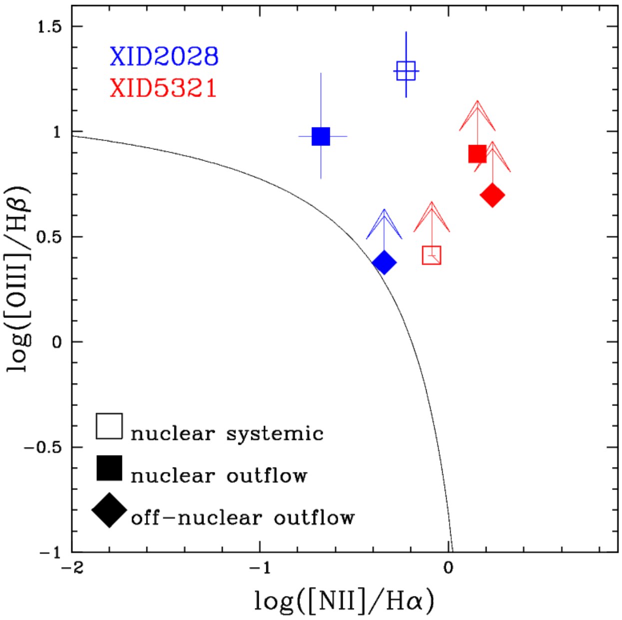

Figure 2.21: Standard diagnostic diagram showing the classification scheme by Kewley et al. (2013). The line drawn in the diagram corresponds to the theoretical redshift-dependent curve used to separate purely SF galaxies from galaxies containing AGN (Kewley et al. 2013). Empty and filled squares correspond to the systemic narrow and outflow components of the nuclear aperture; filled diamonds correspond to the outflow components of the off-nuclear apertures. Blue and red points represents XID 2028 and XID 5321 respectively. Upper arrows represent lower limits, due to undetected H$\beta$ emission line.

absorption in the host galaxy, therefore confirming that the observed high column densities are due to a diffuse obscurer material. In the following we will use the outflow component Balmer ratios to determine the extinction of the [O III] outflowing flux. In fact, those obtained in the SED fitting procedure are related to the continuum (BBB) flux that, being affected by a degeneracy between host and AGN accretion disk emission, are significantly more uncertain.

### Rest-frame optical AGN-SF diagnostics

We used the optical diagnostic Baldwin-Phillips-Terlevich diagram (BPT; Baldwin et al. 1981; see Appendix A.5) as a tool to investigate the nature of the ionizing sources. Figure 5.4 shows the BPT with the results from our spectroscopic analysis. The line drawn in the diagram corresponds to the theoretical redshift-dependent curve used to separate purely SF galaxies from galaxies containing AGN at z = 1.5 (Eq. 1 of Kewley et al. 2013). For both sources, all the systemic and the outflow components observed in the different apertures are consistent with an AGN classification.

We tested other possible line ratio diagnostics (e.g., Ho 2005; Kewley et al. 2006), involving [O III]/[O II] and [O I]$\lambda$6300/H$\alpha$ (detected only in the nuclear spectrum of XID 5321). All of them agree with an AGN photo-ionization origin. We can consequently conclude that, even if present, a star forming radiation fied would play a minor role in ionizing the observed emission lines (similar conclusions have been reached in Rodríguez-Zaurín et al. 2013).

### 2.5.6 Quantifying the outflow energetics

Currently, the estimate of outflow energetics (see Appendix B), allow an unique tool to relate observational items with theoretical predictions (see below). As it is easy to realize, all these quantities are derived from the estimate of the gas mass, which is obtained starting from the luminosity emitted by outflowing gas. Generally, the $H\beta$ luminosity is used to calculate the total amount of ionized gas in AGNs. This has been historically done to estimate the gas mass in BLR and NLR (see Introduction Chapter; Appendix B). In the context of outflowing mass computation, however, this feature is commonly replaced by the brighter [O III] line. This, in fact, has the advantage to not suffer for blending problems with BLR emission. The ionized gas mass can be derived using the Eq. B.5 in case we are able to estimate the electron temperature $T_e$, the electron density $N_e$, and the involved emitting luminosity. Indeed, in order to derive outflow energetics, the spatial scale, i.e. the distance of the outflowing material from the central source, the velocity and the morphology of this perturbed material are required (Appendix B.0.1).

In this Section we introduce the complex issues related to the derivation of all such observational quantities and determine, under reasonable assumptions, the energetics regarding the ionized outflowing gas for both XID 2028 and XID 5321. Such energetics, however, because of the multiphase nature of the outflow phenomena, should be considered as lower limit estimates, since they are related to a fraction of the total ejected material. The presence of outflow signatures in the neutral material (Sect. 2.5.6), will allow us to have also a rough estimate of the mass of the neutral counterpart. We note however that, for a correct comparison with the theoretical prediction, all the molecular, ionized and atomic outflow phases must be taken into account (see Chapter 6).

#### The ionized component

The kinetic power associated with the ionized component can be derived by Eq. B.9, assuming a simplified model in which the wind occurs in a conical region uniformly filled with outflowing ionised clouds. As mentioned above, in order to obtain the kinetic powers, estimates of the following quantities are needed: the electron temperature, $T_e$ , and density, $N_e$ , gas phase metallicity, [O III] emission line luminosity, spatial scale, and outflow velocity.

*Spatial scale:* Our slit-resolved spectroscopic analysis has shown that significant signal in the [O III] shifted components can be detected out to a projected distance of R $\approx$ 11 kpc (see Figure 2.14). Therefore, we assume the outflow extending out to that radius from the central black hole for both sources (see also Cresci et al. 2015a).

*Electron density:* $N_e$ estimate of the outflowing gas is derived from the flux ratios of the OC in the nuclear apertures of the [S II] doublets of XID 5321 (Osterbrock 1989; see also Appendix A.3): $N_e \approx 2000 - 3000$ cm$^{-3}$. Although these values are higher than other values routinely used in the estimate of outflowing power (e.g., Harrison et al. 2014; Liu et al. 2013), they are still comparable with other assumptions adopted in low-z AGN-ULIRGs systems (e.g., Rodríguez-Zaurín et al. 2013; Villar Martín et al. 2014 and references therein). However, these $N_e$ estimates are somewhat ambiguous, given the complexity of the spectral profiles: the fitting procedure often produces strongly degenerate results, because of the presence of the four Gaussian profiles required to reproduce the NC and OC of the doublet in addition to the strong wing of the H$\alpha$ BLR emission. A different strategy is suggested by the availability of the off-nuclear spectrum of XID 5321. In this region, the spectrum is not dominated by the BLR emission. For these reasons, we use the electron density value obtained from the fit to the [S II] doublet in the off-nuclear aperture ($c$) of XID 5321, $N_e = 120$ cm$^{-3}$. This electron density, close to the value commonly used in similar studies, is adopted for both targets (unfortunately, XID 2028 spectra do not permit a similar estimate). We note however that such estimate, although probably less dominated by degeneracy between different Gaussian profiles, is derived from a lower S/N spectrum. The study of the electron density within outflowing material is, for the reasons above mentioned, a delicate issue for the estimate of outflow energetics and requires further examination (see also Chapter 5).

*Metallicity:* Estimates of the metallicity, using the indicators $N2 = [NII]\lambda6583/H\alpha$ (Pettini and Pagel 2004) and $R23 = ([OII]\lambda\lambda3726, 3728 + [OIII]\lambda\lambda4959, 5007)/H\beta$ (e.g., Pilyugin 2001; Yin et al. 2007), based on the assumption of a stellar ionizing radiation field, are not useful because a large contribution from the AGN is present for both sources. For this reason, we assume a solar metallicity in the computation of the kinetic power. We note that, even assuming that the outflows reside in metal-rich regions with $9.0 < 12 + log(O/H) < 9.3$ (Du et al. 2014; Kewley et al. 2013), the metallicity would be at most a factor of 2 greater. This factor is negligible with respect to other sources of uncertainties (see below).

*De-absorbed luminosities:* From the extinctions previously obtained from Balmer decrements of outflow components, we obtain values of $A_{5007} \approx 1.8$ (XID 2028) and $A_{5007} > 0.5$ (XID 5321), corresponding to correction factors of $\approx$ 6 and 2 for the [O III] luminosities of XID 2028 and XID 5321, respectively.

*Outflow velocity:* Finally, following Cano-Díaz et al. (2012) and Cresci et al. (2015a), we assume that the maximum velocity observed $V_{max}$ is indicative of the outflowing velocity of the gas, while lower velocities are due to projection effects (but see the next section for discussion).

Using the values previously indicated and the measured $V_{max}$, we obtain

$$\dot{E}^{ion}(2028) \approx 4 \cdot 10^{43} erg/s,$$

$$\dot{E}^{ion}(5321) \approx 6 \cdot 10^{43} erg/s,$$

adding the flux contributions determined in the off-nuclear apertures. Namely, for each object, we compute the relative kinetic power adding the corresponding flux measured in the outflow components, and using the maximum $V_{max}$ value (see Table 2.3). Consequently, using the same assumptions as above and Eq. B.8, we obtain the corresponding outflow mass rates $\dot{M}^{ion}_{out}(2028) \approx 55\ M_{\odot}/yr$ and $\dot{M}^{ion}_{out}(5321) \approx 50\ M_{\odot}/yr$.

A confirmation that the estimates from [O III] are lower limits, comes from the outflow mass ratio computed comparing the [O III] ionized mass with the H$\beta$ mass estimate, using the measured electron density and assuming an electron temperature $T_e = 2 \cdot 10^4$ K (Cano-Díaz et al. 2012; Osterbrock 1989): $M_{[OIII]}/M_{H\beta} = 0.008\ L_{[OIII]}/L_{H\beta}$. If we assume the same kinematic and extension for H$\beta$ and oxygen emission lines, the corresponding outflow mass rate ratio preserves the same dependency: $\dot{M}_{[OIII]}/\dot{M}_{H\beta} = 0.008\ L_{[OIII]}/L_{H\beta}$. The same applies to the kinetic power ratio.

XID 2028 measured luminosity ratio $L_{[OIII]}/L_{H\beta} \approx 10$ in the nuclear region (i.e., where outflowing H$\beta$ is detected), implies that we are underestimating the ionized mass rate by a factor of $\approx$ 10. XID 5321 upper limit on the flux of undetected outflowing H$\beta$ emission line in the nuclear region (see Section 2.5.5) implies at most a factor of $\approx$ 20 larger ionized mass rate. As a conservative order of magnitude estimates of the ionized kinetic power and mass rate of the targets we will refer, in the following, to the values previously evaluated, multiplied by 10, in order to account for the $L_{[OIII]}/L_{H\beta}$ ratios. Therefore, our inferred mass rates are $\dot{M}^{ion}_{out}(2028) \approx 550\ M_{\odot}\ yr^{-1}$ and $\dot{M}^{ion}_{out}(5321) \approx 500\ M_{\odot}\ yr^{-1}$, and the corresponding kinetic powers are $\dot{E}_{ion(2028) \approx 4 \cdot 10^{44} erg/s}$ and $\dot{E}^{ion}(5321) \approx 6 \cdot 10^{44} erg/s$. For XID 2028, these results are consistent with those obtained from SINFONI near infrared integral field spectroscopy observations: Cresci et al. (2015a) estimate from the H$\beta$ flux an outflow mass rate $> 300\ M_{\odot}/yr$, without extinction correction.

**Kinetic power $V_{out}$ estimators** Usually, kinetic powers are determined taking as $V_out$ the velocity offset (defined as the offset between the Gaussian components of the fitting procedure as well as the non-parametric one, i.e. as $\Delta V$ as well as $V_S$; see, e.g., Harrison et al. (2012) and references therein). However, these are projected velocities and therefore may be not representative of the true outflow velocities. Harrison et al. (2012), found that $FWHM_{OC}/V_S \approx 2$ for two of their sources showing clear BLR components and, assuming that the outflow could be primarily oriented towards us for this kind of sources, suggest that FWHM$_{OC}/2$ may be an adequate approximation of $v_0$ for other sources. However, we did not find the same ratios (the same conclusions are found for the non-parametric $W80/\Delta V$ ratios), suggesting a different geometry.

We also note that estimates of kinetic power through $W80$ value could be similarly arguable: our $W80$ values are lower in the nuclear region than in the off-nuclear ones. This has possibly significant implications: $W80$ may be not reliable when there is a unique extracted spectrum instead of slit-resolved spectroscopy on different apertures, because the line flux of the systemic component in the core is dominating the emission. At larger radii this should not apply, because the NLR flux is almost suppressed. Therefore, $W80$ values greater in the external regions may be not interpreted as accelerating outflows.

We define the line width $W40$, as the velocity width $v50 - v10$ that contains 40% of the emission flux of the line profile of XID 2028, with blueshifted outflow, and as the width $v90 - v50$ of the line profile of XID 5321, with redshifted outflow signatures (Cresci et al. 2015a). These estimators, regarding only the emission of more certain outflowing gas origin, can be useful to quantify possible outflow velocity variations between the different regions. XID 2028 shows a roughly constant value ($W40 = 580 \pm 30$ and $610 \pm 40$ km s$^{-1}$ for the off-nuclear ($a$) and nuclear ($b$) regions respectively), and this may indicate that the outflow is not accelerating. This is not the case for XID 5321, where $w40$ shows a significant variation between the two regions ($W40 = 1730 \pm 20$ and $2380 \pm 200$ km s$^{-1}$ for the nuclear ($b$) and off-nuclear ($c$) apertures), mostly attributable to $v90$ changes. In this source, therefore, an accelerating outflow could be present.

All these arguments suggest that the kinetic powers evaluated both in this study and in others using similar velocity estimators, should be considered only order of magnitude estimates. To give a better feeling of the uncertainties, for these two sources, $V_{max}$ and $W80$ are in reasonable agreement (within $10-30\%$), but $\Delta V \sim 0.3 V_{max}$ implies a variation of a factor of $\sim$ 40 in kinetic power estimates. Improved observational constraints are needed to test kinematic models of these outflows, and allow better estimation of kinetic energy and mass rates.

## Neutral component

Neutral mass outflow rates can be estimated from Eqs. 7-8 of Weiner et al. (2009),

$$\dot{M}^{H}_{out} \simeq 7 \cdot \left(\frac{N_H}{10^{20} cm^{-2}}\right) \left(\frac{R}{5kpc}\right) \left(\frac{V_{out}}{300 kms^{-1}}\right)\ M_{\odot}\ yr^{-1}, \tag{2.1}$$

assuming a flow that extends from radius 0 to R. The study of the ionized phase allowed constrains on the extension $R$ and outflow velocity $V_{max}$; assuming that the neutral component has the same geometrical and kinematic properties, the only missing ingredient to derive the neutral mass rate is the integrated atomic hydrogen column density affected by winds. In the optically thin approach, the ratio of the Equivalent Width (EW) for any two transitions of the same ion can be related to N$_H$: EW doublet ratio in the range $2-1$ corresponds to optical depth in the range $0, +\infty$; Bechtold (2003). Sodium Na I D doublet absorption line is generally used to derive neutral outflow rate (Rupke et al. 2005a,b).

For both XID sources, we use the EW of low ionization Mg II to estimate neutral hydrogen column densities, instead of Na ID because of the difficulties inherent the sodium fits (see Section 2.5.4). This corresponds to assume these absorption lines as in a unique absorbing system. The assumption is justified by the fact that all the absorption lines seem to have same kinematics. Moreover, given that they have roughly the same velocity shift of the outflowing ionized gas, we assume that this absorbing system has the same kinematic and extension of the ionized one, i.e. that neutral and ionized components are closely connected (see also discussion below).

The measured EW ratio of Mg II$\lambda\lambda$2796,2803 of XID 5321 is 1.7, therefore the magnesium column density can be inferred from the EW of Mg II$\lambda$2796 (see Bechtold 2003 for more details). Following the arguments presented in Bordoloi et al. 2013, i.e. assuming no ionization correction ($N_{Mg} = N_{MgII}$), no correction for saturation, and a solar abundance of Mg with a factor of -1.3 dex of Mg depletion onto dust, we obtain a hydrogen column density $N_H(5321) = 3 \cdot 10^{19}$ cm$^{-2}$.

The measured EW of the magnesium lines of XID 2028 are instead consistent with a doublet ratio of $\sim 1$, corresponding to higher optical depths. In this case, the absorption lines would be approaching the flat part of the curve of growth and their column density cannot be inferred from EWs. We estimate an apparent optical depth and a conservative lower limit of the hydrogen column density, $N_H(2028) > 9 \times 10^{19}$ cm$^{-2}$, following the method used by Bordoloi et al. 2013 and using the same assumptions as above.

For the assumptions discussed above, using the maximum $V_{max}$ value and the maximum extension observed for the [O III] emission lines, we obtain mass outflow rate $\dot{M}^H_{out}(2028) > 80\ M_\odot\ yr^{-1}$ and $\dot{M}^H_{out}(5321) > 35\ M_\odot\ yr^{-1}$. Given the adopted assumptions, these results represent lower limits. Adding the previous results (ionized items), we obtain lower limits of the total ionized and neutral mass outflow rate: $\dot{M}^{tot}_{out}(2028) > 630\ M_\odot\ yr^{-1}$ and $\dot{M}^{tot}_{out}(5321) > 535\ M_\odot\ yr^{-1}$.

## 2.6 Discussion

In the previous sections we analysed in great detail the optical, NIR and X–ray spectra of two luminous, obscured QSOs, selected from the XMM-COSMOS survey to be in the "blow-out" phase of galaxy-AGN co-evolution. Although not as extreme as other very luminous QSOs selected from all-sky surveys and thought to be caught in this crucial feedback phase (with $L_{bol} > 10^{47-48}$ erg s$^{-1}$, e.g. the WISE-selected quasars in Eisenhardt et al. 2012; Weedman et al. 2012, or the UKIDSS-selected objects in Banerji et al. 2014, 2012), these two sources are among the most luminous objects at z$\sim$ 1.5 ($L_{bol} > 10^{46}$ erg s$^{-1}$) of the entire X–ray selected sample in the much smaller area covered by the COSMOS survey, thus more representative of the entire luminous population. The availability of a complete and deep multiwavelength coverage within the COSMOS field enables a full characterization of the host galaxy and accretion rates properties of these two extreme sources which is not possible, at similar depths, in other targets given the limited follow-up available.

XID 2028 and XID 5321 are "X–ray loud", as per their selection, based on optically dim counterparts associated with bright X–ray and MIR emissions. In addition, when compared with the average SED of Type 2 AGN with similar bolometric luminosity, the X–ray flux of

XID 2028 and XID 5321 is less absorbed than average (the X–ray slope in Figure 2.11 is flatter than the Lusso et al. 2011 X–ray SED). Differently from our two targets, luminous QSOs detected in large area IR surveys seem to be "X–ray weak": the X–ray weakness can be ascribed to the high column density along the line of sight, as proposed for three WISE-selected QSOs at z$\sim$ 2 (D. Stern et al. 2014), or possibly to an intrinsically low disk/corona emission, as observed in J1234+0907(Banerji et al. 2014). In order to have a complete picture of the complex interplay between the X–ray luminosity, the X–ray absorption, and the winds properties, it is essential to gather a complete sample of sources with deep optical, NIR and X–ray data over a large luminosity range. Despite the relatively high SFR observed (SFR$\sim$ 250 $M_\odot$ $yr^{-1}$), the high X–ray luminosity coupled with the low level of column density observed in the two sources, $N_H \sim 6-7\times10^{21}$ $cm^{-2}$, argues against an obscured accretion phase (e.g., in evolutionary models when the SFR is at its peak, it should be associated with high nuclear and host obscuration; see, e.g., Hopkins et al. 2008). The overall properties extracted from the SEDs and the X–ray spectra, instead, definitely point towards a scenario in which the AGN is caught in the subsequent phase where most of the BH mass has been already fully assembled. This is witnessed by the Broad components observed in the H$\alpha$ region, corresponding to BH masses $M_{BH}\sim10^{9-10}$ M$\odot$ (Bongiorno et al. 2014). The fairly high accretion rates observed in our two targets ($L_{bol}/L_{Edd}\sim 0.01-0.05$) are also in agreement with a scenario in which our targets are caught in the very short blow-out phase (see Fig. 2 of Hopkins et al. 2005), between the obscured and unobscured peaks of bolometric luminosity and accretion rate.

In these two objects, we found clear evidence for the presence of outflow components in all the emission lines investigated in the off-nuclear apertures we extracted for each source (see Section 2.5.3 and Figures 2.14, 2.17 and 2.16). Most importantly, in the hypothesis that these components are tracing outflowing winds, we were able to demonstrate that the outflow has propagated well within the host galaxy (up to 10-12 kpc scale; see Section 2.5.3). Such observed extents, although obtained through NIR integrated spectra, are among the largest reported in the literature for high-z luminous QSOs measured from IFU data. For example, Cano-Díaz et al. 2012 reported clear evidence of outflowing gas on a much smaller scale ($\sim$ 3 kpc, on scale even lower than those sampled by our central apertures). Similarly, Alexander et al. (2010) detected broad and shifted components in J1237 out to 4-8 kpc within the galaxy, on scales comparable to our nuclear apertures. This highlights the power of high resolution slit spectroscopy in unambiguously revealing complex kinematics when applied to luminous QSOs. Larger programs of NIR follow-up of large area and deep fields X–ray selected sources (such as those from XXL and Stripe82) can be exploited to single out the most promising cases.

### 2.6.1 Kinetic Powers

With a solid handling of the most important observational constraints (velocity and spatial scale) needed to derive the outflow kinetic powers and mass outflow rates, and with the additional information we could derive from the absorption systems, we could draw conclusions on their associated energetics and mass outflow rates (see Section 2.5.6). The kinetic power fiducial values obtained can only be attributed to AGN-driven outflows and definitely rule out a SF origin for the outflow. In fact, the kinetic output expected from stellar processes can be derived from the actual SFR ($(\dot{E}_{SF}\sim1.7\times10^{41}\times(SFR/[M_\odot/yr])$ erg/s, following Veilleux et al. 2005); even assuming a 100% coupling of the kinetic power to the stellar winds into energy needed to drive the outflows, this would not be enough to obtain the total inferred kinetic powers ($\gtrsim 5\times10^{44}$ erg/s). Instead, the observed kinetic powers are $\approx$ 20% of the AGN bolometric luminosities, and AGN-driven outflows are therefore favoured compared to the very high coupling needed to sustain SF-driven ejections. An AGN origin for the observed outflowing winds is also supported by our BPT analysis: all the outflow components observed in the different apertures for both sources lie in the region of AGN photo-ionization (see Figure 5.4 and Section 2.5.5).

Order of magnitude estimates of the kinetic power have been obtained for all the targets showing outflows in [O III], in order to rule out even in the the fainter sources the possibility of SF-driven outflows. Because of the absence of spatially resolved information, we assumed for the outflows a much conservative value for the extension ($\sim$ 5 kpc). The energetic powers are derived using the measured fluxes (i.e., without any absorption correction) and $V_{max}$, and assuming the same electron density we derived for the outflow region of XID 5321, $N_e = 120$ cm$^{-3}$. The energetics obtained are compared with the expected values for stellar processes and AGN-driven winds in Fig. 2.22. In systems with substantial SF ongoing among our targets (XID 2028, XID 5321 and XID 5325), the kinetic power predicted from stellar winds may in principle be enough to sustain the kinetic energy associated with the outflows. However, assuming the same correction factor derived for the two brightest sources, [O III]/H$\beta \approx 10$, the energetics expected from stellar processes cannot any more explain the derived values, even assuming high coupling. Briefly, arguments related to the high observed winds velocities ($>$ 1000 km/s) and to the much lower coupling required to the QSO to drive the outflow seem to suggest that the central luminous QSO is the most likely mechanism responsible for the launch of the wind. In Chapter xx we compare the derived outflow energetics to those of other samples from literature, testing models predictions and deriving other stronger evidences favouring an AGN origin for the observed outflows.

*

Despite a remarkable set of common properties in the two targets (similar host galaxies and accretion properties, similar broadening of the lines and spatial extension), XID 2028 and XID 5321 present one striking difference: the outflow component is *blueshifted* in XID 2028 (as observed in basically all the objects with broad [O III] reported in the literature) while in XID 5321 the outflow component is *redshifted*. Below we will therefore summarize separately the properties of the two systems we were able to infer from all the available data.

### 2.6.2 The blueshifted outflow in XID 2028

The interpretation of the data we have for XID 2028 is relatively simple. The absorption lines of XID 2028, tracing the low ionization/neutral gas, show a blueshift nearly like that observed in the emission lines, with $V_S \sim$ -300 km s$^{-1}$ with respect to the systemic velocity, easily explained as outflowing gas along the line of sight. The [O II] emission doublet as sampled by the Keck/DEIMOS spectrum (Figure 2.18) also shows almost the same asymmetries and shifts, within the errors, of [O III] (Figure 2.17; see also Zakamska and Greene 2014 for similar [O II] and [O III] broad profiles observed in SDSS spectra). With respect to the analysis presented in **Brusa2014** and Cresci et al. (2015a) we therefore report, for the first time in this prototypical system, also the presence of an outflow in the lower ionization [O II] emission and in the neutral component.

Under the assumptions discussed in Section 2.5.6, we obtain a lower limit on the outflow mass rate for the neutral component that, added to the ionized component, gives us a lower limit on the outflow mass rate, $\dot{M}^{tot}_{out}(2028) > 630\ M_{\odot}\ yr^{-1}$, without taking into account the presence of a possible molecular component. We also obtain a kinetic power associated with the outflow of $\sim 4 \cdot 10^{44}$ erg s$^{-1}$, where, starting from Equation B.8 for the ionized kinetic power, we

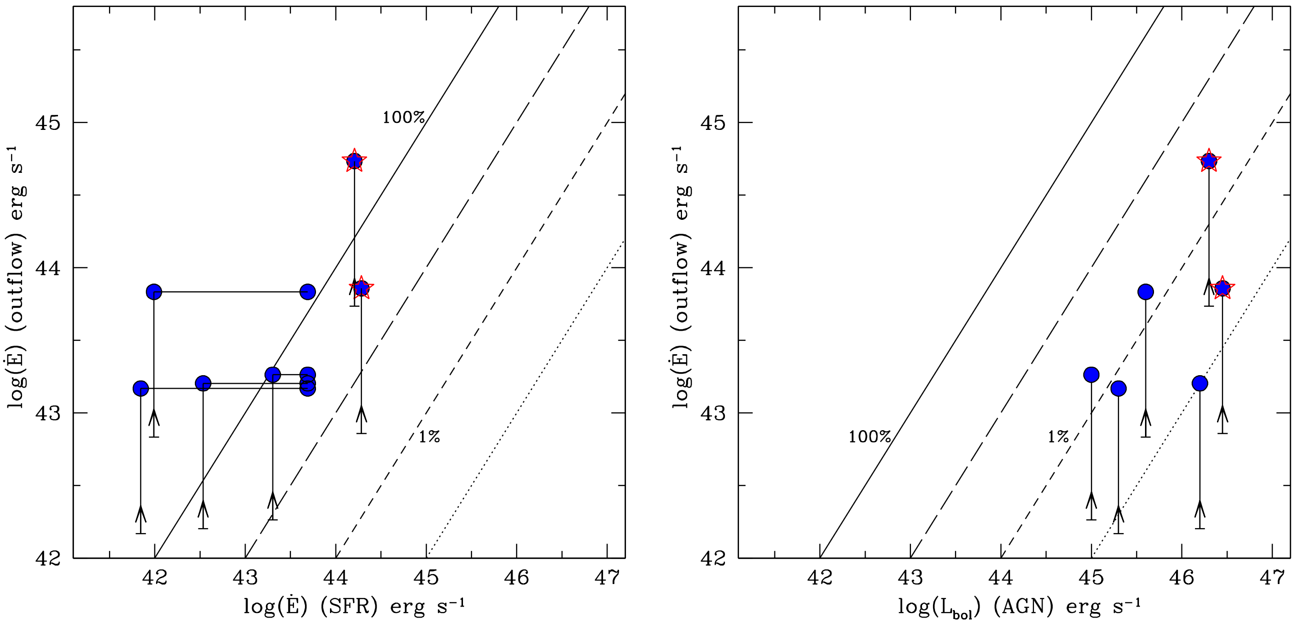

Figure 2.22: (*Left Panel*): Our inferred values of the outflow kinetic energy injection rate against the predicted energy input rate from SF. The solid, long-dashed, dotted and short-dashed lines represent the 100% (one to one correlation), 10%, 1% and 0.1% ratios, respectively. Starred symbols are the sources detected in PACS (XID2028 and XID5321). For sources not detected by Herschel, the predicted energy input from SF estimated from the SFR measured from the SED fitting (left symbol) and from the PACS stacked signal (right symbol) are connected by a solid line. The outflow kinetic powers associated with the the ionised component and derived using Eq. B.9 are shown as lower limits (upward arrows). The value for XID2028 (leftmost starred symbol) has been shifted in the horizontal axis by 0.15 dex for clarity in the plot. Outflow energetics are derived on the basis of the information available from single aperture, nuclear spectra analysed in Section 2.4.1; for the two brightest sources, the estimates we derive thanks to slit-resolved analysis are highlighted as orange stars. (*Right Panel*): our inferred values of the outflow kinetic energy injection rate against the bolometric AGN luminosity as derived from SED multicomponent fitting (see Section 2.5). The lines and symbols have the same meaning as in the left panel. Both the panels show the XID 2028 and XID 5321 kinetic powers values derived in Brusa et al. (2015), i.e. without the constraints derived from slit-resolved analysis.

have taken into account a correction factor of 10 from the comparison between the [O III] and H$\beta$ mass rate estimates in the nuclear region (see Section 2.5.6). Although obtained through different observational constraints, these results are overall consistent with those presented in Cresci et al. 2015a and unambiguously point towards an AGN origin for the observed wind (see Section 2.5.6).

### 2.6.3 The redshifted outflow in XID 5321

For XID 5321 the interpretation of the observational constraints we obtained in our analysis (in particular, the redshifted absorption that shows a velocity shift of the same magnitude of the emission lines) is more complex.

The similarity between the velocity shift of absorption and ionized lines suggests that neutral and ionized gas are closely connected: in fact, some of the ionized outflowing gas could become again neutral (e.g., Emonts et al. 2005). In this case, the redshifted absorption lines observed in XID 5321 could be explained as outflowing absorbers along the line of sight, illuminated by the light of the host galaxy behind the redshifted outflowing material. Figure 2.23 shows a cartoon illustrating the extended host galaxy disk (grey area) and our inferred geometry for the bi-conical outflow (blue and red areas) of XID 5321. In this scenario, the observed outflow should corresponds to the receding red cone, while the blue cone is obscured by the host galaxy. In addition, the AGN system and the associated torus are warped with respect to the galaxy disk.

An outflowing absorbing medium on the line of sight (indicated with dotted-dashed lines in the figure), in or close to the red cone and illuminated by the light of the extended host galaxy behind, could be responsible for the absorption lines observed, with the same kinematics and extension of the ionized outflowing gas.

The cartoon also helps us to understand the origin of the broad wings observed in the [O III]$\lambda$5007 emission line (Figure 2.14). A blue wing could be originated by the near-side of the outflow (in the upper part of the figure), where the velocities have negative projected components along the line of sight. For this reason, these velocities are indicated with cyan arrows. The bulk has instead velocities with positive line of sight components (orange arrows) and determines the core of the line profile. An alternative option is that the bi-conical outflow has a more wider opening angle in such a way that the blue wing is originated by the blue cone extended up to the host galaxy. In these possible scenarios, the positive maximum velocity, $V_{max}$, is indicative of the outflow velocity because it is originated by the gas components at the periphery of the visible cone and closest to the line of sight. All the other gas components have lower velocities because of greater projection effects.

In addition, the proposed geometry also explains why we see the BLR responsible for the emission of the Broad H$\alpha$ (i.e., we have an almost unobscured view to the nucleus), why the broad H$\beta$ is heavily extincted (i.e., probably by the galaxy disk), and why we measure a relatively low X–ray column density (i.e., the line of sight does not fully intercept the torus), therefore justifying the type 1.8 of the source.

XID 5321 [O II] lines show a great spatial extension, allowing us to study the emission in the three apertures (Figure 2.19). It turns out that the [O II] profiles tend to be wider and more redshifted from $a$ to $c$. A possible explanation is that the low ionization component of the outflow could have a wider opening angle than the highly ionization component.

Following the same arguments mentioned above for XID 2028, we obtain a kinetic power associated with the outflow of $\sim 6 \cdot 10^{44}$ erg s$^{-1}$. Following the scenario presented in Figure

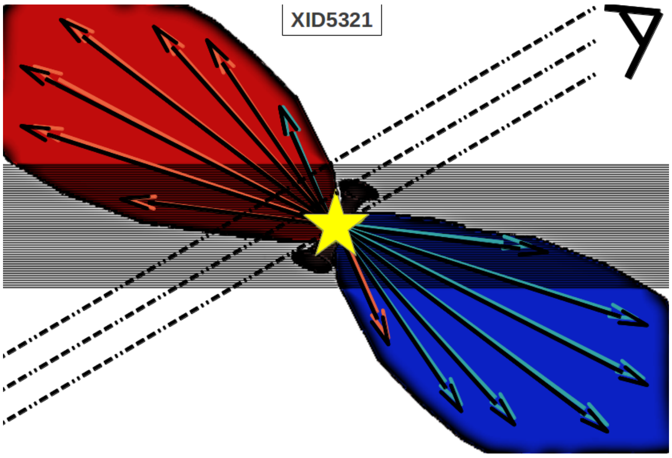

Figure 2.23: Schematic cartoon showing the extended host galaxy (grey area) and conical outflow of XID 5321 (blue and red areas). The blue and red lobes represents the blueshifted and redshifted gas. The yellow star and the cylindrical shape show the position of the driving centre and the torus. The line of sight is indicated.

2.23, a lower limit on the outflow mass rate for the neutral component added to the ionized term was obtained: $\dot{M}^{tot}_{out}(5321) > 535\ M_{\odot}\ yr^{-1}$.

Although the scenario described above seems to fit our diverse constraints and is favoured, we should notice that the redshifted systems of XID 5321 could in principle also be consistent with the existence of an object approaching the AGN, and/or with a kinematics disturbed by a double nucleus in the galaxy. This second scenario may be suggested by the double peak in the H$\alpha$ region (see Figure 2.16): the narrow peak we associate with the [N II]$\lambda$6583 could instead be the H$\alpha$ of a second source blended in the X-shooter spectrum (within $0.8''$ and therefore within $\sim$ 6 kpc from the brightest AGN). In this case, we should see at least a second shifted [O III]$\lambda$5007 emission line too, at observed wavelengths 1240.5 nm. A closer view of the spectrum presented in Figure 2.14 does not allow us to exclude the presence of a weak emission line and high resolution imaging with HST will be vital to disentangle the nature of this source (see, e.g., Greene et al. 2012).

* * *

This material has been published in

- “X-shooter reveals powerful outflows in z $\sim$ 1.5 X-ray selected obscured quasi stellar objects”, by M. Brusa, A. Bongiorno, G. Cresci, M. Perna, A. Marconi, V. Mainieri, R. Maiolino, M. Salvato, E. Lusso, P. Santini, A. Comastri, F. Fiore, R. Gilli, F. La Franca, G. Lanzuisi, D. Lutz, A. Merloni, M. Mignoli, F. Onori, E. Piconcelli, D. Rosario, C. Vignali, G. Zamorani; (2015) MNRAS, 466, 2394

- “Galaxy wide outflows in z $\sim$ 1.5 luminous obscured QSOs revealed through NIR slit-resolved spectroscopy”, by M. Perna, M. Brusa, G. Cresci, A. Comastri, G. Lanzuisi, E. Lusso, A. Marconi, M. Salvato, G. Zamorani, A. Bongiorno, V. Mainieri, R. Maiolino, M. Mignoli; (2015) A&A, 574, 82, 16

and is based on observations undertaken at the European Southern Observatory, Paranal, Chile, under the programme 090.A-0830.

Chapter 3

# A fast ionised wind in a star-forming quasar system at z∼1.5 resolved through adaptive optics assisted near-infrared data

## Abstract

We present a new selection criterion to isolate objects in the "blow-out"/outflowing phase. It is based on the X-ray detection coupled to extreme [O [II]$\lambda\lambda$3726,3729 equivalent widths, probing AGN accretion activity and ongoing star formation in the AGN-galaxy system respectively. The capability of the selection criterion is exploited through high-resolution and high S/N VLT/VIMOS, VLT/SINFONI, and Subaru/IRCS adaptive optics (AO) data of a luminous, X-ray obscured starburst/quasar (SB-QSO) merging system at z$\sim$ 1.5, detected in the XMM-COSMOS field. For the first time, we map the kinematics of the [O III] and H$\alpha$ line complexes and link them with the [O II] emission at high resolution. The high spatial resolution achieved allow us to resolve all the components of the SB-QSO system. Our analysis, with a resolution of few kpc, reveals complexities and asymmetries in and around the nucleus of XID 5395. The velocity field measured via non-parametric analysis reveals different kinematic components with maximum blueshifted and redshifted velocities up to $\simeq$ 1300 km/s that are not spatially coincident with the nuclear core. These extreme values of the observed velocities and spatial location can be explained by the presence of fast moving material. We also spectroscopically confirm the presence of a merging system at the same redshift as the AGN host.

We propose that EW as large as $>$ 150 Å in X-ray selected AGN may be an efficient criterion to isolate objects associated with the short, transition phase of "feedback" in the AGN-galaxy co-evolutionary path. This co-evolutionary path subsequently evolves into an unobscured QSO, as suggested from the different observational evidence (e.g. merger, compact radio emission, and outflow) we accumulated for XID 5395.

## 3.1 Introduction

Many of the most successful models of galaxy formation require the presence of winds, extending over galaxy scales (i.e. $\sim 1-10$ kpc and beyond), that are sufficiently fast and energetic to terminate the SF activity and SMBH growth (e.g. Hopkins et al. 2008; A. King 2005).

The key ingredient to reveal unambiguously the presence of AGN-driven winds in systems at the peak epoch of galaxy evolution (z$\sim$ $1-3$) is spatially resolved near-IR (NIR) spectroscopy, which

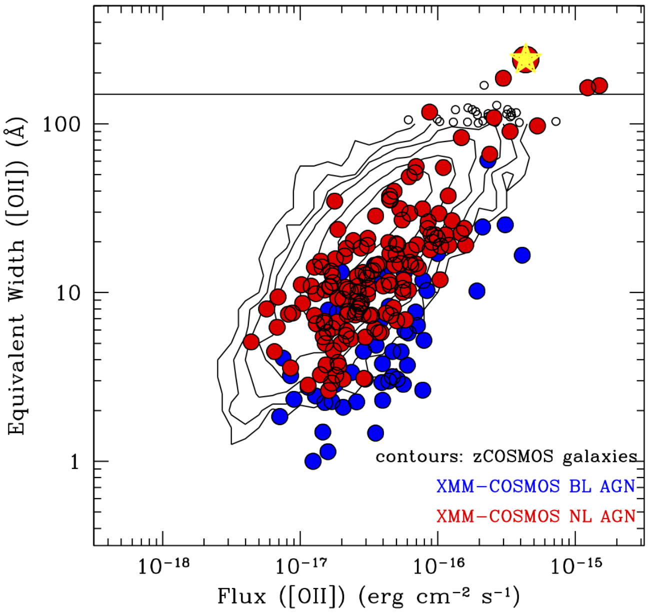

Figure 3.1: Rest-frame EW of the [O II] line plotted against the total line flux for S/N> 3 objects in the zCOSMOS sample within z= $0.5-1.5$ (7338 objects; black contours and small open circles out of the contours) with the XMM-COSMOS sources superimposed (blue = 57 Type 1 AGN, red = 152 Type 2 AGN). XID 5395 is highlighted as a yellow star. Out of the five objects with [O II] EW larger than 150 $\AA$, four are Type 2 QSOs (with $L_X \simeq 10^{44}$ erg/s). XID 5395 is the only one with rest-frame EW larger than 200$\AA$ in the entire sample (yellow starred symbol).

is capable of directly measuring the existence and extension of an outflow of the warm/ionised gas phase traced by the rest-frame [O III]5007 lines. So far, the most convincing detections of outflows on galactic wide ($\sim 5-15$ kpc) scales in radio-quiet AGN in this redshift range have been obtained with seeing-limited IFU data on $\sim$ a dozen unobscured QSOs and/or SMGs (Cano-Díaz et al. 2012; Carniani et al. 2015; Cresci et al. 2015a; Harrison et al. 2012; Perna et al. 2015b; see also Genzel et al. 2014).

The status of the XMM-COSMOS survey Brusa et al. 2010; Cappelluti et al. 2009; Hasinger et al. 2007 in terms of identification, redshift information, and multi-wavelength classifications is such that it is possible to characterise the host galaxy and SMBH properties of the AGN population with unprecedented detail up to z$\sim$3 (e.g. Bongiorno et al. 2012; Brusa et al. 2010; Elvis et al. 2012; Hao et al. 2014; Lusso et al. 2012). Building on this huge investment of telescopes time, we pursued a detailed characterisation of the most luminous ($L_X > 10^{44}$ erg/s) QSO population missed in pencil beam deep surveys (e.g. Mainieri et al. 2011; Merloni et al. 2014). In particular, we displayed in Chapter 2 that the analysis of NIR spectra obtained through an X-shooter campaign of XMM-COSMOS targets selected as outliers in colour-colour diagrams (following Brusa et al. 2010) indeed reveals the presence of outflowing emission in the [O III] lines ($v_{max} \sim 900-1800$ km/s) in six out of eight sources. The existence of such kinematically perturbed, ionised component extended over the full galaxy scale has subsequently been confirmed by slit-resolved spectroscopy in two of these targets (XID 2028 and XID 5321).

In this Chapter, we further explore the luminous X–ray population in XMM-COSMOS in conjunction with the zCOSMOS spectroscopic database (Lilly et al. 2009; Lamareille et al. in preparation) and we propose a new selection criterion based on the integrated [O II]3727 rest-frame EW to isolate sources with kpc-scale outflows in the obscured SB-QSO phase. We test this criterion on the most extreme object (XID 5395) via AO assisted SINFONI and Subaru data.

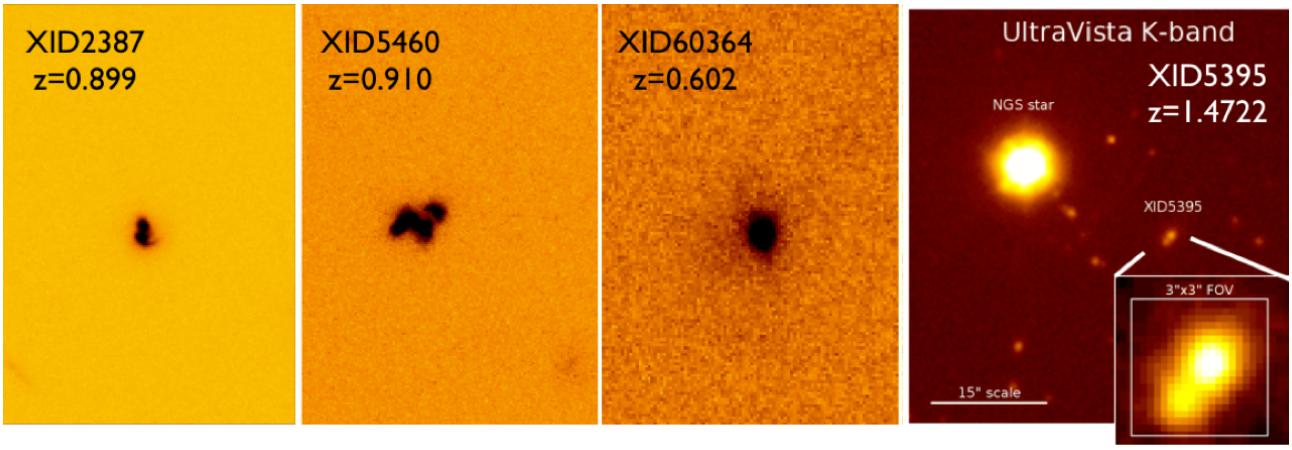

Figure 3.2: HST/ACS I-band images of the three sources with rest-frame EW$>$ 150Å, associated with Type 2 AGN, within the HST COSMOS survey. The XID from the XMM-COSMOS sample and the measured redshift for each source is plotted at the top of each panel. The last panel shows the Ultravista K-band image of the field around XID 5395. The star used for NGS assisted AO observations is also labelled (distance$\sim$ 20"). The inset shows a zoom on the target with the 3"$\times$3" SINFONI FOV superimposed.

The Chapter is organised as follows: Section 3.2 presents the target selection, on the basis of a cross-correlation of the X-ray and emission line information and the properties of our test-case AO study. Section 3.3 presents high-resolution, adaptive optics data obtained with Subaru/IRCS and VLT/SINFONI. Section 3.4.2 presents the integrated and resolved flux and kinematics analysis of all line components, while Section 3.6 discusses the results in the framework of galaxy-AGN co-evolution.

## 3.2 Extreme [O II] emitters and target selection

High rest-frame EW of single ionized oxygen $\lambda\lambda$3726,3729 lines (e.g. EW$>$100 Å) have been used to isolate objects with extreme levels of star formation (e.g. Amorín et al. 2015; see also Contini et al. 2012). We started from the sample of $\sim$ 18000 spectra observed within the zCOSMOS Bright survey (Lilly et al. 2009) and for which we derived accurate line fluxes and parameters from `platefit` measurements, following Lamareille et al. (2009) and Lamareille et al. (in prep.). We limited the analysis to the $\sim$ 7300 galaxies within the redshift range 0.5$<$z$<$1.5 with the doublet of [O II] measurable, and with S/N on the line larger than 3. The values of the rest-frame EW of the [O II] line are plotted against the total line flux for the sample in Figure 3.1 (black contours and small open circles out of the contours; from Lamareille et al. in preparation). The median redshift is $\langle z\rangle$=0.73, i.e. the zCOSMOS [O II] sample is skewed at z$<$ 1 and dominated by the large z=0.67 and z=0.73 structures known in the field Scoville et al. (2007a).

We cross-correlated the [O II] emitters catalogue with the XMM-COSMOS identifications catalogue (Brusa et al. 2010) and we found 209 matches, corresponding to $\sim$ 3% of the overall population. All the XMM-COSMOS AGN are also plotted in Figure 3.1: Type 2/narrow line AGN (NL AGN) are indicated with red circles, while Type 1/broad line AGN (BL AGN) are indicated with blue circles. When considering objects with line fluxes larger than $10^{-17}$ erg cm$^{-2}$ s$^{-1}$ (at lower fluxes there are basically no AGN in our sample), AGN have lower EWs ($EW_{med}$ = 10.8$\AA$) than the overall source population ($EW_{med}$ = 24.0$\AA$), and, among the AGN population, BL AGN have considerably lower EW ($EW_{med}$ = 4.9$\AA$) than NL AGN ($EW_{med}$ = 12.5$\AA$). This is expected, given that the nuclear emission contributes to the continuum used to measure the EW in Type 2 AGN, and dominates in Type 1 AGN.

The fraction of X-ray detected [O II] emitters significantly changes when progressing to extreme

EWs: among the 32 objects with [O II] EW larger than 100Å, six are associated with XMM-COSMOS AGN (∼ 19%). This fraction further increases dramatically when going to EWs> 150$\AA$: four out of five objects (80%) are X–ray AGN and all of them are classified as QSOs ($L_X \simeq 10^{44}$ erg/s) on the basis of the intrinsic X-ray luminosities. Four out of five sources are also [Ne V] emitters, indication of high ionization, and are part of the sample of zCOSMOS selected [NeV] emitters whose properties were discussed in Mignoli et al. (2013) and Vignali et al. (2014).

The HST/ACS cut-outs of the three z< 1 sources with EW> 150Å and associated with X-ray detected sources are shown in Figure 3.2 (first three panels) with the corresponding XID from the XMM-COSMOS catalogue and the associated redshifts from the zCOSMOS spectra. All three sources show clear signs of disturbed morphology with tidal features, which is evidence for double nuclei and extended emission. We therefore propose that high [O II] EW (≃ 150Å) can be used as a reliable proxy to catch star-forming galaxies associated with type 2 obscured QSOs, most likely in a merger phase.

### 3.2.1 XID 5395: a unique SB-QSO system

The source with largest EW in the entire sample is the XMM-COSMOS source XID 5395 (RA=10:02:58.43, DEC=02:10:13.9), a QSO at z=1.472 as measured in the zCOSMOS catalogue (the highest redshift in the [O II] sample) with an intrinsic rest-frame 2-10 keV luminosity of $\sim 7.5 \times 10^{44}$ erg $s^{-1}$ and high obscuration, $N_H \sim 10^{23}$ $cm^{-2}$ (from the analysis presented in Lanzuisi et al. 2015a). The EW measured from the automatic `platefit` procedure Lamareille et al. 2009 is 250Å and is plotted in Figure 3.1 (yellow star).

Unfortunately, this source lies outside the HST/ACS coverage of the central 1.7 degrees of the COSMOS field (Koekemoer et al. 2007; Scoville et al. 2007b) and therefore lacks high-resolution rest-frame UV imaging (but see also Figure 3.5 and Section 4.1). In Figure 3.2 (right-most panel) we show the highest resolution image available for XID 5395 prior to this work (UltraVISTA data release 1, DR1; McCracken et al. 2012) of the field around the QSO and with a zoom on a 3"x3" scale (inset). The UltraVISTA image suggests a complex morphology, possibly associated with two components separated by ∼ 1" (∼ 8.5 kpc).

XID 5395 shares the same level of intrinsic X-ray luminosity as other luminous red QSOs at the same redshift for which outflows in the ionised gas components have been reported (e.g. the X-shooter targets presented in Brusa et al. 2015). However, in contrast to these red QSOs hosted in main-sequence (MS) galaxies, XID 5395 is heavily obscured in the X-rays ($N_H \sim 1.2^{+0.9}_{-0.5} \times 10^{23}$ $cm^{-2}$; to be compared to $\sim 10^{21} - 10^{22}$ $cm^{-2}$ of the X-Shooter sample) and it is hosted in a starburst galaxy (i.e. MS outlier at z=1.5). We fitted the broadband SED of XID 5395, extending from UV to FIR, using the code by Berta et al. 2013. Originally inspired by da Cunha et al. 2008, this code combines the emission from stars, dust heated by star formation, and a possible AGN/torus component. The multi-wavelength photometry extracted from the COSMOS database, and the associated SED fitting decomposition is shown in Figure 3.3. The FIR bump is very well reproduced by a starburst template with SFR$\sim 370$ $M_\odot$ $yr^{-1}$ (see also Delvecchio et al. 2014), while the optical and NIR part of the SED returns a stellar mass of $M_\star \sim 7.8 \times 10^{10}$ $M_\odot$. The AGN emission dominates in the Spitzer bands. We further discuss the host galaxies properties of XID 5395 in Section 5.4.

Finally, XID 5395 is a bright radio source with a 1.4GHz flux of 2.26±0.057 mJy (from the VLA-COSMOS survey; Schinnerer et al. 2010), corresponding to a radio power $P_{1.4GHz} \sim 3 \times 10^{25}$ W $Hz^{-1}$. Chiaberge et al. (2009) classified XID 5395 as 'low power FRI radio source' with a compact morphology and without any evidence of the presence of radio jets (their source #37). The source is also detected in the VLA-COSMOS 3GHz Large Project (Smolčić et al., in preparation) and in the high-resolution VLBA observations (Herrera-Ruiz et al., in prep): from the ratio of total-to-peak flux the radio emission is resolved over the VLA beam (0.7"), but the presence of a faint compact core is confirmed (see Delvecchio et al. in preparation). On the basis of the radio-to-infrared flux ratios ($q_{24} \sim 0$ with a 24 $\mu$m flux of 1.58 mJy as measured by MIPS; $q_{100} \sim 1.24$ with a measured 100 $\mu$m

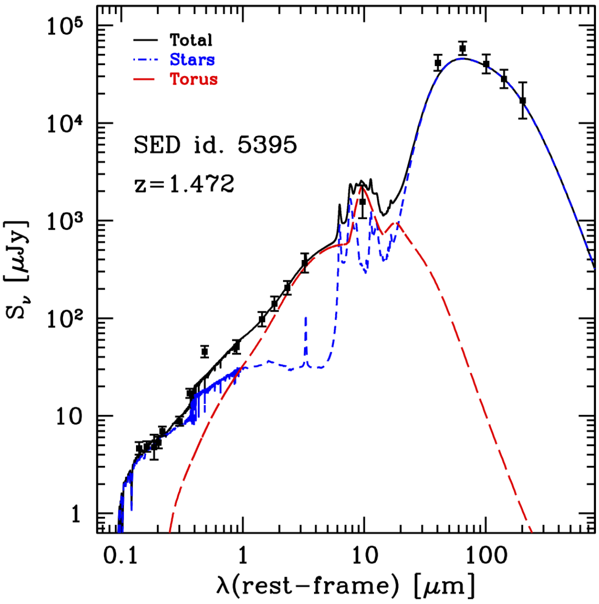

Figure 3.3: SED decomposition obtained with the code by Berta et al. 2013. Filled squares represent the available photometric data, long-dashed red, dashed blue, and solid black lines represent the AGN+torus component, the emission by stars and dust associated with star formation, and the sum of the two, respectively. Bands are, from left to right, u,b,v,g,r,i,z,J,K, IRAC3.6, IRAC4.5, IRAC5.8, IRAC8.0, MIPS24, PACS100, PACS160, SPIRE250,SPIRE350, SPIRE500. The photometric point at λ(rest)∼ 5000 Å is contaminated by broad and bright [O III] emission (see Section 4) and, therefore, is above the best-fit model.

flux from PACS of 39.6 mJy) XID 5395 is classified as 'radio-active' (see Magliocchetti et al. 2014). The radio power exceeds that expected from the Bell 2003 relation given the observed FIR luminosity by one order of magnitude, and this is most likely due to the AGN activity.

### Non-parametric analysis of the [O II] line

The left panel of Figure 3.4 shows a zoom of the optical VIMOS spectrum from the zCOSMOS survey, which is centred around the [O II] emission line. In addition to the unusually bright component in the [O II] emission, XID 5395 also shows a broad and asymmetric profile of the line.

We used non-parametric measurements of the [O II] emission line profile following the prescriptions in Sect. 2.4.1. The best-fit profile and the position of $v$=0 of the cumulative flux are obtained from a multicomponent fit of the 1" integrated spectrum, and adopting the systemic redshift of z=1.4718 (see Section 4.1)[1]. In this way, the velocity measurements are less sensible to the S/N of the data at the observed wavelengths, but are dependent on the goodness of the overall fit profile.

The non-parametric measurements are shown in the left panel of Figure 3.4. We clearly recover the broad profile with $w_{80} \sim 1600$ km/s and extending to absolute velocities higher than 1000 km/s both in the blue and red tails. When compared to the values obtained in a sample of luminous obscured QSOs from the SDSS survey presented in Zakamska and Greene 2014, XID 5395 qualifies as a clear

---

[1] We use a single Gaussian line to model the doublet of the [O II]3727 emission, which has an intrinsic separation of ∼250 km/s with a relative ratio that depends on the density of the gas. The natural profile is not Gaussian. However, we note that the intrinsic doublet separation does not change the non-parametric measurements too much: Indeed, assuming a narrow component of 500 km/s per each of the emission lines in the doublet, the total FWHM measured from a single Gaussian component would be ∼ 600 km/s, which is much lower than the non-parametric measurements discussed below. See also the discussion in Zakamska and Greene (2014).

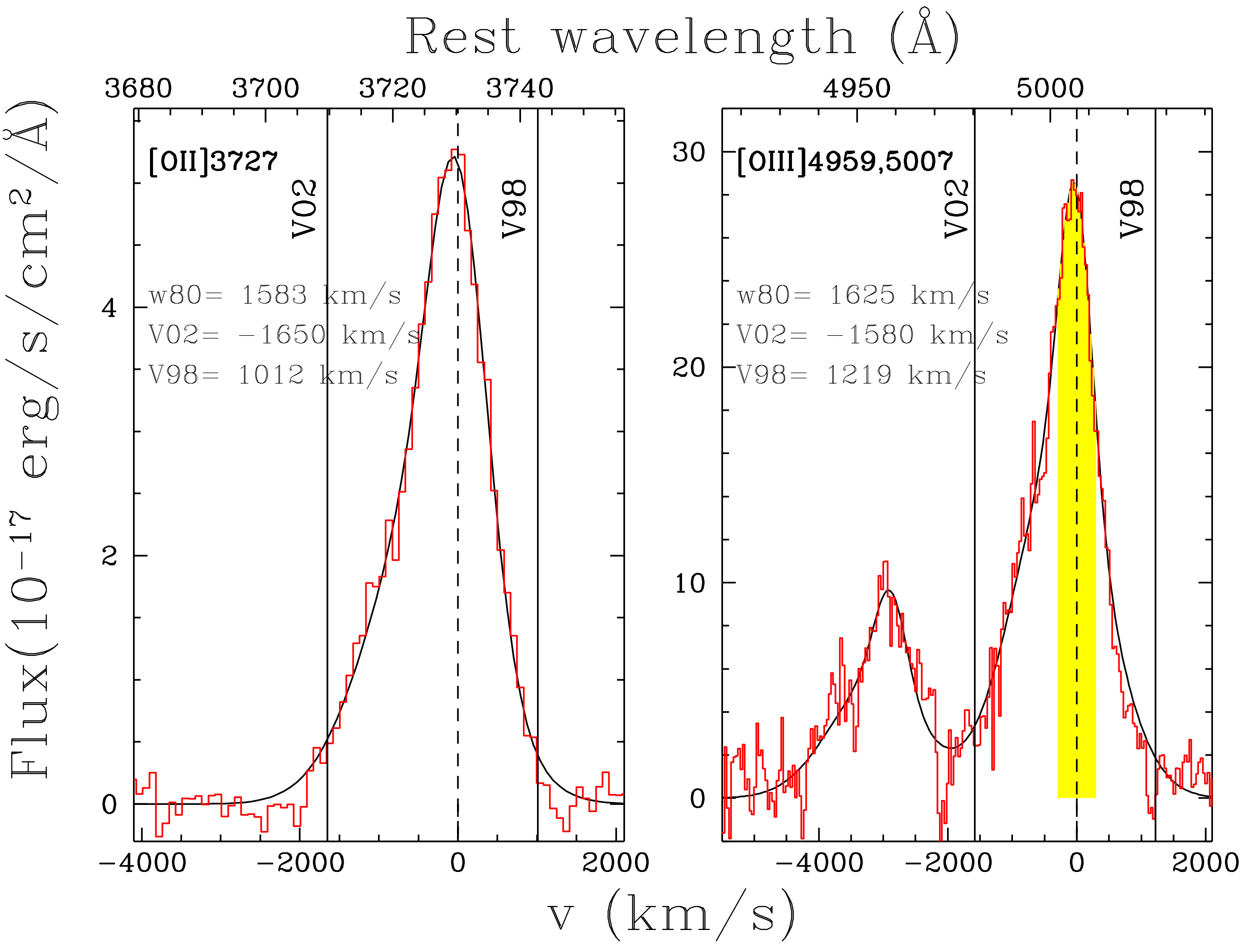

Figure 3.4: *Left panel*: non-parametric analysis of the [O II]3727 doublet emission-line profile for XID 5395 (red histogram) as observed in the VIMOS spectrum. The solid curve is the fit to the profile obtained with a combination of two Gaussian lines (not shown here; see also Figure 3.6). The vertical solid lines show different percentiles to the flux contained in the overall emission-line profile ($v_{05}$ and $v_{95}$) as labelled. The long-dashed line indicates the v=0 systemic as determined in Section 4.1. *Right panel*: same as the left panel, but around the [O III]$\lambda\lambda$4959,5007 emission lines, from the SINFONI spectrum, extracted from an aperture of 1" diameter (see Section 4.1 for details). A clear asymmetry is present in both the [O II] and [O III] emission lines with similar kinematics parameters (as labelled). The yellow shaded region highlights the wavelengths interval corresponding to the peak of the [O III] emission (+/- 300 km/s) in which the map shown in Figure 3.7 (left) is integrated.

outlier; both in the zCOSMOS (galaxy and AGN) and in the SDSS (luminous obscured QSOs) samples there are no other sources with the same extreme properties of the [O II] line.

Similar broad profiles, with large cores and heavy asymmetric wings are also detected in the [O [II] of other 2 out 3 sources isolated with such criterion (Fig. 3.1). XID 60364 is the only one with a symmetric, narrow (FWHM≈ 600 km/s) profile; however, a significant enhancement in the red wing of the [O III] line is also detected, suggesting the presence of signatures of outflows even in this target.

## 3.3 High-resolution adaptive optics data

The pieces of evidence accumulated so far, such as the blueshifted wing in the [O II] emission, simultaneous BH accretion and star formation, and possible merger status, and most importantly the presence of a bright star at a suitable distance needed for AO-assisted observations (see Figure 3.2, right panel), make XID 5395 the perfect target for a detailed study of feedback from AGN in the transition phase of galaxy-AGN co-evolution. We therefore mapped the AGN and the host galaxy in XID 5395 both in imaging and spectroscopy using SUBARU IRCS and SINFONI in AO assisted mode.

### 3.3.1 SUBARU IRCS imaging

We used the Infrared Camera and Spectrograph (IRCS; Kobayashi et al. 2000), installed at the Infrared Nasmyth focus of the Subaru Telescope, in combination with its adaptive optics system AO188 Hayano et al. 2010, to obtain high-resolution infrared images of the field around XID 5395.

We obtained the observations on December 15, 2014. We chose a resolution of 52mas/pixel for a corresponding 54” field of view. We performed observations in imaging mode with IRCS equipped with the H-band (1.33-1.93 $\mu$m range) and K-band (1.86-2.54 $\mu$m range) broadband filters. The H-band data contain the H$\alpha$ emission (redshifted at 1.622 $\mu$m), and can be directly compared to the SINFONI H-band data (see below). The K-band data instead should be free from bright emission lines and should genuinely sample the stellar population of the host galaxy.

We reduced the data using a modified version of the IRAF data reduction pipeline for SUBARU/IRCS. The reduction includes the creation of a bad pixel mask and a skyflat from the data themselves, the flat fielding, sky subtraction, estimate of the dither offsets, and final stacking of the data.

Conditions during the observations were variable with a 0.7-1.0$''$ natural seeing. In the K band, all observations were performed using the Laser Guide Star (LGS) mode. We used a 9 point dither pattern (with 5$''$ stepsize) and 20s exposure time each and a bright star (11 mag in H band) separated 20$''$ for tip-tilt correction. In total, we used 45 frames in the final stacking for a total exposure of 15 minutes. The best image resolution at the TTS position is $\sim 0.1''$ after AO correction. The resolution at the target position is about $\sim 0.2''$. In the H band we also adopted a 9 point dither pattern with 50s exposure time. We used 27 (good) frames in the final stack for a total exposure of 22.5 minutes. We achieve a slightly worse resolution ($\sim 0.24''$) in the H band with respect to the K band.

The images were brought to the COSMOS reference system with an astrometric correction based on UltraVISTA data through a match between the coordinates of a bright point-like source detected in all the images at a projected distance of 10.5$''$ from the QSO. The overall astrometric accuracy of our imaging is $\sim 0.1''$. The IRCS H-band and K-band images are shown in Figure 3.5 (panel c and d). They are compared to the Subaru Suprimecam I band data (panel a; resolution/FWHM$\sim 1''$) and the UltraVISTA H-band data (panel b; resolution/FWHM$\sim$ 0.7”).

The Subaru IRCS data at higher resolution clearly resolve two objects unresolved in the UltraVISTA image. These two objects are labelled as “nucleus” and “south-east (SE) source” in Figure 3.5, and they are separated by $\sim 0.6''$. In addition, an extended feature can be seen in the H-band high-resolution IRCS data (third panel in Figure 3.5), extending from the nucleus towards the north-west (NW) direction. We name this feature “NW plume”. Instead, the IRCS K-band map, which is free of

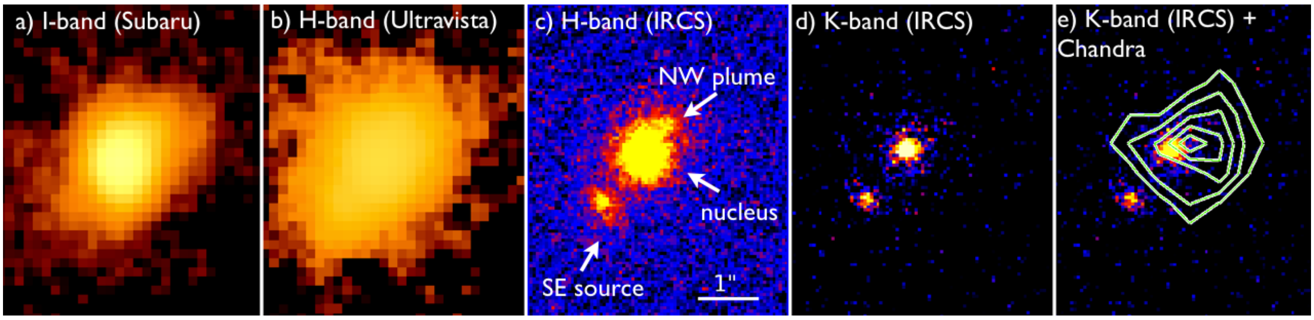

Figure 3.5: From left to right, image cut-outs of XID 5395 at increasing wavelengths and resolution: a) SUBARU Suprimecam I band (FWHM∼1”); b) UltraVISTA H band (FWHM∼0.7”); c) SUBARU IRCS H band (FWHM∼0.2”); d) SUBARU IRCS K band (FWHM∼01”); e) same as panel d) with the X–ray contours superimposed (from *Chandra* Legacy data; Civano et al. 2016). The cutouts have a size of ∼ 4” across (e.g. comparable to the SINFONI FoV). The 1” scale is given for reference in panel c). In the same panel we also indicate different components discussed in the text, as labelled. North is up and east is left. Chandra contours are not corrected for astrometry.

contamination from bright emission lines, appears much more compact ($< 0.4 - 0.5$”) and symmetric, although the overall S/N is worse compared to the H band. The coordinates of the centroids and the magnitudes in the H and K band of all these three components are reported in Table 1. The nucleus clearly dominates the photometry of the entire system, and the value obtained for the nucleus is consistent with the total magnitudes measured in UKIRT and CFHT observations (H=19.7,K=19.6; see also Laigle et al., in preparation for UltraVISTA data).

In the last panel of Figure 3.5, we plot again the K-band IRCS data, superimposed with the *Chandra* Legacy X-ray contours (full band; taken from Civano et al. 2016). The high-resolution *Chandra* image also unambiguously associates the observed X–ray emission with the brightest source detected in our deep Subaru imaging.

## 3.3.2 SINFONI observations and spectral analysis

The observations were performed in AO-assisted mode using the near-infrared (NIR) Integral Field Unit (IFU) Spectrometer SINFONI of the Very Large Telescope (VLT), during the period 94 (from 2015-02-10 to 2015-03-28). XID 5395 was observed in two filters, J and H, to sample the [O III]+H$\beta$ complex (redshifted in the J band, at ∼1.22 $\mu$m) and the H$\alpha$+[N II] complex (redshifted in the H band, at ∼1.69 $\mu$m). We collected a total of six (2) sky and 12 (4) on-source exposures of 600 s each for the J band (H band). The total integration times on source were 120 minutes for the J-band data, and 40 minutes for the H band.

We used a field of view (FoV) of 3x3” in a 2D 64 × 64 spaxel frame. The spectral resolutions are R∼1800 for J and R∼2500 for H. We achieved a spatial resolution of 0.33 and 0.45” for the J and H band, respectively, based on the point spread functions (PSF) obtained in AO-mode taken just before the QSO observations. This roughly corresponds to 2.8 and 3.8 kpc at the redshift of the XID 5395, z=1.5. Standard stars and the respective sky frames were also observed to flux-calibrate the data.

The data reduction process was performed using ESOREX (version 2.0.5). We used the ESOREX jitter recipe to reconstruct the data cube and the IDL routine ”skysub” Davies 2007 to remove the background sky emission. Then, we used my own developed IDL routines to perform the flux calibration on every single cube and to reconstruct a final datacube for each object, co-adding the different pointings. To establish an absolute flux calibration, we matched synthetic J- and H-band photometry obtained from SINFONI 1” integrated spectra with COSMOS J- and H-band photometry. We checked the wavelength calibration against known sky lines in the IR and found good consistency. Finally, we applied an astrometric calibration of the J and H data cube using the IRCS H band.

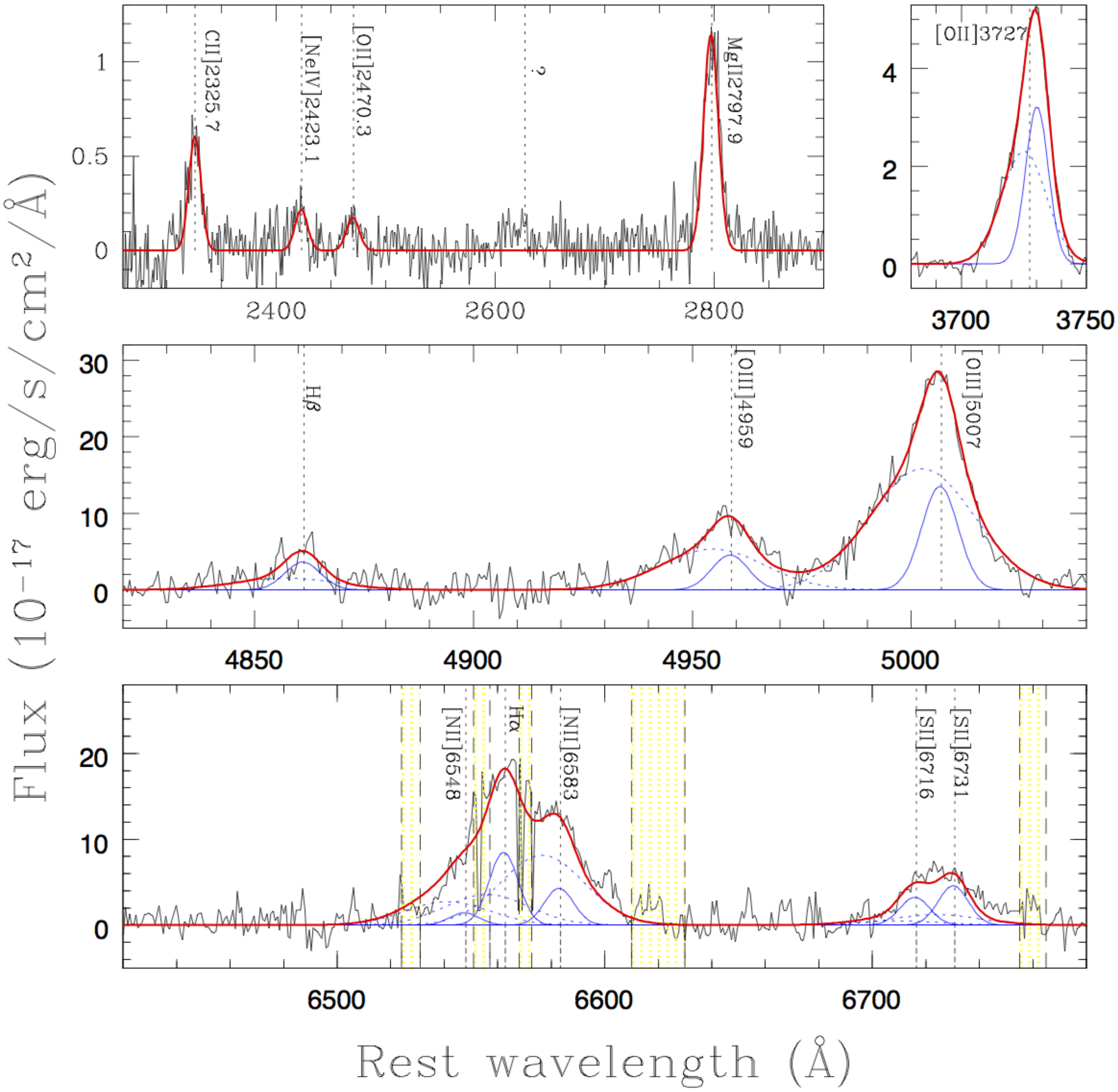

Figure 3.6: *Top:* VIMOS spectrum shows in two zoomed regions the 2300-2900 rest-frame wavelength range and the [O II] emission. *Central:* SINFONI J-band spectrum extracted within an aperture of 1″ diameter from the nucleus around the Hβ+[O III] emission lines region. *Bottom:* SINFONI H-band spectrum extracted within an aperture of 1” diameter from the nucleus around the Hα+[N II]+[S II] emission line region. Spectra are plotted in the rest-frame system; continuum emission has been subtracted from the VIMOS spectrum. Superimposed on the spectra are the best-fit components of our simultaneous, multicomponent fit (solid and dashed blue curves). The red solid curves represent the sum of all model components. From left to right, top to bottom, black dotted lines indicate the wavelengths of the C II], [Ne IV], [O II]2471, Mg II, [O II]3727, Hβ, [O III]λλ4959,5007, [NII]6548, Hα,[N II]6583, and [S II]6716,6731 emission lines. Yellow shaded regions indicate wavelength of intense sky lines in the NIR spectra, affecting mostly the Hα line, which were excluded from the fit. The emission line at $\lambda \sim 2628$ marked with “?” is also observed in the near-UV spectrum of NGC 1068 (see e.g. Raemer, Ruiz, & Crenshaw 1998) without an associated idenfication.

We detected no continuum emission overall the FoV in either SINFONI band. We measure a $3\sigma$ upper limit of $0.6(0.9) \times 10^{-17}$ erg s$^{-1}$ cm$^{-2}$ $\AA^{-1}$ in J (H) band at the position of the nucleus.

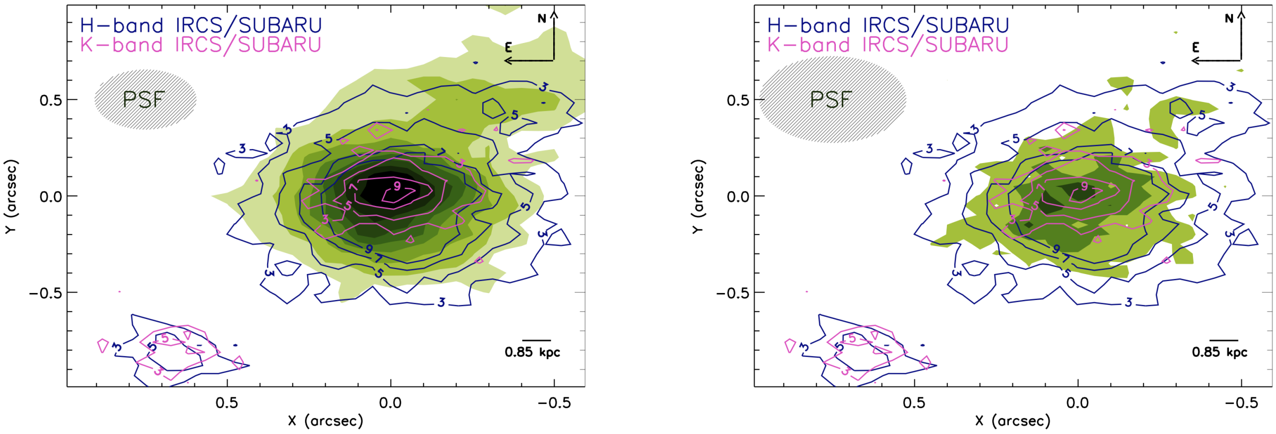

Figure 3.7: (*Left:*) Contours of the Subaru/IRCS H-band (blue) and K-band (magenta) emission taken from Figure 3.5 overlaid on the [O III]$\lambda$5007 channel map obtained integrating the SINFONI datacube on the line core ($\lambda$=1236.1-1238.9 nm; corresponding to the rest-frame range 5001-5012 Å). All contours and colour level starts from $3\sigma$ with steps of +2, as labelled. Spatial scale is given in arcsec. The [O III] systemic emission is overall symmetric, except for a plume extending beyond $0.5''$ ($\sim$ 4.5 kpc) in the north-west direction. (*Right:*) same, but for the H$\alpha$ line, collapsing the channels in the wavelength range $\lambda = 1620.6 - 1624.0$ nm (corresponding to the rest-frame range $6556 - 6570\mathring{A}$). The same plume is also seen in the IRCS H-band data (sampling the H$\alpha$ region), but it is not seen in the IRCS K-band data.

## 3.4 Spatial and spectral analysis

The blueshifted [O II] wing seen in the VIMOS spectrum can be ascribed to the presence of an outflowing wind, which should reveal itself also in the [O III] line with velocities up to 1500-2000 km s$^{-1}$, as suggested for example by the analysis of Zakamska and Greene (2014). To confirm the existence of the outflow and further constrain its properties, we map the [O III]$\lambda$5007 line kinematics in the J-band SINFONI datacube. We also mapped the complex H$\alpha$+[N II] emission sampled by our shallower H-band observations.

### 3.4.1 Integrated VIMOS and SINFONI spectra

From the SINFONI datacubes we extracted a spectrum from an aperture of $1''$ diameter around the nucleus, which is similar to the aperture used to extract the VIMOS spectrum. The full spectrum combined from the J- and H-band SINFONI datacubes, together with the VIMOS spectrum, is shown in Figure 3.6. In the top panel we show a zoom on the spectral region from CII]2326 to MgII (left) and around [O II]3727 (right), in the middle panel around H$\beta$+[O III], and in the bottom panel on the H$\alpha$+[N II]+[S II] emission lines. Following the prescriptions presented in Sect. 2.4.1, we performed a simultaneous fit to reproduce the observed line profiles. With respect to the recipes in the previous Chapter, here we modelled all the emission lines in the entire wavelength range covered by VIMOS, SINFONI J- and H-band spectra, i.e. from C II$\lambda$2325.7 to [SII] doublet, using narrow (NC) and outflow (OC) Gaussian components. The [O II]3726,3728 doublet was treated as a single line with $3727.42\mathring{A}$ as the rest-frame wavelength. The doublet separation is too small to allow a constraint of both NC and OC components. Therefore, in the simultaneous fit, we leave to vary the width of its NC profile, independently from the other Gaussian profiles of the same kinematic component to take the blended nature of the doublet into account.

We adopted as systemic redshift that corresponding to the consistent fit of all the narrow Gaussian

Table 3.1: Emission line properties in the integrated spectra

| height | coordinates | H | K | $f_{H\alpha}$ | $f_{[OIII]}$ | $f_{[OII]}$ | z | FWHM |
|---|---|---|---|---|---|---|---|---|
| Nucleus (integrated 1″) | | | | | | | | |
| (NC) | 10:02:58.39 +02:10:13.94 | 19.70 | 19.90 | 106±13 | 151±7 | 37±2 | 1.4718±0.0001 | 550±20 |
| (OC)$^a$ | ” | ” | ” | 147±31 | 467±6 | 51±2 | 1.4695±0.0001 | 1735±35 |
| NW plume (integrated 0.4″) | | | | | | | | |
| Single Component | 10:02:58.42 +02:10:14.4 | 23.90 | 25.30 | 33±3 | 53±6 | – | 1.4711± 0.0001 | 530±15 |
| SE source | | | | | | | | |
| Single Component | 10:02:58.46 +02:10:13.2 | 22.06 | 21.38 | < 20 | < 10 | – | – | 500 |

Notes: All fluxes in $10^{-17}$erg/s/cm$^2$; all velocities in km/s. $^a$: The centroid of the OC profile is blueshifted of $\Delta v = -272 \pm 22$ km/s.

components in the SINFONI spectra (z=1.4718±0.0001 where the errors are from MC simulations; see Chapter 2); in fact, a possible wavelength shift between the spectra of two different instruments (VIMOS and SINFONI) could affect the rest-frame wavelength. Therefore, in the simultaneous fit the shifts between the NC of each rest-frame optical and rest-frame NIR emission line were constrained independently. We found a VIS-NIR shift of about 240 km/s (Δz=0.002).

The results of the emission line fits (e.g. the fluxes in the H$\alpha$, [O III] and [O II] emission lines, and the centroids of the different components) are reported in Table 1. We measure a ratio of the total flux of the [O III] and [O II] lines of the NC, [O III]/[O II]$_{NC}$ ∼4, in between the value measured in the average spectrum of SDSS Type 2 QSOs (Zakamska et al. 2003; [O III]/[O II]∼ 2) and broad line quasars (Vanden Berk et al. 2001; [O III]/[O II]∼ 6). Instead, the flux ratio in the OC component is twice as large ([O III]/[O II])$_{OC}$ ∼9. Such extreme values of the flux ratios are more similar to what has been observed in high-z Lyman alpha emitters and Lyman-break galaxies (see Nakajima and Ouchi 2014) or green peas galaxies (Cardamone et al. 2009).

We then applied the same non-parametric analysis described in Section 2.1 to the [O III] lines in the spectrum extracted from the 1” aperture. The same asymmetry present in the [O II]3727 emission line doublet, with similar kinematics parameters, is found. A zoom on the [O III]4959,5007 emission lines in the SINFONI spectrum is shown in the right panel of Figure 3.4, with non-parametric quantities labelled.

Finally, we used the Balmer decrements $f(H\alpha)/f(H\beta)$ to estimate the reddening in the overall system. Assuming the Case B ratio of 3.1 (Gaskell and Ferland 1984) and the SMC dust-reddening law, we derived a V-band extinction A$_V$=0.8±0.3, in reasonable agreement with the extinction derived from the SED fitting of the combination of host and galaxy templates (A$_V$ ∼1.1, assuming a Cardelli et al. (1989) extinction law).

### 3.4.2 Spatially resolved analysis

The left panel of Fig. 3.7 shows the SINFONI map extracted in the spectral range $\lambda = 1236.2 - 1238.9$ nm, corresponding to the range where we observed the peak of the emission of the [O III]5007 line in the nucleus spectrum, which is highlighted as a yellow histogram in the right panel of Fig. 3.4 , with a width of 600 km s$^{-1}$. Similarly, in the right panel of Fig. 3.7, we report the map of the peak of the H$\alpha$ emission, at $\lambda = 1620.6 - 1624.0$ nm, integrated over a channel range assuming the same width of 600 km/s as for the [O III] peak. In both panels, we overplot the contours of the Subaru/IRCS H-band (blue) and K-band (magenta) emission taken from Figure 3.5.

The [O III] peak emission is overall symmetric, except for a plume extending beyond 0.5″ (∼ 4.5 kpc) in the North-west direction. This feature is also seen, at lower significance, in the H$\alpha$ emission (right panel of Fig. 3.7) and traces the NW component seen the Subaru/IRCS H-band data (in which the H$\alpha$ is redshifted). We extracted a spectrum from a region of the size of the PSF coincident with the NW plume, and measured all the line fluxes, which are reported in Table 1.

From Fig. 3.7, it is clear that no [O III] and H$\alpha$ emission at the redshift of the system is detected at the position of the SE source (denoted with the magenta and blue contours in the bottom left part

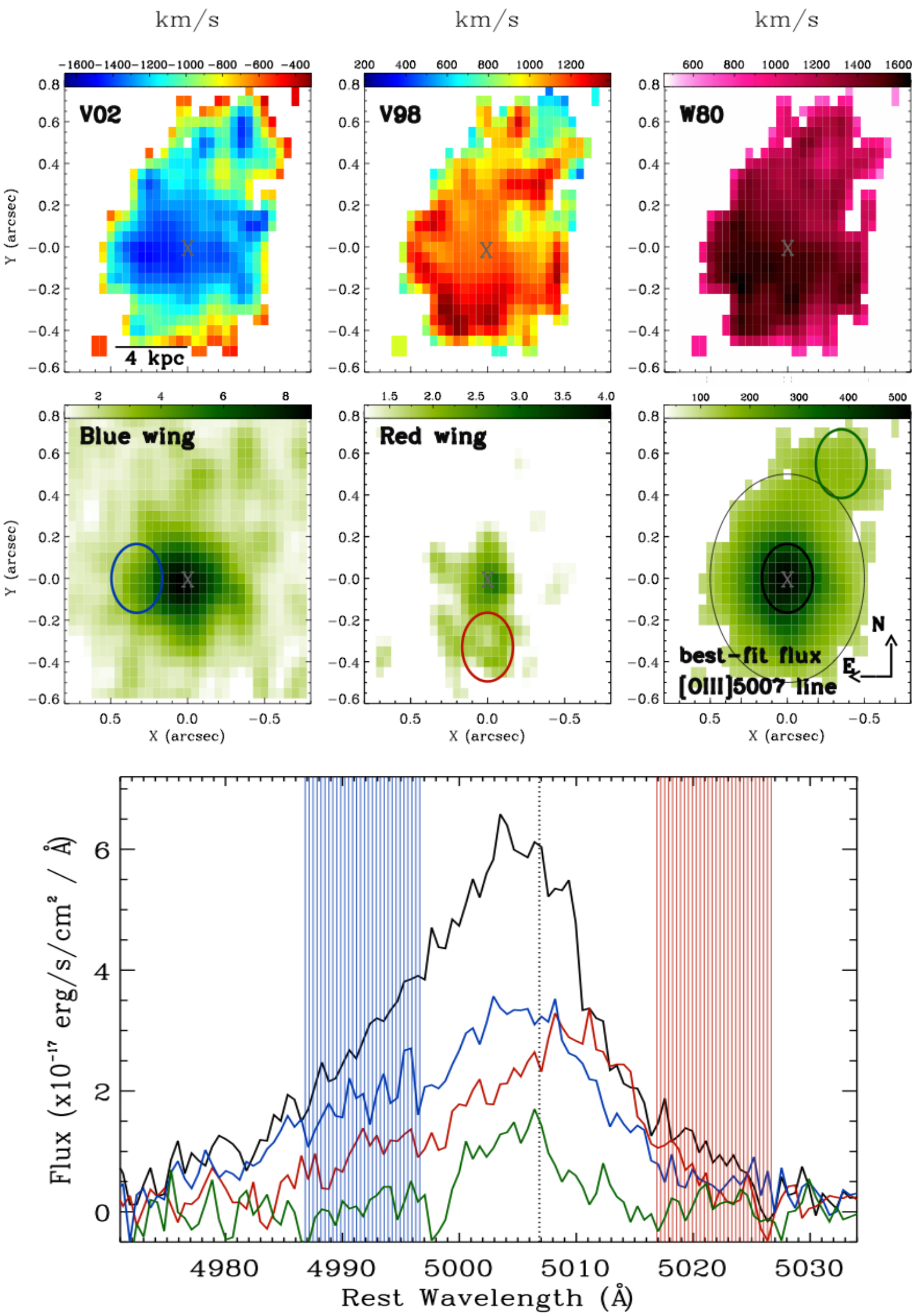

Figure 3.8: *Top panels*: Maps across the field of view of maximum blueshifted velocity ($v_{02}$), maximum redshifted velocity ($v_{98}$), and line width (w80). Blue-(red) shifted velocities as high as $V_{max,blue} \approx -1400$ km/s ($V_{max,red} \approx +1100$ km/s) are found at distances as high as 4 kpc from the centre (indicated with a cross). *Central panels*: SINFONI [O III] maps of the blue ($-1200 \div -600$ km/s), red ($600 \div 1200$ km/s), and total [O III] flux (all scales are in units of $10^{-15}$ erg cm$^{-2}$ s$^{-1}$). In the last panel we also plot as a reference the N-E direction, the J-band PSF, and the 0.4″ and 1″ diameter regions around the nucleus (sse Section 4.1 and 4.2). *Bottom panels:* SINFONI J-band spectra of the [O III] line extracted from three regions of the size of the PSF at the position of the nucleus (black line; from the black circle in the total flux map), of the region with maximum $V_{max,red}$ values (red line; from the red circle in the red wing panel), of the region of maximum $V_{max,blue}$ values (blue line; from the blue circle in the blue wing panel), and at the position of the plume (green line; from the green circle in the total flux map). The shaded regions show the wavelength ranges over which the blue and red wing flux maps have been collapsed.

of the images). We can place a $3\sigma$ upper limit on the [O III] and H$\alpha$ fluxes of $10^{-16}$ and $2\times10^{-16}$ erg cm$^{-2}$ s$^{-1}$, assuming the same redshift of the source and a FWHM of the emission lines of 500 km s$^{-1}$. We searched for emission line features in the entire H- and J-band SINFONI datacubes and could not assign any redshift to the SE source.

### 3.4.3 Kinematic analysis

To map the line emission distributions and the corresponding velocities, we analysed the [O III] emission lines of each spaxel in the field of view separately. We fitted separately the [O III] doublet in order to take advantage from the higher S/N of such lines with respect to the other features (this is mostly due to the fact that the H$\alpha$ complex is associated with shallower H band observations). When the S/N is high enough, the complex [O III] profiles could be decomposed in multiple Gaussian components, while this is not the case where the S/N is lower. We defined the S/N as the ratio between the flux of the best-fit [O III]5007 total profile (or the flux of a Gaussian profile, characterised by a width equal to the FWHM of the NC of the $1''$ spectrum, $\sim 550 km/s$) and an amplitude equal to the standard deviation of the continuum regions in the vicinity of the emission line. In order to study variations of the line profiles across the field in the datacube, the non-parametric approach was used. This, in fact, does not depend on the number of Gaussian components used in each spaxel spectrum, thus also allowing a characterisation of the kinematics in spaxels at the lowest S/N ratio. However, we used an adaptive binning technique such that the high S/N regions were analysed over smaller areas than the low S/N regions. This technique can be summarised as follows: as a first step, we chose to select only those spatial pixels (1x1 pixels) with a S/N ratio equal or higher than 2. When the ratio was lower than this threshold, we tried to increase it integrating the spectrum over larger areas (1x2 and, eventually, 2x2 pixel blocks). Finally, we chose all the pixel blocks with a S/N over the threshold value.

We measured, for the [O III] line, the same parameters extracted for the integrated [O II] and [O III] profiles (see section 2.1.1). The maps across the field of view of the maximum blueshifted velocity ($\mathrm{V_{max,blue}}$), the maximum redshifted velocity ($\mathrm{V_{max,red}}$), and $W80$ are shown in the first three panels of Fig. 3.8. Blue- (red) shifted velocities with values as high as $\mathrm{V_{max,blue}} \approx -1400$ km/s ($\mathrm{V_{max,red}} \approx +1100$ km/s) are found, and the line width $W80$ in the range $800 - 1600$ km/s. The middle panels of Fig. 3.8 show the SINFONI [O III] flux maps of the blue ($-1200 \div -600$ km/s; left), red ($600 \div 1200$ km/s; centre), and total (right) [O III] intensity. In the last panel of Fig. 3.8 we show the [O III] line from spectra extracted from three regions of the size of the PSF at the positions indicated in the central panels and colour coded accordingly: black from the nucleus (black circle in the total flux map), red from the region of maximum $V98$ values (red circle in the red wing panel), and blue from the region of maximum $V02$ values (blue circle in the blue wing panel). The shaded regions show the wavelength ranges over which the blue and red wing flux maps have been collapsed. The w80 measured for the spectra extracted at the maximum velocity regions, at distances $\sim 2-3$ kpc from the centre, have large values ($\sim$ 2000 km s$^{-1}$), which cannot be ascribed to normal gravitational motions of gas in the disk of a galaxy.

Finally, Fig. 3.9 shows the map of the [O III] velocity peak ($v_p$) obtained from our spaxels by spaxels fit with respect to the systemic emission defined in 3.4.1. The results of a t-means test indicate that the velocities around the nucleus region and those in the reddest region have different means with a probability of false correlation P<0.01. Indeed, MonteCarlo analysis reveals that the non-parametric $\mathrm{V_{peak}}$ estimator is characterised by errors of the order of $\sim$ 50 km/s in the nuclear/top regions and of $\sim$ 80 km/s in the bottom regions. Taking the errors into account, the observed variation in $\mathrm{V_{peak}}$ across the FoV from -150 km/s to 150 km/s (a total of 300 km/s) is significant, and may represent the kinematic trace of a rotating disk in the host galaxy, although the gas kinematic appears perturbed by the outflow and/or by interactions.

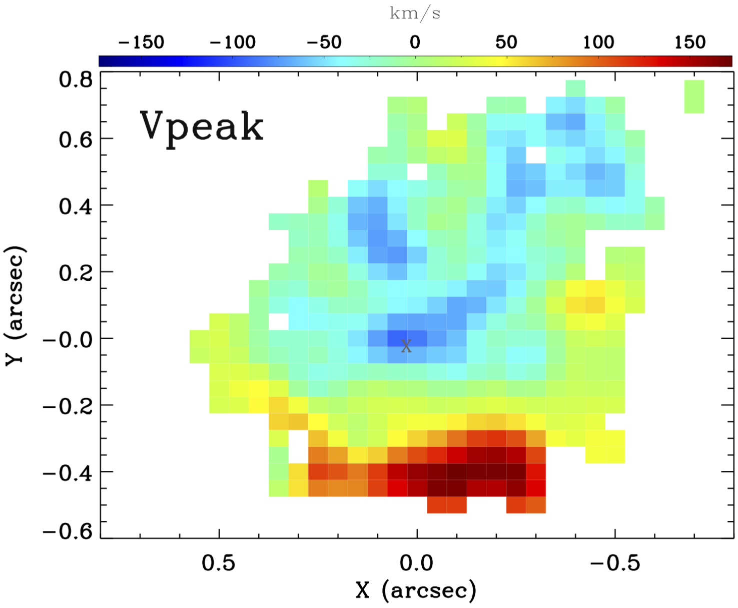

Figure 3.9: Maps of the [O III] velocity peak (see Section 4.2) over the same FoV shown in Fig. 3.8. We measure a variation of Vpeak from -150 km s$^{-1}$ to +150 km s$^{-1}$, which we interpret as evidence for a rotation in the host galaxy.

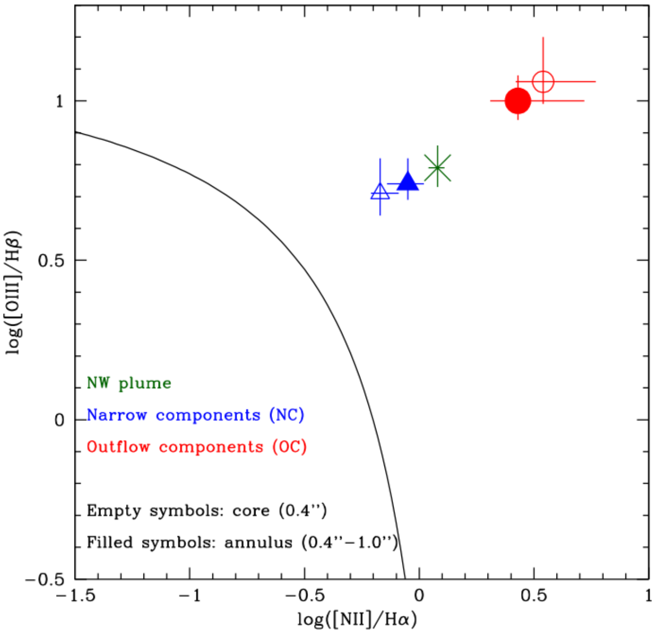

Figure 3.10: Standard diagnostic diagram [O III]/H$\beta$-[NII]/H$\alpha$ with the theoretical z=1.47 curve used to separate purely SF galaxies from galaxies containing AGN (Kewley et al. 2013). The diagnostic ratios from the integrated 0.4" diameter nuclear spectrum (empty symbols) and for the 0.4-1" diameter annular region (filled symbols), for both the OC (red circles) and NC (blue triangles) components are shown. We also plot the value obtained for the NW plume with a green cross.

### 3.4.4 Rest-frame optical flux ratios and ionisation source

We investigated the optical diagnostics routinely used to assess the photo-ionisation origin for the emission lines. In particular, we focused on the BPT diagram (from Baldwin et al. 1981) involving the flux ratios [NII]/H$\alpha$ and [O III]/H$\beta$. The high resolution of the AO data, coupled with the achieved PSF, allowed us to study the ionisation mechanism in two separate regions: an inner region of the size of the PSF (0.4$''$–3.5 kpc diameter; inner black circle in the right panel of the central row in Fig. 3.8) corresponding to the inner $\approx$ 9 kpc$^2$, and an outer annular region of 0.4 to 1" diameter (outer black circle in the right panel of the central row in Fig. 3.8), covering the 1.7 to 8.5 kpc radial distance from the centre, where the highest velocities are detected.

We extracted two spectra separately from these two regions and we fitted simultaneously, with the two kinematics component NC and OC described above, the [O III]+H$\beta$ complex and the H$\alpha$+[N II] complex to compute an excitation map of the galaxy. Figure 5.4 shows the BPT with the results from our analysis. The solid line in the diagram corresponds to the theoretical redshift-dependent curve used to separate galaxies containing AGN from purely SF galaxies at z$\sim$ 1.5 (Kewley et al. 2013). In the figure we plot the diagnostic ratios obtained from the core 0.4$''$ diameter spectrum (empty symbols) and from the $0.4'' - 1.0''$ diameter annular region (filled symbols), separately for the NC (blue triangles) and OC (red circles) components. In all cases the observed diagnostic ratios are consistent with an AGN photo-ionisation of the emission lines; all the data points lie above the Kewley et al. 2013 separation line, and similar conclusions are reached using the BPT diagnostics involving the [SII]/H$\alpha$ ratio (as for the other two obscured QSOs at z$\sim$ 1.5 presented in Chapter 2).

Mahony et al. (2016) report an increase of the ionisation state (higher [N II]/H$\alpha$ ratio) in the regions where the outflowing material is detected in 3C293, a local radio-loud QSO, which is interpreted as evidence of shocks associated with the wind (see also Section 3.5.3). Similarly, shock-ionisation models can predict values of the [O III]/H$\beta$ ratio as high as $\sim$ 10 M. G. Allen et al. 2008). We also report an increase of both line ratios for the OC component with respect to the NC component, in both spectral extractions, which can be interpreted in the same way.

Finally, In Fig. 5.4 we plot the flux ratios observed in the NW plume with a green cross. Also in this case, the ratios are consistent with a photo-ionisation origin from AGN emission.

## 3.5 Discussion

We now discuss the interpretation of the velocity shifts revealed in the fits to the observed integrated [O III] line profiles, and of the high-resolution spatial and spectral analysis obtained through the adaptive optics data presented in the previous sections. We also relate the outflow properties with the X-ray, radio, and host galaxy properties of XID 5395.

### 3.5.1 Outflow properties

The most likely explanation for the OC component, revealed in the simultaneous fit of the VIMOS and SINFONI spectra as a broad and shifted extra-Gaussian component and resolved by the spatial analysis of the [O III] velocity maps, is the presence of an outflowing wind in this SB-QSO system. If this is the case, and assuming a bi-conical geometry, the kinetic power ($P_K$) and mass-outflow rate ($\dot{M}_{out}$) of the ionised component of the outflow can be computed under reasonable assumptions. In particular, estimates of the following quantities are needed (Appendix B.0.1): the electron temperature, $T_e$, and density, $n_e$, gas phase metallicity, emission line luminosity, spatial scale, and wind velocity.

*Electron Temperature, $T_e$*: The electron temperature can be calculated from the flux ratio of two lines with the same ionisation state. For this purpose, we used the [O II]2471/[O II]3727 total flux ratio observed in the VIMOS spectrum and its dependence on the electron temperature as found by Humphrey et al. 2008 (their figure 7). We infer T$_e$ $\approx$ 13000$\pm$500 K. We note that to correctly measure the electron temperature of the outflowing gas one should use the flux of the OC. Unfortunately, for both the faint [O II]2471 and blended [O II]3727 doublet it was not possible to constrain the OC and NC fluxes separately as for other emission lines (see section 4.1). Nevertheless, we postulate that the OC fluxes could contribute more than the NC fluxes (see Fig. 3.6, OIII emission lines), making our estimate a good proxy of $T_e$.

*Electron Density, $N_e$*: An estimate of the electron density can be obtained from the flux ratio in the OC of the [SII]6716,6731 doublet, $R_{[SII]} = f([SII]6717)/f([SII]6731)$. Given that the fitting procedure may produce strongly degenerate results when systemic components are also present (see Sect. 2.5.6), we used the value obtained from the fit to the [S II] doublet ratio in a 0.4-1.0$''$ annulus centred on the target and covering only the south-east quadrant in which the outflow is observed. We obtained $R_{[SII]} = 1 \pm 0.1$, which corresponds to $N_e = 780 \pm 300$ cm$^{-3}$ (Appendix A.3).

*Gas phase metallicity*: For our purposes, we assumed a solar metallicity, as the combination of emission lines available to us does not enable a clean calibration of the metallicity in the presence of strong AGN ionised gas. We note, however, that the assumed metallicity is consistent with that expected from the $T_e$ derived above, following the relation of Jones et al. (2015).

*Emission line luminosity*: Generally, the H$\beta$ luminosity is used to calculate the total amount of gas and mass outflow rate (e.g., Cresci et al. 2015a; Liu et al. 2013). Alternatively, the H$\alpha$ flux can be adopted (see e.g. Genzel et al. 2014). In our case, the H$\beta$ line is faint, while the H$\alpha$ line may suffer from contamination from the hidden broad line region. We have therefore adopted the Cano-Díaz et al. (2012) formalism, which instead employs the [O III] line luminosity. We used the [O III]5007 flux associated with the outflow component in the 1" integrated spectrum (Figure 3.6, panel *a*). As discussed in Carniani et al. (2015), this approach gives most likely a lower limit to the total ionised component, given that in normal situations [O III] traces only a fraction of the gas with respect to H$\beta$.

*Spatial scale*: We adopt a radial extension of 4.3 kpc for the outflowing gas, given that we observe the bluewards emission out to this distance (see Figure 3.8, panel V02, V98; Section 4.2).

*Outflow velocity*: Finally, we considered as outflow velocity the maximum velocity observed $v_{max}$ in the nuclear region ($V_{out} \approx 1600$ km/s; see Section 4.1), and we assumed that lower velocities are due to projection effects (Cano-Díaz et al. 2012; Cresci et al. 2015a).

With all these ingredients, we can derive the mass outflow rate and the outflow kinetic power, from the same formulae we used for the X-Shooter sources (Eqs. B.9 and B.8). We derive for XID 5395 a kinetic power $P_k^{ion} \approx 5 \times 10^{43}$ erg/s and a mass outflow rate $\dot{M} \sim 50\ M_\odot/yr$. These values are consistent overall with those observed for targets at similar bolometric luminosities (Carniani et al. 2015). These values, not corrected for the extinction and regarding only the ionised component of the outflow (but see also the other conservative conditions in 2.5.6, and the discussion in Appendix B.0.1), represent lower limits to the total outflow power.

The inferred $\dot{M}$ ($\approx$50 $M_\odot/yr$) is lower than the observed SFR ($\sim 370\ M_\odot/yr$), which can therefore in principle sustain the wind assuming an unlikely energy-gas coupling of $\approx 80\%$ (see Sect. 2.6; Veilleux et al. 2005). We note, however, that the ionisation diagnostics exclude SF all over the FoV (See 3.4.4) as an origin for the photo-ionisation of the gas. Considering also that the mass outflow rate refers only to the ionised component, while there are indications that the total molecular component may be up to a factor of 10 larger (see e.g. Carniani et al. 2015), and that we observe very high velocities ($\gtrsim 1600$ km/s), we can conclude that a SF-driven mechanism is unlikely to sustain entirely the outflow. Moreover, the derived kinetic power associated with the ionised gas is $\approx 0.5\%$ of the AGN bolometric luminosity inferred from the SED fitting decomposition ($\log L_{bol}$=45.93), and therefore comparable with the coupling we found for the ionized component in XID 2028 and XID 5321 in Chapter 2 ($\approx 2\%$, when we do not correct for [O III]/H$\beta$ flux ratios).

### 3.5.2 Overall geometry and intrinsic properties

The maps tracing the maximum blueshifted and redshifted velocities ($V02$ and $V98$ panels in Fig. 3.8) reveal that these high-velocity components are not spatially coincident with the core, i.e. they are displaced by $\sim 1$ PSF size from the central AGN position, roughly in the east (blueshifted component) and south-east (redshifted component) directions. The outflow is seen mostly in this quadrant, and extends up to $\sim 4.3$ kpc from the nucleus ($\sim 0.5''$).

When looking at the total fluxes associated with the fastest components, we see that the bulk of the approaching outflowing gas has an almost symmetric distribution overall the entire $1''$ diameter region (”blue wing” panel in Fig. 3.8); the receding gas, instead, is present only in the core and along the south direction (”red wing” panel in Fig. 3.8). These projected geometries are consistent with a wide-angle conical outflow, originating from the nucleus and moving towards our line of sight.

Fig. 3.11(a) shows a schematic cartoon of the system, illustrating the host, including the plume in the NW direction, and our inferred geometry for the wide-angle conical outflow. The outflowing region is located between the observer and the host; both approaching and receding gas regions are associated with this unique conical component. While the bulk of the gas has negative velocities (up to -1400 km/s), the far-side of the cone may be responsible for the receding emission with (absolute) lower velocities due to projection effects, as we indeed observe ($+1000$ km s$^{-1}$).

A biconical outflow as depicted in Fig. 3.11(b) may be also consistent with our data. The flux observed in the nucleus in the red channel is a factor of $\sim 3$ lower than that in the blue channel (see the black curve in the bottom panel of Fig. 3.8), which is roughly consistent with the extinction derived from the SED fitting and Balmer ratio decrement ($A_V$=1). In this case, the outflow should be tilted to observe the receding part located beyond the disk in the south direction, which should only be visible at larger distances (larger angles). In both cases, we estimate an opening angle of the cone at least of $\pi/2$.

Unresolved compact jets may inject energy into the gas, heat it, and drive the outflows, as observed in radio-loud systems (Begelman and Cioffi 1989; Wagner et al. 2013). Alternatively, radiative-driven winds can induce shocks in the host and therefore accelerate relativistic particles (e.g. Zubovas and A. King 2012), which then can emit in the radio band. The conical/wide angle geometry inferred for XID 5395 is more consistent with a radiatively wind scenario of an expanding bubble (see e.g. Zakamska et al. 2016b) rather than with a jet-driven outflow scenario, for example as observed in local radio sources with jets and ionised gas outflows (e.g. Cresci et al. 2015b; Mahony et al. 2016). Indeed, although XID 5395 has a radio power typical of radio-loud objects, from the radio data in hand we cannot confirm the presence of a jet (see Section 2.1), which should be in any case confined within the central 1 kpc (the resolution of the VLBA data). The observed excess radio emission with respect to the SFR in XID 5395, which is seen over the scale of the entire galaxy and is co-spatial with the outflow, can therefore be in principle ascribed to radio emission produced in the wind during the shock; this is suggested by Zakamska et al. (2016b) on the basis of a statistical analysis of the correlation between the radio luminosity and the narrow line kinematics in radio-quiet AGN. At luminosities higher than $L_{\rm bol} > 3 \times 10^{45}$ erg/s (as the case of XID 5395), the wind can in principle sustain and also generate high radio luminosities.

### 3.5.3 On the transition nature of XID 5395

From our multi-wavelength and spectroscopic analysis, we have a clear picture of the XID 5395 system, which can be summarised as follows. We have a luminous AGN ($L_{\rm bol} \sim 8 \times 10^{45}$ erg s$^{-1}$), obscured in the X-rays ($N_H \sim 10^{23}$ cm$^{-2}$) and at optical wavelengths ($A_V \sim 1$ from Balmer decrement and SED fitting; see Section 4.1), hosted in a massive ($M_* \sim 7.8 \times 10^{10}$ $M_\odot$), starburst (SFR$\sim$ 370 M$\odot$/yr) disk galaxy, possibly interacting with a lower luminosity system. A wide-angle outflow of ionised gas is launched from the central core at high velocities ($\approx 1600$ km/s), and it is propagating in the ISM in the direction of our line of sight.

The fact that vigorous SF and AGN activity do co-exist in XID 5395 can be seen as a first indication

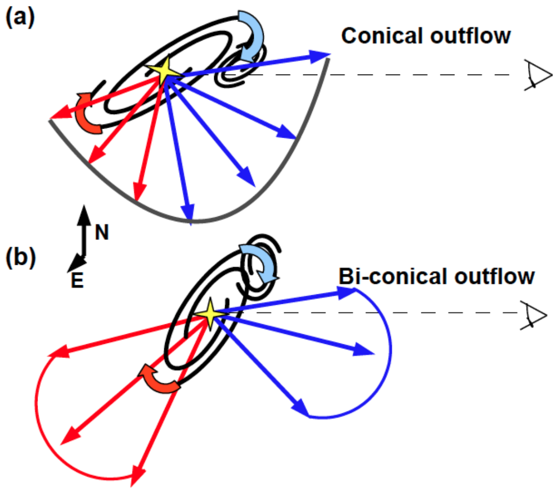

Figure 3.11: A cartoon illustrating the geometry of the system associated with XID 5395, in the conical *(panel a)* and bi-conical *(panel b)* cases, as inferred from our spatial and spectral analysis. The line of sight intercepts the disk of the galaxy, which is rotating and inclined with respect the plane of the sky, so that the approaching part is in the North direction and the receding part is in the South direction, as revealed by the Vpeak map. The (bi)-conical outflow is shown with arrows: blue arrows mark the gas moving towards our direction, and the red arrows mark the gas moving opposite to our line of sight. See text for details.

of the transition nature of this source. Indeed, in the co-evolutionary models of galaxy-AGN evolution (e.g. Hopkins et al. 2008) the phase of maximum and co-eval SF and accretion rate last only ∼few×$10^8$ yr, and is possibly triggered by mergers. The presence of the interacting galaxy seems to confirm that we caught XID 5395 exactly during this crucial and short phase.

Given the steep spectral index observed at 1.4 and 3 GHz ($\alpha$ ∼1.1 - 1.3; Schinnerer et al. 2010; Smolčić et al., in preparation), XID 5395 can be classified as a compact steep spectrum radio source (CSS; see Orienti 2016) with a size comparable to that of the host galaxy (∼few kpc). Compact radio sources at high-z may be intrinsically young sources (e.g. Fanti et al. 1995) in which a dense ISM still prevents the radio emission from expanding at larger scales, which likely evolve over longer timescales into the giant FR I radio galaxies observed at low redshifts. This is a further indication that XID 5395 may be caught in an early stage of its evolution.

Young radio sources and CSS also show disturbed kinematics in the ionised gas (e.g. Gelderman and Whittle 1994) with exceptionally broad widths observed in the [O III] lines Kim et al. 2013. An example of a local CSS source is 3C293 at z=0.045, where the inner jet is clearly resolved and confined within few kpc, while high-velocity ionised gas is seen up to ∼ 10 kpc in IFU data Mahony et al. 2016, see their Figure 7. Moreover, the molecular and ionised gas components reveal different morphologies, which can be explained with the presence of a spherical-like bubble as predicted in simulations (e.g.Wagner et al. 2013; see also discussion in Section 5.2) inflated by the jet itself, but independently expanding in the ISM. In addition to the exceptional broad line widths, 3C293 has other common properties with XID 5395: both sources show similar stellar masses (∼ $10^{11}$ $M_\odot$), red colours and disturbed morphology, indicating the presence of a companion galaxy that can be the remnant of a merger (Floyd et al. 2008; Lanz et al. 2015). XID 5395 can therefore be considered the high-redshift analogue of 3C293, in which the same phenomenon of inflating a spherical-like bubble of gas by an inner jet may be in place. However, we cannot resolve any jet due to resolution limits of the observations, although we have evidence of the presence of a bubble of ionised gas and diffuse radio emission, with a wide opening angle. In fact, as proposed in Section 5.2, the radio diffuse emission can be ascribed to shocks in the dense ISM Zakamska et al. 2016b, suggesting that XID 5395 is in a

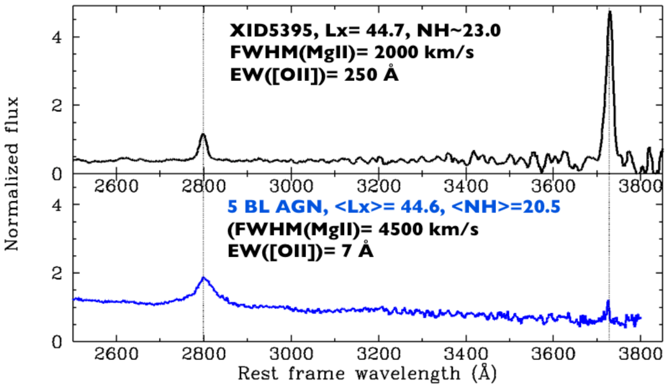

Figure 3.12: Rest-frame VIMOS spectrum of XID 5395 (top) and the average VIMOS spectrum of five unobscured BL AGN (bottom) chosen in the same z and L bins of our target. In both panels, the dotted lines indicate the position of the Mg II (left) and [O II] (right) lines. The y-axis scale is maintained in the two panels to ease a direct comparison of the two spectra; it is clear that the [O II] emission weakens, while the continuum becomes bluer and the Mg II line becomes stronger in the bottom panel.

phase of radiative feedback.

If the source is caught in this short transition phase, in few hundreds Myrs the SF will be likely completely suppressed or inhibited, and the source will evolve into an unobscured QSO. In Figure 3.12, we plot the rest-frame zCOSMOS VIMOS spectrum over the full wavelength range of XID 5395 (upper panel) compared to the average spectrum of five unobscured BL AGN at the same average $< z >$ and of the same intrinsic $<L_X>$ ($L_X \sim 7 \times 10^{44}$ erg s$^{-1}$, bottom panel). From the comparison of the two spectra, we see the emergence of the broad MgII line (from FWHM$\sim$ 2000 km s$^{-1}$ as observed in XID 5395, to FWHM$\sim$ 4000 km s$^{-1}$, as measured in the average BL AGN spectrum), with the continuum moving from flat to blue, and the [O II] line; this line dominates in the spectrum of XID 5395, weakening in the BL AGN spectrum, as expected if SF is inhibited at the end of the co-evolutionary sequence. Red sources with flat rest-frame UV continuum, as observed in XID 5395, have been historically missed in optical surveys of QSO, but gained increasing attention in recent years as signposts of objects in the blow-out phase (see e.g. Banerji et al. 2012; Brusa et al. 2015, 2010; Urrutia et al. 2009; Zakamska et al. 2016a among others).

## 3.6 Summary

We exploited VLT/VIMOS, VLT/SINFONI, and Subaru/IRCS AO data to study the kinematics properties of an X-ray luminous, obscured SB-QSO system at z$\sim$ 1.5, associated with an extreme EW of the [O II] line (EW$\sim$ 200 Å; see Fig. 3.1).

We propose that EW larger than 150 Å, when coupled with an X-ray emitting source, may be a very efficient criterion to isolate objects with disturbed morphology (Fig. 3.2), and possibly associated with an outflowing phase, as witnessed by the broad, asymmetric line profiles of the [O II] and [O III] emission lines in the integrated VIMOS and SINFONI spectra of the target presented in this study (Fig. 3.4). This criterion may complement other diagnostics that have been proposed in the past to isolate such rare objects in X-ray samples, such as those based on the observed red colours of the hosts (e.g. the one presented in Chapter 2; Brusa et al. 2015; Perna et al. 2015a).

The kinematics analysis, coupled with the high spatial resolution achieved through AO observations (few kpc), reveals complexities and asymmetries in and around the nucleus of XID 5395, which are summarised below:

- SUBARU/IRCS data reveal three distinct sources in the proximity of XID 5395 (Fig. 4.2): a central source with a projected transversal size of ∼8.5 kpc ("nucleus") that is associated with the X-ray source; a compact object at about 10 kpc towards the SE direction ("SE source"); an extended source at ∼4 kpc towards the NW direction ("NW plume");

- Within the nucleus, the velocity field measured in the SINFONI data via multicomponent spectral fitting and non-parametric analysis reveals different kinematic components (see the NC and OC components in Fig. 3.6 and the velocity maps in Fig. 3.8); in particular, the maximum blueshifted and redshifted velocities, with absolute values $\approx 1200-1500$ km $s^{-1}$, are not spatially coincident with the nuclear core (the central PSF, $0.4''$). In addition, from the variation of the velocity peaks within the nucleus, we detect signatures of a rotating disk (Fig. 3.9);

- SINFONI data confirm that the NW plume traces an object, possibly a merging galaxy, at the same redshift of the central AGN (see Fig. 3.7) with lower velocity components (e.g. $w80 < 1000$ km/s; see Fig. 3.8) than those reported for the nucleus. Instead, we cannot confirm, nor exclude, that the SE component is at the same redshift as the nucleus, and part of an interacting system at a pre-merger phase, or right after a first pass in the merger path. If this were the case, the SE component should be at least a factor of 10 less luminous/massive;

- The BPT diagram suggests that AGN photo-ionisation is responsible for the line emission ratios observed both in the NW plume and over the entire nucleus (Fig. 5.4) with a possible contribution of shocks towards the external regions.

- We best model the observed emission as depicted in Fig. 3.11: Our line of sight intercepts a wide-angle conical and fast outflow, which originates from the central AGN (Sect. 5.2). The galaxy disk is tilted with respect the outflow cone to observe both the blue and redshifted emissions. The kinetic power, mass outflow rate, and momentum rate inferred from our analysis are in the range expected from AGN feedback models originated by radiatively driven winds (Sect. 5.1);

- Overall, we accumulated different observational evidence (presence of outflow and merger, coeval SF and AGN activity, and compact radio emission; all described in Section 5.4) that XID 5395 is caught in the short, transition phase of "feedback" in the AGN-galaxy co-evolutionary path, and it will subsequently evolve into an unobscured QSO (see Fig. 3.12).

* * *

This material has been published in

- "A fast ionised wind in a star-forming quasar system at z∼1.5 resolved through adaptive optics assisted near-infrared data",
  by M. Brusa, M. Perna,

and is based on observations undertaken at the European Southern Observatory, Paranal, Chile, under the programme 094.A-0250 and the Large Programme 175.A-0839.

Chapter 4

# SINFONI spectra of heavily obscured AGNs in COSMOS: evidence of outflows in a MIR/O target at z $\sim 2.5$

## Abstract

In this Chapter, we present a third selection criterion, based on red mid-infrared to optical and optical to near-infrared colours. In the framework of the most widely accepted co-evolutionary scenario, the criterion should be able to detect buried AGNs in the prelude of the so-called “blow-out phase”, when most of the black hole mass is assembled and the AGN is not powerful enough to release energy in the form of ouflows.

We present new data for four candidate obscured Compton-Thick (CT) quasars at z $\sim 1-2.5$ observed with the SINFONI VLT spectrograph in adaptive optics (AO) mode, and selected from a $24\mu$m Spitzer MIPS survey of the COSMOS field. Near-infrared spectra are analysed to determine principal physical properties through rest-frame optical diagnostics and to search for broad components in the [O III]-H$\beta$ and H$\alpha$-[N II] regions. We also employ X–ray spectral analysis, radio and MIR diagnostics, and SED fitting to study the nature of the sources. We successfully identify three objects for which we had only a photometric redshift estimate. Based on their emission line diagnostics and on ancillary multi-wavelength constraints, we confirm that all four targets harbour obscured AGNs. Indeed, we clearly resolve a fast ($\sim$ 1600 km/s) and extended ($\sim$5 kpc) outflow in the [O III]$\lambda$5007 emission line of one target, MIRO 20581. This feature, the commonly used indicator for ionised outflowing gas, was sampled and detected only for this target. Being the [O III] the best tracer for ionized outflows, on the basis of our analysis, we cannot exclude the presence of outflows in the other sources. Overall, the constraints we obtain from our targets and from other comparative samples from the literature suggest that these optically faint luminous infrared galaxies, hosting obscured AGNs, may represent a brief evolutionary phase between the post-merger starburst and the unobscured quasar phases.

## 4.1 Introduction

In the framework of the evolutionary scenario (Sect. 1.7), during the obscured phase, the SMBH is expected to accrete mass very rapidly, implying a vigorous (although obscured) X-ray emission. In the AGN census, X-ray surveys have been extensively used to probe the assembly and growth of SMBH at high redshift. In particular, since the X-ray radiation is less attenuated than the optical flux, selection criteria based on high X-ray to optical flux ratio ($f_x/f_O$) have been used to select obscured sources at z $\sim 1-2$. Several studies (e.g. Alexander et al. 2002; Del Moro et al. 2009; Della Ceca et al. 2015;

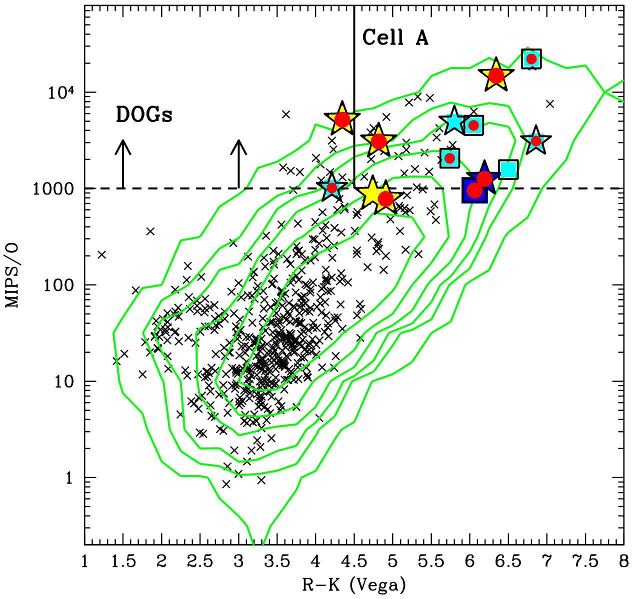

Figure 4.1: $f_{24\mu m}/f_R$ as a function of $R-K$ colour for all the COSMOS 24$\mu$m sources associated with the optical and K-band counterparts (green isodensity contours). Black crosses represent the 1 mJy flux-limited sample. Yellow stars denote the five objects observed with SINFONI; cyan stars and squares denote Melbourne et al. (2011) and Brand et al. (2007) targets, respectively (two targets present in both samples are indicated with stars); blue symbols denote the two brightest sources presented in Chapter 2. Star and square symbols indicate IFU and long-slit observations, respectively. Sources marked with red circles are also detected in the 1 mJy flux limited sample and are those considered for the analysis. The box delimited by a vertical solid line and horizontal dashed line marks the region proposed in Fiore et al. (2009) to select CT AGN (Cell A). The horizontal dashed line sets the criterion for the selection of DOGS.

Fiore et al. 2003; Mignoli et al. 2004) have found that sources with high $f_x/f_O$ are characterised, on average, by red optical to near-infrared colours ($R-K_{Vega} > 5$) and column densities in the X–ray of the order of $10^{21}-10^{23}$ cm$^{-2}$. Moreover, our VLT XSHOOTER observations of a small sample of obscured QSOs at z ∼ 1.5, selected on the basis of their observed red colours and high $f_x/f_O$ ratio, have confirmed the presence of ionised outflowing material in 75% of objects and a dust-reddened type 1 nature (Chapter 2). These objects appear similar to infrared bright ($K_{Vega}$ ≤16) dust-reddened Type 1 QSOs selected by combining radio with near-infrared (NIR) and optical catalogues at lower redshift (z $\lesssim$ 1; Glikman et al. 2004, 2007). Analysing the subsample of 13 objects with strongly disturbed morphology presented by Urrutia et al. (2012), we found that ∼60% of these radio-detected sources show evidence for outflow in the [O III] line profile (see Brusa et al. 2015). The selection criterion introduced in Chapter **??**, based on high [OII] EWs, has proved to be efficient as well in selecting star forming (starburst) systems associated with higly disturbed morphologies. Indeed, these sources are characterized by vigorous X-ray emission ($L_X > 10^{44}$ erg/s) and by the presence of asymmetric [OII] and [O III] profiles. The follow-up SINFONI observations of the the prototype source isolated with this criterion (XID 5395) revealed complex kinematic motions on kpc scales.

However, each selection technique may bias the samples towards particular properties and, chiefly, may bias the characterisation of the outflows (see Chapter 2); to test co-evolutionary models, we need to select and isolate different populations of quasars in the distinct phases of the AGN to galaxy co-evolution (Fig. 1.10), including the initial Compton-Thick[1] phase.

---

[1] We distinguish between moderately obscured (with log($N_H$) = 22−23 cm$^{-2}$), highly obscured (with log($N_H$)

Since most of the absorbed AGN energy is re-emitted in the mid-infrared (MIR), surveys at these wavelengths can potentially recover the elusive obscured accretion missed by X–ray surveys (e.g., Brandt and Alexander 2015). Several criteria based on the MIR emission of high-z sources have been introduced in recent years to search for heavily obscured AGNs at z $\sim 1-3$, and have been applied on Spitzer MIPS observations in multi-wavelength survey fields. Typically, the criteria involve the selection of objects with MIR luminosities typical of AGN, but with faint optical or near-infrared emission (e.g. Dey et al. 2008; Fiore et al. 2008, 2009; Martínez-Sansigre et al. 2005; Riguccini et al. 2015).

For example, Fiore et al. (2009) used the MIPS $24\mu m$ COSMOS catalogue (Sanders et al. 2007) to select a sample of $\sim 60$ candidate obscured AGN/CT QSOs characterised by extreme mid-infrared to optical flux ratio ($f_{24\mu m}/f_R > 1000$) in the area covered by the C-COSMOS Chandra survey (Civano et al. 2012; Elvis et al. 2009). They coupled this selection with a red colour cut $(R-K)_{Vega} > 4.5$, which is able to efficiently pick up objects at the redshift of interest (z $\sim 1-3$). To test the efficiency of the selection, they stacked the Chandra images at the position of the MIPS sources without a direct X–ray detection and recovered a hardness ratio (HR) in the stacking signal larger than that measured for less extreme sources ($f_{24\mu m}/f_R < 1000$ and/or $(R-K) < 4.5$). Still, these sources with $f_{24\mu m}/f_R > 1000$ exhibit evidence of both star formation and AGN activity, and there are contradicting conclusions about how many of the sources selected in this way are actually obscured AGN at z $\sim 1-3$, rather than dusty star-forming objects (e.g. Dey et al. 2008; Donley et al. 2008; Fiore et al. 2009).

In this Chapter we present new SINFONI observations, assisted with adaptive optics (AO), for a sample of four luminous, highly obscured QSOs in the COSMOS field, selected on the basis of their high mid-infrared to optical flux ratios (MIR/O) and red R $-$ K colours. The criterion is based on the positive correlation found by Fiore et al. (2008) between the $f_{24\mu m}/f_R$ and the $f_x/f_O$ ratio for a sample of sources with column density of the order of $10^{22}-10^{23}$ cm$^{-2}$. Fiore et al. (2008) suggested that luminous highly obscured/CT AGNs, which are faint in the X–ray because of high column densities and cannot be selected using their X/O ratio, can be recovered using their MIR/O ratio. Therefore, potentially, in the evolutionary framework, we may be able to select sources in the prelude, or at the beginning, of the blow-out phase.

In the following, we refer to these sources as MIRO targets, as per their high MIR/O flux ratio, and using their MIPS catalogue ID from the COSMOS Spitzer catalogue (Le Floc'h et al. 2009). The main aim of the SINFONI observations, besides the spectroscopic determination of the redshifts of the targets, is to compare the physical properties of the sources selected in different ways (MIR/O vs. X/O) and assess the presence of ionised outflows in line features. Targets selected with a simple MIR/O ratio cut are usually known in the literature as dust-obscured galaxies (DOGs, Dey et al. (2008); see also Riguccini et al. (2011, 2015) for a complete discussion on the DOGs population in COSMOS). In the last section, we compare our results with a compilation of a few DOGs sharing similar properties, e.g. redshift and $24\mu m$ flux.

The Chapter is organised as follows: Sect. 2 presents the sample selection and the ancillary data collected for our MIRO targets; Sect. 3 outlines the VLT observations and data reduction; Sect. 4 exposes the spectroscopic analysis. Sect. 5 presents proof of ionised outflowing material in the X–ray source MIRO20581 and discusses the energetic output associated with the outflow and, finally, we summarise our results and the implications in Sect. 6.

## 4.2 Sample selection

Figure 4.2 shows the mid-infrared to optical flux ratio $f_{24\mu m}/f_R$ versus the (R-K) colour diagnostics diagram proposed in Fiore et al. (2008), applied to the MIPS-selected sources in the COSMOS field (Fiore et al. 2009). The green isodensity contours show the distribution of the full sample of MIPS-selected sources in the COSMOS GO3 data (Le Floc'h et al. 2009) and with associated optical and

---

$= 23-24$ cm$^{-2}$), and CT AGNs (with $\log(N_H) > 24$ cm$^{-2}$).

Table 4.1: MIRO/SINFONI sample: selection properties & log-file of observations

| MIRO (1) | RA (2) | DEC (3) | $z_{phot}$ (4) | R AB (5) | K AB (6) | $f_{24\mu m}$ mJy (7) | R-K Vega (8) | MIPS/O (9) | band (10) | Guide Star (name) (11) | expo (min) (12) | $z_{spec}$ (this work) (13) |
|---|---|---|---|---|---|---|---|---|---|---|---|---|
| 18744 | 10:01:52.2 | 01:56:08.6 | $0.97^{a}$ | 22.8 | 19.6 | 2.08±0.03 | 4.90 | 780 | J | Hip037044 | 50 | 0.97 |
| 10561 | 09:59:43.5 | 01:44:07.6 | 1.54 | 24.6 | 21.4 | 1.70±0.06 | 4.80 | 3090 | J,H | Hip040661 | 50,50 | 1.43 |
| 28704 | 10:01:45.9 | 02:28:53.8 | 1.74 | 26.3 | 21.6 | 1.63±0.02 | 6.35 | 14800 | HK | Hip046054 | 30 | 1.64 |
| 20581 | 10:00:00.6 | 02:15:31.1 | 2.09 | 25.3 | 22.6 | 1.47±0.02 | 4.35 | 5180 | HK | Hip046054 | 80 | 2.45 |
| 18433 | 10:01:44.8 | 01:55:55.8 | 2.59 | 24.6 | 21.6 | 0.44±0.02 | 4.75 | 880 | HK | Hip044598 | 120 | — |

Notes: (1) target name; (2) right ascension; (3) declination; (4) photometric redshifts available prior to the SINFONI observations; (5) and (6): R- and K-band magnitudes; (7) MIPS 24$\mu m$ flux; (8) R-K colour; (9) MIPS 24$\mu m$/O flux ratio; (10) SINFONI filters; (11) guide star name; (12) total integration time on target for each band; (13) spectroscopic redshift.

[a] Spectroscopic redshift available from Magellan IMACS spectrum.

Table 4.2: main properties of the MIRO/SINFONI sample

| MIRO (1) | $N_H$ $10^{23}$ cm$^{-2}$ (2) | log($L_{2-10}$) erg s$^{-1}$ (3) | log($L_{5.8}$) erg s$^{-1}$ (4) | log($L_{bol}$) erg s$^{-1}$ (5) | $S_{radio}$ $\mu$Jy (6) | $q_{24}$ (7) | $M_*$ $10^{11}M_\odot$ (8) | SFR $M_\odot$/yr (9) | log($R_{SB}$)$^{b}$ (10) | E(B-V)$_{host}$ (11) | E(B-V)$_{AGN}$ (12) |
|---|---|---|---|---|---|---|---|---|---|---|---|
| 18744 | $2.4^{+7.5}_{-1.3}$ | 43.82 | 44.85 | 45.11 | 424±28 | 2.3 | 2.0 | 99 | 0.2 | 0.5 | 2.7 |
| 10561 | $2.9^{+1.8}_{-1.3}$ | 43.96 | 45.35 | 45.97 | 72±15 | 0.4 | 1.5 | 196 | 0.3 | 0.7 | 4.0 |
| 28704 | — | — | 45.32 | 47.63 | 154±25 | 2.0 | 0.6 | 11(<25)$^{a}$ | -0.8(<-0.5)$^{a}$ | 0.5 | 4.1 |
| 20581 | $6.8^{+3.0}_{-2.1}$ | 45.00 | 45.89 | 46.61 | 5430 ±60 | -0.6 | 1.9 | 48(<132)$^{a}$ | -0.6(<-0.2)$^{a}$ | 0.6 | 2.0 |

Notes: (1) target name; (2) column density; (3) intrinsic X–ray luminosity; (4) rest-frame 5.8$\mu m$ luminosity; (5) bolometric luminosity; (6) rest-frame 1.4 GHz flux; (7) $q_{24obs} = log(f_{24\mu m}/f_{1.4GHz})$ (Bonzini et al. 2013); (8) stellar mass; (9) star formation rate; (10) starburstiness, defined as the ratio between the specific star formation rate (sSFR=SFR/M$_*$) and that expected for main-sequence galaxies at given computed stellar mass and spectroscopic redshift (sSFR$_{MS,z}$), according to the relation of Whitaker et al. 2012; (11) galaxy reddening ; (12) AGN reddening.

[a] Values in the parenthesis refer to measurements constrained using upper limits in the FIR SED (see Figure 4.5).

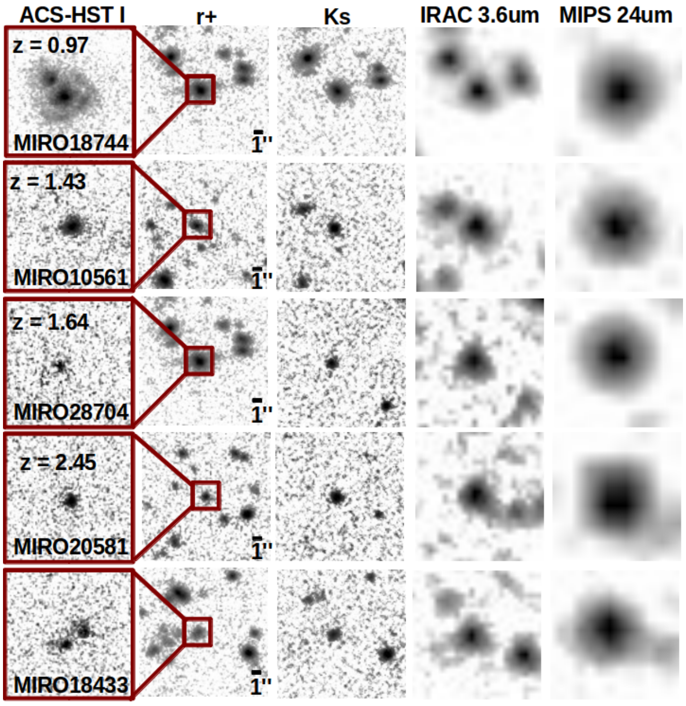

Figure 4.2: From left to right: ACS-HST I, r+ SUBARU, Ks COSMOS, IRAC 3.6 $\mu$m, MIPS 24 $\mu$m band cut-outs of the five MIRO targets. The target name, position, angular scale, and redshift derived from the SINFONI data are also labelled. For display purposes, 3″ × 3″ ACS-HST cut-outs show the regions in the red boxes superimposed on the r+ panels.

K-band counterparts ($\sim$ 15000 sources), while the black crosses are the sources detected at fluxes larger than 1 mJy at $24\mu m$ ($\sim$ 550). The box in the top right corner in the colour-colour space, delimited by vertical solid line and horizontal dashed line, marks the region where CT AGN are expected in more than 60% of the MIPS-selected sources (cell A in Fiore et al. 2009). All the sources above the horizontal dashed line are instead usually referred to as DOGs in the literature.

From the Le Floc'h et al. (2009) MIPS selected sample, using SINFONI natural guide star (NGS) mode, we observed five targets marked as yellow stars in Figure 4.2 and listed in Table 4.1, with the fluxes in the R-, K-, and MIPS $24\mu$m band used for the selection. Three out of five are classified as DOGs (MIRO 10561, MIRO 28704, MIRO 20581) and two out of five are also in Cell A of Fiore et al. (2009; MIRO 10561, MIRO 28704)[2]. The main selection criteria, in addition to the high MIPS/O fluxes and red R-K colour, were the proximity to a bright AO star and a photometric redshift broadly in the range $z \sim 1-3$ so that rest-frame optical lines are redshifted in the SINFONI J, H, or K filters (four targets). In addition, for only one source (MIRO 18744) a spectroscopic redshift was available from the IMACS/Magellan follow-up of X–ray sources in the COSMOS field (Trump et al. 2007), and we proposed to observe its H$\alpha$+[N II] region with SINFONI (J band).

In Figure 4.2 we also show the $z \sim 2$ DOGs presented in Melbourne et al. (2011, cyan stars) and in Brand et al. (2007, cyan squares) for which K-band magnitude is available, and the two $z \sim 1.5$ dust-reddened type 1 sources presented in Chapter 2 (XID 2028 and XID 5321; blue symbols). The properties of these targets are discussed in Section 4.6, in order to compare our results with those previously reported in literature.

The ACS ($3'' \times 3''$), R-band, K-band, IRAC3.6$\mu$m, and MIPS ($15'' \times 15'$') cut-outs[3] of the five targets are shown in Figure 4.2. We also included the IRAC 3.6$\mu$m images to verify blending problems in the MIPS emission: for all but MIRO18433, we can safely say that the majority of the emission at $24\mu$m is correctly associated with the K-band and optical counterpart (e.g. our SINFONI targets), and that the observed colours do not suffer from bad photometry. MIRO18744 may show evidence for an ongoing merger: tidal tails and double nuclei are distinguishable in the ACS cut-out. MIRO18433, instead, presents two components in the ACS cut-out (last row of Figure 4.2), which are strongly blended at optical and infrared wavelengths and preclude an accurate SED fitting decomposition and a correct photometric redshift derivation. Indeed, it is the only source for which no spectral features have been detected in the SINFONI HK band in two hour observations (see Table 4.1) and the only one below the 1mJy flux limited sample (red circles in Figure ). For all the above reasons, MIRO18433 was excluded from the subsequent analysis.

### 4.2.1 Identikit via ancillary data

Previous works (e.g. Alexander et al. 2002; Donley et al. 2008) have demonstrated that red optical to near-infrared colours and high MIR-optical ratios can identify both AGN and star-forming galaxies. In the following, we briefly discuss the multi-wavelength properties of the SINFONI targets to assess which one among SF or AGN activity is the dominating process. We note however that all four of our targets have $f_{24\mu m} > 1$ mJy, and that the $24\mu$m emission is, on average, increasingly dominated by AGN contribution at higher $f_{24\mu m}$ (e.g., Brand et al. 2006; Dey et al. 2008). In the subsequent analysis (e.g. X–ray and SED fits), we made use of the spectroscopic redshift obtained from our SINFONI observations, as described in Sect. **??**.

---

[2] At the time of observations, all the targets were selected within the cell A. Differences from the current situation shown in Figure 4.2 are due to the fact that we now use an improved version of the COSMOS photometric catalogue (Laigle et al. 2016) in which the photometry is slightly changed. The colours in the figure are all related to the "total flux" measurements.

[3] The cut-outs are extracted from the public COSMOS cut-outs page: `http://irsa.ipac.caltech.edu/data/COSMOS/index_cutouts.html`

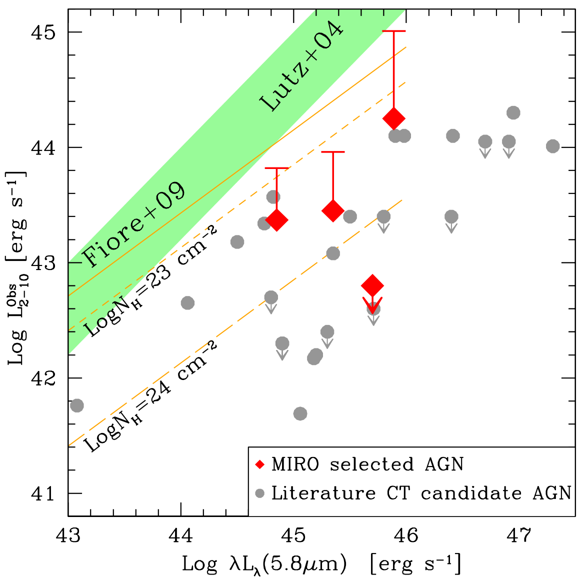

Figure 4.3: Log($L_X^{Obs}$ ) vs Log($L_{5.8\mu m}$) for several CT candidates. Grey circles represent literature CT candidate AGN (see Lanzuisi et al. 2015b for more details). Red diamonds represent our MIRO targets; intrinsic X–ray luminosities of the X–ray detected objects are also indicated with upper bars. The green shaded area is the relation of Lutz et al. (2004) for a sample of low-redshift, unobscured AGN. The orange solid line is the relation for high-redshift unobscured AGN (Fiore et al. 2009), while the dashed and long dashed lines are the expected relation for a $10^{23}$ cm$^{-2}$ and $10^{24}$ cm$^{-2}$ absorber.

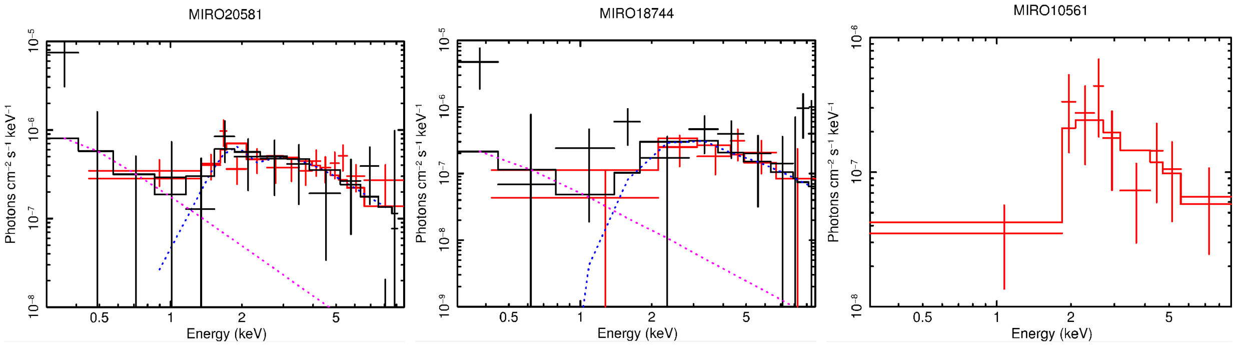

Figure 4.4: X–ray spectra of MIRO 20581 (left), MIRO 18744 (centre) from XMM and Chandra, and MIRO 10561 (right) from Chandra. The XMM (black) and Chandra (red) data of MIRO 20581 and MIRO 18744 are fitted with a double power law (as shown in the model components). The MIRO 10561 *Chandra* data are instead fit with a single absorbed power law.

1. *MIR-X–ray diagnostics.* The AGN intrinsic hard X–ray luminosity and the infrared luminosity re-emitted by the torus follow a tight correlation (Gandhi et al. 2009; Lutz et al. 2004). Figure 4.3 shows the distribution of rest-frame observed X–ray luminosity ($L_X^{Obs}$) vs. $L_{5.8\mu m}$ for several samples of CT candidate AGN[4] collected by Lanzuisi et al. 2015b (with the addition of XMM ID 5371; **Civano2015** ) and for our MIRO targets (red diamonds).
   For all of the sources, the rest-frame 5.8$\mu m$ luminosities were obtained using a simple power-law interpolation between the 24 and 8$\mu$m observed-frame luminosities. We computed the X–ray luminosities on the basis of the available XMM and *Chandra* data in the COSMOS field. More specifically, MIRO20581 and MIRO18744 are both detected in the X–rays, in the XMM-COSMOS (XID70135 and XID60205: **Cappelluti2007**; Brusa et al. 2010) and C-COSMOS (CID451 and CID401; Civano et al. 2012) surveys, while MIRO10561 is detected in the deeper COSMOS-Legacy survey (CID 3587 in the Civano et al. 2015 catalogue and Marchesi et al. in preparation). The remaining source, MIRO28704, is instead undetected down to a luminosity of $\log(L_X) \sim 42.8$ in the 2-10 keV band.
   The Lutz et al. (2004; green shaded area) and Fiore et al. (2009, orange solid line) relations represent the tight X–ray to mid-IR correlations found for the low- and high-redshift ($z > 1$) unobscured AGN, respectively. The Lutz et al. (2004) relation has also been confirmed recently at higher redshift by Mateos et al. (2015). These relations, however, have been calibrated at low luminosities, and require extrapolations to high luminosities (i.e. $\log(\lambda L_\lambda(5.8\mu m)) > 46$). A flattening of the MIR-Xray relation at the highest luminosities has been found by the recent work of D. Stern (2015). Assuming that both the hard X–ray and the infrared luminosities are related to the AGN activity (see below; Figure 4.5), and given that the mid-IR is largely independent of obscuration, a lower $L_X$ to $L_{5.8}$ ratio with respect to that observed for unobscured AGN suggests that the observed $L_X$ are affected by obscuration (e.g. D. Stern et al. 2014). All the MIRO sources lie below these relations at values consistent with the presence of a heavily obscured absorber: the long- (short-) dashed line in Figure 4.3 marks the $N_H = 10^{24}$ ($10^{23}$) cm$^{-2}$ locus, computed from the Fiore et al. relation. Therefore, the $N_H$ loci in the figure are computed with the most conservative approach: using the Lutz et al. relation, the dashed lines would be steeper than those obtained from the Fiore et al. Therefore, the intrinsic X–ray luminosity would be larger and, as a consequence, the $N_H$ needed to explain the observed luminosities of the MIRO targets would also be larger.

2. *X–ray spectra.* The X–ray spectra of the three X–ray detected MIR/O are shown in Fig. 4.4. Given the low photon statistics available for all the detected sources (in the range 20-150 net counts) we applied the Cstat statistic (Cash 1979) to the unbinned data and assumed a very simple model to recover a rough estimate of the nuclear obscuration and instrinsic luminosity: a power-law with photon index fixed to $\Gamma = 1.9$ plus obscuration at the source redshift (plus galactic $N_H$).

   In the XMM-detected sources, a second component is required by the data to model the soft emission. Indeed, as demonstrated in Lanzuisi et al. (2015b), given the complexity of the X–ray emission and the concurrent presence of other processes, such as scattering components or emission from star formation, heavily obscured AGN can be missed when fitting low-counting statistics data compatible with a single power-law model. For all these sources we derive column density of $N_H \approx 2.5 - 7 \times 10^{23}$ cm$^{-2}$ with high uncertainties (see Table 2). Although they are characterised by a high obscuration, the X–ray detected sources are not in the Compton Thick regime, as expected given current X–ray surveys limits and sensitivities (e.g. Georgakakis et al. 2010; Lanzuisi et al. 2009). The rest-frame intrinsic X–ray luminosities are also listed in Table 4.2. The most luminous of the three sources is MIRO20581 with an X–ray luminosity $\sim 10^{45}$ erg s$^{-1}$, while the other two sources have inferred intrinsic luminosities slightly below $10^{44}$ erg

---

[4] All the sources with upper limits to the X–ray luminosity have been preselected as AGN candidates using a variety of methods specifically designed to discriminate between SF and AGN galaxies.

$s^{-1}$. These luminosities exceed of about 2 dex those expected from stellar processes given the observed SFR (see below).

3. *SED fitting*: Figure 4.5 shows the SED fitting decomposition of the four targets considered in the paper, which were obtained making use of a modified version of the magphys code (da Cunha et al. 2008) designed to take into account a possible AGN emission component (Berta et al. 2013) and a modestly absorbed galaxy component. These targets have stellar masses in the range $0.6 - 2 \times 10^{11}$ $M_\odot$ and SFR of $10 - 100$ $M_\odot$/yr, and are in (or below) the main sequence (MS) of star-forming galaxies (see Whitaker et al. 2012), as suggested by their starbustiness, $R_{SB}$=sSFR/sSRF$_{MS,z}$ (see Table 4.2). For two sources, MIRO20581 and MIRO28704, the far-infrared emission is not well constrained (see Figure 4.5), hence, in the table SFR and $R_{SB}$ upper limits are also reported (in parentheses); these values were computed treating the FIR upper limits as real detections.

   In all cases the (observer frame) NIR emission is dominated by the host galaxy light and the AGN disk component suffers considerably extinction (E(B-V) $= 2 - 4$). According to the SED fitting decomposition, the 5.8$\mu$m luminosity is dominated by the torus emission ($\langle L^{torus}_{5.8\mu m}/L^{total}_{5.8\mu m}\rangle =$ 87%), in agreement with the results from the bright DOG sample presented in Riguccini et al. (2015). This also confirm that the X–ray to mid-IR diagnostic discussed above is a reliable instrument to test the X–ray obscuration of the MIRO targets.

   According to the criteria in Dey et al. (2008), who classified dust-obscured galaxies in AGN-dominated ("power-law" DOGs) and SF-dominated ("bump DOGs") on the basis of the rest-frame optical to mid-infrared SED shape (see their Section 3.1.2, and their fig. 5), all four MIRO targets would be classified as power-law DOGs, although MIRO 18744 appears to show intermediate characteristics between the two classes.

4. *Radio*: All the targets are also detected in the Very Large Array (VLA) observations of the COSMOS field (Schinnerer et al. 2010). Fiore et al. (2009) reported that QSOs selected on the basis of the MIR/O excess at z∼1.5 are more radio luminous than unobscured type 1 QSOs of similar luminosity and redshift, when the intrinsic 5.8 $\mu$m luminosities are compared (see also Martínez-Sansigre et al. 2005). MIRO20581 is the only radio loud target ($q_{24obs} = -0.6$, being $q_{24obs} = log(f_{24\mu m}/f_{1.4GHz})$; see Bonzini et al. 2013, Fig.2) in our SINFONI sample, with $L_{1.4GHz} = 4.5 \times 10^{25}$ W $Hz^{-1}$. MIRO20581 is also detected in the 3GHz survey of the COSMOS field (**Smolcic2015** ?) and is one of the most luminous sources in the Very Long Baseline Array (VLBA) COSMOS catalogue (**HerreraRuiz2015** ). The Jansky Very Large Array (JVLA) measurements for MIRO 20581, at 3 and 1.4 GHz, imply an inverted radio spectral index, which is consistent with a compact radio source rather than with a diffuse star-forming region. Indeed, we derive a SFR a factor of $10-40$ larger than the SED fitting estimate for MIRO20581 using the relation between the 1.4 GHz luminosity and the SFR introduced by Condon 1992. Therefore, the radio luminosity is interpreted as due to AGN activity. MIRO18744 and MIRO28704 are also detected in the VLBA catalogue and even in these cases, possible signatures of compact radio cores are present.

5. *High ionisation diagnostics*: For MIRO18744 a IMACS Magellan spectrum is available (Trump et al. 2007), sampling the rest-frame range 2850-4600 Å. The spectrum shows a prominent [NeV]3425 emission line, an unambiguous sign of obscured nuclear activity (Lanzuisi et al. 2015a; Mignoli et al. 2013).

The main properties of our SINFONI sample discussed above are reported in Table 4.2, with the targets sorted by decreasing MIPS flux and increasing redshift. Overall, the multi-wavelength constraints we have in our 24$\mu m$ bright SINFONI targets suggest unambiguously the presence of obscured AGN activity. These characteristics correspond to those expected for objects caught in the post-merger, dust-enshrouded phase of rapid black hole growth (see e.g. Fiore et al. 2008, 2009; Hopkins et al. 2008).

## 4.3 SINFONI observations and data reduction

The observations were obtained in service mode using the near-infrared spectrometer VLT SINFONI in AO-assisted mode, during period 92A (from 2013-12-28 to 2014-03-30). All the targets in the sample were observed in one or two of the SINFONI filters (J, H, K, or HK), depending on the initial redshift guess. We note that the program has only been partially executed ($\sim 45\%$) and, therefore, our targets have not been observed with all the requested filters and/or for the entire requested time. We used a field of view (FoV) of $8'' \times 8''$ in a 2D $64 \times 64$ spaxel frame. The spectral resolutions are R$\sim$1800 for J, R$\sim$2900 for H and R$\sim$1400 for HK.

We achieved a spatial resolution of 0.2" (FWHM) based on the point spread functions (PSF) obtained in NGS AO-mode, which roughly corresponds to 0.9 kpc at the average redshifts of z = 1.5. This spatial resolution is in agreement with those obtained in other SINFONI AO-assisted observations (e.g., Bouché et al. 2013; Cresci et al. 2009). Our targets do not extend more than $\sim 1 - 2''$ in diameter, and were therefore observed with on-source dithering in order to use the object exposure with the closest MJD as an approximation of a sky exposure. The information about the observations for each object are shown in Table 4.1.

Besides the objects of the sample, a set of standard stars and their respective sky frames were also observed to flux calibrate the data. Guide star names are also reported Table 4.1. The stars have R magnitudes in the range $15 < R < 16$.

We refer to the Sect. 3.3.2 for the description of the data reduction process.

## 4.4 Data analysis and spectral fits

Here, we briefly discuss the general data analysis and results of the spectral fits. In the following sections, we describe the more detailed spatially resolved analysis for our best case, MIRO 20581.

Figure 4.6 shows the one-dimensional integrated spectra, extracted in a $1 - 2''$ diameter aperture, according to the compactness of the source. H$\alpha$+[N II] complex is detected in each target, with the exception of MIRO 28704, for which the low quality spectrum allow the detection of the only H$\alpha$ emission[5]. [O III] feature is detected only in MIRO 20581. Such line is not covered by the SINFONI spectra of two out three other sources, because of the incompleteness of the observations (MIRO 28704; see Sect. 4.3) and the wavelength coverage of the instrument (MIRO 18744; [O III] expected at $\lambda_{obs} \approx 0.986 \mu m$). For MIRO 10561, both [O III] and continuum emission in the vicinity of oxygen line (redshifted in the J band) are not detected.

We simultaneously fitted each of the emission lines (from only one, H$\alpha$ in MIRO28704 to a total of six, H$\beta$, [O III] doublet, [N II] doublet and H$\alpha$, for MIRO20581) with Gaussian line profiles. When more than one emission line is detected, we constrained the centroids and the line flux ratios according to atomic physics, while the widths were fixed to be the same as each emission line (see Sect. 2.4.1).

As in Chapter 2, we chose as spectroscopic redshift the one which produces the best-fit of the narrow components of the emission lines. We report a redshift of 0.97 for MIRO18744, consistent with the redshift already available from the Magellan spectrum. For the remaining three sources, we are able to assign, for the first time, a spectroscopic redshift from our line fit (see column 13 in Table 4.1).

---

[5] The narrow feature at $\lambda \approx$6584 $\mathring{A}$ is associated with a wrong skyline subtraction. We discard the possibility that the observed line is HeI$\lambda$10830 at z = 0.6. We fitted the SED imposing this redshift. This fit produced a significantly larger Chi square, four times the value obtained imposing z = 1.64. Indeed, at z = 0.6 the source would be undetected down to a luminosity of log(L$_X$ )$\sim$ 42.2 in the 2-10 keV band; with a bolometric luminosity estimated by this SED fitting decomposition of log(L$_{bol}$) = 45.3, MIRO28704 would have a very unusual bolometric correction of the order of k$_{bol}$=L$_{bol}$/L$_X$ > 1000.

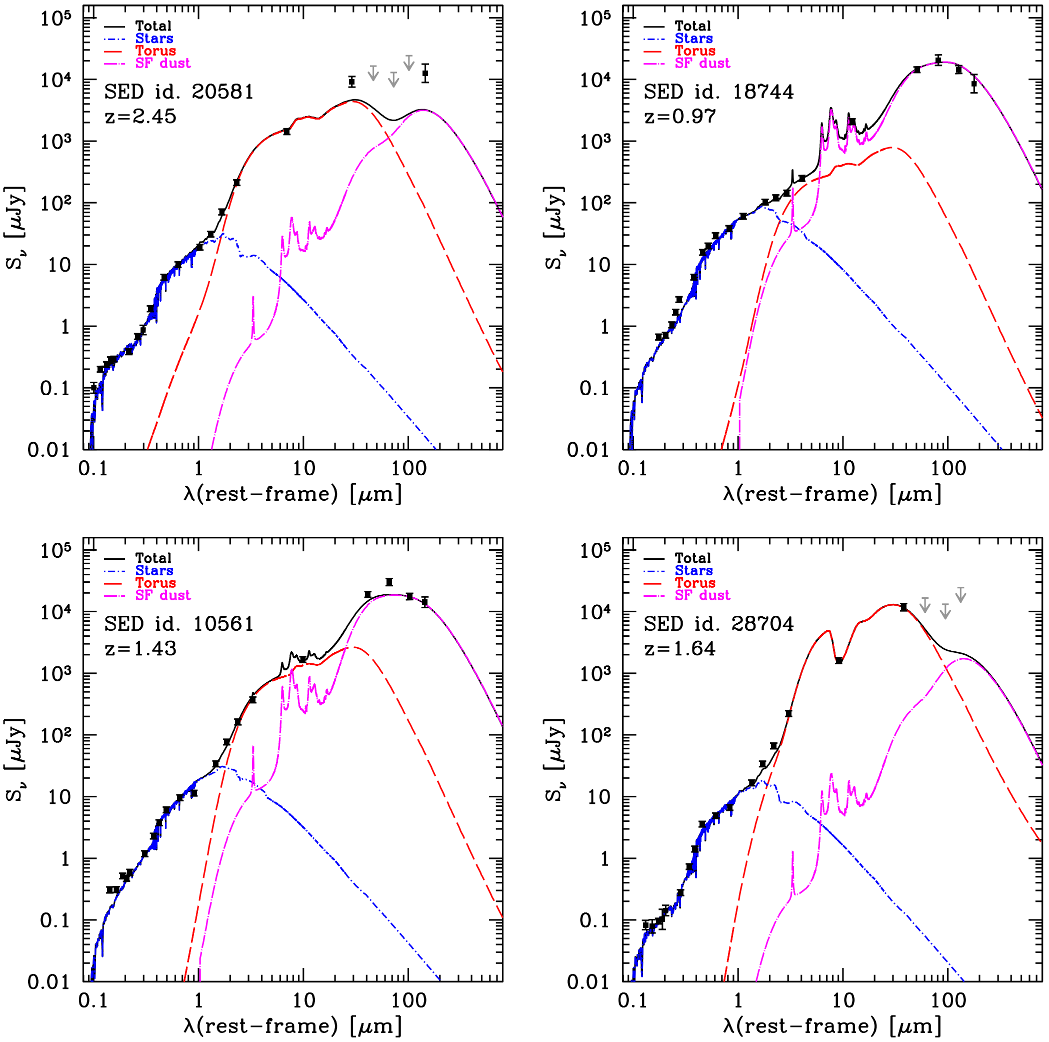

Figure 4.5: SED fitting of MIRO targets. The black dots represent the observed data points (in each panel, from left to right: SUBARU U, B, g, V, r, i, z; VISTA Y, J, H, and Ks; the four Spitzer IRAC bands, Spitzer MIPS24; Hershel PACS, and SPIRE). The blue line shows the integrated extincted emission originating from the host galaxy. The magenta line represents the star formation contribution for dust absorption, partially redistributed across the MIR/FIR range in a self-consistent way (Berta et al. 2013; da Cunha et al. 2008; Delvecchio et al. 2014). The red line reproduces the AGN contribution and incorporates both the accretion disc and torus emission. The black solid line represents the sum of all components.

setup[subfigure]labelformat=empty

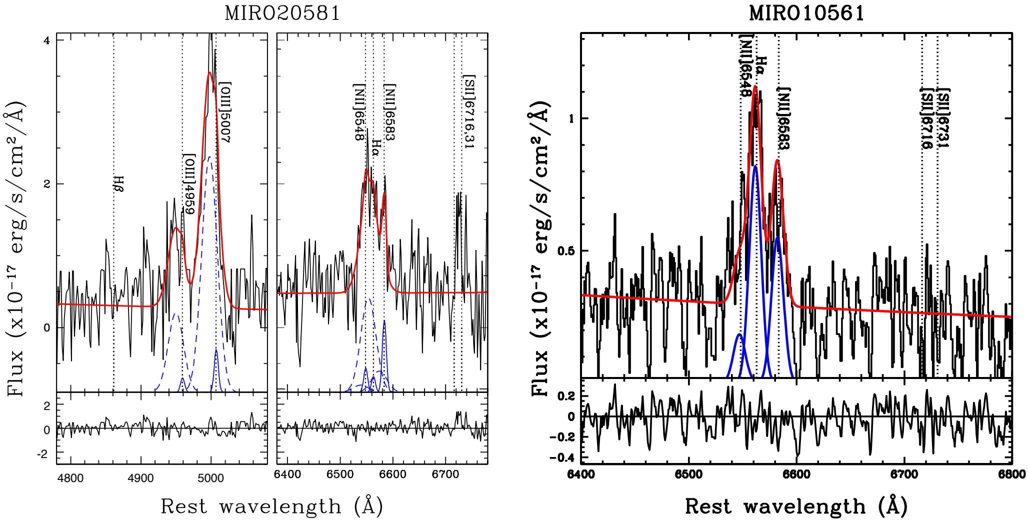

(a) a (b) b

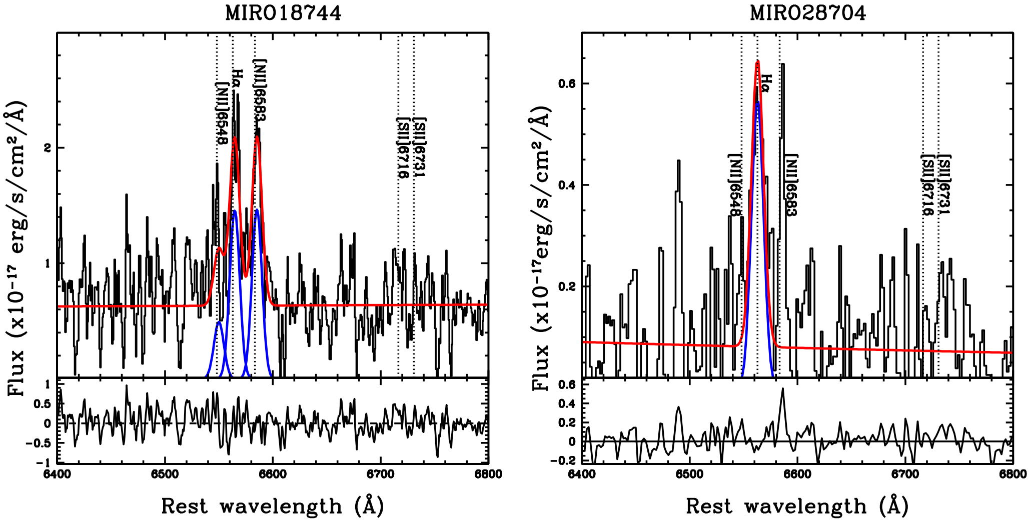

(c) c (d) d

Figure 4.6: **(a)** MIRO20581 HK-band spectrum around the [O III] (left) and the H$\alpha$+[N II] complex (right). Superimposed on the spectrum are the best-fit components (solid and dashed blue curves, with arbitrary normalisation to ease the visualisation). The red solid curves represent the sum of all components, including the power law. Dotted lines mark the wavelengths of the H$\beta$, [OII] doublet, H$\alpha$, [N II], and [SII] doublet. **(b)** MIRO 10561 H-band integrated spectrum around the H$\alpha$+[N II] complex.**(c)** MIRO 18744 J-band integrated spectrum around the H$\alpha$+[N II] complex.; **(d)** MIRO 28704 HK-band integrated spectrum around the H$\alpha$+[N II] complex. See (a) for the description of superimposed curves in (b), (c), and (d) panels. In the bottom panel of each fit, the residuals with respect to the best fit are shown.

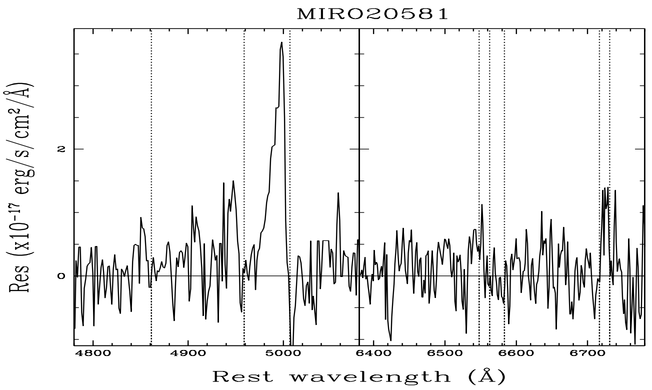

Figure 4.7: MIRO20581 residuals in the [O III] and H$\alpha$ range obtained by fitting the observed lines with only NLR and BLR components (See Section 5; to be compared to Panel a of Figure 4.6).

Table 4.3: Emission line properties in the integrated spectra

| MIRO (1) | (2) | $f_{H\alpha}$ (10$^{-17}$ erg/s/cm$^2$) (3) | $f_{[OIII]}$ (4) | $\log(f_{[NII]}/f_{H\alpha})$ (5) | $\log(f_{[OIII]}/H\beta)$ (6) | FWHM (km/s) (7) |
|---|---|---|---|---|---|---|
| 18744 | | 32.4±4.9 | - | 0.12±0.08 | - | 565±20 |
| 10561 | | 11.8±1.3 | - | -0.10±0.07 | - | 560±25 |
| 28704 | | 9.4±1.9 | - | - | - | 430±100 |
| 20581 | NC | $4^{+3}_{-2}$ | $2.5^{+2.5}_{-1.5}$ | $0.88^{+0.30}_{-0.24}$ | $> -0.47$ | 360±70 |
| | OC | 43.5±14.8 | 95±6 | -0.16±0.51 | $> 0.47$ | 1600±100$^{b}$ |
| | NC$^{a}$ | $4^{+3}_{-2}$ | $2.5^{+2.5}_{-1.5}$ | $0.55^{+0.30}_{-0.65}$ | $> -0.47$ | 370±75 |
| | OC$^{a}$ | 24±13 | 95±6 | -0.28±0.6 | $> 0.47$ | 1600±100$^{b}$ |

Notes: (1) target name; (2) kinematic component: NC = narrow component, OC = outflow component; (3) H$\alpha$ flux; (4) [O III] flux; (5) diagnostic [N II]/H$\alpha$ flux ratio; (6) diagnostic [O III]/H$\beta$ flux ratio; (7) kinematic component width.

[a] These results were obtained following the second approach illustrated in Sec. 4.5, adding a BLR component for the H$\alpha$ profile.

[b] The centroid of the OC profile is blueshifted ∼ 550 km/s.

The values are in general agreement with the photometric estimates available within the COSMOS survey (Ilbert et al. 2009; Salvato et al. 2011), with an accuracy of $|z_{phot} - z_{spec}|/(1 + z_{spec}) \lesssim 0.1$. The results of the emission line fits are reported in Table 4.3.

To investigate the nature of the ionising source, we derive emission line ratios diagnostics [N II]/H$\alpha$ and [O III]/H$\beta$. MIRO 20581 is the only source for which both [N II]/H$\alpha$ and [O III]/H$\beta$ ratio are available to classify the source according to the BPT diagostic (see Appendix A.5); this source lies in the AGN photo-ionisation region. For two out three of the remaining sources, although with large uncertainties due to low-quality spectra, we derive [N II]/H$\alpha$ ratios consistent with an AGN origin (Veilleux and Osterbrock 1987), in agreement with the classification discussed in Section 2.1. All the derived diagnostic line ratios are reported in Table 4.3.

## 4.5 The ionised outflow in MIRO20581

We now concentrate on MIRO20581. To reproduce the line profiles in the [O III] and H$\alpha$ region we had to introduce an extra blueshifted and broad (FWHM ≈ 1600 km/s) component (see Figure 4.6, panel *a*). Broad H$\alpha$ profiles may be ascribed to the presence of ionised outflowing gas (e.g. Genzel et al. 2014); however, the nuclear H$\alpha$ emission may suffer from severe contamination by the presence of the BLR motion and therefore may be considered a less reliable tracer of outflows and the associated energetics. This is especially the case when high-velocity BLR wings are not detected, possibly because of low S/N, and it is therefore difficult to discriminate between a BLR emission and outflow components at lower velocities (i.e., out to $\approx 1000 - 2000$ km/s in velocity space, to be compared to $> 3000$ km/s more typical for BLR wings).

To investigate the ionised gas emission in MIRO20581 at best, and taking the considerations above into account, we simultaneously fitted the H$\beta$+[O III] and H$\alpha$+[N II] regions (see Section 4.4 for details) using two approaches. To reproduce the line profiles of all the emission lines, we fitted the two regions

1. with two sets of Gaussian profiles: one to account for the presence of narrow components (NC), with FWHM$\lesssim$550 km/s, and one for the presence of outflow components (OC; see Sect. 2.4.1), with FWHM>550 km/s;

2. using the same components as above, namely the NC and OC components, and adding a broader profile (the BC component, with FWHM$\gtrsim$1900 km/s) to account for the presence of the H$\alpha$ emission originated in the BLR.

The two fits have acceptable low residuals and adequately represent the shape of the line profiles, hence, it is not possible to confirm or exclude the presence of the BLR emission in this source, at least with this S/N. The results of these two approaches are reported in Table 4.3. If present, the H$\alpha$ BLR emission would have a FWHM of about 2500-3000[6] km/s. The NII/H$\alpha$ ratio depends on the detailed modelling but, in both cases, the emission lines remain in the AGN photo-ionisation region (see previous Section).

We performe an additional tentative fit with a different combination of Gaussian profiles, using only NC and BLR components. A visual inspection of the H$\alpha$ region shows how it is possible to obtain good residuals even with this approach (Fig. 4.7): the residuals are comparable with those obtained with the first approach (see Fig. 4.3, panel a). We note that such tentative fit marks the blue emission in the [O III] profile, which require prominent OC to be modelled.

### 4.5.1 Spatial analysis

Figure 4.8, panel *a* shows the contour plot of the median SINFONI datacube in steps of $1\sigma$ starting from $3\sigma$ over the entire HK wavelength range (green scale). The standard deviation $\sigma$ was computed in a $1.25 - 1.75''$ annulus centred on the target. The astrometry in the SINFONI datacube was performed using the Ks COSMOS cut-out, obtaining a match between the coordinates of the peak of intensity in the Ks COSMOS cut-out and in the median SINFONI datacube. In the figure, the Ks COSMOS contours are over-imposed on the SINFONI datacube (cyan solid curves). We also show the HST/ACS F814W contours at higher resolution (magenta curves; see also Figure 4.2).

Figure 4.8, panel b shows the [O III] map integrated on the continuum-subtracted total line profile (grey scale) with over-imposed contour levels (starting from 3 $\sigma$) of the emission of the line core ($5000 - 5014\AA$) and of the blueward part ($4973 - 5000\AA$) of the line profile. Blueshifted emission is found out to a distance of $R = 0.6''$ (associated with region B), i.e. 4.8 kpc from the nucleus. Instead, the core emission is less extended and could be associated with the narrow component of the [O III] profile.

### 4.5.2 Kinematic analysis

To map the line emission distributions and corresponding velocities, following the method we applied for the brightest X-Shooter sources XID 2028 and XID 5321 (Fig. 2.14), a nuclear and an off-nuclear spectra are extracted from two $3 \times 2$ spaxel regions ($\approx 3 \times 2$ kpc) close to the central and off-nuclear peaks in the [O III] channel map (Fig. 4.8, panel *b*, regions A and B labelled with black boxes; see

---

[6] The lower value has been obtained fitting the entire H$\alpha$+[N II] profile with only one Gaussian.

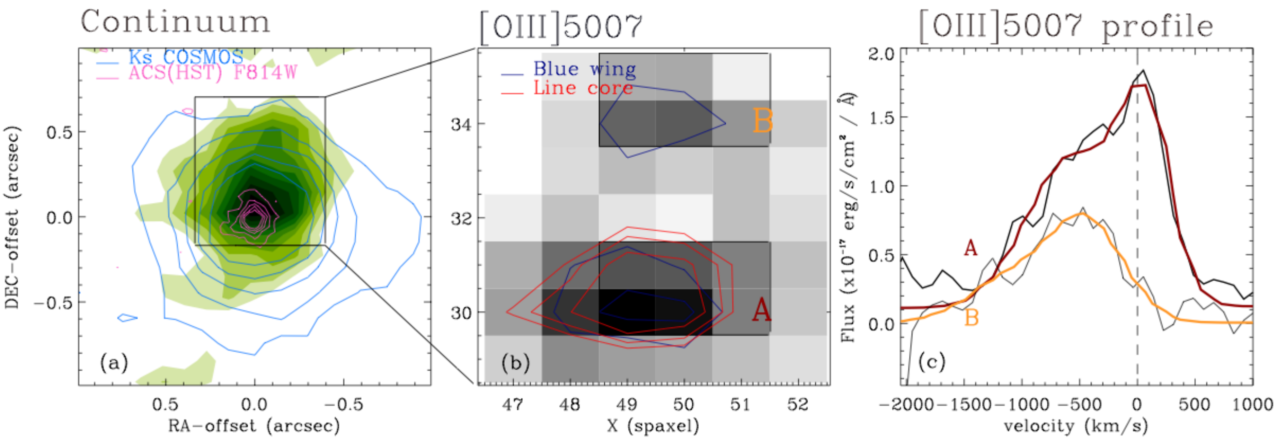

Figure 4.8: *(a):* MIRO20581 contour plot of the median SINFONI datacube over the entire HK wavelength range (green scale, in steps of 1 $\sigma$ starting from 3 $\sigma$), with over-imposed the Ks COSMOS (cyan; starting from 3 $\sigma$, in steps of 3 $\sigma$) and ACS HST contours (magenta; starting from 3 $\sigma$, in steps of 3 $\sigma$). *(b):* [O III]5007 channel map obtained integrating the continuum-subtracted SINFONI datacube on the total line profile (4973-5024 $\AA$) of the region selected in panel (a). The contours levels are in steps of 1 $\sigma$ (starting from 3 $\sigma$) and show the [O III] emission coming from the core (5000-5014 $\AA$) and from the bluer ($4973-5000\AA$) part of the line profile. *(c)*: [O III] line profiles obtained from integrated spectra over the spaxels selected in the two regions A and B in panel (b). Vertical dashed lines represent the systemic velocity obtained from the 1″ integrated spectrum.

also Cresci et al. 2015a). In Figure 4.8, panel (c) we show the integrated spectra over the two regions: red and orange solid lines represent the nuclear and off-nuclear line profiles, respectively.

In both cases, the [O III] profiles are broad, with FWHM = 1400 − 1200 km/s, and maximum velocities of 1600 − 1650 km/s (nuclear and off-nuclear spectrum). In the off-nuclear region, the emission line centroid is blueshifted ∼700 km/s.

### 4.5.3 Outflow properties

Assuming that the shifted [O III] component can be associated with an outflowing wind, the kinetic power ($P_K^{ion}$) and mass-outflow rate ($\dot{M}_{out}^{ion}$) of the outflow can be computed under reasonable assumptions in the case of a biconical geometry, following the prescription yet introduced for XID 2028, XID 5321 (Chapter 2) and XID 5395 Chapter **??** . For MIRO 20581, the electron density of the outflowing gas cannot be estimated directly from the data because of the low quality spectra in the [SII] region (see Figure 4.6), while the metallicity indicators (Pettini and Pagel 2004; Yin et al. 2007) are not useful because of the AGN ionising radiation; we therefore assume standard values of $n_e$ (100 cm$^{-3}$) and metallicity (solar). The [O III]5007 flux associated with the outflow component in the 1″ integrated spectrum (Figure 4.6, panel *a*) is used to estimate the luminosity of the outflowing gas. We further adopt a spatial extension of 4.8 kpc for the outflowing gas (see Figure 4.8, panel *b*). Finally, we considered as outflow velocity the maximum velocity observed $v_{max}$ in the nuclear region ($v_{out}$ = 1600 km/s; see Sect. 4.5.2), assuming that lower velocities are due to projection effects (Cano-Díaz et al. 2012; Cresci et al. 2015a).

We derive a kinetic power $P_k^{ion}$=1.5× 10$^{44}$ erg s$^{-1}$ and an outflow mass rate $\dot{M}_{out}^{ion}$=190 M$_\odot$ yr$^{-1}$, consistent with the values observed for targets at similar bolometric luminosities Carniani et al. 2015. The values, not corrected for extinction and only regarding the ionised component of the outflow ( see ...), represent lower limits to the total outflow power and mass rate.

The kinetic power is ≈ 0.4% of the AGN bolometric luminosity also inferred from the SED fitting decomposition, in rough agreement with the results we obtained in the previous Chapters (see Sect. 3.5.1).

## 4.6 Discussion

We analysed the NIR SINFONI spectra of four candidate obscured QSOs, selected from the COSMOS survey on the basis of red mid-infrared to optical and optical to near-infrared colours.

Broad profiles in the [O III] and H$\alpha$ lines with FHWM $> 550$ km/s (OC component), which are commonly used as signposts of outflows, have only been detected in one source, MIRO20581. We cannot exclude the presence of faint OC components in the other sources, given the low quality of the spectra and lack of information regarding the [O III] emission, which is a better optical tracer for outflows. Overall, the integrated spectra of the other three sources have low S/N (with emission lines detected at $\sim 3\,\sigma$) and faint outflow components in the H$\alpha$+[N II] could still be present. Alternatively, the high obscuration of the sample, as established via the SED decomposition, the X–ray spectra, and the X–ray to mid-IR ratios (see Section 4.2.1), might suggest that these sources are in the rapid black hole growth phase, an epoch at which the scaling relations between host galaxies and black hole properties are not yet established and winds have not yet been launched (A. King 2005). If it is the case, MIRO20581 is different from these other three sources. We investigate this scenario in the following section.

### 4.6.1 Comparison with literature

In this section, we compare the properties of our MIRO targets with those of a sample of AGN-dominated DOGs reported in the literature and discuss their main similarities and differences. Several studies have shown that DOGs with large $f_{24\mu m}$ flux ($\gtrsim 1$ mJy) exhibit higher AGN activity, higher concentration, and smaller physical size. Vice versa, DOGs with lower $f_{24\mu m}$ exhibit higher SF activity and larger physical size (Melbourne et al. 2011; Riguccini et al. 2015). Although it is shown that the rest-frame optical morphologies of the most luminous DOGs have little sign of ongoing mergers (Bussmann et al. 2009; Melbourne et al. 2009, 2008), there are also indications of non-regular gas kinematics in their host galaxies (Melbourne et al. 2011) and, moreover, several arguments suggest that they could be post-merger products of gas-rich mergers (see e.g. Melbourne et al. 2009). Merger simulations were able to reproduce their colours and luminosities and indicate an infrared to optical drop as gas consumption and AGN-driven wind terminate both SF and BH growth (Narayanan et al. 2010).

Brand et al. (2007) studied NIR Keck spectra of a sample of ten AGN-dominated DOGs selected in the 9 deg$^2$ NOAO Deep Wide-Field Survey Boötes field (Jannuzi and Dey 1999). Most of their spectra have low S/N and it is not possible to rule out the presence of outflows in the observed emission lines, but a prominent broad (FWHM $\approx 1600$ km/s) [O III] profile was detected in one target, SST24 J1428+34. H$\alpha$ or H$\beta$ BLR have been found in 70% of them. Melbourne et al. (2011) instead presented a sample of four AGN-dominated DOGs with high spatial resolution Keck OSIRIS integral field spectroscopy. The sources were also selected in the Boötes field and the main selection criteria was the strong H$\alpha$ BLR detection in available NIR spectroscopic observations (e.g. from the same Brand et al. 2007 sample). They found that the BH masses of their sample are small for their host galaxy luminosities when compared with z $\sim 2$ and local unobscured AGNs (see their Section 5.1). Indeed, they did not find any evidence of outflows in the hosts, which corresponds with the above-cited predictions of A. King (2005)(da riferirsi all'intro). They also reported SFRs $< 100\ M_\odot\ yr^{-1}$ for all targets. Finally, the Brusa et al. 2015 sample has been selected on the basis of red R-K colours (with a cut at K$_{AB} < 19$), and high X/O ratio. The latter selection criterion is roughly equivalent to the high MIR/O ratio (see Fiore et al. 2008). To confirm this, we added the two brightest sources (XID2028 and XID5321; Perna et al. 2015a) in the Brusa et al. 2015 sample in Figure 4.2 (with blue star and square), as representative of the entire sample. Evidence of outflows have been found in 75% of objects and a similar percentage of BLR emissions have been found.

Overall, all these sources have similar colours and MIR/O ratios to those of our MIRO targets (see Figure 4.2; cyan stars and squares represent the sources in Melbourne et al. 2011 and Brand et al. 2007 samples with K-band measurement). While BLR emission may be present only in one out four of our targets (MIRO20581; see Section 4.5), a large number of Brusa et al. 2015, Melbourne et al. 2011, and Brand et al. 2007 obscured QSOs exhibit BLR emission. However, as already mentioned, the Melbourne et al. 2011 targets were preselected to have a strong H$\alpha$ detection and, in general, all the targets in these three comparative samples have strong K-band emission (K$_{AB} \lesssim 20$): the Brusa et al. 2015 sample has been selected requiring a K$_{AB} < 19$; the Boötes field from which the Melbourne et al. 2011 and Brand et al. 2007 DOGs were selected, has considerably shallower NIR observations than the COSMOS field (K$_{AB} < 23$, McCracken et al. 2010; K$_{AB} < 20.8$, Dey et al. 2008, respectively). On the contrary, for the observations proposed in this work, we did not impose any flux threshold. Hence, it seems that the presence of BLR emission is related to the K-band flux. This offers a possible, simple interpretation. All these targets are AGN-dominated DOGs at z∼ 2; therefore, an higher K-band flux may correspond to a higher rest-frame optical AGN continuum emission, which is proper of AGN showing BLR emission. Vice versa, our sample, with K$_{AB} \gtrsim 20$, is dominated by rest-frame optical host-galaxy continuum emission (see Figure 4.5). The X–ray absorption is fully consistent with type 2 (or 1.9, in the case of MIRO 20581) classification obtained by the SINFONI spectra.

The only object in which we detected the outflow, MIRO201581, stands out with respect to the other targets. Although sharing the same X–ray luminosities of the Brusa et al. 2015 targets, the X–ray spectrum of MIRO20581 shows a high column density (N$_H \approx 7 \times 10^{23}$ cm$^{-2}$) that is larger than those observed for the X/O targets (N$_H \approx 10^{21.6}$ cm$^{-2}$, Perna et al. 2015a). This difference may be attributed mainly to line of sight effects, which intersect a larger portion of the torus in MIRO20581 with respect to the Perna et al. 2015a targets, and would also explain the fact that we do not detect a dominant BLR component in the H$\alpha$ in MIRO20581. Alternatively, the high extinction seen in the SED in both the AGN and host-galaxy components may be related to large scales obscurations.

Assuming that the H$\alpha$+[N II] complex of MIRO20581 is composed of NC, OC, and a BLR component, its black hole mass can be estimated using the Bongiorno et al. 2014 formula, assuming a FWHM of the H$\alpha$ BLR emission of 3000 km/s (see Section 4.5), log(M$_{BH}$/M$_\odot$)=8.4. Considering the stellar mass estimated by SED fitting decomposition (log(M$_*$/M$_\odot$)=11), we measure a central black hole to stellar mass ratio of the host of ∼0.002, comparable with the ratios of unobscured QSO at the same redshift (Bongiorno et al. 2014; Merloni et al. 2010). Hence, it seems that outflows are present only in sources for which the $M_{BH} - M_*$ relation has been fixed, in agreement with the predictions of A. King 2005.

From the comparison between L$_{bol}$ (Table 4.2) and the Eddington luminosity associated with the M$_{BH}$, we also infer a high Eddington ratio (L$_{bol}/L_{Edd} \sim 1$). All these properties (high Eddington ratio, high extinction, M$_{BH}$/M$_* \sim 0.002$) point towards the interpretation that MIRO20581 could be associated with the beginning of the blow-out phase. On the other hand, its SFR and starbustiness are low (but still within ±0.6 dex of the MS; see Table 4.2), indicating perhaps an advanced state of the ongoing process of negative feedback (see also Balmaverde et al. 2016). We underline that its FIR emission is not well constrained (see Figure 4.5); hence we calculated as upper limit a SFR = 132 M$_\odot$/yr, treating the FIR upper limits as real detections. A higher SFR, and consequently a higher sSFR, may be more consistent with the beginning of a blow-out phase in which the effects of feedback are still marginal and the SF is still occurring.

In the Narayanan et al. 2010 simulations, AGN-dominated DOGs appear after the peak of the star formation, and therefore not necessarily associated with Starburst phase, given that the time scales of the two processes are not the same. Indeed, results recently presented in Riguccini et al. (2015) showed that 50% of AGN-dominated DOGs detected by Herschel display sSFRs that place them in or above the MS, while the remaining 50% are below the MS, indicating perhaps an ongoing quenching of the star formation due to the AGN activity. In this scenario, small SFRs observed in dust-obscured, massive main-sequence galaxies hosting AGNs, such those of MIRO10561, MIRO28704, MIRO18744, and those presented in Melbourne et al. (2011), may be associated with systems that are still actively growing their black holes.

### 4.6.2 Outflows, starbursts, and luminous AGNs

Figure 4.9 shows the position of MIRO 20581 in the "starburstiness" ($R_{SB}$) versus stellar mass plane. MIRO 20581 is shown as a pink starred circle: from the host galaxy properties the source is below the main sequence.

Our recent works, presented in Chapter 2 and **??**, based on X-shooter and SINFONI follow-up observations of COSMOS red quasars at z$\sim$ 2, revealed the presence of galaxy-scale ionised outflow (extending out to $4-15$ kpc) in starburst systems (XID 5395) and in normal MS galaxies (e.g., XID 2028 and XID 5321). In Fig. 4.9 we plot the two luminous QSOs from the XMM-COSMOS sample with spatially resolved outflows as starred blue circles and the SB-QSO XID 5395 as a starred red circle. When considering all the luminous XMM-COSMOS sources with detected outflows altogether, XID5395, XID2028, XID 5321 and MIRO 20581 (and the other X-shooter sources with outflows; Fig. 2.2), all of them are in the massive tail ($M_* = 8\times10^{10} - 5\times10^{11}$ $M_\odot$) of the MS galaxy, but have clearly different star-forming properties, spanning the entire range from below to above the MS.

In Figure 4.9 we also plot, for comparison, a compilation of objects at z$=1-2$ for which spatially resolved spectroscopic data are available, $\sim$ 90 targets observed within various programmes (Contini et al. 2012; Genzel et al. 2014; Mancini et al. 2011: SINS (Spectroscopic Imaging survey in the Near-infrared with SINFONI), SINS/zC-SINF (the continuation of SINS in the COSMOS field), represented as triangles in the figure, MASSIV (Mass Assembly Survey with SINFONI in VVDS; green squares). In the starburstiness vs. stellar mass plot, XID 5395 lies in the same locus occupied by a sample of eight QSOs at z$\sim$ 2.5, originally selected as submillimetre galaxies, with kpc-scales outflow detected by NIR IFU data (Harrison et al. 2012; see Fig. 2.2). On the contrary, the only source from the galaxy sample with the same extreme host properties of XID 5395 (the triangle above the "starbursts" threshold in Figure 4.9, D3a-6397, reported in Genzel et al. 2014), shows a massive, rotating disk with no sign of outflow (see Cresci et al. 2009) or AGN activity, at least according to the BPT classification.

The fact that the outflow presence does not depend on the host galaxy properties (in particular the starburstiness), but is rather associated with the presence of AGN in massive systems corroborates the results reported in Förster Schreiber et al. 2014 and Genzel et al. 2014, based on the detailed analysis of H$\alpha$ emission in NIR stacked spectra of star-forming galaxies at z$\sim$ 2 (see also similar results for less luminous systems presented in Cimatti et al. 2013). Moreover, comparing XID5395 and D3a-6397 discussed above (e.g. both are starburst galaxies), we see a clear outflow in the galaxy with a strong AGN. This may be seen as further indication that the "starburstiness" can be a good method to select objects in the outflowing phase only when coupled with the presence of a luminous AGN. The luminous AGNs in which we detect the outflow in the individual spectra (starred symbols in Figure 4.9), with $L_{bol} > 10^{46}$ erg s$^{-1}$, are the tip of the iceberg of the overall population hosting AGN, and because they are more luminous they obviously show the features with higher statistics. Moreover, given that we were able to spatially map the [O III] emission instead of the H$\alpha$ region, our results are less affected by possible contamination from the BLR emission (see Fig. 4.7).

The outflow presence also does not seem to correlate with the nuclear obscuration revealed in the X-rays. The four XMM-COSMOS sources with detected outflows, selected in different ways, show column densities ranging from $N_H \sim 5\times10^{21}$ cm$^{-2}$ (mild obscuration) to $N_H \sim 5\times10^{23}$ cm$^{-2}$ (heavy obscuration; see also Harrison et al. (2016) for a lack of correlation of the outflows on the nuclear obscuration). The only common feature is a considerable extinction in the optical band (e.g. they are all classified as red/reddened AGN) and an intrinsic X-ray luminosity that is higher than $> 10^{44.5}$ erg/s. Although the high X–ray luminosity can be ascribed to a selection effect, all these sources show a contribution of the X–ray emission to the bolometric luminosity that is on average higher than that observed for classic blue quasars of similar bolometric luminosity; we measure $k_{bol}$ $\sim$10 for outflowing sources, while Lusso et al. 2012 reported $k_{bol} \sim 30$ for typical X-ray selected Type 1 QSOs of $L_{bol} \sim 10^{46}$ erg s$^{-1}$. Such low bolometric corrections (higher contribution of $L_X$ to $L_{bol}$) may be related to a balance of disk (directly related to $L_{bol}$) and corona (directly related to $L_X$) emissions that are different from what is observed in typical blue, unobscured QSO. This can in turn be ascribed to the very processes governing the accretion and ejection mechanisms of material in the accretion disk

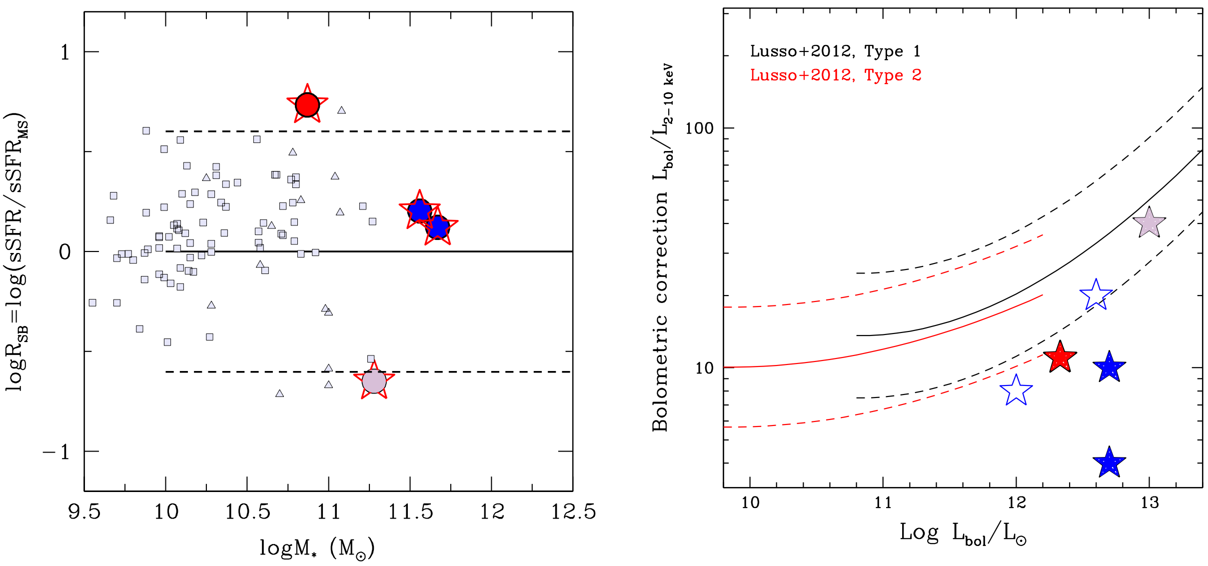

Figure 4.9: (*left:*) Logarithm of the starburstiness, $R_{SB}$, defined as the ratio of the sSFR to that expected for MS galaxies as parametrised by Whitaker et al. (2012), as a function of the logarithm of the stellar mass. XID5395 is the red star. We also plot, with starred symbols, two additional sources from XMM-COSMOS for which the outflows have been revealed: XID2028 at z∼ 1.6, from Cresci et al. 2015a, blue; and XID70135/MIRO20581 at z∼ 2.5 from Perna et al. 2015b, grey. Green squares are objects from the MASSIV survey Contini et al. 2012 in the redshift range z=1-2; yellow triangles are sources at z= $1-2$ in the Genzel et al. 2014 IFU sample. We also plot, with small grey triangles, all the other sources in the Genzel et al. 2014 samples in the redshift range z=$2-3$. The shaded red region indicates the range of sSFR and stellar mass of the targets in Harrison et al. 2012. (right:) X-ray bolometric corrections as a function of the bolometric luminosity for the same sources in the left panel, and for XID 175 and XID 18. The black and red curves represent the best-fitting relations obtained by Lusso et al. (2012) for type 1 and type 2 AGNs in the COSMOS field, respectively.

region during the short-lived wind phase.

## 4.7 Summary

The main results from the multi-wavelength analysis and the SINFONI data on the small sample of mid-infrared bright, red quasars we presented in this Chapter are as follows.

- All the sources but MIRO 28704, selected from the 24$\mu m$ Spitzer MIPS survey as candidate obscured QSO, are confirmed highly ($N_H \approx 2.5-7\times10^{23}$ cm$^{-2}$) obscured AGN from our detailed analysis. For MIRO28704, we only found indications of a CT nature (See Sect. 4.2.1).
- We successfully provided a spectroscopic redshift for three objects for which we had only a photometric estimate (see Sect. 4.3).
- We revealed the presence of a powerful ionised outflow extended out to ∼ 4.8 kpc in MIRO 20581. The large velocity (≈ 1600 km/s) and outflow mass rate (≈ 2000 $M_\odot/yr$) are not sustainable by star formation. The inferred Eddington ratio ($\lambda_{Edd} \sim 1$), together with its highly obscured nature, point towards the interpretation that this source may be caught in the blow-out phase.
- We collected several arguments that point towards the fact that luminous ($f_{24\mu m} > 1$ mJy) AGN-dominated DOGs may be objects in the transition phase between the post-merger starburst and

unobscured QSO phases. The occurrence of outflows seems to be associated with the end of the rapid BH growth, when the $M_{BH} - M_*$ relation has been already established (See Section 6.1).

- The efficiency of the mid-infrared to optical and optical to near-infrared colours selection criteria in detecting objects in the blow-out phase may be lower when compared to other selection criteria (e.g. Brusa et al. 2015; Glikman et al. 2007). This may be because higher obscuration could be associated with a still ongoing process of BH growth, preceding the blow-out phase (Fig. 1.10). To confirm this statement, however, higher S/N spectra are required. Since MIRO 20581 is the only target with outflow and an X–ray luminosity of $10^{45}$ erg $s^{-1}$ (see Section 2), we suggest that sources in the blow-out phase can be most efficiently isolated from shallow X–ray surveys rather than solely on their high MIR/O colours (see also Brusa et al. 2015);
- Although this proposal is still on the basis of a small sample, we propose that outflowing QSO may be associated with objects with a higher contribution of $L_X$ to $L_{\rm bol}$ than the average observed in typical blue, unobscured QSOs.

* * *

This material has been published in

- “SINFONI spectra of heavily obscured AGNs in COSMOS: Evidence of outflows in a MIR/O target at z $\sim$ 2.5 ”, by M. Perna, M. Brusa, M. Salvato, G. Cresci, G. Lanzuisi, S. Berta, I. Delvecchio, F. Fiore, D. Lutz, E. Le Floc’h, V. Mainieri and L. Riguccini; (2015) A&A, 583, 72.

and is based on observations undertaken at the European Southern Observatory, Paranal, Chile, under the programme 092.A-0884.

Chapter 5

# An X-ray/SDSS sample: outflowing gas characterization

## Abstract

We collect a large statistical spectroscopic sample of X-ray/SDSS AGNs at z<0.8 having a high signal-to-noise ratio in [O III]$\lambda$5007 line in order to study the faint wings of the emission profile associated with AGN-driven outflows. We derive the incidence of ionized and atomic outflows and relate the outflow velocity to AGN type, distinguishing between type 1 and type 2 AGNs, and different AGN power tracers. The relative incidence of redshifted and blueshifted outflows in different classes of AGNs unveil a clear disagreement with the unification model prediction. Furthermore, we show for the first time a well defined positive trend between outflow velocity and X-ray luminosity, as well as a significant correlation with [O III] luminosity. We also derive for the first time average values for the plasma properties of outflowing gas. Our results are favouring electron densities of the order of 1000 cm$^{-3}$. As a consequence, the outflow energetic estimates usually derived assuming standard ($N_e = 100$ cm$^{-3}$) might strongly overestimate the AGN impact on the host galaxy. Finally, we discuss our results regarding outflow incidence in cold and ionized phase and X-ray "loudness" in a context allowing two different stages for the feedback phase: an initial stage of the blow-out phase, characterized by dust obscuration and the presence of multiphase outflowing gas, and a later stage in which the line of sight has yet been cleaned and the cold component has been heated or exhausted.

## 5.1 Introduction

With the advent of high resolution, sensitive integral field spectrografohs (IFS) and millimetre interferometers, it is now possible to study in details the feedback phenomena, characterizing the galaxy-wide extension and the morphology of the ejected material as well as the masses and the energetics related to outflows (e.g., Cicone et al. 2014; Cresci et al. 2015a; Harrison et al. 2012, 2014). However, both the triggering feedback mechanisms and the physical processes responsible for the coupling between the AGN winds and the ISM resulting in outflows remain largely unknown. The full characterization of the AGN-host galaxy system is needed to discriminate between the details of various model realizations (Sect. 1.7): multiwavelength data are essential to derive nuclear and host properties, while synergies between major facilities (e.g., ALMA, NOEMA, SINFONI, MUSE) are required to study the multiphase wind/ISM interactions. In this respect, we note that spatially resolved measurements so far have been mostly limited to small/biased samples (see previous Chapters), and do not permit the exploration of a wide parameter space for the study of the feedback phenomena.

A different strategy is given by the analysis of large samples of spatially integrated spectra from

Sloan Digital Sky Survey (SDSS). In recent times, a number of studies have focused on the analysis of the kinematics of the [O III]$\lambda$5007 line with the main goal of inferring the presence of ionized outflows (**Komossa2008**; Bae and Woo 2014; Woo et al. 2016). By combining SDSS with multi-wavelength data sets, several constraints on the properties and the effects of such outflows can be derived, at least in a statistical sense. For example, Mullaney et al. (2013), combining SDSS data with radio luminosity ($L_{1.4GHz}$), found a strong correlation between $L_{1.4GHz}$ and the width of [O III], suggesting a connection between the presence of compact radio cores and the outflow phenomena (see also Zakamska et al. 2016b; see Woo et al. 2016 for a different interpretation). Other recent studies related the presence of outflows with star formation activity using several diagnostics from Herschel and Spitzer data (**Wylezalek2016**; Balmaverde et al. 2016), pointing to different conclusions regarding the role of AGN feedback. Despite some contradictory conclusions, all these works have shown that a large fraction of SDSS AGNs presents signatures of outflows in their ionized phase, from ∼ 20-40% to ∼ 50-70% depending on whether the objects are type 2 or type 1 AGNs (**VeronCetty2001**; Woo et al. 2016).

Moving to higher redshifts, our recent works in the framework of XMM-COSMOS survey (reported in Chapter 2, **??** and 4) have shown that, despite their spread in obscuration, host galaxies properties and radio emission, luminous obscured AGN at z ∼ 1.5 with evidence of outflows collected so far (∼10 sources), appear to be associated with systems with low X-ray $k_{bol}$ corrections (median $L_{bol}$ /$L_X \approx$ 10, to be compared with more typical ratios of ∼ 40 at the same median bolometric luminosity (Lusso et al. 2012, see Fig. 4.9)). In order to validate a connection between outflow phenomena and X-ray loudness, a systematic study of outflow signatures in X-ray selected samples is needed.

In this Chapter we present a large sample of X-ray selected AGN at $z < 0.8$, for which SDSS spectra are available. This sample permits an analogue to the analysis derived by previous works that combined optical spectroscopic analysis with radio and/or infrared wavelength bands and it extends the analysis for the first time to a X-ray selected sample. We present the X-ray/SDSS sample selection procedure and the results obtained from relevant optical diagnostics. We focus on the incidence of outflows that can be derived studying ionized and atomic features in optical spectra, which is crucial to better constrain the temporal lengths of the different AGN phases in the context of evolutionary models (Fig 1.10). We also derive the X-ray bolometric corrections for each X-ray selected AGN and test the role of X-ray activity in the context of the feedback phase. In the second part of this Chapter, we focus on the estimate of the electron temperature ($T_e$) and density ($N_e$) of the unperturbed and the outflowing ionised gas in the NLRs. Plasma properties of unperturbed NLR gas are nowadays well constrained to average $N_e$ of the order of $\approx 250 - 400$ cm$^{-3}$ and $T_e$ of $\sim 1.5 \times 10^4$ K. The physical conditions within the outflowing regions are instead mostly unknown, because of the faintness of the outflow wings of the emission lines involved in the diagnostics generally used to derive such information (see, e.g., **Rice2006**; De Robertis and Osterbrock 1986; Vaona et al. 2012). The knowledge of these properties is crucial because can reduce the actual uncertainties in the outflow energetics by a factor of ten, pointing to improve our understanding of the AGN outflow phenomenon and its impact on galaxy evolution.

The Chapter is organized as follows: in Section 5.2 we outline our sample selection procedure; in Section 5.3 we describe our multicomponent line fitting routine and the different emission line diagnostics. BPT diagrams are used to discriminate between star forming galaxies and AGNs among the X-ray selected sources. In section 5.5 we derive the outflow fraction for the total sample and for different subsamples comparing the results with standard Unified model predictions. In section **??** we test the if a X-ray loudness is actually associate with outflow phenomena. In section 5.7, temperature- and density-sensitive emission line ratio diagnostics are used to derive the electron density and temperature for both NLR and outflowing gas. Finally, we summarize our results and their implications in the Discussion section (Sect. 5.8).

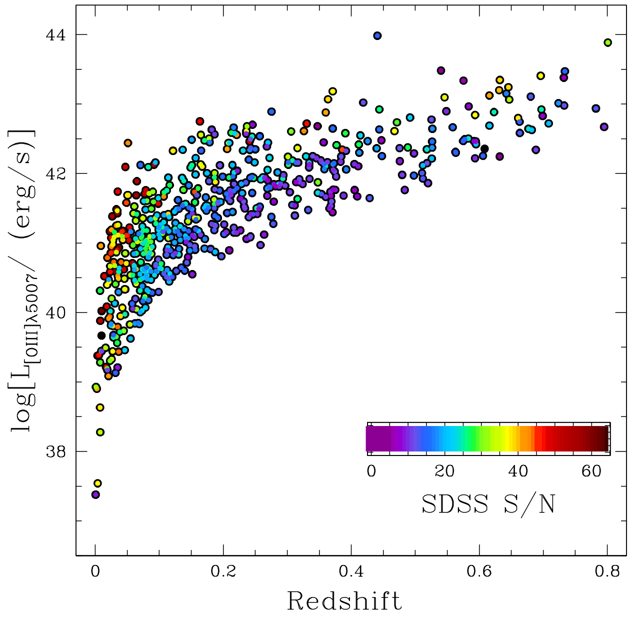

Figure 5.1: [O III]$\lambda$5007 total luminosity vs. redshift for the 624 candidate AGNs, colored by nominal SDSS signal to noise ratio as labelled in the colourbar.

## 5.2 Sample

We construct our AGN sample by analyzing SDSS Data release 7 (DR7) spectra associated with X-ray emission taking advantage from previous studies in which the identification of the X-ray emmitting sources with optical counterparts has been performed through accurate methods. In particular, we consider:

- the catalog compiled by **Georgakakis2011** obtained from the Serendipitous XMM Survey in the area of the SDSS (XMM/SDSS), containing 2067 X-ray point sources with spectroscopic observations from the SDSS DR7 (**Abazajian2009** );
- the **Jin2012** sample of 51 unobscured type 1 AGNs selected to have high-quality spectra from both XMM-Newton and the SDSS DR7;
- the **Wu2011** catalog, whose 1034 objects are identified by matching the *Swift* pointings with SDSS DR5 quasar catalog;
- the Trichas et al. (2013) catalog, containing 617 matched sources from the Chandra Source Catalog and the SDSS DR7 spectroscopic sample (CSC/SDSS) at z<0.4.

From this original sample of 3769 targets, we select the z < 0.8 galaxies, to include in the SDSS wavelength coverage the [O III] emission line. We exclude all sources with S/N in the [O III] region $\lesssim$ 10, in order to *i)* unveil and analyse the faint wings of the [O III] profile, *ii)* to exclude line-less galaxies, which are tipically red galaxies with no sign of AGN activity. After a final check for possible duplicates in the catalogs, we obtain a X-ray/SDSS sample containing 624 unique objects. Figure 5.1 shows the [O III]$\lambda$5007 and intrinsic $2 - 10$ keV X-ray luminosities (**da aggiungere**) plotted against redshift, color-coded according to increasing S/N of each SDSS spectrum.

The SDSS spectra are downloaded from the SDSS archive and re-analysed using our multicomponent fitting routine. X-ray properties are obtained from available spectral analysis results published by **Jin2012** and **Wu2012**. The **Georgakakis2011** subsample are re-analysed extracting the spectra from XMM archive, a applying standard spectral fit procedures with a simple or double power-law model to correct the luminosity for moderate absorption (**Lanzuisi2013** ). Finally, the X-ray information from the Trichas et al. paper are excluded from our current analysis because of severe disagreements between our optical analysis results and the quoted X-ray fluxes. We are currently re-analysing the Chandra spectra to obtain the missing X-ray information.

## 5.3 Spectral Analysis

### 5.3.1 Multicomponent simultaneous spectral fit

To characterize the nuclear accretion properties and determine kinematic and physical properties of the emitting gas in the NLR, we proceed applying the fitting prescriptions exposed in Sect. 2.4.1 and 2.4.1. For each target, we perform a simultaneous fit in the H$\alpha$ and H$\beta$ regions and derive non-parametric estimators for the [O III] line.

Figure 5.2 plots five examples of different types of sources found in our sample: blue ($a$) and red ($b$) spectra of type 1 AGNs, in which Fe II emission and/or BC could be present; low-luminosity type 1 AGNs which continuum is dominated by stellar emission ($c$); red spectra in which the same asymmetric profile is found in all optical emission lines and is therefore associated uniquely to OC, without clear sign of BLR Balmer emission ($d$); objects with double peaked emission lines, modelled with two NC emission together with an OC ($e$).

We note that, with respect to the source presented in the previous Chapters, these AGN spectra often present significant Fe II emission. As described in Appendix B, such emission is strongly blended with BLR H$\beta$ emission and the red wing of the [O III] line. As a result, in order to derive correct BLR profiles and non-parametric kinematics for the doubly ionized oxygen, an adequate modelling of the iron emission is required. We use theoretical model templates of Kovačević et al. (2010) to reproduce such emission. Two representative best-fit results showing strong blending with both [O III] and H$\beta$ lines are shown in Fig. C.2.

Through our own line fitting routine we found 441 broad line (BL) AGNs, comprising both type 1 and type 1.9 sources, and 165 type 2 AGN candidates. We excluded from any further analysis 7 [O III] double peaked galaxies[1], 5 red galaxies with high sky residuals at $\approx 5000\mathring{A}$ responsible for bad estimate of the S/N in the [O III] region, and 6 galaxies with strong and complex stellar continuum in the proximity of H$\alpha$ region. In order to confirm the nature of the AGN candidates and to discriminate between SF and AGN photo-ionized emission lines in faint type 1.9 AGNs, we derive emission line diagnostics (Appendix A.5).

### 5.3.2 BPT emission line diagnostics

BLR emission in detected in 441 sources. Although the presence of BLR emission represent an unambiguous indicator for AGN presence in the nucleus, some of our targets show concomitant stellar continuum and BLR features, indicating the presence of low-luminosity (or obscured) AGNs. In particular, about 20% of our BL AGNs are type 1.9 sources. We use the optical BPT diagnostic diagram (Baldwin et al. 1981) as a further tool to investigate the nature of the ionizing sources of the optical emission lines for such objects and to constrain the nature of the type 2 AGN candidates.

Prior to compute the line flux ratios, we fit the stellar continuum using penalised pixel fitting (pPXF; Cappellari 2016; Cappellari and Emsellem 2004) and correct the Balmer line fluxes taking into account the stellar features from the ppxf best-fit model. In fact, underlying stellar absorption of the Balmer lines are expected to be not negligible in low-luminosity AGNs and to shape the emission line profiles. pPXF routine is a program developed by Cappellari et al. to extract the galaxy stellar kinematics (i.e., stellar velocity dispersion $\sigma_*$) from absorption-line spectra; to adopt the procedure

---

[1] Double peaked profiles could be associate both with biconical QSO winds and binary AGNs; SDSS spectra do not allow a separation between the two classes of objects (see discussion in Yuan et al. 2016, Sec. 3.2) and are therefore excluded.

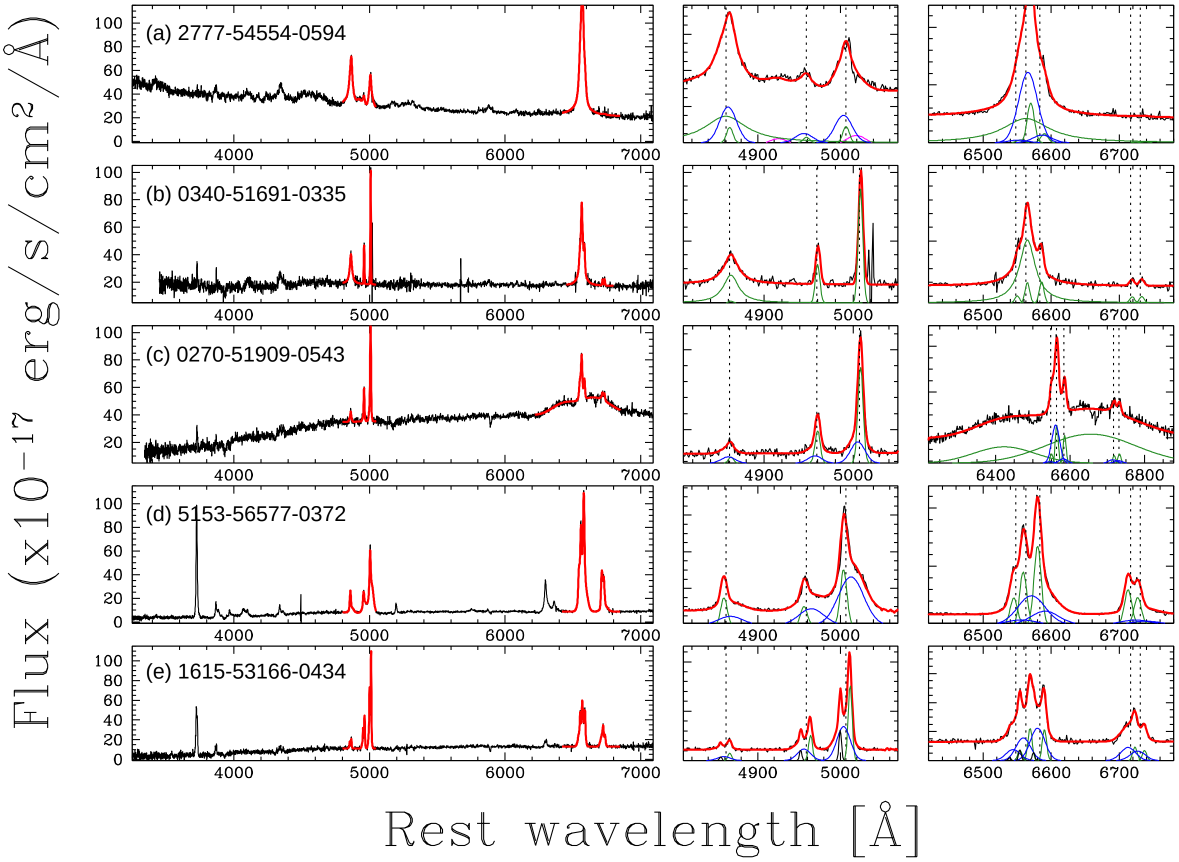

Figure 5.2: Five examples of spectra illustrating our fitting method. For each object, we show on the left the spectrum (black curves) and the best-fit model (red curves). Central and right panels show the zoomed regions around the H$\beta$ and the H$\alpha$ emission, respectively. The dashed vertical lines mark the location of H$\beta$, [O III] doblet, H$\alpha$, [NII] and [SII] doublets. Best-fit NC and BC profiles are highlighted with green curves; OC and FeII emission are shown with blue and magenta curves respectively. Finally, black Gaussian profiles shown a second set of NC used to fit doublet peaked galaxies. In the rows are shown the spectra of various AGN types. From top to bottom: (a) a blue spectrum of a type 1 AGN, with broad BLR Lorentzian profiles, Fe II emission and blue wings associated with outflows; (b) a reddened type 1 AGN without evidence of outflow; (c) a low-luminosity type 1 AGN, which continuum is dominated by stellar emission. For this target, we observe a complex BLR H$\alpha$ profile, modelled with two strong BC, and no BLR H$\beta$ emission. (d) a candidate type 2 AGN, without evidence of BLR emission but with strong emission from outflowing gas detected for all the optical emission lines; (e) a candidate type 2 AGN, with double peaked emission lines and an outflow component.

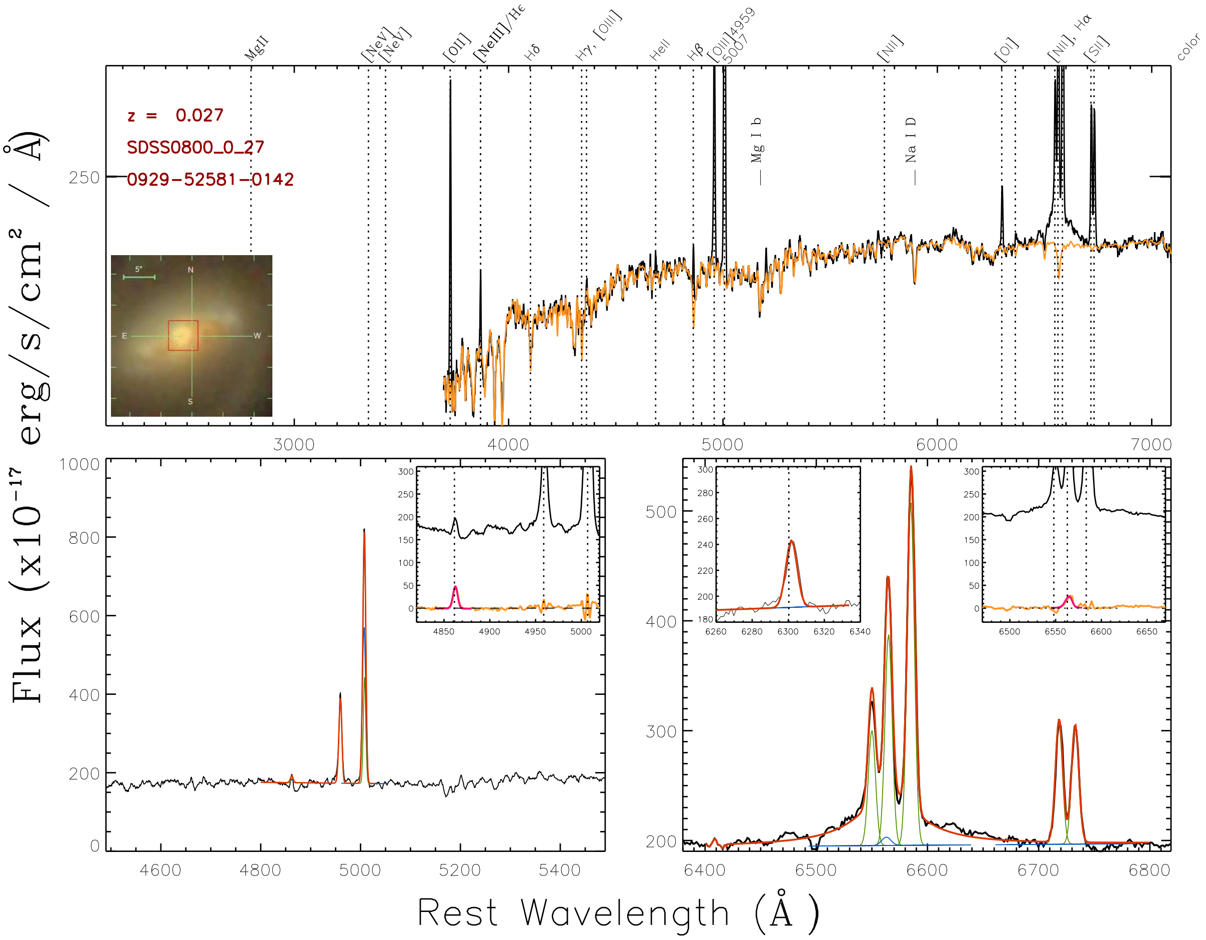

Figure 5.3: (*top panel:*) pPXF best-fit model results for a type 1.9 AGN (orange curve) superimpressed on the rest-frame SDSS spectrum. All the prominent emission lines and the analysed features are highlighted with vertical dotted lines; the positions of MgIb and NaID absorption lines are also marked. The inset on the right shows the SDSS cutout of the galaxy, with a red square marking the spatial region from which the 3″ spectrum has been obtained. (*bottom panels:*) Fit results from the multicomponent simultaneous fit in the H$\beta$-[O III] (left) and H$\alpha$-[NII] (right) regions. Green and blue curves show the NC and OC gaussian profiles, while the red lines represent the total best-fit profile. The insets on the right of each panel show the excess in the balmer emission lines found after the correction for the pPXF best-fit model (orange curves); the original spectrum is also shown for a qualitative evaluation of the contribution of stellar absorption feature in the observed emission line. Purple gaussian profiles represent best-fit results associated with significative ($>5\sigma$) residuals. The insets on the left of the panels show the best-fit models of H$\gamma$-[O III]$\lambda$4363 and [OI]$\lambda$6300 when a significative detection for [O III]$\lambda$4363 and [OI]$\lambda$6300 is found.

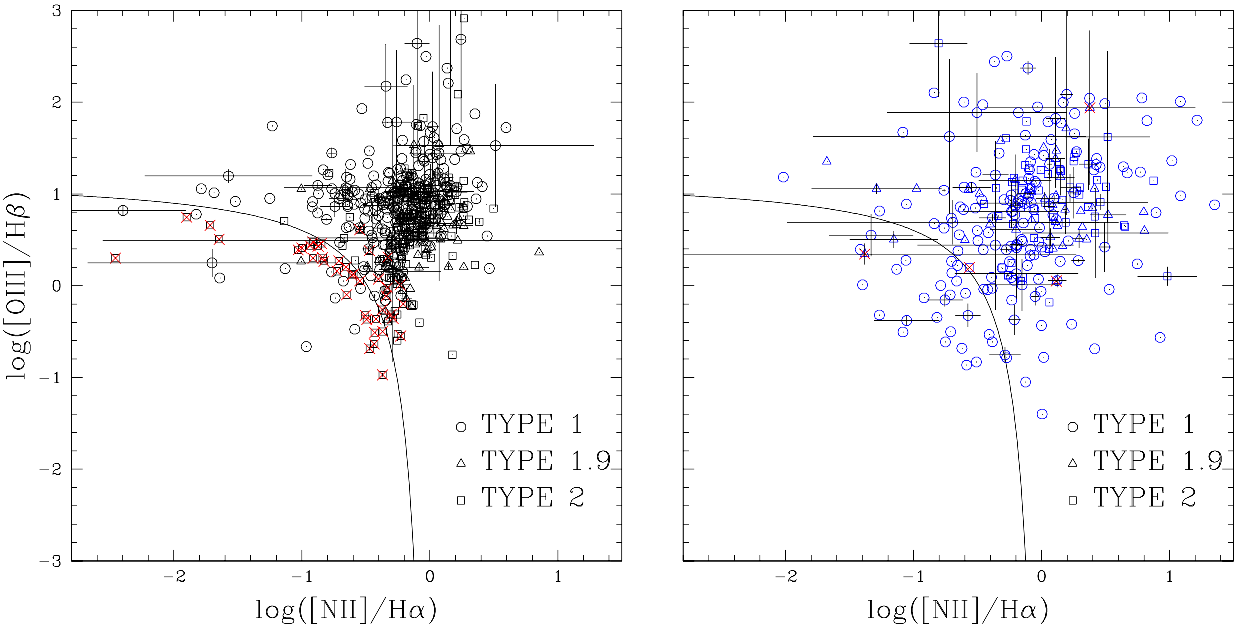

(a) (b)

Figure 5.4: BPT diagrams – Standard diagnostic diagram showing the classification scheme by Kewley et al. (2013). The lines drawn in the diagram correspond to the theoretical redshift-dependent curves at z=0 used to separate purely SF galaxies from galaxies containing AGN. Black and blue symbols correspond to the systemic NC and outflow OC flux ratios, respectively. Representative error bars are shown only for an small fraction of targets. Circles, squares and triangles denote Type 1, type 2 and type 1.9 AGNs respectively. Red crosses highlight the SF galaxies discarted from the sample.

for BL AGNs, a window of $1.2 \times 10^4$ km/s around the expected position of permitted emission lines is excluded from the fit. pPXF method is able to well reproduce the continuum emission of $\sim 250$ (to check) sources (we discarded all best-fit results associated with errors $>20\%$ in velocity dispersion parameter). Figure 5.3 shows an example of a pPXF best-fit model for a type 1.9 AGN candidate (orange curve in the top panel). In the bottom panels are shown the results obtained from the multicomponent simultaneous fit (red curves) and, in the insets, the excess in the Balmer emission lines found after the correction for the pPXF best-fit model. We found that the Balmer stellar absorption features can actually determine underestimates in the fluxes, with median values of $\approx 5\%$ and $\approx 20\%$ of the H$\alpha$ and H$\beta$ respectively. We note that, as expected, such absorption features affect only the narrow emission components.

Figure 5.4 shows the BPT diagrams obtained from our spectroscopic analysis, after the correction from stellar features, for both NC (left) and OC (right). The lines drawn in the diagrams correspond to the theoretical curve (at $z = 0$) used to separate purely SF galaxies from galaxies containing AGN (Eq. 1 of Kewley et al. 2013). For almost all the sources, the systemic NC and the OC are consistent with an AGN classification. OC measurements are more scattered because of their associated lower intensities: this determine an important degeneracy in the fit results, in particular for type 1 AGNs (blue circles) for which an higher number of components must be taken into account (namely: NC, OC and BCs).

We excluded from the following analysis **45** targets (marked with red crosses in the figure). For these sources, the SF nature highlighted by the BPT diagrams, has been confirmed by the concomitance of red spectra and low X-ray luminosities (i.e. $< 10^{42}$ erg/s). We note that the exclusion of few targets above the theoretical transitional curve is due to a conservative approach that takes into account:

- a possible stellar absorption feature contribution in those sources for which low S/N spectra do not allow stellar features modelling, but for which we expect some contribution (i.e., type 1.9 and type 2 sources). In order to take into account this effect, we derive representative shifts in the BPT diagram due to possible underestimates in Balmer flux estimate, assuming that all H$\alpha$ and H$\beta$ fluxes are reduced by a factor of 3× the median pPXF corrections mentioned above. These 'corrections' correspond to a downward shift of $\approx 0.2$ in log[[O III]/H$\beta$], and a left shift of $\approx 0.1$ in log[[NII]/H$\alpha$].
- the error bars associated with each source, due to strong degeneracy in the fitting procedures when low S/N spectra are analysed.

About 14% of our targets have z > 0.4 and the H$\alpha$ region is not covered by the SDSS spectra. For these targets it is therefore not possible to use the BPT diagnostic. However, these sources are generally associated with blue spectra, and 95% of them show unambiguous BLR H$\beta$ emission. For the remaining 5 % (4 targets) we observed [O III]/H$\beta$ consistent with the average value observed for the entire sample (log[O III]/H$\beta \sim 1$), for both NC and, when present, OC. We therefore confirm the AGN nature for all the z > 0.4 targets.

Summarizing, thanks to the BPT diagnostic coupled with a visual inspection of the spectra and the available X-ray analysis, we obtained a final sample of 548 AGNs (361 type 1, 80 type 1.9, 107 type 2).

## 5.4 The nuclear properties

We use single-epoch technique to determine the BH masses of our subsample of BL AGNs. Such technique combines the virial theorem with the $r_{BLR} - L$ relation (see Introduction Chapter), allowing an estimate of the black hole mass from measurements of the BLR line width and the AGN luminosity. Different empirical relations have been calibrated in the last years (e.g., **Vestergaard2006**; Bongiorno et al. 2014; Shen et al. 2011) for various BLR line width and AGN luminosity indicators. Here we adopt the SE relations calibrated by Greene and Ho (2005),

$$log\left(\frac{M_{BH,SE}}{M_\odot}\right) = 6.30 + 0.55\ log\left(\frac{L(H\alpha)}{10^{42} erg/s}\right) + 2\ log\left(\frac{FWHM}{10^3 km/s}\right),$$

$$log\left(\frac{M_{BH,SE}}{M_\odot}\right) = 6.56 + 0.56\ log\left(\frac{L(H\beta)}{10^{42} erg/s}\right) + 2\ log\left(\frac{FWHM}{10^3 km/s}\right). \tag{5.1}$$

These relations replace the $\lambda L_\lambda$ at 5100$\mathring{A}$ ($L$(5100$\mathring{A}$) hereinafter) usually associated to SE relations calibrated on Balmer lines (B.1), with their BLR luminosities, and are based on the tight correlations found between Balmer and continuum luminosities in type 1 AGNs with strong non-thermal nuclear continuum (see their fig. 2). We adopt such relations in order to mitigate the effects of host galaxy contamination at 5100$\mathring{A}$ in our sample. Figure 5.5 shows the Balmer luminosities against the 5100$\mathring{A}$ continuum luminosity for our BL AGNs. The two panels display a significant displacement from the Greene and Ho relation at lower Balmer luminosities ($L(H\alpha)$ and $L(H\beta) \lesssim 10^{42}$ erg/s), due to the enhancement in the continuum luminosity $L(5100\mathring{A})$, which is strongly contaminated by the host galaxy emission. We derive black hole masses in the typical range $10^6 - 10^9$ M$_\odot$ (see Introduction Chapter).

In order to derive the black hole masses, we adopt the FWHM measured from the best-fit model of the BLR profile as line width (see, e.g., Shen et al. (2011)). Such procedure takes into account the additional multiple Gaussian (and/or Lorentzian) components required to reproduce peculiar broad H$\alpha$ and H$\beta$ BLR line profiles (see, e.g., Fig. 5.2).

We also estimate AGN bolometric luminosities. We note that, in order to derive a X-ray bolometric correction and test in a statistical way the results we obtained in the previous Chapters, the bolometric luminosity should be derived from SDSS spectral information. In fact, contrary to the small samples

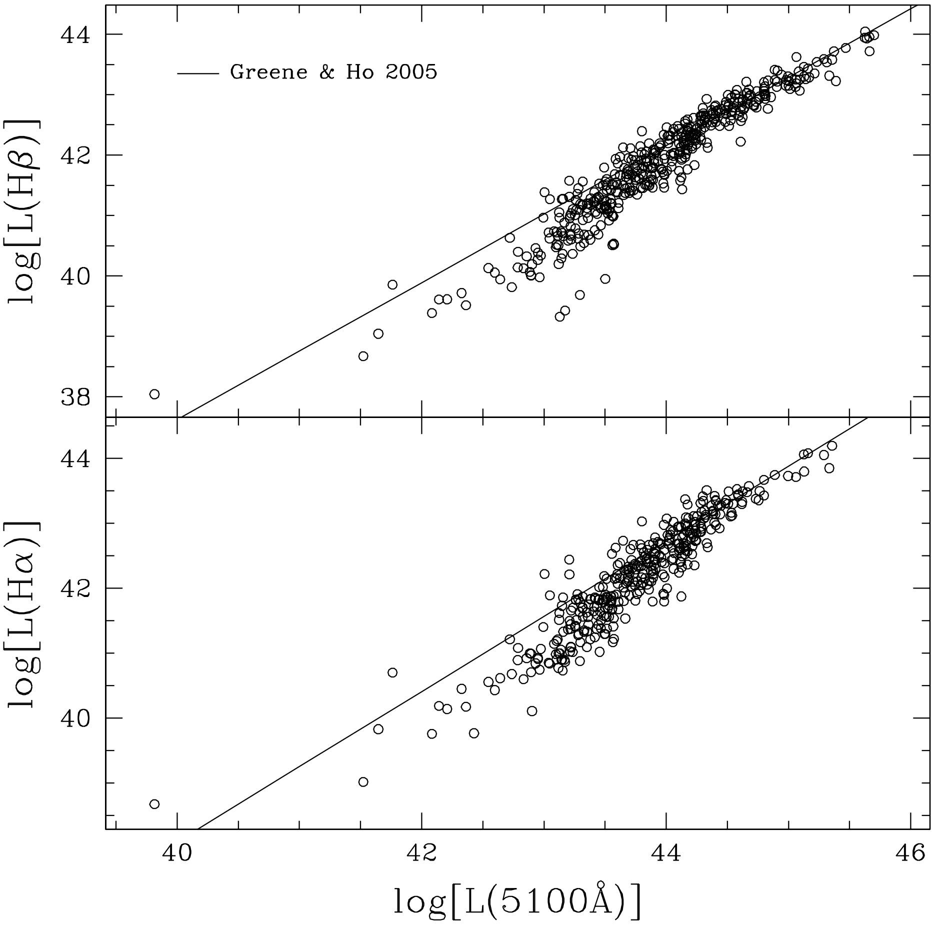

Figure 5.5: $L_{H\alpha}-$ (bottom panel) and $L(H\beta) - L(5100\mathring{A}$ (bottom) correlations. The solid lines represent the Greene and Ho (2005) correlations obtained from a sample of type 1 AGN with low galaxy contribution in the optical continuum emission. A significant displacement from such correlations is found for our low-luminosity AGN subsample, in which the continuum emission at $5100\mathring{A}$ is dominated by host galaxy emission.

at higher redshifts carefully selected in the COSMOS field and for which we could derive all the critical nuclear AGN properties through SED fitting procedures, this SDSS sample do not allow such accurate approach. The more common AGN power indicators in optical regime the are the [O III] line and the 5100$\mathring{A}$ continuum luminosities. In particular, the unperturbed NC of the [O III] line is usually referred as a good tracer of the AGN luminosity (e.g., **Panessa2006**; **Jin2012** while the OC emission may be due to different processes, such as shocks). However, we exclude the use of [O III] line in order to reduce possible spurios correlations in our analysis (e.g., the outflow velocity estimators depend on the NC flux of the [O III] line). We choose to use the 5100$\mathring{A}$ indicator, taking advantage from the above mentioned BLR-continuum luminosity relations to 'correct' the observed $L(5100\mathring{A})$ in the low-luminosity regime, and applying the luminosity-dependent bolometric correction $b(5100\mathring{A}) = 53 - log[L(5100\mathring{A})]$[2], presented by Netzer and Trakhtenbrot (2014).

## 5.5 Incidence of outflows

To constrain the fraction of AGNs with ionized gas outflows and compare our results with literature, we derived the $W80$ and $V_{max}$ non-parametric velocity estimators for the [O III] emission line. In order to discriminate between gravitational and outflow processes, we choose a conservative velocity threshold $V_{max}$ = 650 kms/s, on the basis of the line width distribution of massive BOSS galaxies below z≈ 0.8 (Thomas et al. 2013; see Appendix A.2.1).

Figure 5.6 (top panel) shows the distribution of sources with outflows against the V$_{max}$, for three subsamples defined on the basis of the presence/absence of blue or red prominent wings in the [O III] profile: we found signature of outflows in ≈ 42% of AGNs, of which 33% and 7% have respectively blue and red prominent wings, while only 3% show symmetric profiles. Lower panels in the figure show the distributions for given spectral type, i.e. splitting the sample in type 2, type 1.9 and type 1 AGNs. We note that the fraction of outflows increases going from type 2 to 1, up to over 50% in type 1 AGN. In particular, we note that the relative fraction of blue/red outflows are roughly similar in each spectral type: the fraction of incoming outflows are always ∼ 5 times that of receding outflows. In the context of the unified model, in type 1 AGNs the torus structure should force the outflowing gas toward our direction, i.e. we should be able to observe more sources with blue outflows. On the contrary, in type 2 AGNs, the torus axis should be perpendicular to our line of sight and the ejected material should emerge along that direction. In such a case, in principle, we do not expect to observe a larger number of blue outflows than red ones, which we instead are actually observing.

Figure 5.7 shows the distributions of the two velocity estimators against the total [O III] (on the left) and the intrinsic X-ray $2-10$ keV (centre) luminosities, as well as the black hole masses for the BL AGN subsample (right panels). We discuss here the major results for each pair of indicators:

$V_{out}$ vs. $L_{[OIII]}$: Both the non-parametric estimators show a positive correlation with increasing [O III] luminosity: moving from lower to higher luminosities, an increasing number of targets exhibit higher [O III] velocities. A clear trend appear when we consider the average velocities in bin of luminosity (red-yellow points in the lower and central panels). We also investigate how the fraction of AGNs with/without outflows changes as a function of the [O III] luminosity: the left top panel shows the number of AGNs with V$_{max}$ above/below the velocity threshold value. We found that above $L_{[OIII]} \approx 10^{42}$ erg/s the fraction of AGNs with outflows becomes $> 50\%$. Assuming a bolometric correction of $\sim 3 \times 10^3$ for the [O III] line (Heckman et al. 2004), this corresponds to a bolometric luminosity of $\approx 10^{45}$ erg/s, which is consistent with the luminosity threshold proposed by **Veilleux2013**, obtained studying the incidence of molecular outflows in ULIRGs hosting AGNs, and by Zakamska and Greene (2014) and Woo et al. (2016), derived analysing ionized outflows in obscured and type 2 QSOs.

$V_{out}$ vs. $L_X$: The same results are found when we consider the X-ray luminosities (central panels):

---

[2] va introdotto nel cap precedente... Bolometric corrections convert a luminosity at a specific wavelength to $L_{bol}$, considering typical AGN SED.

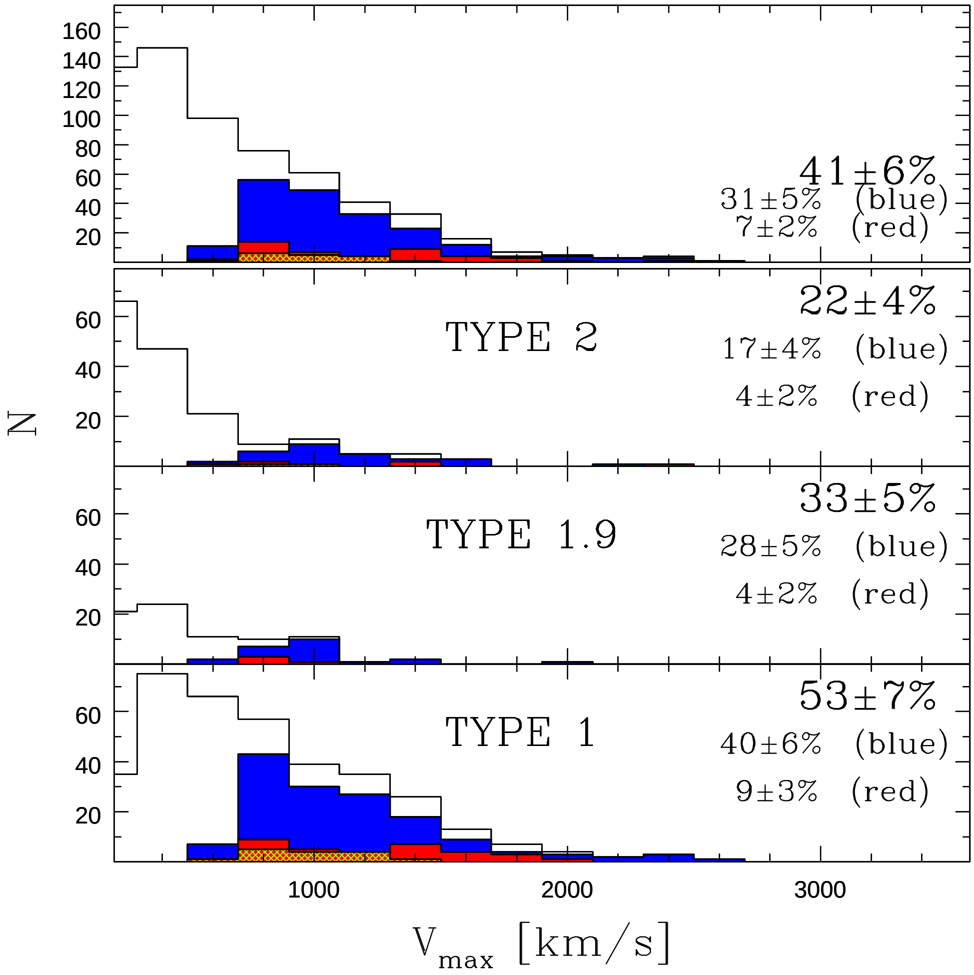

Figure 5.6: Distributions of sources with ionized outflows as a function of the outflow velocity $V_{max}$. Top panel show velocity distribution for approaching, receding and symmetric outflows, represented with blue, red and green histograms. The lower panels show same velocity distributions for subsamples defined on the basis of the AGN type. For each panel, the fraction of AGNs with outflow is highlighted, together with the fraction of receding and approaching outflows. The errors indicate Poisson uncertainty.

a clear trend with increasing $L_X$ is observed, both with $W80$ and $V_{max}$ measures. Even in this case, in the high-luminosity regime, the number of sources with outflows is higher than the one without signatures of winds (upper panel). We underline that this is the first time we observe such correlations between X-ray activity and outflow effects. We note that the histogram displays a bimodal distribution. This is due to the presence in the low-luminosity regime of a small group of AGNs (purple symbols in the panels) from the Georgakakis et al. (2010) parent sample, for which we cannot derive the intrinsic X-ray luminosity because associated with poor detections (i.e., $< 100$ counts in the $2-10$ keV band). For these sources we show the observed X-ray luminosities. Their location in the $L_{[OIII]}$ panels (purple symbols) imply that they are, on average, associated with luminous optical AGNs (with $L_{bol} \approx 10^{44}$ erg/s) and, hence, suggest that are also X-ray obscured. In this respect, the bimodal histogram in the figure is only due to observational arguments. Indeed, if corrected for extinction, these sources would underline the correlation between X-ray luminosity and outflow velocity.

$V_{out}$ vs. M$_{BH}$: We found the same positive correlations also in the right panels. This trends are expected since the M$_{BH}$ is derived from Eq. 5.1, i.e. is proportional to a third indicator of the bolometric luminosity, the BLR balmer emission. As for [O III] and X-ray luminosities, here we find a black hole mass threshold of $10^8$ M$_\odot$. We stress that such result allow an interesting confirmation of the evolutionary model predictions (see Chapter 1.6): comparing the gas bulge binding energy of a typical massive galaxy of $M_{bulge} \sim 10^{11}$ M$_\odot$, $\sigma_* \sim 300$ km/s and a gas fraction $f_{gas} = 0.162$,

$$E_{bulge} \sim f_{gas} M_{bulge} \sigma_*^2 \approx 10^{59}\ erg,$$

with the predicted ouflow energy computed under the assumption of a small coupling factor with the released SMBH energy ($\approx 1\%$, as we actually found in our high redhshift samples),

$$E_{out} \sim 0.01 \times E_{BH} \approx 10^{59} M_8\ erg,$$

we find that only when the SMBH reaches a M$_{BH} \sim 10^8$ M$_\odot$ it is powerful enough to release such energy in the form of powerful outflows.

### 5.5.1 Neutral outflows – Mg Ib - Na ID diagnostic

The Na I D$\lambda\lambda$5890,5896 absorption features can be used to directly probe the neutral phase of outflowing gas (Rupke et al. 2005a; Villar Martín et al. 2014, e.g., ). Figure 5.3 shows a strong sodium line, well reproduced by the pPXF procedure, i.e. through stellar absorption. This is due to the fact that both stellar and interstellar absorption could be at the origin of the line. Therefore, in order to study the neutral outflowing gas component we need to discriminate between the two contributions. A simple diagnostic used to unveil the presence of neutral gas in the ISM is by comparing the EW of NaI D with that of Mg Ib triplet at 5167, 5173 and 5184$\mathring{A}$, which are of pure stellar origin. Similar mechanisms by which sodium and magnesium are created in stars explain the simple relation EW(NaI D) = 0.75×EW(MgI b) (**Heckman2000**; Rupke et al. 2005a; Villar Martín et al. 2014); any deviation from that to higher EW(NaI D) is therefore interpreted as due to the presence of interstellar absorption in the NaI D.

We derive a first order estimate for EW(MgIb) from the best-fit pPXF profile. The EW of NaI D is instead derived modelling the spectra around the absorption feature. HeI$\lambda$5876 emission and NaI D absorption are fitted constraining the central wavelengths and FWHMs using the simultaneous fit results. The diagnostic comparing Mg Ib and Na ID EWs is shown in fig 5.8 (left). The majority of AGNs show NaI D dominated by stellar contribution, while only a small fraction of objects is located well below the correlation. We note that we do not find any difference in the location of sources with or without [O III] outflows (blue and black symbols respectively in the figure). The second line in the diagram shows the EW(NaI D)=3×EW(MgI b) relation, and marks the starburst-driven outflow region proposed by Rupke et al. (2005a): they found that the majority (80%) of the galaxies below this line have outflows. Although the high fraction of outflows found in ionized gas, this plot shows

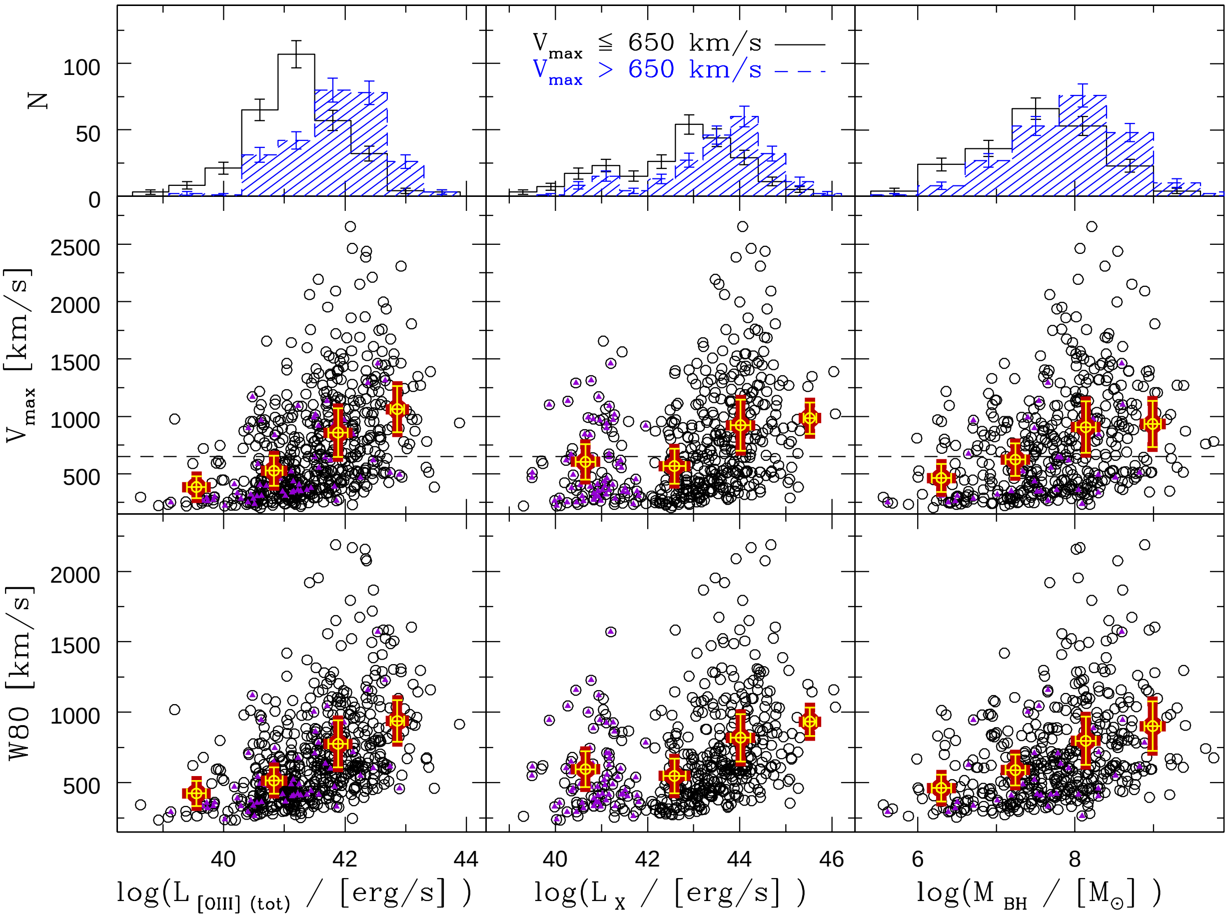

Figure 5.7: (*central and bottom panels:*) Non-parametric velocity $W80$ and $V_{max}$ estimators as a function of [O III] (left) and intrinsic 2-10keV X-ray (right) luminosity. Red dots represent average velocity in bin of luminosity; the associated error bars show the standard deviation for each bin. (*top panels:*) Fraction of AGNs with $V_{max}$ < 650 km/s (black line) and $V_{max}$ > 650 km/s (blue dashed line) as a function of [O III] (left) and X-ray (right) luminosity.

only one target below the Rupke et al. relation. This source, Mkn848, is the only one for which we detect a neutral outflow.

In Fig. 5.8 (right panels) we show the spectra around the MgI b and NaI D absorption features for two sources with enhanced EW(NaI D). We note that while the magnesium profile is well fitted by pPXF procedure (orange curves), the NaI D absorption is strongly underestimated. In panels [II] and [IV] we show our fitting decomposition of the HeI-NaID system after removing the stellar continuum. Mkn848 exhibits a broad absorption profile with a $V_{max}$ ≈1250 km/s, even higher than the maximum velocity associated with the ionized outflowing gas (≈ 900 km/s).

The almost complete absence of neutral outflows in our sample is consistent with the results found by Villar Martín et al. (2014). Studying a sample of 21 SDSS type 2 QSOs at z<0.1, they found ionized outflows in all but one target without any signature of atomic outflow in NaID absorption features. Our results are also consistent with more recent work published by Sarzi et al. (2016). Instead, the fraction of outflows in NaI D increases up to 45% in Seyfert ULIRGs (Rupke et al. 2005a) and in sources exhibiting both SF and AGN activity (Sarzi et al. 2016).

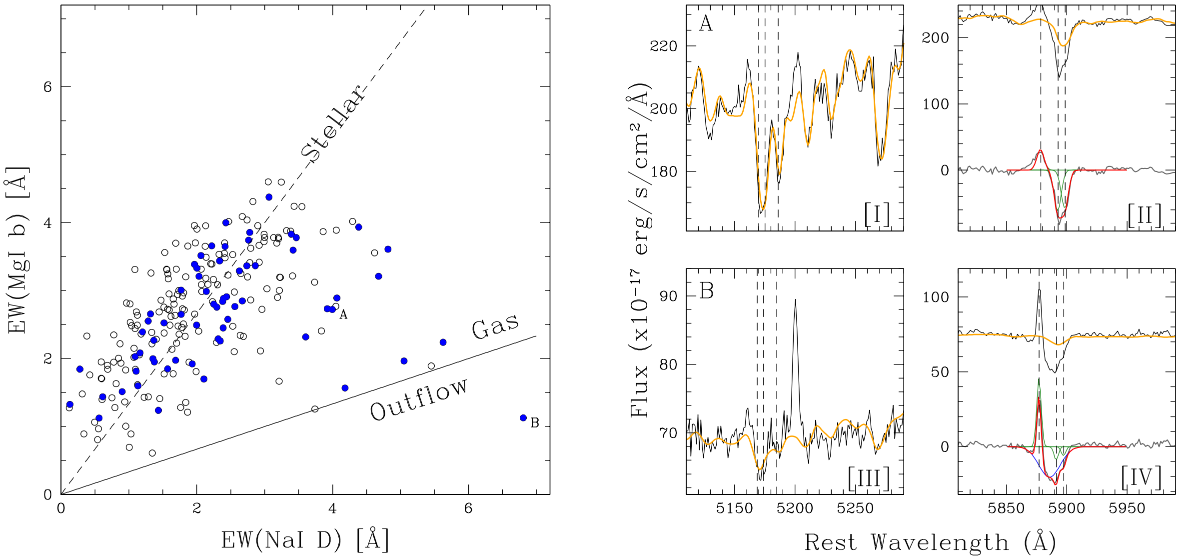

Figure 5.8: (*left:*) EW of the NaI D versus MgI b absorption lines. Open black and solid blue points represents sources with and without ionized outflows respectively (i.e. V$_{max} \lessgtr$ 650 km/s). The dashed line marks the ratio at which the sodium is expected on the basis of observed magnesium EW (Heckman+2000); the solid line marks the starburst-driven outflow region proposed by Rupke+05. A and B letters indicate the sources for which the spectra are shown on the right. (*right:*) SDSS spectra of MKN848_0_21 and UGC6527_0_30 (marked with A and B letters in the MgIb–NaID diagram) around the MgIb and NaID absorption features. Orange curves show the best-fit pPXF results. Vertical lines represent the systemic of MgI b triplet ([I] and [III] panels), and HeI and NaID doublet ([II] and [IV] panels). Panels [II] and [IV] show our fit results. Green, blue and red curves represent the NC, OC and the total best-fit model respectively.

## 5.6 X-ray loudness

In this section we derive the X-ray bolometric corrections ($k_{bol}$) to test the X-ray loudness role in the outflow phenomena. We derive the bolometric corrections computing the ratio between the intrinsic X-ray luminosity and $L_{bol}$, as derived in Sect. 5.4. We compare our results with the relation found by Lusso et al. (2012) and derived studying the X-ray selected AGN population in the COSMOS field (see also Sect. 2.2).

Figure 5.9 (left) shows the derived $k_{bol}$ against the AGN bolometric luminosities for our X-ray/SDSS sample. Square and circle symbols mark type 2 and BL AGNs respectively. We note that the latter subsample is likely associated with more reliable $L_{bol}$ estimates, being the values relative to the low-luminosity population corrected for host contamination (see above). Therefore we focus the analysis on such subsample (which, however, include 80% of the entire sample). For these sources, we differentiate between targets with kinematic indication of outflows in the [O III] line (with $V_{max}$ > 650 km/s), colour-coded for increasing velocities, and those with narrow [O III] profiles (empty circles).

From a visual inspection, it seems that the X-ray/SDSS sources are broadly distributed over the entire plane, regardless the presence/absence of signatures of outflows in their ionized gas component. To simplify the visualization, we also show in Fig. 5.9 (right) the source distribution normalizing (in log space) the $k_{bol}$ with the value expected from the Lusso et al. (2012) relation ($k_{bol-L12}$; black curve in the figure), considering only the luminosity range in which the relation has been calibrated (i.e., $\log(L_{bol}/L_\odot)$ in the range $10.8 - 13.5$). The histogram shows that the entire sample of BL AGNs (grey curve) is actually following the expected relation for X-ray selected AGNs, displaying a gaussian distribution[3]. Most important, the distributions of sources with/without outflows are similar, i.e. we do not report any excess in the number of sources with outflows at negative $\log(k_{bol}/k_{bol-L12})$. This results therefore seems to disprove the idea of a X-ray loudness associated with the feedback phase. We refer to the Section **??**for a detailed discussion about this results.

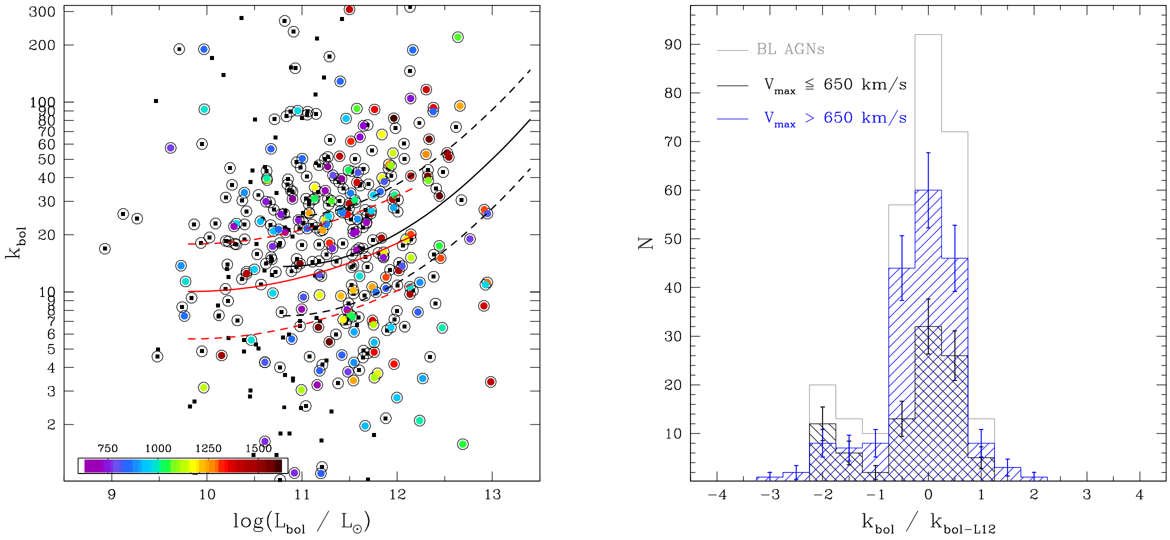

Figure 5.9: (*left panel:*) $k_{bol}$ vs. $L_{bol}$. Black symbols represent type 2 AGNs, while colourcoded circles mark the type 1 and type 1.9 sources. The black and red curves represent the best-fitting relations obtained by Lusso et al. (2012) for type 1 and type 2 AGNs in the COSMOS field, respectively. (*right:*) Distribution of the normalized (in log space) $k_{bol}$ values with respect to those expected from the relation for X-ray selected AGNs (black curve in the left panel) for the BL X-ray/SDSS sample (grey histogram). Blue and black histograms represent the distributions for sources with and without outflow signatures.

## 5.7 The plasma properties in the outflowing gas

Electron density ($N_e$) and electron temperature ($T_e$) of AGN-driven outflow regions are largely unknown. These quantities are nowadays important sources of uncertainties in outflow kinematic estimates for the ionised phase. In Appendix B.0.1 we show how these quantities enter in the determination of the ionized outflowing mass and, as a consequence, of the outflow energy. For example, the [O III] emissivity term in Eq. B.5 shows a weak dependence on electron density over several order of magnitudes, but a difference of a factor of three easily emerges when we consider electron temperature of $1\times$ instead of $2\times10^4$ K [4]. Moreover, the outflow mass shows an inverse proportionality to the electron density. Outflow energetics have been usually derived in the past assuming given values for electron temperature and density (see Chapter 2, **??**, 4). While a general consensus is found for a $T_e = 1\times10^4$ K (e.g., Cresci et al. 2015a; Harrison et al. 2014), several values are used for the electron density, spanning on order of magnitude or more: for example, 1000 cm$^{-3}$ has been assumed by Cano-Díaz et al. 2012, 500 cm$^{-3}$ by Carniani et al. 2015, and 100 cm$^{-3}$ by a large number of authors (e.g., Cresci et al. 2015a; see also Chapter 2 and 4).

---

[3] A large fraction ($\sim 70\%$) of sources responsible of the observed peak at $\log(k_{bol}/k_{bol-L12}) \approx -2$ is associated with $L_{bol} < 10^{11.5}$ L$_\odot$, i.e. are found the low-luminosity regime for which we apply the $L(H\alpha) - L(5100\mathring{A})$ correction to derive the $k_{bol}$. We therefore likely associate such low ratios to wrong estimate in the bolometric luminosities.

[4] [O III] emissivity from PyNeb (**Luridiana2015** )

Few diagnostic ratios involving forbidden lines can be used to derive these properties in regions with densities $\lesssim 10^4$ cm$^{-3}$ (depending on the critical density of the involved forbidden transitions). In particular, we have seen how [SII]$\lambda\lambda$6716,6731 and doubly ionized oxygen (involving [O III]$\lambda\lambda$4959,5007 and [O III]$\lambda$4363) diagnostics are pontentially useful to measure $N_e$ and $T_e$ (Appendix A; Chapter 2 and **??**). Unfortunately, the faintness of the involved emission lines (in particular, [O III]$\lambda$4363 and [SII] doublet) make challenging the measurement of these quantities. For example, Vaona et al. (2012) derived reliable estimates of the electron temperature of the unperturbed NLR gas only for $\sim$ 500 objects, starting from a parent sample of $\sim$ 2500 SDSS AGNs. The fact that the OC are generally fainter that the unperturbed narrow components ones, makes further difficult to derive such diagnostic informations. Only for a handful of previous studies it was possible to derive, although with large uncertainties, such physical properties for the ionized outflowing gas. These works are generally based on single luminous targets (e.g., in the framework of this Thesis, XID 5395 and XID 5321) or, in the best cases, on small number of sources (e.g., Westmoquette et al. 2012) or stacked spectra (Harrison et al. 2012). These few results point to large ranges of values for the electron densities, from $\approx 10^2$ to $> 10^3$ (see, e.g., Rodríguez Zaurín et al. 2013), and are at the origin of the variety of assumed N$_e$ values in literature (see above). To the best of our knowledge, the electron temperature has been derived only for six targets (those presented by Villar Martín et al. 2014 and Nesvadba et al. 2008 and XID 5395, presented in Chapter **??**), with $T_e \approx 1.5 \times 10^4$ K.

Taking advantage of the large sample collected, we analyse the SDSS spectra to best constrain these quantities for both the unperturbed and outflowing gas.

### 5.7.1 Electron density diagnostics

We measure the NLR diagnostic ratio $R_{[SII]} = f(\lambda6716)/f(\lambda6731)$ for all AGNs with no severe and ambiguous blending with H$\alpha$ BLR emission (see, e.g., the *c* panel in Fig. 5.2) and without signatures of outflows revealed in simultaneous fits, resulting in a sample of 121 AGNs. In fact, when OC components are revealed, the doublet lines are usually severely blended and, in general, the fitting procedure does not give unambiguous results. From this sample we obtained the distribution shown in Fig 5.10, left (grey histogram).

To study the electron density of the outflowing regions, we focus the analysis on those AGNs with the simplest spectral profiles, i.e. with well defined [SII] wings modelled with only two kinematic components and, as before, without strong blending with BC. Although the large number of targets with intense [SII] emission and the large fraction of sources with outflows, only 28 sources satisfy the above mentioned conditions. This reflects the difficulties in the electron density measurements. The fitted spectra are shown in Fig. C.-9. From this sample, we compute the $R_{[SII]}$ for both NC and OC. The $R_{[SII]}(NC)$ distribution (fig 5.10, left; black curve) has a smaller spread when compared with that of the AGN sample without OC components, because of the particular selection. The $R_{[SII]}(OC)$ distribution (blue area) cover a larger range of values and is peaked at lower ratios.

From each [SII] intensity ratio we could derive an estimate of the electron density from Eq. A.2, taking into account the depencence on the electron temperature. This means that for each source, in order to derive at best the $N_e$, we should be able to detect and analyse all the emission lines needed for electron density and temperature diagnostics. Unfortunately, the faintness of the temperature-sensitive emission line [O III]$\lambda$4363 do not allow spectral analysis for all but 4 of our targets selected to study the [SII] emission. Therefore, we choose to follow a statistical approach, and derive an average electron temperature selecting a different sample in which [O III]$\lambda$4363 is well detected.

### 5.7.2 Electron Temperature diagnostics

We carefully select a sample of sources with well detected and unblended [O III]$\lambda$4363 line to study the electron temperature of narrow and outflow emitting gas through temperature-sensitive diagnostic ratio $R_{OIII} = f(\lambda\lambda 4959, 5007)/f(\lambda 4363)$[5]. The faintness of the emission line and the vicinity of the permitted H$\gamma\lambda$4342 BLR emission strongly reduce the number of useful sources. To allow the analysis of the outflow wings in such faint emission line we narrow down the sample selecting only those targets with well detected (S/N> 10) [O III]$\lambda$4363. Furthermore, we discard all those sources with broad H$\gamma\lambda$4342 BLR profiles after a visual inspection. This reduced the sample to 8 sources. We fit simultaneously the oxygen line at 4363$\AA$ and the Balmer line at 4342$\AA$ imposing the same systemics, widths and sets of gaussian components as obtained from the simultaneous fit in the H$\alpha$ and H$\beta$ regions. From such analysis, we derive the $R_{OIII}$ distribution for both the NC and OC components.

In order to better constrain the estimate of the electron temperature for the NC, we also consider other 10 sources selected with a shallower cut in the S/N (i.e. imposing a S/N> 5): for these targets, in fact, the spectral analysis do not require any decomposition and gives reliable results also for such faint emission lines. The derived $R_{OIII}$ distributions derived for NC (18 AGNs) and OC (8 AGNs) are shown in Fig. 5.10 (right panel; black and blue shaded areas, respectively).

We note that the $R_{OIII}(OC)$ distribution is located closely around the median position of that of $R_{OIII}(NC)$. This could suggest that, on average, NC and OC share similar electron temperatures. Given that the samples are really small to point toward any conclusion, we tested this hypotesis using additional 26 targets with [O III]$\lambda$4363 detected with 5<S/N< 10 and showing evidence of outflows. If we assume the same temperature for both outflowing and systemic ionized gas, the amplitude fractions OC/NC should be the same in [O III]$\lambda$5007 and [O III]$\lambda$4363. We fitted the emission lines with this additional constrain. The fit results are shown in fig. 5.11. The first four rows show the 10 targets with S/N>5 without outflows (fitted with a single gaussian component), and the 8 S/N> 10 sources with outflow components (fitted with free amplitude ratios). The last seven rows show the 26 targets with 5<S/N<10, fitted with constrained OIII amplitude ratios.

We note that the profiles are generally well reproduced under this assumption. Of course, the low quality of the spectra do not allow a strong result significance. However, the fact that the derived $R_{[OIII]}$ show a similar distribution to the other targets, may confirm our hypothesis. In Fig. 5.10, right, we showed with dashed blue curve the distribution obtained adding these 26 targets to the outflow sample.

### 5.7.3 Results: the plasma properties

From the final $R_{[OIII]}$ distribution we take the median value, with the uncertainties defined by the 68% confidence intervals, to compute a fiducial estimate of the electron temperature through the Osterbrock and Ferland (2006) formula: $T_e = 1.7^{+1.1}_{-0.3} \times 10^4$ K (see also Appendix A.2.2). We used this median temperature to derive fiducial electron densities from Eq. **??**, for both NC and OC emission:

$$N_e(NC) = 500^{+400}_{-300} cm^{-3},$$

$$N_e(OC) = 1000^{+2000}_{-700} cm^{-3}.$$

Such value for the NC have been derived for larger samples of SDSS Seyferts by other authors in the past decade (e.g., Vaona et al. 2012; Z. T. Zhang et al. 2013). Our estimates are totally consistent with the median values indicated by these authors ($N_e \approx 400$ and $T_e \approx 1.5 \times 10^4$ K).

Although with large uncertainties, the outflow condition estimates are, to the best of our knowledge, the first average estimates from a medium size sample ($\approx$ 30 targets). Indeed, despite the fact that our average values for NC and OC are still comparable within the errors, our analysis suggest that the outflowing gas may actually be characterized by a large range of electron densities, possibly favouring the high-density regime. As a consequence, the most common assumption to derive outflow energetics ($N_e = 100$ cm$^{-3}$) may overestimate such measurements even by a factor of 10.

---

[5] Another temperature sensitive lines ratio is given by the [NII] diagnostic ratio, $R_{NII}$ =. We found in our sample 7 [NII]$\lambda$5755 emission lines with a S/N > 5. This line in not affected by any blending but, unfortunately, the [NII]$\lambda\lambda$6550,6585 doublet is severely blended within the Ha-[NII] complex for 5/7 sources, when OC components and/or BLR emission are present. Therefore, we decided to discart this diagnostic.

D. Xu et al. (2007) studied the NLR emission of $\sim$ 100 SDSS type 1 AGNs. They observed a negative trend between the electron density and the blueshift of the [O III] wing. This result conflicts with our measurements. However, we note that, currently, all these results are limited to small samples: the trend suggested by D. Xu et al. (2007) is based on the measurement of low $N_e$ in 6 out 54 sources with signature of outflows. Indeed, they derived the $N_e$ without any separation between narrow and outflow components, making the comparison difficult.

### 5.7.4 Possible bias in T$_e$ due to [O III]$\lambda$4363 selection

The fact that we are computing the electron temperature only for those sources with intense [O III]$\lambda$4363 could strongly bias our results by favouring targets with higher $T_e$ (see Appendix A). We compute $1\sigma$ upper limits for all those sources without clear detection and, from the median value of their $R_{OIII}$ distribution, we derive an upper limit on the electron temperature of $\approx 3 \times 10^4$ K. Unfortunately, this value is not useful to our purpose. However, the fact that we did not observe any difference in the average Te between the SN> 10 and 5 <SN< 10 samples, could suggest that the bias is, if any, negligible. The same behaviour can be seen for the large sample studied by Z. T. Zhang et al. (2013), for which the same NLR electron temperature has been found for both their two [O III]$\lambda$4363 luminosity subclasses of Seyferts.

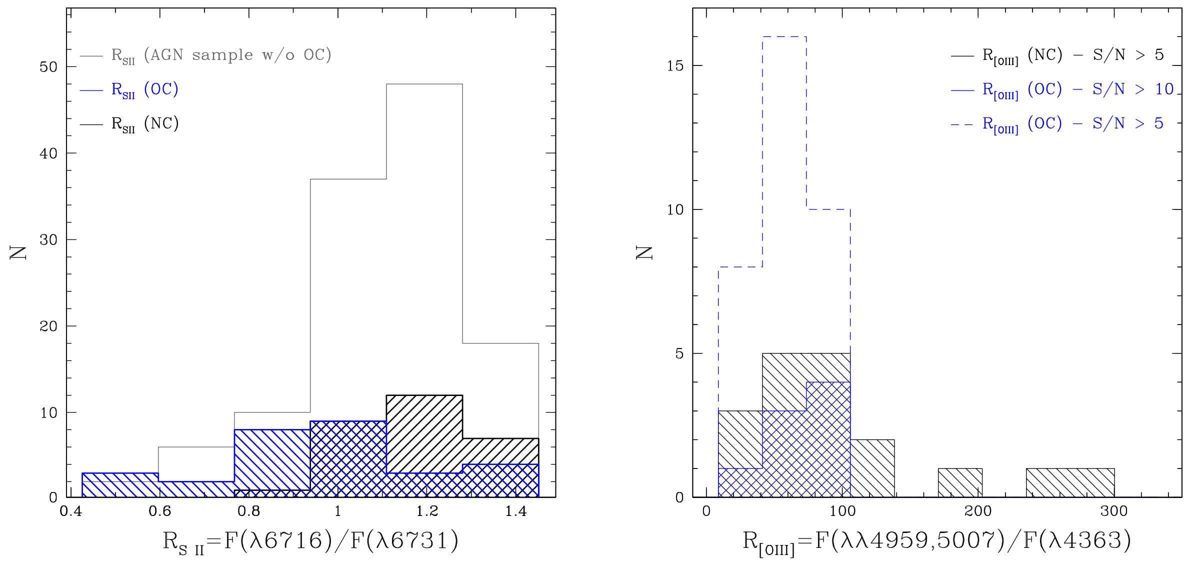

Figure 5.10: (*left:*) [SII]$\lambda\lambda$6716,6731 ratio distributions. The grey solid line mark the distribution for the AGN sample without evidence of outflows from our line fitting routine; Vertical dashed lines mark the related median and 68% interval. The black and blue shaded areas denote the distributions for NC and OC [SII] ratios. (*right:*) [O III] ratio distributions. Gray shaded area mark the $R_{[OIII]}$ distribution for the unperturbed ionised gas (NC). Blue shaded area denotes the outflow emission $R_{[OIII]}$ distribution of S/N>10 sources. The blue dashed line show the $R_{[OIII]}$ histogram of the outflow components of all S/N>5 sources, analysed as described in the text.

### 5.7.5 Outflowing gas ionization mechanisms

The unambiguous separation between NC and OC components in the SII emission lines allow the study of a second diagnostic diagram for the medium size sample of 28 AGNs, combining [O III]/H$\beta$ with [SII]/Halpha (see Appendix A.5). Indeed, we find well detected [OI]$\lambda$6300 emission lines in all but (1?) sources (see Fig. C.-9). Therefore, taking advantage from simultaneous analysis results, we fit this faint emission constraing the systemics and the FWHM of NC and OC components and derive the intensity ratio needed for a third diagnostic diagram, [O III]/H$\beta$ vs. [SII]/Halpha, proposed by (; see Appendix) .

Figure 5.12 shows the three diagnostic diagrams, [O III]/H$\beta$ versus [NII]/H$\alpha$, [SII]/H$\alpha$ and [OI]/H$\alpha$ for both NC (open black symbols) and OC (blue circles). The lines drawn in the diagrams correspond to the optical classification scheme of **Keylew2006**; Kewley et al. (2013): in the second and third diagram, the diagonal line marks the LINER locus. Over-plotted on the figure are the results from our fitting routine for the 28 sources with well constrained [SII] components. Their OC appear associated with same level of ionization of NC but slightly larger [O III]/H$\alpha$ and larger [SII]/H$\alpha$ and [OI]/H$\alpha$ ratios. The second and third diagnostic diagrams demonstrate clearly a LINER-like emission for the outflow components. Such kind of line ratios are generally associated with ionization by fast radiative shocks (e.g., Allen+2008; but see also Belfiore+16). Shock model results have been made available for a large range of physical parameters: pre-shock density $N_e^{pre}$, shock velocity, magnetic field and abundances. We superimposed on the figure a grid of shock model with assumed solar abundance and a pre-shock density of 100 cm$^{-3}$ (ITERA; Groves and M. Allen 2010). The grid shows different line ratios for various values of magnetic field and shock velocities (up to 1000 km/s). The models, however, fail to reproduce the exact position of our sources in the BPT diagrams. We tested all available shock models from the ITERA library without any improvement.

It is possible that most extreme set of parameters are needed to reproduce the shocks in AGN-driven outflows: under particular assumptions, shock velocities and gas velocity dispersion can be similar, and therefore even greater than 1000 km/s (see **McElroy2014** discussion). Radiation pressure-dominated photo-ionization models easily reproduce the loci occupied by NC measurements but, as the shock models, fail to cover the highest [O III]/H$\beta$ and [S II]/H$\alpha$ratios.

Another strong evidence for shock excitation interpretation is given by the observed correlation between the gas kinematics and ionization state (Dopita and Sutherland 1995). The line ratios produced in photo-ionized regions should be independent of the gas kinematics, while are expected to correlate with the kinematics of the shock-ionized material (see McElroy+15, Ho+14, Arribas2014). In the lower panels of Fig. 5.12 we showed the FWHM against [NII]/H$\alpha$, [S II]/H$\alpha$ and [O III]/H$\beta$ ratios for both NC and OC. We note that the FWHM should not suffer for strong degeneracy between the [SII] doublet and [NII]-H$\alpha$ complex components, because derived from our simultaneous fits. We used a Spearman rank correlation coefficient to determine the significance of the observed trend between line ratios and velocities. We found coefficients of $\approx 0.45$ with probabilities of $\lesssim 0.01$ for the correlation being observed by chance, for both NC and OC separately. The same correlation has been found by **Arribas2014** for narrow components (but not for the outflow components), confirming the complex kinematic conditions within the NLR.

## 5.8 Discussion

We analysed SDSS optical and X-ray (see Sect. 5.1) spectra of a large sample of **548** AGN at z < 0.8, comprising type 1 (361), type 1.9 (80) and type 2 (107) sources. We combined ionized emission line and neutral absorption feature information modelled through multicomponent simultaneous fitting, non-parametric measurement and pPXF analysis, in order to derive physical conditions (e.g., ionized levels, plasma properties) and kinematic conditions of both warm and cold gas components of the ISM. In particular, analysing the [O III] line profiles, we derive the outflow incidence in the warm phase of the NLR: we found that $\approx 40\%$ of AGNs exhibit signatures of outflows. Such fraction is strongly dependent on the AGN power: our analysis suggests a clear positive correlation between the outflow velocity and the AGN power traced by the [O III] luminosity. Such trend have been reported and also related with similar correlations between radio luminosity and [O III] width (e.g., Mullaney et al. 2013). However, the observed correlation between radio luminosity and stellar mass (and stellar velocity dispersion) may easily explain the trend with the [O III] widths, resulting in a challenging interpretation (see, e.g., the discussion in Woo et al. 2016; Zakamska et al. 2016b). We show for the first time that a well defined positive trend is also observed for X-ray luminosity. Such tracer is unambiguously associated with AGN activity at $L_X > 10^{42}$ erg/s.

The sodium absorption system at $\lambda\lambda5890{,}5896$ is well detected in 36% of our sample. This allowed the investigation of the kinematic of the cold phase of the NLR: we detect the presence of ISM absorption in $\approx 15\%$ of sources, of which $\approx 50\%$ are associated with the presence of ionized outflow. However, we find atomic outflow in only one target. We derive therefore an incidence for the atomic outflows of $< 1\%$. Similar results in literature suggest that the atomic outflows may be associated with earlier stages of the feedback phase. Rupke et al. (2005b) and Sarzi et al. (2016) found that sodium outflow are generally associated with sources exhibiting both strong SF and AGN activity. Our analysis for XID 2028 and XID 5321 actually showed a concomitant intense star formation activity (SFR $\approx 250$) and outflowing processes involving both atomic and ionized gas (Chapter 2). An example of local source displaying similar properties is the closest ULIRG-QSO Mrk 231. This source may be considered a local analogue of our brightest X-Shooter sources, displaying similar SFR (140 $M_\odot$/yr) and bolometric luminosity ($5 \times 10^{45}$ erg/s). Indeed, both cold (neutral and atomic) and warm outflows are revealed in its host galaxy (see **Feruglio2015** and references therein). Our X-ray/SDSS target with both atomic and ionized outflow signatures is a luminous infrared galaxy associated with an ongoing merger (ref).

We derived the X-ray bolometric correction and proved that the X-ray/SDSS sample characterized by the presence of ionized outflows do not show any deviation from the typical behaviour of the population of X-ray selected AGNs in the COSMOS field. This result may rule out the proposed role of X-ray emission in the feedback phase. In the previous section we displayed our selection and analysis limitations in deriving such $k_{bol}$ corrections. Here we suggest a scenario which explain our analysis results for both outflow incidence and X-ray emission. Both the absence of atomic counterpart in our SDSS sample and the different X-ray bolometric corrections may be explained postulating that the high-z sources isolated with the proposed selection criteria and the X-ray/SDSS targets are representing different evolutionary stages within the blow-out phase: the X-ray (and optical) obscured AGNs are associated with the initial stages of the feedback, when atomic gas is still present in the ISM and the AGNs are obscured by galactic scale dust, while the BL AGNs are tracing later stages, in which the LOS has yet been cleaned and the cold component has been heated of exhausted. In this context, the low $k_{bol}$ of our obscured QSOs could be associated with underestimate in their bolometric luminosities due to not well constrained disk emission components in the SED fitting decomposition (see, e.g., Fig. 2.11). Such conclusion is suggested by the simple assumption that similar physical nuclear conditions are the origin of outflow phenomena within the entire length of the blow-out phase, regardness the different redshift ranges covered by X-ray/SDSS sample and the X-ray obscured QSOs.

In the second part of this Chapter, we derived the plasma properties for both narrow line and outflowing component emission. For the first time we derived an estimate of the electron temperature and density of the outflowing gas for medium size samples. We found indications suggesting that $T_e$ may be similar in both outflowing and unperturbed gas. This may suggest that the shock responsible for such outflows (see Sect. ) is associated with short cooling time scales (see M. G. Allen et al. 2008)??. We found a wide range of values in electron density in the outflowing gas of these sources, with a distribution characterized by a medium value of 1000 cm$^{-3}$ and a 68% interval going from 300 to 3000 cm. These values, if compared with those we obtained for the narrow-line gas, $N_e = 500 \pm 350$, or those obtained from other authors for larger samples, with typical values of few 100 , suggest that the most typical assumption in deriving crucial outflow energetics may be strongly underestimated and that the energetics may be overestimated of a factor of 10.

Other indications in literature suggest even higher $N_e$ in the outflowing regions: Villar Martín et al. (2015), studying high-ionization lines such as [Fe X] and [Ne V], proposed electron density up to $10^5$ cm . However, such emission lines have high ionization potential and critical densities (; see Table A.1) and are usually associated with more internal regions (see **Rose2015a**; **Rose2015b** in which such lines have been proposed to occupy a region between the BLR and the inner walls of the torus; see also Fig. 1.6). When we consider kpc-scale outflows, typical electron density may be more similar to those of narrow emission lines in NLR rather than in the nuclear regions. A slightly higher density may be explained by a possible compression due to the AGN wind on the ISM material. Indeed, we need to consider that the SII, because of its low IP, may arise from the external region of the [O III] emitting zone. All these considerations, based on the results we obtained from a medium size sample and on speculative arguments, suggest a more conservative approach in the estimate of the outflow energetics.

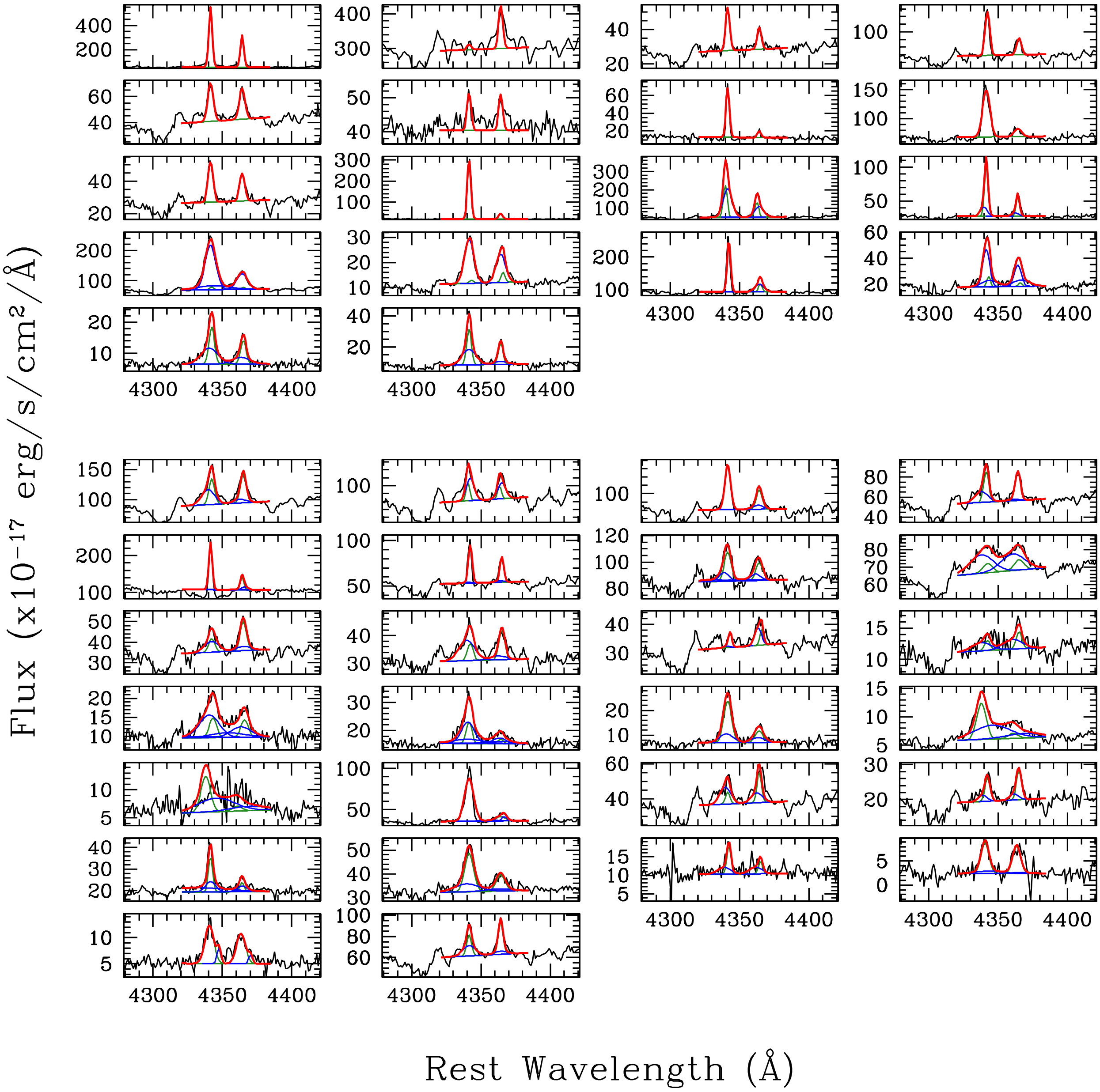

Figure 5.11: Zoom in the region of [O III]$\lambda$4363-H$\gamma\lambda$4342 lines for the 43 sources for which we could determine the $R_{[OIII]}$. For each spectrum are superimposed the best-fitting components presented in Section xx: solid green curves represent the systemic component (NC); blue curves the OC.

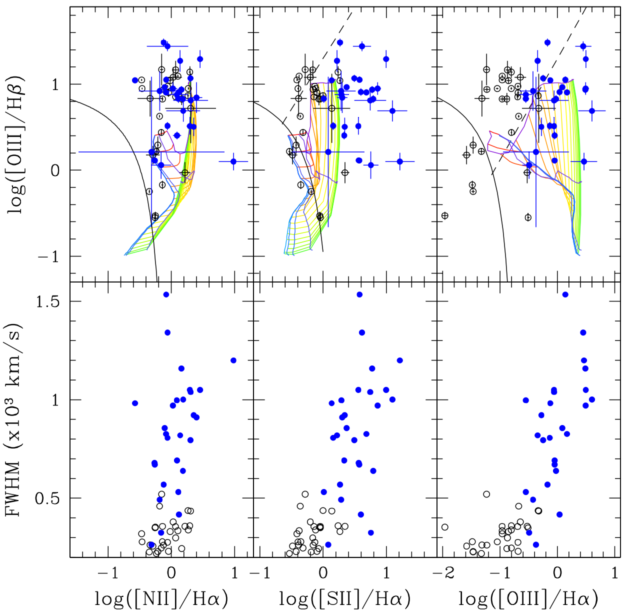

Figure 5.12: (*Top panels*:) [O III]/H$\beta$ versus [NII]/H$\alpha$, [SII]/H$\alpha$ and [OI]/H$\alpha$ BPT diagrams for the 29 sources used to derive the outflow electron density. Shock model grids are overplotted, with increasing velocities, from 100 to 1000 km/s (red to green lines), and magnetic field (blue to purple curves). (*Bottom panels*:) FWHM plotted against log([NII]/H$\alpha$), on the left, and log([SII]/H$\alpha$), on the right. Both NC (open black) and OC (solid blue symbols) are shown.

CHAPTER 6

# Conclusions

## 6.1 Comparison with models

Large scale outflows, according to the most popular models (**Costa2014**; Faucher-Giguère and Quataert 2012; A. King and K. Pounds 2015; Zubovas and A. King 2012), emerge from the interaction between a nuclear AGN-driven wind and the ISM of the host galaxy. All these models investigate a scenario originally proposed by A. King (2003), and based on simple assumed wind properties derived from observational arguments. Several works (e.g., **PoundsReeves2009**; K. A. Pounds et al. 2003; Tombesi et al. 2011, 2015, 2010) give strong evidence for the presence of high velocity winds, of the order of $v \approx 0.1 - 0.4c$, in the form of blueshifted X-ray absorption lines, most likely to be produced close to the accretion disk (sub-pc scales; e.g., **Tombesi2012** ). These features can be interpreted as material expelled with a mass rate of $\dot{M}_w \sim 1$ M$_\odot$/yr (i.e. close to the Eddington accretion limit, for typical AGN of $M_{BH} = 10^8$ M$_\odot$). The high incidence of these ultra-fast outflows (UFO) translates to a large covering fraction of the absorbers, thereby implying large opening angles for the emerging nuclear wind. These nuclear wind properties translate in the following model assumptions:

- The SMBH accretes at the Eddington limit. This implies in an accreting mass rate $\dot{M}_{Edd} = L_{Edd}/\eta c^2$.
- A significant fraction of the accreted mass results in the accretion disk wind. For simplicity, it is generally assumed that $\dot{M}_w$ is equal to the $\dot{M}_{Edd}$ and that the wind is quasi-spherical.

The Eddington accreting mass rate and the quasi-spherical geometry result in a high opacity in the wind and an optical depth to electron scattering of $\approx 1$ (A. R. King and K. A. Pounds 2003). As a consequence, on average, every photon emitted by the accretion disk scatters about once before escaping to infinity, giving up all its momentum to the wind, whose total momentum should be of the order of the photon momentum, or equivalently for their rates:

$$\dot{M}_w v \simeq L_{Edd}/c,$$

where $v$ is the wind velocity. Therefore, the transport of energy resulting in such winds in the vicinity of the disk is due to radiation pressure.

Combining the wind momentum rate with the Eddington accretion rate, we obtain:

$$\dot{M}_w v \simeq L_{Edd}/c = \eta c \dot{M}_{Edd},$$

from which, adopting the assumption $\dot{M}_w = \dot{M}_{Edd}$ and an efficiency $\eta \approx 0.1$,

$$v \simeq \dot{M}_{Edd}/\dot{M}_w \eta c \sim 0.1c. \tag{6.1}$$

The outflow velocity in the vicinity of the accretion disk is therefore fixed at a value actually observed in UFOs.

The above mentioned assumptions also define the kinetic outflow rate:

$$\dot{E} = \frac{1}{2}\dot{M}_w v^2 \simeq \frac{1}{2}\frac{L_{Edd}}{c}v,$$

from which we obtain, using Eq. 6.1,

$$\dot{E} \simeq 0.05 L_{Edd}. \tag{6.2}$$

With a velocity of $\sim 0.1c$, the wind gas is hypersonic, and must drive simultaneously a reverse shock and a forward shock into the host ISM (). At this point , the interaction between the inner wind and the ISM, regulated by the shock and resulting in large scale outflows, depends on different conditions in the galaxy. If some cooling process removes significant energy from the shocked wind gas on time scales shorter than the flow-time, most of the initial energy is lost, and the outflow kinetic rate results $\dot{K}_{out} << \dot{K}_w$. The shocked region then is very narrow (see A. King and K. Pounds 2015, fig. 8) and the wind can be imagined to collide with the ISM directly (**Costa2014** ), fully transferring its momentum. In such a case, defining the so-called "momentum driven mode", we should observe a momentum rate in the large scale outflow

$$\dot{P_o}ut \approx L_{Edd}/c. \tag{6.3}$$

In the opposite limit in which the cooling processes are not efficient, we have the "energy driven mode": in this case the shock wind gas preserve its energy rate, and $\dot{K}_{out} \approx \dot{E}_w$. Explicating the equation we derive:

$$\dot{M}_w v^2 \simeq \dot{M}_{out} v_{out}^2,$$

or equivalently, written using the momentum rate $\dot{P} = \dot{M}v$,

$$\dot{P}_w v \simeq \dot{P}_{out} v$$

$$\frac{\dot{P}_{out}}{\dot{P}_w} \simeq \frac{v}{v_{out}} \approx 20 \tag{6.4}$$

using $v = 0.1c$ and an outflow velocity of 1500 km/s.

The measurement of kinetic and momentum rate for the observed large-scale outflows can be compared with Eq 6.2, to constrain the actual amount of energy coupled with the ISM, and with Eq. 6.3 and 6.4, to test which one between the two driven modes is actually responsible for the outflows. We note, however, that such predictions are referred to the energetics of the entire amount of ejected material, and that any comparison involving only a specific component phase of the outflow may translate in a challenging meaning.

Table **??** shows the relevant outflow measurements of the four targets analysed in the previous Chapters. We prefer to restrict the comparison with model predictions to the only sources for which we were able to constrain the extension of the outflows, in order to limit, as best we can, the uncertainties in the energetics (see below). Motivated by the results obtained in Chapter 2, **??**, 4, the outflow mass rates and the energetics are re-computed assuming an electron temperature of $1.7 \times 10^4$ K for all but XID 5395 source, for which we were able to derive $T_e = 1.3 \times 10^4$ K. Moreover, for the two sources for which it was not possible to infer electron density, XID 2028 and MIRO 20581, we derive the outflow properties using the average electron density we found in Chapter 5, $N_e = 1000$ cm$^{-3}$. We underline that the different electron temperature and density reflect in the coefficient of the equations used to derive the outflow mass rates and energetics. Here we report the two equations we used through the Thesis (Eq. B.8 and B.9 ), but assuming $T_e = 1.7 \times 10^4$ and $N_e = 1000$ cm$^{-3}$:

$$\dot{M}_{out} = 60 \frac{C L_{44}([OIII]) V_{out,3}}{N_{e,3} R_{kpc} 10^{[O/H]-[O/H]_{\odot}}} \; M_{\odot} s^{-1}, \tag{6.5}$$

Table 6.1: Outflow mass rates and energetics

| | XID 2028 | XID 5321 | XID 5395 | MIRO 20581 |
|---|---|---|---|---|
| $\dot{M}^{ion}_{out}$ (M$_\odot$/yr) | 2 | 20 | 50 | 70 |
| $\dot{K}_{out}$ (erg s$^{-1}$) | $2{\times}10^{42}$ | $2 \times 10^{43}$ | $5{\times}10^{43}$ | $5 \times 10^{42}$ |
| $\dot{K}_{out}/L_{bol}$ | 0.01% | 0.1% | 0.5% | 0.01% |
| $\dot{P}_{out}/(L_{bol}/c)$ | 0.03 | 0.4 | 2 | 0.5 |

Notes: Energetic values obtained from Eq. 6.5, 6.1, or Eq. B.8, B.9 depending on the measured/assumed electron densities and temperatures. A solar metallicity is assumed.

and the kinetic power

$$\dot{E}_{out} = 1.9 \times 10^{43} \frac{CL_{44}([OIII])V^3_{out,3}}{N_{e,3}R_{kpc}10^{[O/H]-[O/H]_\odot}}\ erg\ s^{-1},$$

The kinetic powers we obtained are lower than the value expected from Eq. 6.2, of a factor of 10 to 500. Similarly, the momentum flux ratio values are equal or lower unity.

When we compare our results with literature, we find that our measurements are in general agreement with those of other authors. Figure 6.1 shows the kinetic power vs. the bolometric luminosity (upper panel) and the momentum flux vs. the nuclear $\dot{P}_w$ for a compilation of targets with outflows detected in molecular (squared symbols) or ionized (circular symbols) phase collected by Carniani et al. (2015, see also Stern2016). The compilation includes also the z ≈ 1.5 X-Shooter targets we presented in Chapter 2 (orange symbols). We note that the outflow energetics are derived assuming an electron density $N_e = 500$ cm$^{-3}$ for all sources and that a shell-like geometrical configuration is assumed instead of the bi-conical one used in this Thesis (see Appendix B.0.1). As a consequence, the value reported here are 15× lower than those in Fig. 2.22. This highlights the current uncertainties in outflow energetics: different assumptions in all the other quantities in Eq. 6.5, 6.1 (e.g., see Sect. 2.5.6 for a discussion on the outflow velocity estimators) may easily account discrepancies of the same order of magnitude. Regardless these discrepancies, we find that the kinematic power derived from the ionized gas component is always $\lesssim$ of 0.1% of the bolometric luminosity. However, we note that all the kinetic energy rates derived from H$\beta$ emission are higher than those obtained from [OIII] flux. This is likely due to the fact that the warm phase of the outflow traced by the [OIII] line account only of a small fraction of the total amount of the ejected material. We mentioned this argument in Chapter 2 when the comparison between the H$\beta$ and [OIII] outflow energetics displayed a discrepancy of a factor of 10. Moreover, the kinetic energy rate associated with the cold molecular phase are even higher than those obtained from H$\beta$, approaching the expected 5% of the bolometric luminosity (Eq. 6.2). We conclude therefore that the ionized phase account only a small fraction of the ejected material. Such conclusion is also confirmed by more recent models (e.g., **ZubovasKing2014** ), which predict that most of the outflow mass is in the molecular phase. The lower panel in Fig. 6.1 shows that all the momentum rates associated with molecular component are higher than those of the ionized gas. In particular, the momentum fluxes estimated for the molecular outflows are consistent with the expected relation for the energy conserving models.

So far, we collected a large number of indirect evidences about the mechanisms governing the outflow phenomena. The fact that the ionized phase traces only a small fraction of the total amount of gas has been inferred observing the warm and cold phases in different objects. This highlights the necessity of synergies between major facilities to study the interaction between the nuclear wind and all the ISM gas phases. The observational connection between the hot phase of the wind, traced by UFOs, and the kpc-scale outflows, traced by cold gas components, has been proved only recently. Tombesi et al. (2015), characterizing for the first time both the X-ray absorption material and the ISM molecular gas in a type 1 AGN-ULIRG, showed that both the hot and the cold phases are partecipating in the outflow and that the two components are actually associated with momentum fluxes expected by energy conserving models predictions, with a $\dot{P}_w \approx L_{bol}/c$ for the nuclear UFO, and

$\dot{P}_{out} \approx 20 L_{bol}/c$ for the molecular outflow. The same results have been obtained by **Feruglio2015** for a second source, Mrk 321, again testing the hot and the molecular phases.

## 6.2 Feedback signatures

Synergies between major facilities are also needed to prove the effects of these outflows on the host galaxy. In fact, the ejected material is expected to sweep away the gas and to prevent the SF, but also, as exposed by several authors (**ZubovasKing2014**; **Silk2013** ), to induce SF in the host through enhancing the turbulence in the ISM. For one of the z $\sim$ 1.5 targets we presented in Chapter 2, XID 2028, we collected several arguments pointing to a direct evidence of the impact of the observed outflow on the host galaxy. Combining the spatially resolved kinematic information we derived from SINFONI datacube analysis with rest-frame U-band flux from HST-ACS we found that the current SF in the host galaxy marks the boundary of the outflow region traced by the ionized [OIII] line (Fig. 6.2), i.e. the outflow and the SF regions anti-correlate (see also Cano-Díaz et al. 2012; Carniani et al. 2016; Cresci et al. 2015b for similar results). This suggests that the outflow may actually prevent the SF removing the gas (negative feedback), but also trigger the SF by induced pressure at the edge of the outflow region (positive feedback).

Follow-up observations collected so far are all confirming this scenario. In particular, with the PdBI interferometer, through the observation of the molecular CO(3-2) transition, we infer a value for the molecular gas mass in the range $\mathrm{M}_{gas} = 2.1 - 9.5 \times 10^{10}$ $\mathrm{M}_{\odot}$. When compared to that expected for $\mathrm{M}_{\star} > 10^{11}$ $\mathrm{M}_{\odot}$ systems with the same observed specific-SFR and at the same redshift, the molecular gas fraction is consistent with a scenario where the gas in the host galaxy of XID 2028 has been already partly depleted by the effects of the strong QSO feedback (see Fig. 6.3; **Brusa2015b** ). Furthermore, the XID 2028 depletion time-scale ($\mathrm{M}_{gas}$/SFR), i.e. the ratio at which the gas is converted into stars, is much lower than that of other MS galaxies and is actually similar to that of other obscured QSOs associated with molecular outflows (Fig. 6.3, right). The PdBI data provided an independent, yet indirect, evidence for our proposed scenario. In fact, the poor spatial resolution (see **Brusa2015b** fig. 1) does not enable the investigation of the distribution of molecular gas within the galaxy, and to unveil the possible presence of molecular outflows (or the depletion of molecular gas) in the region associated with ionized outflow. We recently obtained ALMA data for this target. Preliminary results show a well detected ($10\sigma$) CO(5-4) line, with an extended blue wing tracing the ionized outflow emission, hence directly confirming that the depletion in molecular gas is related to feedback effects.

## 6.3 Outlook

The work in this thesis has demonstrated that powerful outflows are very common in AGN hosts. Kinematic and physical characterization of ionized emitting gas have been derived analysing rest-frame near-UV and optical long-slit and integral field spectroscopic data, obtained at ESO-VT (X-Shooter, SINFONI), as well as archival spectra (SDSS). The presence of outflow signatures in spatially integrated spectra have been inferred by the presence of complex [O III]$\lambda$5007 line profiles, generally displaying extended wings at bluer (and, sometimes, redder) wavelengths up to $\approx 1000 - 1500$ km/s in velocity space (with respect to the host galaxy systemic), and FWHM (of the total profile) of the order of 1000 km/s. When follow-up observation allowed spatially resolved investigation, through integral field or slit-resolved spectroscopy, we confirmed that such complex profiles are actually associated with different kinematic structures, with narrow components, tracing the unperturbed ionized gas, and outflow components, likely associated with more extended structures (up to $\sim$ 10 kpc from the central SMBH) and characterized by FWHM $\approx 600 - 2000$ km/s.

Furthermore, we were able to derive the outflow mass rates and energetics from the [O III] outflow emission. We also collected several arguments pointing to the fact that such estimates represent lower limit for the energetics of the outflow, characterized by a multicomponent gas phase, in which the warm ionized gas traced by the [O III] account only a small fraction ($\lesssim 10\%$) of the total amount of the ejected material. Such arguments highlights the necessity of a major facility synergy to trace all the outflow gas phases in the ISM of an AGN-host galaxy system in the feedback stage.

The comparison with model predictions indicates that the powerful, wide scale outflows observed locally and at z $\sim$ 2 are consistent with an energy conserving scenario. Such comparisons are mostly based on molecular (and X-ray) observations which, so far, provided best reliable energetic estimates.

The analysis of signatures of outflows in the host galaxy represents an important but partial step towards the characterization of the outflow phenomena. The study of host galaxy properties (e.g., SF activity, stellar mass, morphology) are crucial to determine the conditions required to switch on the feedback phase and to unveil the effects of such outflows. Through this thesis, we analysed all the ancillary multiwavelength data to constrain the host galaxy properties for the small samples at z $\sim$ 1.5 in the COSMOS field, but non-conclusive indications are found. The correspondence between luminous red sources associated with a X-ray loudness and the "feedback phase with prominent outflows" may not be exclusive, because the physical conditions that determine the presence and observability of an outflow (e.g. the wind velocity, fraction of energy released, properties in the ISM in which the outflows propagate) *and* the observed host galaxies properties of AGN (e.g. the time-scales of accretion and star formation processes, the viewing angle and/or the amount of obscuring material in the system) may vary from source to source. This translates into the fact that galaxy-wide outflows can also be observed in blue and unobscured AGNs, especially at the highest luminosity, for which the line of sight may be cleaner for the combination of both viewing angle and larger energetics. Further investigation is required to understand this particular phase of the AGN-galaxy evolution.

In the next few years the ESO Large Programme SUPER (a `SINFONI` Survey for Unveiling the Physics and Evolution of Radiative feedback, PI: V. Mainieri) will undertake this task by targeting, with the needed resolution and depth, a sample of $\sim$40 AGN at z $\sim$2. Gas kinematics for [O III], H$\alpha$ and H$\beta$ lines with $\sim$ 1 kpc spatial resolution will allow to constrain the geometric and energetic outflow properties, probing four decades in AGN bolometric luminosity. In addition, multiple diagnostics should be employed to select the best cases and to study the effect of feedback from AGN in action. Significant advances on this topic will come with the analysis of other large and unbiased samples both at high redshift, from infrared spectra of AGN selected from multiwavelength surveys (e.g. KASHz survey), and locally with even more large samples from optical spectra (e.g., MaNGA survey). Finally, the molecular component of the outflows is still to be explored in detail, and follow-up observations with NOEMA and ALMA are needed to obtain the full picture on the energetics and processes that dominate the outflows. The cold component may be the material most interested by the feedback phenomena and, being the immediate fuel from which stars form, it is also a crucial phase to be probed to test the effects of feedback. The study of the molecular gas content in obscured/unobscured AGNs with strong evidence of feedback in act, and in Compton thick AGNs, tracing the initial phases of a merging system (hence in the prelude of the blow-out stage), may allow an important test for the evolutionary scenario. In fact, according to the AGN feedback paradigm, CT QSOs should be associated with more massive gas reservoirs than their unobscured QSO descendants. In this respect, we have started an experiment studying the CO(1-0) transition observed with the JVLA telescope to trace the cold gas content in a small sample of Compton Thick (CT) QSOs at z $\sim$ 2, associated with intense SF activity. This will allow important constraints for the understanding of feedback processes.

AGN feedback is a relative young topic and, so far, few direct (and non-certain) indications of its impact on galaxy evolution have been collected. Current studies show promising early results. New observations over the next years, combining multiwavelength information from radio to X-ray bands and taking advantage from current and future facilities (e.g., JWST, SKA, SPICA, EUCLID, Athena, eROSITA) will lead to improved theoretical frameworks which will define rapid improvement in our understanding of outflow phenomena.

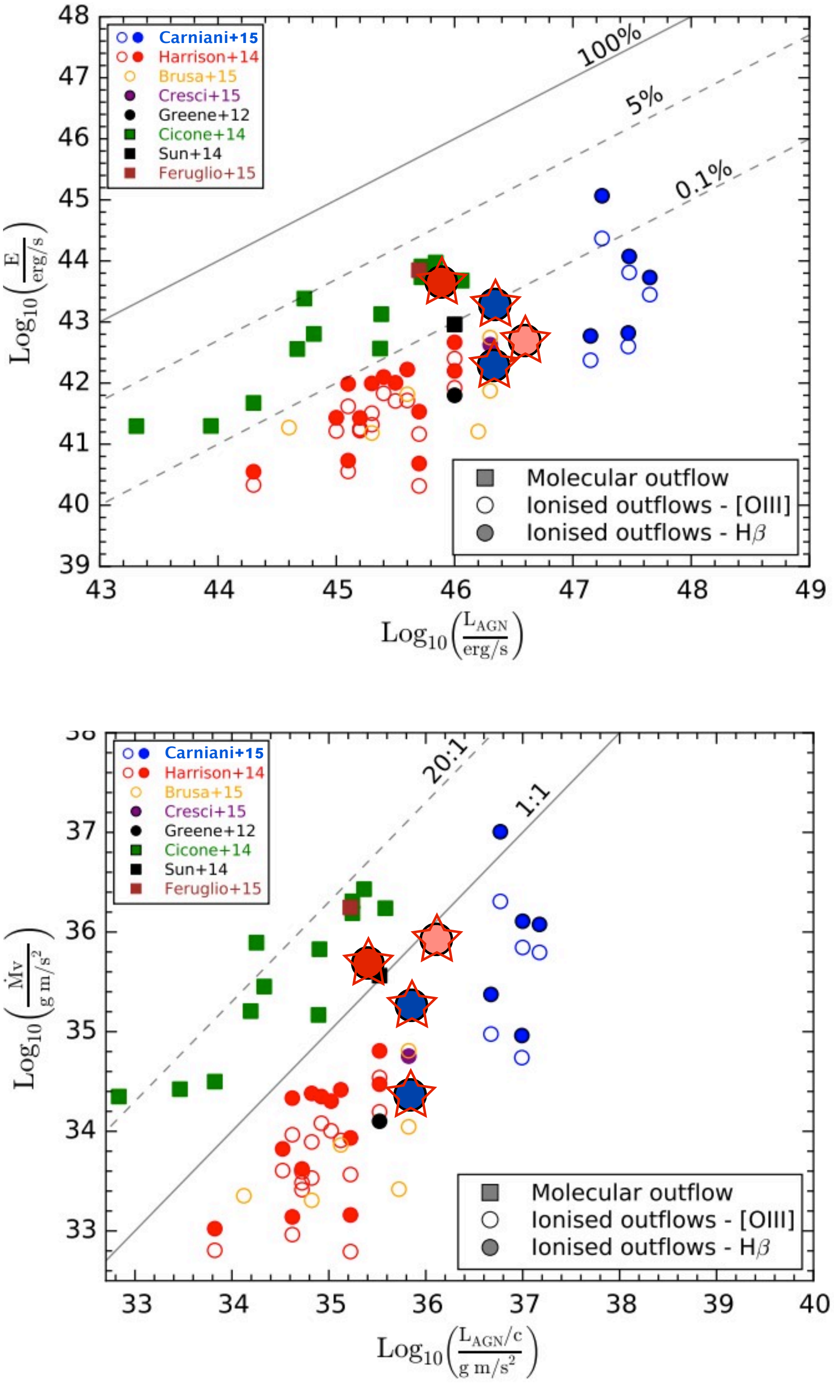

Figure 6.1: [OIII]$\lambda$5007 total luminosity vs. redshift for the 624 candidate AGNs, colored by nominal SDSS signal to noise ratio as labeled in the colorbar.

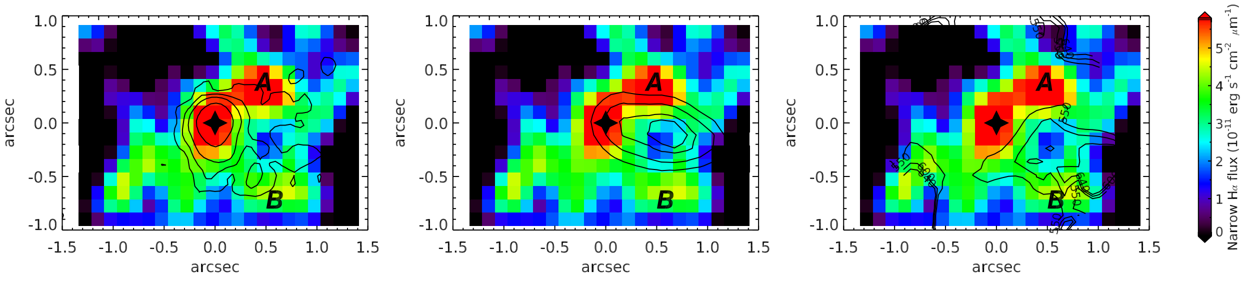

Figure 6.2: Narrow H$\alpha$ map. The map is obtained integrating the single broad Gaussian H$\alpha$ fit residuals on the spectral channels $1.7015 < \lambda < 1.7047$ $\mu m$. In the *left panel* the HST-ACS rest frame U band contours are superimposed in black (ACS level relative to the peak are 0.008, 0.015, 0.022, 0.05, 0.1, 0.5). The same pattern is obtained by these two independent tracers of star formation in the host galaxy, with two additional clumps of star formation (marked with A and B) elongated at the west of the QSO (marked with a star). In the *central panel* the blue wing contours from Fig. **??**, tracing the outflow position, are plotted for comparison. A clear anti-correlation between the outflow location and the star formation tracers suggests that the outflowing material is sweeping the gas along the outflow core ('negative feedback'), while is compressing the gas at its edges inducing star formation at the locations marked as $A$ and $B$ on the map ('positive feedback'). The *right panel* shows the $W_{40}$ lie width contours (i.e. the velocity width of the line that contains 80% of the emission line flux such that $W_{40} = v_{50} - v_{10}$, where $v_{50}$ and $v_{10}$ are the velocities at the 50th and 10th percentiles, respectively; velocity levels 900, 1000, 1200 km/s) over-plotted on the narrow H$\alpha$ residuals. It can be seen how the shape of the H$\alpha$ residuals, including the discontinuity between the central clump and the south west one, is anti correlated with regions of large line emission, $W_{40} > 550$ $km/s$, due to the outflowing gas.

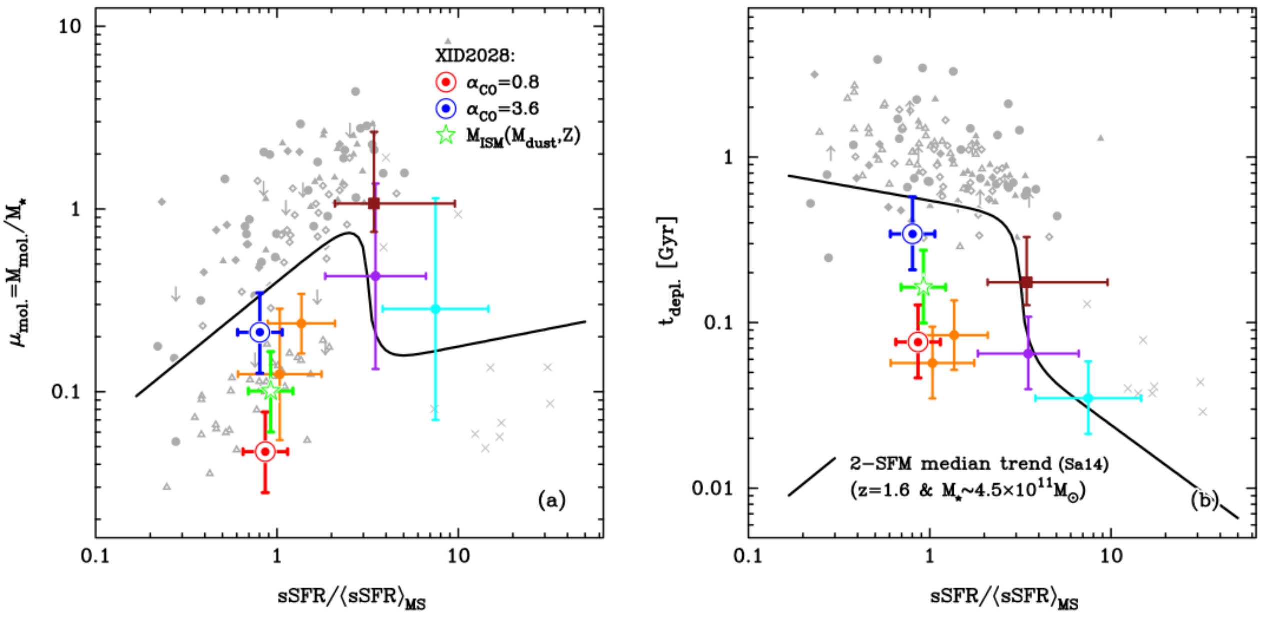

Figure 6.3: Gas fraction $\mu_{\rm mol}$ *(Left panel)* and depletion timescale *(Right panel)* plotted versus the sSFR-excess for the same samples and with the same color code presented in Figure 3. The values for XID2028 are slightly offset in the x-axis for clarity. All quantities are normalized to the expected values for normal and starburst galaxies predicted by the calibration presented in **Sargent2014** The black line traces the expected variation (median) with sSFR for a MS spiral galaxy with identical mass and redshift as XID2028 (see **Sargent2014** ). The step at sSFR/<sSFR>∼4 reflects the transition from the main sequence locus to the sSFR-regime where high-SFE starbursts dominate. XID2028 lies a factor ∼2 to ∼10 below the black line, i.e. it shows significant lower gas fraction and depletion time scale than those expected for the properties of the its host galaxy.

# Bibliography

[1] T. F. Adams and D. W. Weedman. “Emission-line luminosities of Seyfert galaxies”. In: ApJ 199 (July 1975), pp. 19–30 (cit. on p. 10).

[2] D. M. Alexander and R. C. Hickox. “What drives the growth of black holes?” In: NewAR 56 (June 2012), pp. 93–121 (cit. on p. 31).

[3] D. M. Alexander, I. Smail, et al. “Rapid growth of black holes in massive star-forming galaxies”. In: NATURE 434 (Mar. 2005), pp. 738–740 (cit. on p. 21).

[4] D. M. Alexander, A. M. Swinbank, et al. “Searching for evidence of energetic feedback in distant galaxies: a galaxy wide outflow in a z $\sim$ 2 ultraluminous infrared galaxy”. In: MNRAS 402 (Mar. 2010), pp. 2211–2220 (cit. on pp. 30, 67).

[5] D. M. Alexander, C. Vignali, et al. “The Chandra Deep Field North Survey. X. X-Ray Emission from Very Red Objects”. In: AJ 123 (Mar. 2002), pp. 1149–1162 (cit. on pp. 93, 97).

[6] J. T. Allen, P. C. Hewett, et al. “A strong redshift dependence of the broad absorption line quasar fraction”. In: MNRAS 410 (Jan. 2011), pp. 860–884 (cit. on p. 30).

[7] M. G. Allen, B. A. Groves, et al. “The MAPPINGS III Library of Fast Radiative Shock Models”. In: ApJS 178, 20-55 (Sept. 2008), pp. 20–55 (cit. on pp. 87, 132).

[8] R. Amorín, E. Pérez-Montero, et al. “Extreme emission-line galaxies out to z ˜ 1 in zCOSMOS. I. Sample and characterization of global properties”. In: A&A 578, A105 (June 2015), A105 (cit. on p. 75).

[9] R. Antonucci. “A panchromatic review of thermal and nonthermal active galactic nuclei”. In: A&AT 27 (2012), pp. 557–602 (cit. on p. 16).

[10] R. Antonucci. “Unified models for active galactic nuclei and quasars”. In: ARA&A 31 (1993), pp. 473–521 (cit. on p. 14).

[11] R. Antonucci and J. S. Miller. “Spectropolarimetry and the nature of NGC 1068”. In: ApJ 297 (Oct. 1985), pp. 621–632 (cit. on p. 14).

[12] K. Aoki, T. Kawaguchi, and K. Ohta. “The Largest Blueshifts of the [O III] Emission Line in Two Narrow-Line Quasars”. In: ApJ 618 (Jan. 2005), pp. 601–608 (cit. on p. 24).

[13] H. Awaki, K. Koyama, et al. “X-ray implications of a unified model of Seyfert galaxies”. In: PASJ 43 (Apr. 1991), pp. 195–212 (cit. on p. 14).

[14] H.-J. Bae and J.-H. Woo. “A Census of Gas Outflows in Type 2 Active Galactic Nuclei”. In: ApJ 795, 30 (Nov. 2014), p. 30 (cit. on pp. 51, 114).

[15] J. A. Baldwin, M. M. Phillips, and R. Terlevich. “Classification parameters for the emission-line spectra of extragalactic objects”. In: pasp 93 (Feb. 1981), pp. 5–19 (cit. on pp. 62, 87, 116, 168, 169).

[16] B. Balmaverde, A. Marconi, et al. “Is there any evidence that ionized outflows quench star formation in type 1 quasars at z $<$ 1?” In: A&A 585, A148 (Jan. 2016), A148 (cit. on pp. 108, 114).

[17] M. Banerji, A. C. Fabian, and R. G. McMahon. “ULASJ1234+0907: the reddest type 1 quasar at z = 2.5 revealed in the X-ray and far-infrared”. In: MNRAS 439 (Mar. 2014), pp. L51–L55 (cit. on pp. 30, 66, 67).

[18] M. Banerji, R. G. McMahon, et al. “Heavily reddened quasars at z ∼ 2 in the UKIDSS Large Area Survey: a transitional phase in AGN evolution”. In: MNRAS 427 (Dec. 2012), pp. 2275–2291 (cit. on pp. 30–32, 66, 91).

[19] J. Bechtold. “Quasar absorption lines”. In: Galaxies at High Redshift. Ed. by I. Pérez-Fournon, M. Balcells, et al. 2003, pp. 131–184 (cit. on p. 66).

[20] M. C. Begelman and D. F. Cioffi. “Overpressured cocoons in extragalactic radio sources”. In: ApJL 345 (Oct. 1989), pp. L21–L24 (cit. on p. 89).

[21] E. F. Bell. “Estimating Star Formation Rates from Infrared and Radio Luminosities: The Origin of the Radio-Infrared Correlation”. In: ApJ 586 (Apr. 2003), pp. 794–813 (cit. on p. 77).

[22] A. J. Benson, R. G. Bower, et al. “What Shapes the Luminosity Function of Galaxies?” In: ApJ 599 (Dec. 2003), pp. 38–49 (cit. on p. 18).

[23] M. C. Bentz, K. D. Denney, et al. “The Low-luminosity End of the Radius-Luminosity Relationship for Active Galactic Nuclei”. In: ApJ 767, 149 (Apr. 2013), p. 149 (cit. on p. 12).

[24] M. C. Bentz, J. L. Walsh, et al. “The Lick AGN Monitoring Project: Broad-line Region Radii and Black Hole Masses from Reverberation Mapping of H$\beta$”. In: ApJ 705 (Nov. 2009), pp. 199–217 (cit. on p. 12).

[25] S. Berta, D. Lutz, et al. “Panchromatic spectral energy distributions of Herschel sources”. In: A&A 551, A100 (Mar. 2013), A100 (cit. on pp. 76, 77, 100, 102).

[26] R. D. Blandford and C. F. McKee. “Reverberation mapping of the emission line regions of Seyfert galaxies and quasars”. In: ApJ 255 (Apr. 1982), pp. 419–439 (cit. on p. 12).

[27] R. D. Blandford, H. Netzer, et al., eds. Active Galactic Nuclei. 1990, p. 97 (cit. on pp. 168, 169).

[28] A. D. Bolatto, S. R. Warren, et al. “Suppression of star formation in the galaxy NGC 253 by a starburst-driven molecular wind”. In: NATURE 499 (July 2013), pp. 450–453 (cit. on p. 18).

[29] A. Bongiorno, R. Maiolino, et al. “The $M_{BH}$-$M_*$ relation for X-ray-obscured, red QSOs at $1.2 < z < 2.6$”. In: MNRAS 443 (Sept. 2014), pp. 2077–2091 (cit. on pp. 33, 35, 40, 48, 67, 108, 120).

[30] A. Bongiorno, A. Merloni, et al. “Accreting supermassive black holes in the COSMOS field and the connection to their host galaxies”. In: MNRAS 427 (Dec. 2012), pp. 3103–3133 (cit. on pp. 31, 33, 49, 74).

[31] M. Bonzini, P. Padovani, et al. “The sub-mJy radio sky in the Extended Chandra Deep Field-South: source population”. In: MNRAS 436 (Dec. 2013), pp. 3759–3771 (cit. on pp. 96, 100).

[32] R. Bordoloi, S. J. Lilly, et al. “The dependence of Galactic outflows on the properties and orientation of zCOSMOS galaxies at z ∼ 1”. In: ArXiv e-prints (July 2013) (cit. on p. 66).

[33] N. Bouché, M. T. Murphy, et al. “Signatures of Cool Gas Fueling a Star-Forming Galaxy at Redshift 2.3”. In: Science 341 (July 2013), pp. 50–53 (cit. on p. 101).

[34] K. Brand, M. J. I. Brown, et al. “The Chandra XBoötes Survey. III. Optical and Near-Infrared Counterparts”. In: ApJ 641 (Apr. 2006), pp. 140–157 (cit. on p. 97).

[35] K. Brand, A. Dey, et al. “Optical Line Diagnostics of z ∼ 2 Optically Faint Ultraluminous Infrared Galaxies in the Spitzer Boötes Survey”. In: ApJ 663 (July 2007), pp. 204–217 (cit. on pp. 94, 97, 107, 108).

[36] W. N. Brandt and D. M. Alexander. “Cosmic X-ray surveys of distant active galaxies. The demographics, physics, and ecology of growing supermassive black holes”. In: A&ARv 23, 1 (Jan. 2015), p. 1 (cit. on p. 95).

[37] M. Brusa, A. Bongiorno, et al. “X-shooter reveals powerful outflows in z ∼ 1.5 X-ray selected obscured quasi-stellar objects”. In: MNRAS 446 (Jan. 2015), pp. 2394–2417 (cit. on pp. 32, 33, 35, 37, 38, 48, 60, 69, 76, 91, 94, 107, 108, 111).

[38] M. Brusa, F. Civano, et al. “The XMM-Newton Wide-field Survey in the Cosmos Field (XMM-COSMOS): Demography and Multiwavelength Properties of Obscured and Unobscured Luminous Active Galactic Nuclei”. In: ApJ 716 (June 2010), pp. 348–369 (cit. on pp. 25, 29, 31, 33, 41, 48, 57, 74, 75, 91, 99).

[39] M. Brusa, A. Comastri, et al. “XMM-Newton observations of Extremely Red Objects and the link with luminous, X-ray obscured quasars”. In: A&A 432 (Mar. 2005), pp. 69–81 (cit. on p. 31).

[40] M. Brusa, M. Perna, et al. “A fast ionised wind in a star-forming quasar system at z $\sim$ 1.5 resolved through adaptive optics assisted near-infrared data”. In: aap 588, A58 (Apr. 2016), A58 (cit. on p. 38).

[41] L. Burtscher, K. Meisenheimer, et al. “A diversity of dusty AGN tori. Data release for the VLTI/MIDI AGN Large Program and first results for 23 galaxies”. In: A&A 558, A149 (Oct. 2013), A149 (cit. on p. 16).

[42] R. S. Bussmann, A. Dey, et al. “Hubble Space Telescope Morphologies of z $\sim$ 2 Dust Obscured Galaxies. I. Power-Law Sources”. In: ApJ 693 (2009), pp. 750–770 (cit. on p. 107).

[43] M. Cano-Díaz, R. Maiolino, et al. “Observational evidence of quasar feedback quenching star formation at high redshift”. In: A&A 537, L8 (Jan. 2012), p. L8 (cit. on pp. 30, 55, 64, 67, 74, 88, 106, 127, 140, 173).

[44] M. Cappellari. “Improving the full spectrum fitting method: accurate convolution with Gauss-Hermite functions”. In: ArXiv e-prints (July 2016) (cit. on p. 116).

[45] M. Cappellari and E. Emsellem. “Parametric Recovery of Line-of-Sight Velocity Distributions from Absorption-Line Spectra of Galaxies via Penalized Likelihood”. In: PASP 116 (Feb. 2004), pp. 138–147 (cit. on p. 116).

[46] N. Cappelluti, M. Brusa, et al. “The XMM-Newton wide-field survey in the COSMOS field. The point-like X-ray source catalogue”. In: A&A 497 (Apr. 2009), pp. 635–648 (cit. on pp. 31, 74).

[47] C. Cardamone, K. Schawinski, et al. “Galaxy Zoo Green Peas: discovery of a class of compact extremely star-forming galaxies”. In: MNRAS 399 (Nov. 2009), pp. 1191–1205 (cit. on p. 83).

[48] J. A. Cardelli, G. C. Clayton, and J. S. Mathis. “The relationship between infrared, optical, and ultraviolet extinction”. In: ApJ 345 (Oct. 1989), pp. 245–256 (cit. on p. 83).

[49] S. Carniani, A. Marconi, et al. “Fast outflows and star formation quenching in quasar host galaxies”. In: A&A 591, A28 (June 2016), A28 (cit. on p. 140).

[50] S. Carniani, A. Marconi, et al. “Ionised outflows in z $\sim$ 2.4 quasar host galaxies”. In: A&A 580, A102 (Aug. 2015), A102 (cit. on pp. 24, 30, 74, 88, 106, 127, 139).

[51] W. Cash. “Parameter estimation in astronomy through application of the likelihood ratio”. In: ApJ 228 (Mar. 1979), pp. 939–947 (cit. on p. 99).

[52] G. Cecil, J. Bland-Hawthorn, et al. “Jet- and Wind-driven Ionized Outflows in the Superbubble and Star-forming Disk of NGC 3079”. In: ApJ 555 (July 2001), pp. 338–355 (cit. on p. 22).

[53] R. Centeno and H. Socas-Navarro. “A New Approach to the Solar Oxygen Abundance Problem”. In: ApJL 682, L61 (July 2008), p. L61 (cit. on p. 171).

[54] M. Chiaberge, G. Tremblay, et al. “Low-Power Radio Galaxies in the Distant Universe: A Search for FR I at $1 < z < 2$ in the Cosmos Field”. In: ApJ 696 (May 2009), pp. 1103–1115 (cit. on p. 76).

[55] C. Cicone, R. Maiolino, et al. “Massive molecular outflows and evidence for AGN feedback from CO observations”. In: A&A 562, A21 (Feb. 2014), A21 (cit. on pp. 18, 24, 46, 113, 172).

[56] A. Cimatti, M. Brusa, et al. “Active Galactic Nucleus Feedback at z ˜ 2 and the Mutual Evolution of Active and Inactive Galaxies”. In: ApJ 779, L13 (Dec. 2013), p. L13 (cit. on p. 109).

[57] L. Ciotti, J. P. Ostriker, and D. Proga. “Feedback from Central Black Holes in Elliptical Galaxies. III. Models with Both Radiative and Mechanical Feedback”. In: ApJ 717 (July 2010), pp. 708–723 (cit. on p. 21).

[58] F. Civano, M. Elvis, et al. “The Chandra COSMOS Survey. III. Optical and Infrared Identification of X-Ray Point Sources”. In: ApJS 201, 30 (Aug. 2012), p. 30 (cit. on pp. 95, 99).

[59] F. Civano, S. Marchesi, et al. “The Chandra Cosmos Legacy Survey: Overview and Point Source Catalog”. In: ApJ 819, 62 (Mar. 2016), p. 62 (cit. on p. 80).

[60] C. Collet, N. P. H. Nesvadba, et al. “Kinematic signatures of AGN feedback in moderately powerful radio galaxies at z $\sim$ 2 observed with SINFONI”. In: A&A 586, A152 (Feb. 2016), A152 (cit. on pp. 24, 30, 163).

[61] J. J. Condon. “Radio emission from normal galaxies”. In: ARA&A 30 (1992), pp. 575–611 (cit. on p. 100).

[62] T. Contini, B. Garilli, et al. “MASSIV: Mass Assemby Survey with SINFONI in VVDS. I. Survey description and global properties of the $0.9 < z < 1.8$ galaxy sample”. In: A&A 539, A91 (Mar. 2012), A91 (cit. on pp. 75, 109, 110).

[63] G. Cresci, E. K. S. Hicks, et al. “The SINS Survey: Modeling the Dynamics of $z \sim 2$ Galaxies and the High-z Tully-Fisher Relation”. In: ApJ 697 (May 2009), pp. 115–132 (cit. on pp. 101, 109).

[64] G. Cresci, V. Mainieri, et al. “Blowin’ in the Wind: Both ”Negative” and ”Positive” Feedback in an Obscured High-z Quasar”. In: ApJS 799, 82 (Jan. 2015), p. 82 (cit. on pp. 30, 53–55, 63–65, 68, 70, 74, 88, 106, 110, 113, 127).

[65] G. Cresci, A. Marconi, et al. “The MAGNUM survey: positive feedback in the nuclear region of NGC 5643 suggested by MUSE”. In: A&A 582, A63 (Oct. 2015), A63 (cit. on pp. 89, 140).

[66] D. J. Croton, V. Springel, et al. “The many lives of active galactic nuclei: cooling flows, black holes and the luminosities and colours of galaxies”. In: MNRAS 365 (Jan. 2006), pp. 11–28 (cit. on p. 21).

[67] B. Czerny and M. Elvis. “Constraints on quasar accretion disks from the optical/ultraviolet/soft X-ray big bump”. In: ApJ 321 (Oct. 1987), pp. 305–320 (cit. on p. 13).

[68] E. da Cunha, S. Charlot, and D. Elbaz. “A simple model to interpret the ultraviolet, optical and infrared emission from galaxies”. In: MNRAS 388 (Aug. 2008), pp. 1595–1617 (cit. on pp. 76, 100, 102).

[69] X. Dai, F. Shankar, and G. R. Sivakoff. “2MASS Reveals a Large Intrinsic Fraction of BALQSOs”. In: ApJ 672, 108-114 (Jan. 2008), pp. 108–114 (cit. on p. 30).

[70] R. I. Davies. “A method to remove residual OH emission from near-infrared spectra”. In: MNRAS 375 (Mar. 2007), pp. 1099–1105 (cit. on p. 80).

[71] M. de Kool, N. Arav, et al. “Keck HIRES Observations of the QSO FIRST J104459.6+365605: Evidence for a Large-Scale Outflow”. In: ApJ 548 (Feb. 2001), pp. 609–623 (cit. on p. 30).

[72] M. M. De Robertis and D. E. Osterbrock. “An analysis of the narrow line profiles in Seyfert 2 galaxies”. In: ApJ 301 (Feb. 1986), pp. 727–741 (cit. on pp. 39, 114).

[73] A. Del Moro, M. G. Watson, et al. “An extreme EXO: a type 2 QSO at $z = 1.87$”. In: A&A 493 (Jan. 2009), pp. 445–451 (cit. on p. 93).

[74] R. Della Ceca, F. J. Carrera, et al. “Exploring the active galactic nuclei population with extreme X-ray-to-optical flux ratios ($f_x/f_o > 50$)”. In: MNRAS 447 (Mar. 2015), pp. 3227–3242 (cit. on p. 93).

[75] I. Delvecchio, C. Gruppioni, et al. “Tracing the cosmic growth of supermassive black holes to $z \sim 3$ with Herschel”. In: MNRAS 439 (Apr. 2014), pp. 2736–2754 (cit. on pp. 18, 19, 49, 76, 102).

[76] A. Dey, B. T. Soifer, et al. “A Significant Population of Very Luminous Dust-Obscured Galaxies at Redshift $z \sim 2$”. In: ApJ 677, 943-956 (Apr. 2008), pp. 943–956 (cit. on pp. 95, 97, 100, 108).

[77] T. Di Matteo, V. Springel, and L. Hernquist. “Energy input from quasars regulates the growth and activity of black holes and their host galaxies”. In: NATURE 433 (Feb. 2005), pp. 604–607 (cit. on pp. 20, 21).

[78] S. D’Odorico, H. Dekker, et al. “X-shooter UV- to K-band intermediate-resolution high-efficiency spectrograph for the VLT: status report at the final design review”. In: vol. 6269. Society of Photo-Optical Instrumentation Engineers (SPIE) Conference Series. July 2006 (cit. on p. 35).

[79] X. Dong, T. Wang, et al. “Broad-line Balmer decrements in blue active galactic nuclei”. In: MNRAS 383 (Jan. 2008), pp. 581–592 (cit. on pp. 61, 168).

[80] J. L. Donley, G. H. Rieke, et al. “Spitzer’s Contribution to the AGN Population”. In: ApJ 687, 111-132 (Nov. 2008), pp. 111–132 (cit. on pp. 95, 97).

[81] M. A. Dopita and R. S. Sutherland. “Spectral Signatures of Fast Shocks. II. Optical Diagnostic Diagrams”. In: ApJ 455 (Dec. 1995), p. 468 (cit. on p. 131).

[82] P. Du, J.-M. Wang, et al. “Outflows from active galactic nuclei: the BLR-NLR metallicity correlation”. In: MNRAS 438 (Mar. 2014), pp. 2828–2838 (cit. on p. 64).

[83] J. P. Dunn, M. Bautista, et al. “The Quasar Outflow Contribution to AGN Feedback: VLT Measurements of SDSS J0318-0600”. In: ApJ 709 (Feb. 2010), pp. 611–631 (cit. on p. 30).

[84] R. J. H. Dunn and A. C. Fabian. “Investigating AGN heating in a sample of nearby clusters”. In: MNRAS 373 (Dec. 2006), pp. 959–971 (cit. on p. 21).

[85] R. J. H. Dunn and A. C. Fabian. "Investigating heating and cooling in the BCS and B55 cluster samples". In: MNRAS 385 (Apr. 2008), pp. 757–768 (cit. on p. 21).

[86] A. S. Eddington. "On the radiative equilibrium of the stars". In: MNRAS 77 (Nov. 1916), pp. 16–35 (cit. on p. 4).

[87] P. R. M. Eisenhardt, J. Wu, et al. "The First Hyper-luminous Infrared Galaxy Discovered by WISE". In: ApJ 755, 173 (Aug. 2012), p. 173 (cit. on p. 66).

[88] M. Elvis, F. Civano, et al. "The Chandra COSMOS Survey. I. Overview and Point Source Catalog". In: ApJS 184 (Sept. 2009), pp. 158–171 (cit. on p. 95).

[89] M. Elvis, H. Hao, et al. "Spectral Energy Distributions of Type 1 Active Galactic Nuclei in the COSMOS Survey. I. The XMM-COSMOS Sample". In: ApJ 759, 6 (Nov. 2012), p. 6 (cit. on p. 74).

[90] M. Elvis, B. J. Wilkes, et al. "Atlas of quasar energy distributions". In: ApJS 95 (Nov. 1994), pp. 1–68 (cit. on p. 5).

[91] B. H. C. Emonts, R. Morganti, et al. "A jet-induced outflow of warm gas in 3C293". In: MNRAS 362 (Sept. 2005), pp. 931–944 (cit. on p. 70).

[92] H. Engel, L. J. Tacconi, et al. "Most Submillimeter Galaxies are Major Mergers". In: ApJ 724 (Nov. 2010), pp. 233–243 (cit. on p. 21).

[93] S. M. Faber, A. C. Phillips, et al. "The DEIMOS spectrograph for the Keck II Telescope: integration and testing". In: Instrument Design and Performance for Optical/Infrared Ground-based Telescopes. Ed. by M. Iye and A. F. M. Moorwood. Vol. 4841. Proceedings of the SPIE. Mar. 2003, pp. 1657–1669 (cit. on p. 57).

[94] A. C. Fabian. "Observational Evidence of Active Galactic Nuclei Feedback". In: ARA&A 50 (Sept. 2012), pp. 455–489 (cit. on pp. 24, 30).

[95] A. C. Fabian, R. V. Vasudevan, and P. Gandhi. "The effect of radiation pressure on dusty absorbing gas around active galactic nuclei". In: MNRAS 385 (Mar. 2008), pp. L43–L47 (cit. on p. 5).

[96] C. Fanti, R. Fanti, et al. "Are compact steep-spectrum sources young?" In: A&A 302 (Oct. 1995), p. 317 (cit. on p. 90).

[97] C.-A. Faucher-Giguère and E. Quataert. "The physics of galactic winds driven by active galactic nuclei". In: MNRAS 425 (Sept. 2012), pp. 605–622 (cit. on p. 137).

[98] L. Ferrarese, H. C. Ford, and W. Jaffe. "Evidence for a Massive Black Hole in the Active Galaxy NGC 4261 from Hubble Space Telescope Images and Spectra". In: ApJ 470 (Oct. 1996), p. 444 (cit. on pp. 14, 15).

[99] L. Ferrarese and D. Merritt. "A Fundamental Relation between Supermassive Black Holes and Their Host Galaxies". In: ApJL 539 (Aug. 2000), pp. L9–L12 (cit. on p. 18).

[100] C. Feruglio, R. Maiolino, et al. "Quasar feedback revealed by giant molecular outflows". In: A&A 518, L155 (July 2010), p. L155 (cit. on p. 24).

[101] F. Fiore, M. Brusa, et al. "The HELLAS2XMM survey. IV. Optical identifications and the evolution of the accretion luminosity in the Universe". In: A&A 409 (Oct. 2003), pp. 79–90 (cit. on pp. 31, 93).

[102] F. Fiore, A. Grazian, et al. "Unveiling Obscured Accretion in the Chandra Deep Field-South". In: ApJ 672, 94-101 (Jan. 2008), pp. 94–101 (cit. on pp. 26, 95, 101, 107).

[103] F. Fiore, S. Puccetti, et al. "Chasing Highly Obscured QSOs in the COSMOS Field". In: ApJ 693 (Mar. 2009), pp. 447–462 (cit. on pp. 31, 94, 95, 98–101).

[104] T. C. Fischer, D. M. Crenshaw, et al. "Determining Inclinations of Active Galactic Nuclei via their Narrow-line Region Kinematics. I. Observational Results". In: ApJS 209, 1 (Nov. 2013), p. 1 (cit. on pp. 16, 24, 163).

[105] D. J. E. Floyd, D. Axon, et al. "Hubble Space Telescope Near-infrared Snapshot Survey of 3CR Radio Source Counterparts. II. An Atlas and Inventory of the Host Galaxies, Mergers, and Companions". In: ApJS 177, 148-173 (July 2008), pp. 148–173 (cit. on p. 90).

[106] N. M. Förster Schreiber, R. Genzel, et al. "The Sins/zC-Sinf Survey of z $\sim$ 2 Galaxy Kinematics: Evidence for Powerful Active Galactic Nucleus-Driven Nuclear Outflows in Massive Star-Forming Galaxies". In: ApJ 787, 38 (May 2014), p. 38 (cit. on pp. 34, 109).

[107] H. Fu and A. Stockton. “Extended Emission-Line Regions: Remnants of Quasar Superwinds?” In: ApJ 690 (Jan. 2009), pp. 953–973 (cit. on p. 24).

[108] J. M. Gabor, R. Davé, et al. “Quenching massive galaxies with on-the-fly feedback in cosmological hydrodynamic simulations”. In: MNRAS 417 (Nov. 2011), pp. 2676–2695 (cit. on p. 18).

[109] P. Gandhi, H. Horst, et al. “Resolving the mid-infrared cores of local Seyferts”. In: A&A 502 (Aug. 2009), pp. 457–472 (cit. on pp. 48, 99).

[110] C. M. Gaskell and A. J. Benker. “AGN Reddening and Ultraviolet Extinction Curves from Hubble Space Telescope Spectra”. In: ArXiv e-prints (Nov. 2007) (cit. on p. 9).

[111] C. M. Gaskell and G. J. Ferland. “Theoretical hydrogen-line ratios for the narrow-line regions of active galactic nuclei”. In: PASP 96 (June 1984), pp. 393–397 (cit. on pp. 61, 83, 168).

[112] K. Gebhardt, R. Bender, et al. “A Relationship between Nuclear Black Hole Mass and Galaxy Velocity Dispersion”. In: ApJ 539 (Aug. 2000), pp. L13–L16 (cit. on p. 18).

[113] R. Gelderman and M. Whittle. “An optical study of compact steep-spectrum radio sources. 1: The spectroscopic data”. In: ApJS 91 (Apr. 1994), pp. 491–505 (cit. on p. 90).

[114] R. Genzel, N. M. Förster Schreiber, et al. “Evidence for Wide-spread Active Galactic Nucleus-driven Outflows in the Most Massive z $\sim$ 1-2 Star-forming Galaxies”. In: ApJ 796, 7 (Nov. 2014), p. 7 (cit. on pp. 74, 88, 104, 109, 110).

[115] A. Georgakakis, M. Rowan-Robinson, et al. “Infrared Excess sources: Compton thick QSOs, low-luminosity Seyferts or starbursts?” In: MNRAS 406 (July 2010), pp. 420–433 (cit. on pp. 99, 124).

[116] R. Gilli, A. Comastri, and G. Hasinger. “The synthesis of the cosmic X-ray background in the Chandra and XMM-Newton era”. In: A&A 463 (Feb. 2007), pp. 79–96 (cit. on p. 13).

[117] E. Glikman, M. D. Gregg, et al. “FIRST-2Mass Sources below the APM Detection Threshold: A Population of Highly Reddened Quasars”. In: aPj 607 (May 2004), pp. 60–75 (cit. on p. 94).

[118] E. Glikman, D. J. Helfand, et al. “The FIRST-2MASS Red Quasar Survey”. In: ApJ 667 (Oct. 2007), pp. 673–703 (cit. on pp. 94, 111).

[119] E. Glikman, T. Urrutia, et al. “FIRST-2MASS Red Quasars: Transitional Objects Emerging from the Dust”. In: ApJ 757, 51 (Sept. 2012), p. 51 (cit. on pp. 9, 30, 48).

[120] G. L. Granato, G. De Zotti, et al. “A Physical Model for the Coevolution of QSOs and Their Spheroidal Hosts”. In: ApJ 600 (Jan. 2004), pp. 580–594 (cit. on p. 21).

[121] J. E. Greene and L. C. Ho. “A Comparison of Stellar and Gaseous Kinematics in the Nuclei of Active Galaxies”. In: ApJ 627 (July 2005), pp. 721–732 (cit. on pp. 11, 120, 121).

[122] J. E. Greene, N. L. Zakamska, and P. S. Smith. “A Spectacular Outflow in an Obscured Quasar”. In: ApJ 746, 86 (Feb. 2012), p. 86 (cit. on p. 71).

[123] J. E. Greene, N. L. Zakamska, et al. “Feedback in Luminous Obscured Quasars”. In: ApJ 732, 9 (May 2011), p. 9 (cit. on p. 46).

[124] J. E. Greene, N. L. Zakamska, et al. “The Growth of Black Holes: Insights from Obscured Active Galaxies”. In: ApJ 702 (Sept. 2009), pp. 441–459 (cit. on p. 46).

[125] J. L. Greenstein. “Red-Shift of the Unusual Radio Source: 3C 48”. In: NATURE 197 (Mar. 1963), pp. 1041–1042 (cit. on p. 3).

[126] B. Groves and M. Allen. “ITERA: IDL Tool for Emission-line Ratio Analysis”. In: ArXiv e-prints (Feb. 2010) (cit. on p. 131).

[127] M. Guainazzi and S. Bianchi. “On the origin of soft X-rays in obscured AGN: answers from high-resolution spectroscopy with XMM-Newton”. In: MNRAS 374 (Feb. 2007), pp. 1290–1302 (cit. on p. 13).

[128] F. Haardt and L. Maraschi. “X-ray spectra from two-phase accretion disks”. In: ApJ 413 (Aug. 1993), pp. 507–517 (cit. on p. 12).

[129] K. N. Hainline, R. C. Hickox, et al. “Gemini Long-slit Observations of Luminous Obscured Quasars: Further Evidence for an Upper Limit on the Size of the Narrow-line Region”. In: ApJ 787, 65 (May 2014), p. 65 (cit. on p. 11).

[130] F. Hamann, K. T. Korista, et al. “Metallicities and Abundance Ratios from Quasar Broad Emission Lines”. In: ApJ 564 (Jan. 2002), pp. 592–603 (cit. on p. 30).

[131] H. Hao, M. Elvis, et al. “Spectral energy distributions of type 1 AGN in XMM-COSMOS - II. Shape evolution”. In: MNRAS 438 (Feb. 2014), pp. 1288–1304 (cit. on p. 74).

[132] C. M. Harrison, D. M. Alexander, et al. “Energetic galaxy-wide outflows in high-redshift ultraluminous infrared galaxies hosting AGN activity”. In: MNRAS 426 (Oct. 2012), pp. 1073–1096 (cit. on pp. 24, 30, 32, 34, 41, 46, 47, 51, 55, 65, 74, 109, 110, 113, 128).

[133] C. M. Harrison, D. M. Alexander, et al. “Kiloparsec-scale outflows are prevalent among luminous AGN: outflows and feedback in the context of the overall AGN population”. In: ArXiv e-prints (Mar. 2014) (cit. on pp. 24, 55, 63, 113, 127).

[134] C. M. Harrison, D. M. Alexander, et al. “The KMOS AGN Survey at High redshift (KASHz): the prevalence and drivers of ionized outflows in the host galaxies of X-ray AGN”. In: MNRAS 456 (Feb. 2016), pp. 1195–1220 (cit. on pp. 24, 30, 46–48, 55, 109).

[135] G. Hasinger, N. Cappelluti, et al. “The XMM-Newton Wide-Field Survey in the COSMOS Field. I. Survey Description”. In: ApJS 172 (Sept. 2007), pp. 29–37 (cit. on pp. 31, 74).

[136] Y. Hayano, H. Takami, et al. “Commissioning status of Subaru laser guide star adaptive optics system”. In: Adaptive Optics Systems II. Vol. 7736. procspie. July 2010, 77360N (cit. on p. 79).

[137] T. M. Heckman, L. Armus, and G. K. Miley. “On the nature and implications of starburst-driven galactic superwinds”. In: ApJS 74 (Dec. 1990), pp. 833–868 (cit. on p. 30).

[138] T. M. Heckman and P. N. Best. “The Coevolution of Galaxies and Supermassive Black Holes: Insights from Surveys of the Contemporary Universe”. In: ARA&A 52 (Aug. 2014), pp. 589–660 (cit. on pp. 3, 163).

[139] T. M. Heckman, G. Kauffmann, et al. “Present-Day Growth of Black Holes and Bulges: The Sloan Digital Sky Survey Perspective”. In: ApJ 613 (Sept. 2004), pp. 109–118 (cit. on pp. 18, 122).

[140] T. M. Heckman, G. K. Miley, et al. “Narrow-Line Profiles in Active Nuclei”. In: Bulletin of the AAS. Vol. 12. BAAS. Sept. 1980, p. 809 (cit. on p. 9).

[141] R. C. Hickox, J. R. Mullaney, et al. “Black Hole Variability and the Star Formation-Active Galactic Nucleus Connection: Do All Star-forming Galaxies Host an Active Galactic Nucleus?” In: ApJ 782, 9 (Feb. 2014), p. 9 (cit. on p. 24).

[142] L. C. Ho. “[O II] Emission in Quasar Host Galaxies: Evidence for a Suppressed Star Formation Efficiency”. In: ApJ 629 (Aug. 2005), pp. 680–685 (cit. on p. 62).

[143] S. F. Hönig, T. Beckert, et al. “Radiative transfer modeling of three-dimensional clumpy AGN tori and its application to NGC 1068”. In: A&A 452 (June 2006), pp. 459–471 (cit. on p. 14).

[144] P. F. Hopkins, L. Hernquist, et al. “A Cosmological Framework for the Co-Evolution of Quasars, Supermassive Black Holes, and Elliptical Galaxies. I. Galaxy Mergers and Quasar Activity”. In: ApJS 175, 356-389 (Apr. 2008), pp. 356–389 (cit. on pp. 21, 23, 51, 67, 73, 90, 101).

[145] P. F. Hopkins, L. Hernquist, et al. “A Physical Model for the Origin of Quasar Lifetimes”. In: ApJL 625 (June 2005), pp. L71–L74 (cit. on pp. 21, 30, 67).

[146] P. F. Hopkins, L. Hernquist, et al. “A Unified, Merger-driven Model of the Origin of Starbursts, Quasars, the Cosmic X-Ray Background, Supermassive Black Holes, and Galaxy Spheroids”. In: ApJS 163 (Mar. 2006), pp. 1–49 (cit. on pp. 21, 25).

[147] A. Humphrey, M. Villar-Martín, et al. “Deep spectroscopy of the FUV-optical emission lines from a sample of radio galaxies at z ˜ 2.5: metallicity and ionization”. In: MNRAS 383 (Jan. 2008), pp. 11–40 (cit. on p. 87).

[148] O. Ilbert, P. Capak, et al. “Cosmos Photometric Redshifts with 30-Bands for 2-deg$^2$”. In: ApJ 690 (Jan. 2009), pp. 1236–1249 (cit. on p. 104).

[149] F. James and M. Roos. “Minuit - a system for function minimization and analysis of the parameter errors and correlations”. In: Computer Physics Communications 10 (Dec. 1975), pp. 343–367 (cit. on p. 40).

[150] B. T. Jannuzi and A. Dey. “The NOAO Deep Wide-Field Survey”. In: Photometric Redshifts and... Ed. by R. Weymann, L. Storrie-Lombardi, et al. Vol. 191. Astronomical Society of the Pacific Conference Series. 1999, p. 111 (cit. on p. 107).

[151] T. Jones, C. Martin, and M. C. Cooper. “Temperature-based Metallicity Measurements at z=0.8: Direct Calibration of Strong-line Diagnostics at Intermediate Redshift”. In: ApJ 813, 126 (Nov. 2015), p. 126 (cit. on p. 88).

[152] D. Kakkad, V. Mainieri, et al. “Tracing outflows in the AGN forbidden region with SINFONI”. In: A&A 592, A148 (Aug. 2016), A148 (cit. on pp. 24, 30).

[153] D. Kashino, J. D. Silverman, et al. “The FMOS-COSMOS Survey of Star-forming Galaxies at z $\sim$ 1.6. I. H$\alpha$-based Star Formation Rates and Dust Extinction”. In: ApJ 777, L8 (Nov. 2013), p. L8 (cit. on pp. 34, 47).

[154] S. Kaspi, D. Maoz, et al. “The Relationship between Luminosity and Broad-Line Region Size in Active Galactic Nuclei”. In: ApJ 629 (Aug. 2005), pp. 61–71 (cit. on p. 12).

[155] S. Kaspi, P. S. Smith, et al. “Reverberation Measurements for 17 Quasars and the Size-Mass-Luminosity Relations in Active Galactic Nuclei”. In: ApJ 533 (Apr. 2000), pp. 631–649 (cit. on p. 12).

[156] G. Kauffmann and M. Haehnelt. “A unified model for the evolution of galaxies and quasars”. In: MNRAS 311 (Jan. 2000), pp. 576–588 (cit. on p. 21).

[157] R. C. Kennicutt Jr. “Star Formation in Galaxies Along the Hubble Sequence”. In: ARA&A 36 (1998), pp. 189–232 (cit. on p. 41).

[158] L. J. Kewley, M. A. Dopita, et al. “Theoretical Evolution of Optical Strong Lines across Cosmic Time”. In: ApJ 774, 100 (2013), p. 100 (cit. on pp. 10, 62, 64, 87, 119, 131, 168).

[159] L. J. Kewley, B. Groves, et al. “The host galaxies and classification of active galactic nuclei”. In: MNRAS 372 (Nov. 2006), pp. 961–976 (cit. on pp. 62, 168, 170).

[160] L. J. Kewley, C. A. Heisler, et al. “Optical Classification of Southern Warm Infrared Galaxies”. In: ApJS 132 (Jan. 2001), pp. 37–71 (cit. on pp. 10, 168–170).

[161] E. E. Khachikian and D. W. Weedman. “The Hubble diagram for Seyfert galaxies and related objects”. In: IAU Colloq. 37: Decalages vers le Rouge et Expansion... Ed. by C. Balkowski and B. E. Westerlund. 1977, pp. 411–424 (cit. on p. 3).

[162] É. Y. Khachikyan and D. W. Weedman. “A spectroscopic study of luminous galactic nuclei”. In: Astrophysics 7 (July 1971), pp. 231–240 (cit. on p. 3).

[163] É. Y. Khachikyan and D. W. Weedman. “An atlas of Seyfert galaxies”. In: ApJ 192 (Sept. 1974), pp. 581–589 (cit. on pp. 3, 4).

[164] M. Kim, L. C. Ho, et al. “Evidence for Active Galactic Nucleus Driven Outflows in Young Radio Quasars”. In: ApJL 768, L9 (May 2013), p. L9 (cit. on p. 90).

[165] A. King. “Black Holes, Galaxy Formation, and the $M_{BH}$-$\sigma$ Relation”. In: ApJ 596 (Oct. 2003), pp. L27–L29 (cit. on pp. 20, 137).

[166] A. King. “The AGN-Starburst Connection, Galactic Superwinds, and $M_{BH}$-$\sigma$”. In: ApJL 635 (Dec. 2005), pp. L121–L123 (cit. on pp. 73, 107, 108).

[167] A. R. King and K. A. Pounds. “Black hole winds”. In: MNRAS 345 (Oct. 2003), pp. 657–659 (cit. on p. 137).

[168] A. King and K. Pounds. “Powerful Outflows and Feedback from Active Galactic Nuclei”. In: ARA&A 53 (Aug. 2015), pp. 115–154 (cit. on pp. 20, 24, 137, 138, 172).

[169] N. Kobayashi, A. T. Tokunaga, et al. “IRCS: infrared camera and spectrograph for the Subaru Telescope”. In: Optical and IR Telescope Instrumentation and Detectors. Ed. by M. Iye and A. F. Moorwood. Vol. 4008. SPIE. Aug. 2000, pp. 1056–1066 (cit. on p. 79).

[170] A. M. Koekemoer, H. Aussel, et al. “The COSMOS Survey: Hubble Space Telescope Advanced Camera for Surveys Observations and Data Processing”. In: ApJS 172 (Sept. 2007), pp. 196–202 (cit. on pp. 55, 76).

[171] J. Kormendy and L. C. Ho. “Coevolution (Or Not) of Supermassive Black Holes and Host Galaxies”. In: ARA&A 51 (Aug. 2013), pp. 511–653 (cit. on pp. 16, 18, 19).

[172] J. Kormendy and R. C. Kennicutt Jr. “Secular Evolution and the Formation of Pseudobulges in Disk Galaxies”. In: ARA&A 42 (Sept. 2004), pp. 603–683 (cit. on p. 20).

[173] A. T. Koski. “Spectrophotometry of Seyfert 2 galaxies and narrow-line radio galaxies”. In: ApJ 223 (July 1978), pp. 56–73 (cit. on pp. 10, 11).

[174] J. Kovačević, L. Č. Popović, and M. S. Dimitrijević. “Analysis of Optical Fe II Emission in a Sample of Active Galactic Nucleus Spectra”. In: ApJS 189 (July 2010), pp. 15–36 (cit. on pp. 9, 38, 116, 175).

[175] F. La Franca, F. Fiore, et al. “The HELLAS2XMM Survey. VII. The Hard X-Ray Luminosity Function of AGNs up to z = 4: More Absorbed AGNs at Low Luminosities and High Redshifts”. In: ApJ 635 (Dec. 2005), pp. 864–879 (cit. on p. 18).

[176] C. Laigle, H. J. McCracken, et al. “The COSMOS2015 Catalog: Exploring the 1 z 6 Universe with Half a Million Galaxies”. In: ApJS 224, 24 (June 2016), p. 24 (cit. on p. 97).

[177] E. S. Laird, K. Nandra, et al. “On the X-ray properties of sub-mm-selected galaxies”. In: MNRAS 401 (Feb. 2010), pp. 2763–2772 (cit. on p. 21).

[178] F. Lamareille, J. Brinchmann, et al. “Physical properties of galaxies and their evolution in the VIMOS VLT Deep Survey. I. The evolution of the mass-metallicity relation up to z $\sim$ 0.9”. In: A&A 495 (Feb. 2009), pp. 53–72 (cit. on pp. 75, 76).

[179] A. Lamastra, N. Menci, et al. “Probing AGN triggering mechanisms through the starburstiness of the host galaxies”. In: A&A 559, A56 (Nov. 2013), A56 (cit. on p. 24).

[180] L. Lanz, P. M. Ogle, et al. “Jet-ISM Interaction in the Radio Galaxy 3C 293: Jet-driven Shocks Heat ISM to Power X-Ray and Molecular $H_2$ Emission”. In: ApJ 801, 17 (Mar. 2015), p. 17 (cit. on p. 90).

[181] G. Lanzuisi, M. Perna, et al. “The most obscured AGN in the COSMOS field”. In: A&A 578, A120 (June 2015), A120 (cit. on pp. 38, 76, 100).

[182] G. Lanzuisi, E. Piconcelli, et al. “Revealing X-ray obscured quasars in SWIRE sources with extreme mid-IR/optical flux ratios”. In: A&A 498 (Apr. 2009), pp. 67–81 (cit. on p. 99).

[183] G. Lanzuisi, G. Ponti, et al. “Active Galactic Nucleus X-Ray Variability in the XMM-COSMOS Survey”. In: ApJ 781, 105 (Feb. 2014), p. 105 (cit. on p. 51).

[184] G. Lanzuisi, P. Ranalli, et al. “Compton thick AGN in the XMM-COSMOS survey”. In: A&A 573, A137 (Jan. 2015), A137 (cit. on pp. 98, 99).

[185] E. Le Floc’h, H. Aussel, et al. “Deep Spitzer 24 $\mu$m COSMOS Imaging. I. The Evolution of Luminous Dusty Galaxies - Confronting the Models”. In: ApJ 703 (Sept. 2009), pp. 222–239 (cit. on pp. 95, 97).

[186] S. J. Lilly, V. Le Brun, et al. “The zCOSMOS 10k-Bright Spectroscopic Sample”. In: ApJS 184 (Oct. 2009), pp. 218–229 (cit. on pp. 74, 75).

[187] S. L. Lípari and R. J. Terlevich. “Evolutionary unification in composite active galactic nuclei”. In: MNRAS 368 (May 2006), pp. 1001–1015 (cit. on p. 30).

[188] G. Liu, N. L. Zakamska, and J. E. Greene. “Similarity of ionized gas nebulae around unobscured and obscured quasars”. In: ArXiv e-prints (Jan. 2014) (cit. on p. 30).

[189] G. Liu, N. L. Zakamska, et al. “Observations of feedback from radio-quiet quasars - II. Kinematics of ionized gas nebulae”. In: MNRAS 436 (Dec. 2013), pp. 2576–2597 (cit. on pp. 30, 39, 46, 47, 63, 88).

[190] E. Lusso, A. Comastri, et al. “Bolometric luminosities and Eddington ratios of X-ray selected active galactic nuclei in the XMM-COSMOS survey”. In: MNRAS 425 (Sept. 2012), pp. 623–640 (cit. on pp. 5, 31, 33, 35, 74, 109, 110, 114, 126, 127).

[191] E. Lusso, A. Comastri, et al. “The bolometric output and host-galaxy properties of obscured AGN in the XMM-COSMOS survey”. In: A&A 534, A110 (Oct. 2011), A110 (cit. on pp. 49, 50, 67).

[192] E. Lusso, J. F. Hennawi, et al. “The Obscured Fraction of Active Galactic Nuclei in the XMM-COSMOS Survey: A Spectral Energy Distribution Perspective”. In: ApJ 777, 86 (Nov. 2013), p. 86 (cit. on pp. 35, 49, 50).

[193] D. Lutz. “Far-Infrared Surveys of Galaxy Evolution”. In: ARA&A 52 (Aug. 2014), pp. 373–414 (cit. on p. 5).

[194] D. Lutz, R. Maiolino, et al. “The relation between AGN hard X-ray emission and mid-infrared continuum from ISO spectra: Scatter and unification aspects”. In: A&A 418 (May 2004), pp. 465–473 (cit. on p. 99).

[195] D. Lutz, A. Poglitsch, et al. “PACS Evolutionary Probe (PEP) - A Herschel key program”. In: A&A 532, A90 (Aug. 2011), A90 (cit. on p. 33).

[196] D. Lynden-Bell. “Note on N Galaxies and mini-quasars”. In: MNRAS 155 (1971), p. 119 (cit. on p. 3).

[197] P. Madau and M. Dickinson. “Cosmic Star-Formation History”. In: ARA&A 52 (Aug. 2014), pp. 415–486 (cit. on pp. 16, 18, 19).

[198] M. Magliocchetti, D. Lutz, et al. “The PEP survey: infrared properties of radio-selected AGN”. In: MNRAS 442 (July 2014), pp. 682–693 (cit. on p. 77).

[199] J. Magorrian, S. Tremaine, et al. “The Demography of Massive Dark Objects in Galaxy Centers”. In: AJ 115 (June 1998), pp. 2285–2305 (cit. on p. 16).

[200] E. K. Mahony, J. B. R. Oonk, et al. “Jet-driven outflows of ionized gas in the nearby radio galaxy 3C 293”. In: MNRAS 455 (Jan. 2016), pp. 2453–2460 (cit. on pp. 87, 89, 90).

[201] V. Mainieri, A. Bongiorno, et al. “Black hole accretion and host galaxies of obscured quasars in XMM-COSMOS”. In: A&A 535, A80 (Nov. 2011), A80 (cit. on pp. 33–35, 51, 74).

[202] R. Maiolino. “Obscured active galactic nuclei”. In: X-ray Astronomy: Stellar Endpoints, AGN, and the Diffuse X-ray 599 (Dec. 2001), pp. 199–208 (cit. on p. 13).

[203] R. Maiolino, S. Gallerani, et al. “Evidence of strong quasar feedback in the early Universe”. In: MNRAS 425 (Sept. 2012), pp. L66–L70 (cit. on pp. 24, 172).

[204] C. Mancini, N. M. Förster Schreiber, et al. “The zCOSMOS-SINFONI Project. I. Sample Selection and Natural-seeing Observations”. In: ApJ 743, 86 (Dec. 2011), p. 86 (cit. on p. 109).

[205] A. Marconi and L. K. Hunt. “The Relation between Black Hole Mass, Bulge Mass, and Near-Infrared Luminosity”. In: ApJ 589 (May 2003), pp. L21–L24 (cit. on p. 18).

[206] B. E. Markarian. “Galaxies with an Ultraviolet Continuum”. In: Astrofizika 3 (1967) (cit. on p. 6).

[207] B. E. Markarian. “Galaxies with Ultraviolet Continuum II”. In: Astrofizika 5 (1969) (cit. on p. 6).

[208] A. Martínez-Sansigre, S. Rawlings, et al. “The obscuration by dust of most of the growth of supermassive black holes”. In: NATURE 436 (Aug. 2005), pp. 666–669 (cit. on pp. 95, 100).

[209] S. Mateos, X. Barcons, et al. “XMM-Newton observations of the Lockman Hole IV: spectra of the brightest AGN”. In: A&A 444 (Dec. 2005), pp. 79–99 (cit. on p. 12).

[210] S. Mateos, F. J. Carrera, et al. “Revisiting the relationship between 6 $\mu$m and 2-10 keV continuum luminosities of AGN”. In: MNRAS 449 (May 2015), pp. 1422–1440 (cit. on p. 99).

[211] T. A. Matthews and A. Sandage. “Optical Identification of 3C 48, 3C 196, and 3C 286 with Stellar Objects.” In: ApJ 138 (July 1963), p. 30 (cit. on p. 3).

[212] H. J. McCracken, P. Capak, et al. “The COSMOS-WIRCam Near-Infrared Imaging Survey. I. BzK-Selected Passive and Star-Forming Galaxy Candidates at z gsim 1.4”. In: ApJ 708 (Jan. 2010), pp. 202–217 (cit. on p. 108).

[213] H. J. McCracken, B. Milvang-Jensen, et al. “UltraVISTA: a new ultra-deep near-infrared survey in COSMOS”. In: A&A 544, A156 (Aug. 2012), A156 (cit. on p. 76).

[214] R. McElroy, S. M. Croom, et al. “IFU observations of luminous type II AGN - I. Evidence for ubiquitous winds”. In: MNRAS 446 (Jan. 2015), pp. 2186–2204 (cit. on pp. 11, 24).

[215] B. R. McNamara, F. Kazemzadeh, et al. “An Energetic AGN Outburst Powered by a Rapidly Spinning Supermassive Black Hole or an Accreting Ultramassive Black Hole”. In: ApJ 698 (June 2009), pp. 594–605 (cit. on p. 22).

[216] J. Melbourne, R. S. Bussman, et al. “High-Redshift Dust Obscured Galaxies: A Morphology-Spectral Energy Distribution Connection Revealed by Keck Adaptive Optics”. In: AJ 137 (June 2009), pp. 4854–4866 (cit. on p. 107).

[217] J. Melbourne, V. Desai, et al. “Morphologies of High-Redshift Dust-Obscured Galaxies from Keck Laser Guide Star Adaptive Optics”. In: AJ 136 (Sept. 2008), pp. 1110–1117 (cit. on p. 107).

[218] J. Melbourne, C. Y. Peng, et al. "The Black Hole Masses and Star Formation Rates of z>1 Dust Obscured Galaxies: Results from Keck OSIRIS Integral Field Spectroscopy". In: AJ 141, 141 (Apr. 2011), p. 141 (cit. on pp. 94, 97, 107, 108).

[219] N. Menci, F. Fiore, et al. "The Blast Wave Model for AGN Feedback: Effects on AGN Obscuration". In: ApJ 686, 219-229 (Oct. 2008), pp. 219–229 (cit. on p. 46).

[220] A. Merloni, A. Bongiorno, et al. "On the Cosmic Evolution of the Scaling Relations Between Black Holes and Their Host Galaxies: Broad-Line Active Galactic Nuclei in the zCOSMOS Survey". In: ApJ 708 (Jan. 2010), pp. 137–157 (cit. on pp. 12, 108).

[221] A. Merloni, A. Bongiorno, et al. "The incidence of obscuration in active galactic nuclei". In: MNRAS 437 (Feb. 2014), pp. 3550–3567 (cit. on pp. 16, 33, 35, 74).

[222] M. Mignoli, L. Pozzetti, et al. "The HELLAS2XMM survey. V. Near-Infrared observations of X-ray sources with extreme X/O ratios". In: A&A 418 (May 2004), pp. 827–840 (cit. on pp. 31, 34, 94).

[223] M. Mignoli, C. Vignali, et al. "Obscured AGN at z $\sim$ 1 from the zCOSMOS-Bright Survey. I. Selection and optical properties of a [Ne v]-selected sample". In: A&A 556, A29 (Aug. 2013), A29 (cit. on pp. 76, 100).

[224] R. Mor, H. Netzer, and M. Elitzur. "Dusty Structure Around Type-I Active Galactic Nuclei: Clumpy Torus Narrow-line Region and Near-nucleus Hot Dust". In: ApJ 705 (Nov. 2009), pp. 298–313 (cit. on p. 14).

[225] C. W. Morgan, C. S. Kochanek, et al. "The Quasar Accretion Disk Size-Black Hole Mass Relation". In: ApJ 712 (Apr. 2010), pp. 1129–1136 (cit. on p. 5).

[226] J. A. Morse, G. Cecil, et al. "Inclined Gas Disks in the Lenticular Seyfert Galaxy NGC 5252". In: ApJ 505 (Sept. 1998), pp. 159–173 (cit. on p. 17).

[227] J. R. Mullaney, D. M. Alexander, et al. "Defining the intrinsic AGN infrared spectral energy distribution and measuring its contribution to the infrared output of composite galaxies". In: MNRAS 414 (June 2011), pp. 1082–1110 (cit. on p. 5).

[228] J. R. Mullaney, D. M. Alexander, et al. "Narrow-line region gas kinematics of 24 264 optically selected AGN: the radio connection". In: MNRAS 433 (July 2013), pp. 622–638 (cit. on pp. 46, 114, 131).

[229] J. R. Mullaney, E. Daddi, et al. "The Hidden "AGN Main Sequence": Evidence for a Universal Black Hole Accretion to Star Formation Rate Ratio since z $\sim$ 2 Producing an M $_{BH}$-M $_*$ Relation". In: ApJ 753, L30 (July 2012), p. L30 (cit. on p. 18).

[230] F. Müller-Sánchez, M. A. Prieto, et al. "Outflows from Active Galactic Nuclei: Kinematics of the Narrow-line and Coronal-line Regions in Seyfert Galaxies". In: ApJ 739, 69 (Oct. 2011), p. 69 (cit. on p. 16).

[231] K. Nakajima and M. Ouchi. "Ionization state of inter-stellar medium in galaxies: evolution, SFR-M$_*$-Z dependence, and ionizing photon escape". In: MNRAS 442 (July 2014), pp. 900–916 (cit. on p. 83).

[232] K. Nandra, I. M. George, et al. "On the Dependence of the Iron K-Line Profiles with Luminosity in Active Galactic Nuclei". In: ApJL 488 (Oct. 1997), pp. L91–L94 (cit. on p. 13).

[233] K. Nandra and K. Pounds. "GINGA Observations of the X-Ray Spectra of Seyfert Galaxies". In: MNRAS 268 (May 1994), p. 405 (cit. on p. 12).

[234] D. Narayanan, A. Dey, et al. "A physical model for z ˜ 2 dust-obscured galaxies". In: MNRAS 407 (Sept. 2010), pp. 1701–1720 (cit. on pp. 107, 108).

[235] N. P. H. Nesvadba, C. De Breuck, et al. "The black holes of radio galaxies during the "Quasar Era": masses, accretion rates, and evolutionary stage". In: A&A 525, A43 (Jan. 2011), A43 (cit. on p. 24).

[236] N. P. H. Nesvadba, M. D. Lehnert, et al. "Evidence for powerful AGN winds at high redshift: dynamics of galactic outflows in radio galaxies during the "Quasar Era"". In: A&A 491 (Nov. 2008), pp. 407–424 (cit. on pp. 24, 27, 128).

[237] H. Netzer. "Revisiting the Unified Model of Active Galactic Nuclei". In: ARA&A 53 (Aug. 2015), pp. 365–408 (cit. on pp. 9, 24, 51).

[238] H. Netzer. The Physics and Evolution of Active Galactic Nuclei. Nov. 2013 (cit. on pp. 5, 9, 26).

[239] H. Netzer and B. Trakhtenbrot. “Bolometric luminosity black hole growth time and slim accretion discs in active galactic nuclei”. In: MNRAS 438 (Feb. 2014), pp. 672–679 (cit. on p. 122).

[240] K. Oh, S. K. Yi, et al. “A New Catalog of Type 1 AGNs and its Implications on the AGN Unified Model”. In: ApJS 219, 1 (July 2015), p. 1 (cit. on p. 9).

[241] F. Onori, F. La Franca, et al. “Detection of faint broad emission lines in type 2 AGN: I. Near infrared observations and spectral fitting”. In: MNRAS (Sept. 2016) (cit. on p. 16).

[242] M. Orienti. “Radio properties of Compact Steep Spectrum and GHz-Peaked Spectrum radio sources”. In: Astronomische Nachrichten 337 (Feb. 2016), p. 9 (cit. on p. 90).

[243] D. E. Osterbrock. Astrophysics of gaseous nebulae and active galactic nuclei. 1989 (cit. on pp. 63, 64).

[244] D. E. Osterbrock and G. J. Ferland. Astrophysics of gaseous nebulae and AGNs. 2006 (cit. on pp. 5, 9–11, 26, 39, 129, 162, 163, 167, 172).

[245] P. Padovani. “The faint radio sky: radio astronomy becomes mainstream”. In: ArXiv e-prints (Sept. 2016) (cit. on pp. 3, 5).

[246] K. L. Page, J. N. Reeves, et al. “XMM-Newton spectroscopy of high-redshift quasars”. In: MNRAS 364 (Nov. 2005), pp. 195–207 (cit. on p. 13).

[247] A. Pancoast, B. J. Brewer, and T. Treu. “Modelling reverberation mapping data - I. Improved geometric and dynamical models and comparison with cross-correlation results”. In: MNRAS 445 (Dec. 2014), pp. 3055–3072 (cit. on p. 12).

[248] A. Pancoast, B. J. Brewer, et al. “Erratum: Modelling reverberation mapping data - II. Dynamical modelling of the Lick AGN Monitoring Project 2008 data set”. In: MNRAS 448 (Apr. 2015), pp. 3070–3070 (cit. on p. 12).

[249] F. Panessa and M. Giroletti. “Sub-parsec radio cores in nearby Seyfert galaxies”. In: MNRAS 432 (June 2013), pp. 1138–1143 (cit. on p. 6).

[250] M. Perna, M. Brusa, et al. “Galaxy-wide outflows in z $\sim$ 1.5 luminous obscured quasars revealed through near-IR slit-resolved spectroscopy”. In: A&A 574, A82 (Feb. 2015), A82 (cit. on pp. 33, 38, 91, 107, 108).

[251] M. Perna, M. Brusa, et al. “SINFONI spectra of heavily obscured AGNs in COSMOS: Evidence of outflows in a MIR/O target at z $\sim$ 2.5”. In: A&A 583, A72 (Nov. 2015), A72 (cit. on pp. 30, 38, 74, 110).

[252] G. C. Perola, G. Matt, et al. “Compton reflection and iron fluorescence in BeppoSAX observations of Seyfert type 1 galaxies”. In: A&A 389 (July 2002), pp. 802–811 (cit. on p. 13).

[253] B. M. Peterson. An Introduction to Active Galactic Nuclei. Feb. 1997 (cit. on p. 4).

[254] B. M. Peterson. “Variability of Active Galactic Nuclei”. In: Advanced Lectures on the Starburst-AGN. Ed. by I. Aretxaga, D. Kunth, and R. Mújica. 2001, p. 3 (cit. on p. 4).

[255] M. Pettini and B. E. J. Pagel. “[OIII]/[NII] as an abundance indicator at high redshift”. In: MNRAS 348 (Mar. 2004), pp. L59–L63 (cit. on pp. 64, 106).

[256] E. Piconcelli, E. Jimenez-Bailón, et al. “The XMM-Newton view of PG quasars. I. X-ray continuum and absorption”. In: A&A 432 (Mar. 2005), pp. 15–30 (cit. on pp. 12, 13).

[257] L. S. Pilyugin. “Oxygen abundances in dwarf irregular galaxies and the metallicity-luminosity relationship”. In: A&A 374 (Aug. 2001), pp. 412–420 (cit. on p. 64).

[258] Planck Collaboration, P. A. R. Ade, et al. “Planck 2013 results. XVI. Cosmological parameters”. In: A&A 571, A16 (Nov. 2014), A16 (cit. on pp. 19, 20).

[259] D. Porquet, J. N. Reeves, et al. “XMM-Newton EPIC observations of 21 low-redshift PG quasars”. In: A&A 422 (July 2004), pp. 85–95 (cit. on p. 13).

[260] K. A. Pounds, J. N. Reeves, et al. “A high-velocity ionized outflow and XUV photosphere in the narrow emission line quasar PG1211+143”. In: MNRAS 345 (Nov. 2003), pp. 705–713 (cit. on p. 137).

[261] M. L. Prevot, J. Lequeux, et al. “The typical interstellar extinction in the Small Magellanic Cloud”. In: A&A 132 (Mar. 1984), pp. 389–392 (cit. on p. 49).

[262] S. I. Raimundo, A. C. Fabian, et al. “Radiation pressure, absorption and AGN feedback in the Chandra Deep Fields”. In: MNRAS 408 (Nov. 2010), pp. 1714–1720 (cit. on p. 51).

[263] L. Riguccini, E. Le Floc’h, et al. “Dust-obscured star formation and the contribution of galaxies escaping UV/optical color selections at z $\sim$ 2”. In: A&A 534, A81 (Oct. 2011), A81 (cit. on p. 95).

[264] L. Riguccini, E. Le Floc’h, et al. “The composite nature of Dust-Obscured Galaxies (DOGs) at z $\sim$ 2-3 in the COSMOS field - I. A far-infrared view”. In: MNRAS 452 (Sept. 2015), pp. 470–485 (cit. on pp. 95, 100, 107, 108).

[265] J. Rodríguez Zaurín, C. N. Tadhunter, et al. “The importance of warm, AGN-driven outflows in the nuclear regions of nearby ULIRGs”. In: MNRAS 432 (June 2013), pp. 138–166 (cit. on pp. 24, 46, 128).

[266] J. Rodríguez-Zaurín, C. N. Tadhunter, et al. “The importance of warm, AGN-driven outflows in the nuclear regions of nearby ULIRGs”. In: MNRAS 432 (June 2013), pp. 138–166 (cit. on pp. 62, 63).

[267] D. J. Rosario, P. Santini, et al. “The Mean Star Formation Rate of X-ray selected Active Galaxies and its Evolution from z=2.5: Results from PEP-Herschel”. In: ArXiv e-prints (Mar. 2012) (cit. on p. 31).

[268] D. S. Rupke and S. Veilleux. “Breaking the Obscuring Screen: A Resolved Molecular Outflow in a Buried QSO”. In: ApJL 775, L15 (Sept. 2013), p. L15 (cit. on pp. 39, 58).

[269] D. S. Rupke and S. Veilleux. “Integral Field Spectroscopy of Massive, Kiloparsec-scale Outflows in the Infrared-luminous QSO Mrk 231”. In: ApJ 729, L27 (Mar. 2011), p. L27 (cit. on pp. 24, 58).

[270] D. S. Rupke, S. Veilleux, and D. B. Sanders. “Outflows in Infrared-Luminous Starbursts at z < 0.5. I. Sample, Na I D Spectra, and Profile Fitting”. In: ApJS 160 (Sept. 2005), pp. 87–114 (cit. on pp. 66, 124, 125).

[271] D. S. Rupke, S. Veilleux, and D. B. Sanders. “Outflows in Infrared-Luminous Starbursts at z < 0.5. II. Analysis and Discussion”. In: ApJS 160 (Sept. 2005), pp. 115–148 (cit. on pp. 66, 132).

[272] K. Sakamoto, S. Aalto, et al. “An Infrared-luminous Merger with Two Bipolar Molecular Outflows: ALMA and SMA Observations of NGC 3256”. In: ApJ 797, 90 (Dec. 2014), p. 90 (cit. on p. 18).

[273] E. E. Salpeter. “Accretion of Interstellar Matter by Massive Objects.” In: ApJ 140 (Aug. 1964), pp. 796–800 (cit. on pp. 4, 9).

[274] M. Salvato, O. Ilbert, et al. “Dissecting Photometric Redshift for Active Galactic Nucleus Using XMM- and Chandra-COSMOS Samples”. In: ApJ 742, 61 (Dec. 2011), p. 61 (cit. on pp. 31, 104).

[275] A. Sandage. “The Existence of a Major New Constituent of the Universe: the Quasistellar Galaxies.” In: ApJ 141 (May 1965), p. 1560 (cit. on p. 3).

[276] D. B. Sanders and I. F. Mirabel. “Luminous Infrared Galaxies”. In: ARA&A 34 (1996), p. 749 (cit. on p. 21).

[277] D. B. Sanders, M. Salvato, et al. “S-COSMOS: The Spitzer Legacy Survey of the Hubble Space Telescope ACS 2 deg$^2$ COSMOS Field I: Survey Strategy and First Analysis”. In: ApJS 172 (Sept. 2007), pp. 86–98 (cit. on p. 95).

[278] D. B. Sanders, B. T. Soifer, et al. “Warm ultraluminous galaxies in the IRAS survey - The transition from galaxy to quasar?” In: ApJ 328 (May 1988), pp. L35–L39 (cit. on p. 21).

[279] P. Santini, D. J. Rosario, et al. “Enhanced star formation rates in AGN hosts with respect to inactive galaxies from PEP-Herschel observations”. In: A&A 540, A109 (Apr. 2012), A109 (cit. on pp. 31, 33).

[280] W. L. W. Sargent. “A Spectroscopic Survey of Compact and Peculiar Galaxies”. In: ApJ 160 (May 1970), p. 405 (cit. on p. 6).

[281] M. Sarzi, S. Kaviraj, et al. “Cold-gas outflows in typical low-redshift galaxies are driven by star formation, not AGN”. In: MNRAS 456 (Feb. 2016), pp. L25–L29 (cit. on pp. 125, 132).

[282] F. G. Saturni, D. Trevese, et al. “A multi-epoch spectroscopic study of the BAL quasar APM 08279+5255. II. Emission- and absorption-line variability time lags”. In: A&A 587, A43 (Mar. 2016), A43 (cit. on pp. 12, 173).

[283] C. Scannapieco, M. Wadepuhl, et al. “The Aquila comparison project: the effects of feedback and numerical methods on simulations of galaxy formation”. In: MNRAS 423 (June 2012), pp. 1726–1749 (cit. on p. 21).

[284] S. Schindler, A. Castillo-Morales, et al. “Discovery of depressions in the X-ray emission of the distant galaxy cluster RBS797 in a CHANDRA observation”. In: A&A 376 (Sept. 2001), pp. L27–L30 (cit. on p. 21).

[285] E. Schinnerer, M. T. Sargent, et al. “The VLA-COSMOS Survey. IV. Deep Data and Joint Catalog”. In: ApJS 188 (June 2010), pp. 384–404 (cit. on pp. 33, 34, 76, 90, 100).

[286] M. Schmidt. “3C 273 : A Star-Like Object with Large Red-Shift”. In: NATURE 197 (Mar. 1963), p. 1040 (cit. on p. 3).

[287] M. Schmidt. “Large Redshifts of Five Quasi-Stellar Sources.” In: ApJ 141 (Apr. 1965), p. 1295 (cit. on p. 3).

[288] R. Schneider, S. Bianchi, et al. “The origin of the far-infrared continuum of z $\sim$ 6 quasars. A radiative transfer model for SDSS J1148+5251”. In: A&A 579, A60 (July 2015), A60 (cit. on p. 51).

[289] A. Schulze, A. Bongiorno, et al. “The cosmic growth of the active black hole population at 1 <z <2 in zCOSMOS, VVDS and SDSS”. In: MNRAS 447 (Mar. 2015), pp. 2085–2111 (cit. on p. 12).

[290] N. Scoville, H. Aussel, et al. “Large Structures and Galaxy Evolution in COSMOS at z < 1.1”. In: ApJS 172 (Sept. 2007), pp. 150–181 (cit. on p. 75).

[291] N. Scoville, H. Aussel, et al. “The Cosmic Evolution Survey (COSMOS): Overview”. In: ApJS 172 (Sept. 2007), pp. 1–8 (cit. on pp. 31, 76).

[292] C. K. Seyfert. “Nuclear Emission in Spiral Nebulae.” In: ApJ 97 (1943), p. 28 (cit. on p. 3).

[293] N. I. Shakura and R. A. Sunyaev. “Black holes in binary systems. Observational appearance.” In: A&A 24 (1973), pp. 337–355 (cit. on p. 5).

[294] Y. Shen and B. C. Kelly. “The Demographics of Broad-line Quasars in the Mass-Luminosity Plane. I. Testing FWHM-based Virial Black Hole Masses”. In: ApJ 746, 169 (Feb. 2012), p. 169 (cit. on p. 38).

[295] Y. Shen, G. T. Richards, et al. “A Catalog of Quasar Properties from Sloan Digital Sky Survey Data Release 7”. In: ApJS 194, 45 (June 2011), p. 45 (cit. on pp. 5, 120).

[296] D. Sijacki, M. Vogelsberger, et al. “The Illustris simulation: the evolving population of black holes across cosmic time”. In: MNRAS 452 (Sept. 2015), pp. 575–596 (cit. on p. 21).

[297] J. Silk and M. J. Rees. “Quasars and galaxy formation”. In: A&A 331 (Mar. 1998), pp. L1–L4 (cit. on p. 20).

[298] L. Silva, G. L. Granato, et al. “Modeling the Effects of Dust on Galactic Spectral Energy Distributions from the Ultraviolet to the Millimeter Band”. In: ApJ 509 (Dec. 1998), pp. 103–117 (cit. on p. 6).

[299] A. Soltan. “Masses of quasars”. In: MNRAS 200 (July 1982), pp. 115–122 (cit. on pp. 16, 18).

[300] V. Springel, T. Di Matteo, and L. Hernquist. “Modelling feedback from stars and black holes in galaxy mergers”. In: MNRAS 361 (Aug. 2005), pp. 776–794 (cit. on p. 21).

[301] D. Stern. “The X-Ray to Mid-infrared Relation of AGNs at High Luminosity”. In: ApJ 807, 129 (July 2015), p. 129 (cit. on p. 99).

[302] D. Stern, G. B. Lansbury, et al. “NuSTAR and XMM-Newton Observations of Luminous, Heavily Obscured, WISE-selected Quasars at z $\sim$ 2”. In: ApJ 794, 102 (Oct. 2014), p. 102 (cit. on pp. 67, 99).

[303] J. Stern, C.-A. Faucher-Giguère, et al. “Constraining the Dynamical Importance of Hot Gas and Radiation Pressure in Quasar Outflows Using Emission Line Ratios”. In: ApJ 819, 130 (Mar. 2016), p. 130 (cit. on p. 172).

[304] M. Symeonidis, B. M. Giblin, et al. “AGN are cooler than you think: the intrinsic far-IR emission from QSOs”. In: MNRAS 459 (June 2016), pp. 257–276 (cit. on p. 5).

[305] L. J. Tacconi, R. Genzel, et al. “Submillimeter Galaxies at z $\sim$ 2: Evidence for Major Mergers and Constraints on Lifetimes, IMF, and CO-$H_2$ Conversion Factor”. In: ApJ 680, 246-262 (June 2008), pp. 246–262 (cit. on p. 21).

[306] D. Thomas, O. Steele, et al. “Stellar velocity dispersions and emission line properties of SDSS-III/BOSS galaxies”. In: MNRAS 431 (May 2013), pp. 1383–1397 (cit. on pp. 122, 163).

[307] F. Tombesi, M. Cappi, et al. “Evidence for Ultra-fast Outflows in Radio-quiet Active Galactic Nuclei. II. Detailed Photoionization Modeling of Fe K-shell Absorption Lines”. In: ApJ 742, 44 (Nov. 2011), p. 44 (cit. on p. 137).

[308] F. Tombesi, M. Meléndez, et al. “Wind from the black-hole accretion disk driving a molecular outflow in an active galaxy”. In: NATURE 519 (Mar. 2015), pp. 436–438 (cit. on pp. 137, 139).

[309] F. Tombesi, R. M. Sambruna, et al. “Discovery of Ultra-fast Outflows in a Sample of Broad-line Radio Galaxies Observed with Suzaku”. In: ApJ 719 (Aug. 2010), pp. 700–715 (cit. on p. 137).

[310] M. Trichas, P. J. Green, et al. “Empirical Links between XRB and AGN Accretion Using the Complete z 0.4 Spectroscopic CSC/SDSS Catalog”. In: ApJ 778, 188 (Dec. 2013), p. 188 (cit. on p. 115).

[311] J. R. Trump, C. D. Impey, et al. “Magellan Spectroscopy of AGN Candidates in the COSMOS Field”. In: ApJS 172 (Sept. 2007), pp. 383–395 (cit. on pp. 97, 100).

[312] T. Urrutia, R. H. Becker, et al. “The FIRST-2MASS Red Quasar Survey. II. An Anomalously High Fraction of LoBALs in Searches for Dust-Reddened Quasars”. In: ApJ 698 (June 2009), pp. 1095–1109 (cit. on pp. 21, 30, 91).

[313] T. Urrutia, M. Lacy, et al. “Spitzer Observations of Young Red Quasars”. In: ApJ 757, 125 (Oct. 2012), p. 125 (cit. on pp. 30, 46, 48, 94).

[314] C. M. Urry and P. Padovani. “Unified Schemes for Radio-Loud Active Galactic Nuclei”. In: PASP 107 (Sept. 1995), p. 803 (cit. on pp. 14, 15).

[315] D. E. Vanden Berk, G. T. Richards, et al. “Composite Quasar Spectra from the Sloan Digital Sky Survey”. In: AJ 122 (Aug. 2001), pp. 549–564 (cit. on p. 83).

[316] L. Vaona, S. Ciroi, et al. “Spectral properties of the narrow-line region in Seyfert galaxies selected from the SDSS-DR7”. In: MNRAS 427 (Dec. 2012), pp. 1266–1283 (cit. on pp. 10, 11, 114, 128, 129).

[317] S. Veilleux, G. Cecil, and J. Bland-Hawthorn. “Galactic Winds”. In: ARA&A 43 (Sept. 2005), pp. 769–826 (cit. on pp. 22, 30, 67, 88).

[318] S. Veilleux and D. E. Osterbrock. “Spectral classification of emission-line galaxies”. In: ApJS 63 (1987), pp. 295–310 (cit. on pp. 104, 169).

[319] J. Vernet, H. Dekker, et al. “X-shooter, the new wide band intermediate resolution spectrograph at the ESO Very Large Telescope”. In: A&A 536, A105 (Dec. 2011), A105 (cit. on p. 35).

[320] M. Villar Martín, E. Bellocchi, et al. “Deconstructing the narrow-line region of the nearest obscured quasar”. In: MNRAS 454 (Nov. 2015), pp. 439–456 (cit. on p. 132).

[321] M. Villar Martín, B. Emonts, et al. “The triggering mechanism and properties of ionized outflows in the nearest obscured quasars”. In: MNRAS 440 (June 2014), pp. 3202–3219 (cit. on pp. 63, 124, 125, 128).

[322] M. Villar-Martín, A. Humphrey, et al. “Ionized outflows in SDSS type 2 quasars at z $\sim$ 0.3-0.6”. In: MNRAS 418 (Dec. 2011), pp. 2032–2042 (cit. on pp. 24, 51).

[323] B. Villarroel and A. J. Korn. “The different neighbours around Type-1 and Type-2 active galactic nuclei”. In: Nature Physics 10 (June 2014), pp. 417–420 (cit. on p. 16).

[324] F. Vito, R. Maiolino, et al. “Black hole accretion preferentially occurs in gas-rich galaxies”. In: MNRAS 441 (June 2014), pp. 1059–1065 (cit. on p. 16).

[325] A. Y. Wagner and G. V. Bicknell. “Relativistic Jet Feedback in Evolving Galaxies”. In: ApJ 728, 29 (Feb. 2011), p. 29 (cit. on p. 21).

[326] A. Y. Wagner, M. Umemura, and G. V. Bicknell. “Ultrafast Outflows: Galaxy-scale Active Galactic Nucleus Feedback”. In: ApJL 763, L18 (Jan. 2013), p. L18 (cit. on pp. 89, 90).

[327] J. Wang and D. W. Xu. “Identifying AGN Balmer absorptions and stratified narrow emission-line region kinematics in SDSS J112611.63+425246.4”. In: A&A 573, A15 (Jan. 2015), A15 (cit. on p. 39).

[328] D. W. Weedman. “Seyfert galaxies”. In: ARA&A 15 (1977), pp. 69–95 (cit. on pp. 3, 4, 9).

[329] D. W. Weedman, L. Sargsyan, et al. “Infrared Classification and Luminosities for Dusty Active Galactic Nuclei and the Most Luminous Quasars”. In: ApJ 761, 184 (Dec. 2012), p. 184 (cit. on pp. 31, 66).

[330] B. J. Weiner, A. L. Coil, et al. “Ubiquitous Outflows in DEEP2 Spectra of Star-Forming Galaxies at z = 1.4”. In: ApJ 692 (Feb. 2009), pp. 187–211 (cit. on p. 65).

[331] M. S. Westmoquette, D. L. Clements, et al. “Spatially resolved observations of warm ionized gas and feedback in local ULIRGs”. In: MNRAS 424 (July 2012), pp. 416–456 (cit. on pp. 24, 46, 55, 128).

[332] K. E. Whitaker, P. G. van Dokkum, et al. “The Star Formation Mass Sequence Out to z = 2.5”. In: ApJL 754, L29 (Aug. 2012), p. L29 (cit. on pp. 33, 34, 96, 100).

[333] J.-H. Woo, H.-J. Bae, et al. “The Prevalence of Gas Outflows in Type 2 AGNs”. In: ApJ 817, 108 (Feb. 2016), p. 108 (cit. on pp. 114, 122, 131).

[334] D. Xu, S. Komossa, et al. “The Narrow-Line Region of Narrow-Line and Broad-Line Type 1 Active Galactic Nuclei. I. A Zone of Avoidance in Density”. In: ApJ 670 (Nov. 2007), pp. 60–73 (cit. on pp. 10, 11, 130).

[335] S. Y. Yin, Y. C. Liang, and B. Zhang. “A Study on the Revised R$_{23}$-P Method for Metallicity Estimates Based on $\sim$20,000 SDSS Galaxies”. In: The Central Engine of Active Galactic Nuclei. Ed. by L. C. Ho and J.-W. Wang. Vol. 373. Astronomical Society of the Pacific Conference Series. Oct. 2007, p. 686 (cit. on pp. 64, 106).

[336] D. G. York, J. Adelman, et al. “The Sloan Digital Sky Survey: Technical Summary”. In: AJ 120 (Sept. 2000), pp. 1579–1587 (cit. on p. 6).

[337] S. Yuan, M. A. Strauss, and N. L. Zakamska. “Spectroscopic identification of type 2 quasars at z 1 in SDSS-III/BOSS”. In: MNRAS 462 (Oct. 2016), pp. 1603–1615 (cit. on p. 116).

[338] N. L. Zakamska and J. E. Greene. “Quasar feedback and the origin of radio emission in radio-quiet quasars”. In: ArXiv e-prints (Feb. 2014) (cit. on pp. 39, 57, 58, 68, 77, 82, 122).

[339] N. L. Zakamska, F. Hamann, et al. “Discovery of extreme [O III] $\lambda$5007 Å outflows in high-redshift red quasars”. In: MNRAS 459 (July 2016), pp. 3144–3160 (cit. on p. 91).

[340] N. L. Zakamska, K. Lampayan, et al. “Star formation in quasar hosts and the origin of radio emission in radio-quiet quasars”. In: MNRAS 455 (Feb. 2016), pp. 4191–4211 (cit. on pp. 89, 90, 114, 131).

[341] N. L. Zakamska, M. A. Strauss, et al. “Candidate Type II Quasars from the Sloan Digital Sky Survey. I. Selection and Optical Properties of a Sample at 0.3<Z<0.83”. In: AJ 126 (Nov. 2003), pp. 2125–2144 (cit. on p. 83).

[342] R. Zamanov, P. Marziani, et al. “Kinematic Linkage between the Broad- and Narrow-Line-emitting Gas in Active Galactic Nuclei”. In: ApJ 576 (Sept. 2002), pp. L9–L13 (cit. on p. 24).

[343] Y. B. Zel’dovich and I. D. Novikov. “” In: Dokl. Akad Nauk SSSR 158 (Oct. 1964), p. 311 (cit. on pp. 4, 9).

[344] K. Zhang, X.-B. Dong, et al. “The Blueshifting and Baldwin Effects for the [O III] $\lambda$5007 Emission Line in Type 1 Active Galactic Nuclei”. In: ApJ 737, 71 (Aug. 2011), p. 71 (cit. on p. 24).

[345] Z. T. Zhang, Y. C. Liang, and F. Hammer. “Modelling the narrow-line regions of active galaxies in the Sloan Digital Sky Survey - I. Sample selection and physical conditions”. In: MNRAS 430 (Apr. 2013), pp. 2605–2621 (cit. on pp. 10, 11, 129, 130).

[346] K. Zubovas and A. King. “The M-$\sigma$ relation in different environments”. In: MNRAS 426 (Nov. 2012), pp. 2751–2757 (cit. on pp. 30, 89, 137).

## Appendix A

# Diagnostics in AGN emission lines

Rest-frame optical and near-ultraviolet emission lines have been handsomely used to throughout this thesis. These features contain a large amount of information about the physical and kinematic conditions in the line-emitting gas. In this appendix we provide brief details of the production mechanisms of the main emission lines and the diagnostic methods used in this thesis.

## A.1 Permitted and Forbidden Lines

Optical-UV emission lines in AGNs cover a wide range of ionization. Table A.1 lists the main emission lines studied throughout this thesis, together with the ionization potential (IP; from few eV to $\gtrsim$100 eV) required for the production of the ions responsible of a given emission line. Two types of emission lines are referred to throughout this thesis: permitted lines and forbidden lines. Permitted lines are those that have high transition probabilities ($A \approx 10^{-8}$–$10^{-10}$ s$^{-1}$), i.e. very short decay times of spontaneous photon emission. These lines can be produced in both high-density and low-density environments. The most prominent permitted lines in the optical regime are H$\alpha\lambda$6563 and H$\beta\lambda$4861. These lines are part of the Balmer emission line series and correspond to emissions of photons by electrons in excited states n=3 (H$\alpha$) and n=4 (H$\beta$) transitioning to the second principle energy-level (n=2). H$\alpha$ and H$\beta$ lines are referred to recombination lines because are formed by captures of electrons into excited levels that are cascading by downward radiative transitions to the ground levels. In contrast, forbidden lines have extremely small transition probabilities ($10^{-3}$–1 s$^{-1}$) and can be produced only in low-density regions. A forbidden line is the product of the energy radiated by spontaneous radiative decays from collisionally-excited energy-levels and is observed as long as the density is much less than a related "critical density" at which, by definition, collisional de-excitation happens as often as radiative decays. In fact, in collisional de-excitation no radiation is emitted. This provides a useful diagnostic: if we do not see certain lines of an ion, we can infer that the electron density is too high for their radiation to occur. Critical density argument is particularly useful to derive upper limits for the electron density in NLR and BLR gas. In particular, the observation of typical narrow-lines spectra in AGNs such as [SII] features (characterized by small critical densities) suggests for the NLR and electron density $N_e \lesssim 10^4$ cm$^{-3}$. On the other hand, broad-line gas should be associated with densest regions: the presence of the semi-forbidden[1] CIII]$\lambda$1909 broad line, characterized by a critical density of $10^{10}$ cm$^{-3}$, suggests that the BLR is characterized by electron density of the order of $10^9$ cm$^{-3}$.

---

[1] Semi-forbidden lines are associated with intermediate transition probabilities between those of typical permitted and forbidden lines.

Table A.1: Principal optical-near UV emission lines in AGNs. All emission lines are identified by their air wavelengths. The ionization potential (IP), i.e., the potential energy required to achieve the ionic stage responsible for the emission line, is expressed in eV ($1.6 \times 10^{-12}$ erg). Few relevant critical densities are also reported (taken from the values listed by Appenzeller & Ostreicher1988; Wei1988;Osterbrock and Ferland 2006;Peterson1997)

| line | lambda ($\AA$) | IP (eV) | $\log(N_c)$ (cm$^{-3}$) |
|---|---|---|---|
| C III] | 1908.10 | 24.38 | 10 |
| C II] | 2325.73 | 11.26 | |
| [NeIV] | 2423.12 | 63.45 | |
| [OII] | 2470.28 | 13.62 | |
| Mg II | 2797.93 | 7.65 | |
| [Ne V] | 3345.86 | 97.11 | |
| [Ne V] | 3425.86 | 97.11 | 7.3 |
| [O II] | 3727.42 | 13.62 | 4.2;3.5 |
| [Ne III] | 3868.75 | 40.96 | 7.0 |
| [Ne III](+H$\delta$) | 3968.77 | 40.96 | 7.0 |
| H$\gamma$ | 4340.46 | – | |
| [O III] | 4363.21 | 35.12 | 7.5 |
| He II | 4685.71 | 24.59 | |
| H$\beta$ | 4861.32 | | |
| [O III] | 4958.91 | 35.12 | |
| [O III] | 5006.84 | 35.12 | 5.8 |
| [Fe VII] | 5720.71 | 99 | 7.6 |
| [N II] | 5753.04 | 14.53 | 6.6 |
| He I | 5875.66 | – | – |
| [Fe VII] | 6086.29 | 99 | 7.6 |
| [O I] | 6300.31 | – | 6.3 |
| [O I] | 6363.78 | – | |
| [Fe X] | 6374.54 | 235.04 | 9.7 |
| [N II] | 6548.04 | 14.53 | |
| H$\alpha$ | 6562.79 | – | |
| [N II] | 6583.46 | 14.53 | 4.9 |
| [S II] | 6716.43 | 10.36 | 3.2 |
| [S II] | 6730.81 | 10.36 | 3.6 |

## A.2 [OIII] emission lines

The main forbidden emission line used throughout this thesis is the doublet [O III]$\lambda\lambda$4959,5007. The O III species denote twice-ionised oxygen (IP 35.12 eV). $O^{2+}$ has 6 electrons, with two electrons in the 1s sub-shell, two electrons in the 2s sub-shell and two electrons in the 2p sub-shell. The energy-level diagram of this ion is shown in Fig. A.1, left. Its ground levels, the $^3$P term, are closer than in the figure and can be treated as a single level. The first excited level is $^1D_2$; well above there is the $^1S_0$ level. Energies of the order of the eV are enough to excite the $O^{2+}$ ions. The relative number of [O III]$\lambda$5007 and [O III]$\lambda$4959 photons is set by the ratio of their associated A-values (i.e., = 2.9; Osterbrock and Ferland 2006) and is responsible of the familiar [O III]$\lambda\lambda$4959,5007 doublet with a fixed flux ratio of 2.9.

### A.2.1 [O III]$\lambda$5007 as kinematic tracer of AGN-ionized gas

Typical [O III] line profiles show widths of the order of few hundred of km/s. In high density environments, i.e. with electron densities approaching their critical density $N_c$ ($\approx 10^6$ cm$^{-3}$), the $^1D_2$ excited state is de-excited by collisions before it can be de-excited by photon production. This is why the [O III] doublet is not produced in the high-density BLR and can therefore be used to trace the gas distribution and the kinematics in the NLR. In fact, this feature is a prominent line and do not suffer from particular blending with adjacent emission lines (but see Sect. xx; FeII..) or by stellar absorption (Heckman and Best 2014). Fine-scale morphology of the ionized gas can be derived from HST narrow-band imaging, HST long-slit spectroscopy and ground-based IFU studies (). Very extended (kpc-scale) NLR (bi-)cones are usually observed in the local Universe (see, e.g., Figs. 1.5, 1.6).

The [O III] line profile analysis allow a way for understanding the gas motion within the NLR. Emission line features are generally well modelled by a Gaussian profile. However, strong emission lines, such as [O III], may sometime display a more complex shape, with a distinct, prominent Gaussian profile in the central part (the “line core”) and asymmetric wings, extending at bluer and, occasionally, redder wavelengths. Such composite profiles can be easily modelled by two (or, rarely, more) different Gaussians (i.e., with distinct FWHM, amplitude and central wavelength). Through the thesis we differentiate between Narrow component (NC), which broadening is due to gravitational effets, and Outflow component (OC), responsible of heavier broadening caused by non-gravitational, outflow processes due to AGN (or star formation) activity within the host galaxy. The former component is associated with Gaussian profiles whose FWHM is related to the width of the stellar absorption features (refe). Typical FWHM of stellar components in massive galaxies is $\approx$ 550 km/s (Thomas et al. 2013). Such value has been obtained from the analysis of a very large sample of SDSS/Barionic Oscillation Spectroscopic Survey (BOSS) sources, a survey designed to target the more massive galaxies between redshift 0.15 and 0.70. We define a blunt threshold at 550-600 km/s to distinguish between the NLR or, more in general, the ISM ionized gas emission under the gravitational effects of the galaxy, and outflowing gas emission components: we indicate as NC the Gaussian lines with FWHM $\lesssim 550 - 600$ km/s and as OC lines with broader widths. We note that the ionized gas within the NLR of an AGN may be interested by outflow phenomena, and that therefore a distinction between NLR component and outflow component is misleading. Typical examples are given by the (bi-)conical NLR of local galaxies, in which the AGN-ionized gas shows a combination of gravitational and non-gravitational motions (see, e.g., Fischer et al. 2013). Finally, we note also that merging events may as well be responsible for critical broadening. However, Gaussian components with FWHMs higher than 550-600 km/s are not common even in SMGs at high redshift, i.e. where the gas kinematics may be severely affected by ongoing galaxy mergers (Collet et al. 2016).

We will see in Chapter B.0.1 that the separation between unperturbed and outflowing gas is essential to derive the exact amount of mass ejected from the SMBH, in the case of AGN-driven outflows. Furthermore, from the study of the geometrical configuration and the kinematics of such material, important quantities useful to characterize the outflow can be derived, both in terms of the

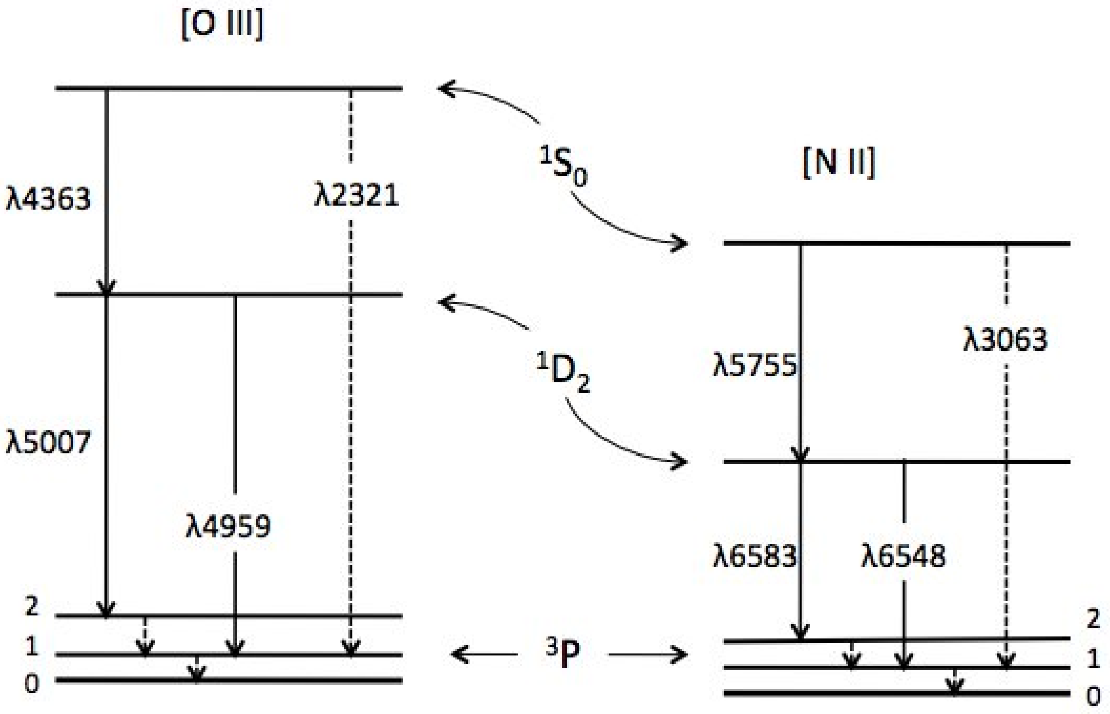

Figure A.1: Energy-level diagram for lowest terms of [OIII], all from ground $2p^3$ configuration, and for [NII] of the same isoelectric sequence. Emission lines in the optical regime are represented with dashed lines, while solid lines mark features in UV and IR. Energy separation within the ground $^3P$ has been exaggerated for clarity.

effects on the host galaxy (e.g., quantifying the depletion time...) and in advances in the knowledge of the mechanisms responsible for such phenomena.

### A.2.2 [OIII] as temperature-sensitive lines

The $2s^22p^2$ electron configuration is particularly important because can be treated as a 3-level atom. This energy-level sequence, whose emission lines fall in the optical regime, is proper of $O^{2+}$ and nitrogen $N^+$ (N II; see Fig. A.1). Proceeding by direct physical reasoning it is possible to introduce the temperature diagnostics. More detailed treatments and the derivations can be found in ...

A collision of a free electron with kinetic energy greater than the energy separation between the first two states, may excite the ion to $^1D_2$. Every excitation is then followed by emission of a photon either in $\lambda5007$ or $\lambda4959$, with relative probabilities close to 3:1. Intuitively, collisions with more energetic free photoelectrons are needed to excite the $O^{2+}$ ions in the upper state from where $\lambda4363$ is emitted than to populate the lower energy levels. So the line strength ratio $(\lambda5007 + \lambda4959)/\lambda4363$ immediately tells us how hot the electron plasma in the ionized region is. In a cool environment, the flux ratio will be lower than in a hotter environment. On the other hand, collisions with electrons of any energy may de-excite the ions from higher to lower levels, without any emitted photon. The ratio of the intensities of different transitions should depend therefore on the physical conditions of the gas, i.e. is sensitive to the electron temperature and the electron density.

The full statistical equilibrium between the transition into and out of a specific level can be worked out considering all the radiative and collisional transitions under the assumptions of low density (i.e. below the critical densities). An analytic solution is given for the ratio between the $^1D_2$-$^3P$ to the $^1S_0$-$^3P$ transition:

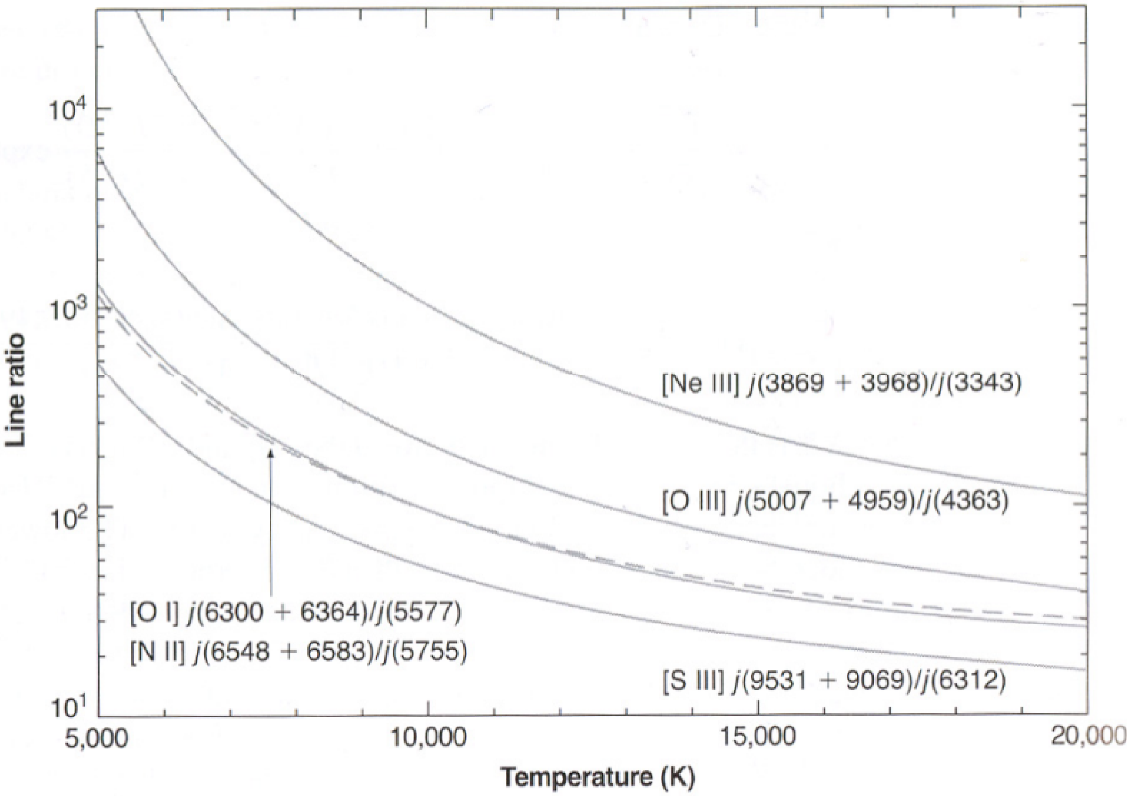

Figure A.2: Few temperature-sensitive ratios as a function of the electron temperature. [NII] ratio is indicated with dashed line for clarity. All the analytic solutions refer to low-density regimes.

$$R_{OIII} = F(\lambda 5007 + 4959)/F(\lambda 4363) = \frac{7.90 \times exp(3.29 \times 10^4/T_e)}{1 + 4.5 \times 10^{-4} N_e T_e^{1/2}} \tag{A.1}$$

$$\approx 7.90 \times exp(3.29 \times 10^4/T_e)$$

because of the weak dependence from $N_e$. Because of this dependence, the OIII ratio is considered the 'thermometer' of ionized regions.

$R_{OIII}$ is quite large because of the weakness of $\lambda$4363 line, and is therefore rather difficult to measure accurately. Indeed, higher densities ($N_e > N_c$) imply a relevant role of collisional de-excitations that are not taken into account in Eq. A.1. The lower $^1$D term has a considerably longer radiative lifetime than the $^1S_0$ term, so it is collisionally excited at lower electron densities than the latter. As a result, above the critical density, we would observe a weakening of $\lambda\lambda$4959,5007 lines. At the same time, the collisional excitation of $^1S_0$ from the excited $^1D_2$ level begins to strengthen the intensity of $\lambda$4363. It is therefore important to know the electron density in the environment in which [O III] photons are emitted.

The [N II] lines, sharing the same energy-level diagram of [O III], allows another temperature estimation, taking advantage from the the ratio of $\lambda\lambda$6548,6583 to $\lambda$5755. This ratio is especially important, since [N II] lines are stronger in the outer parts of the ionized regions, where the ionization is lower (a doubly ionized N require a IP of only 30 eV, lower than that required to produce $O^{2+}$). However, the low critical density of the upper level responsible of the $\lambda$6584 line (Nc=1.8e4) and the blending within the H$\alpha$-[N II] complex (with the possible emission from BLR gas) make this diagnostic not useful. Other ions with similar temperature-sensitive ratios include SIII9533/6310, NeV3425/2974, [O II]2471/3727 ecc. All these ratio, falling out of the optical regime (widely studied in this thesis),

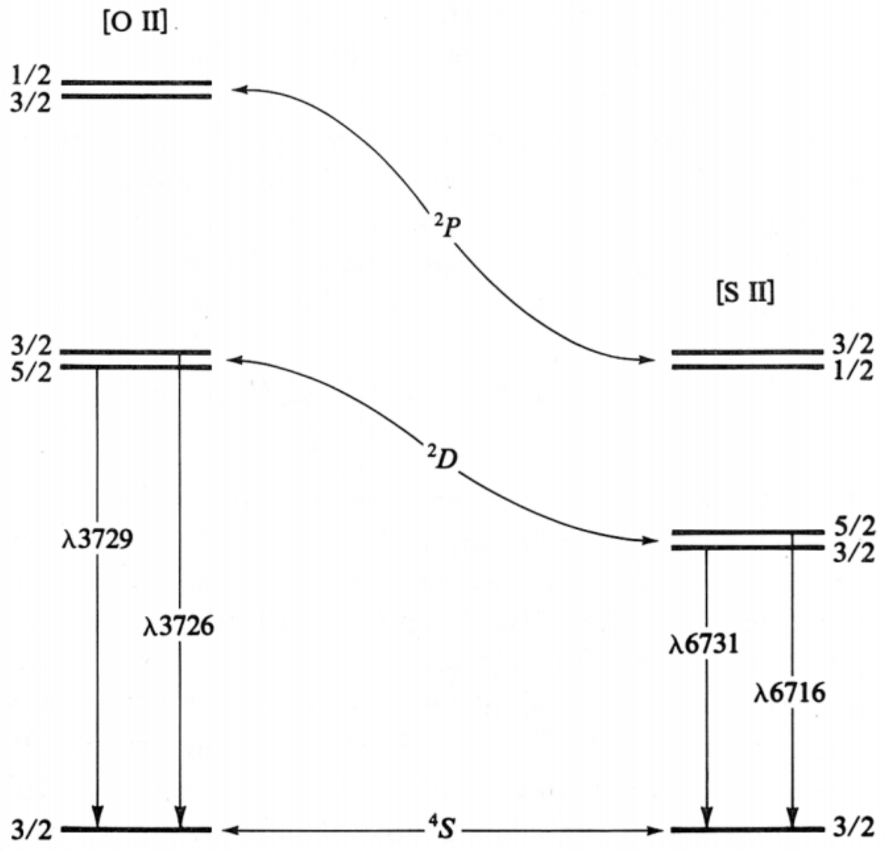

Figure A.3: Few temperature-sensitive ratios as a function of the electron temperature. [NII] ratio is indicated with dashed line for clarity. All the analytic solutions refer to low-density regimes.

are not used in this thesis, with the exception of the latter in Chapter xx. The dependence with the electron temperature are shown in Fig A.4 for few of them.

## A.3 Density-sensitive lines

Electron density in narrow-line gas can be derived through standard nebular diagnostic methods that quantify the effects of collisional de-excitation. This can be done by comparing the intensities of two lines of the same ion emitted by different levels with almost the same excitation energy. In the optical regime, [SII]λλ6716,6731 and [OII]λλ3726,3729 satisfy this requirement. Their energy-level diagram is shown in Fig. A.3. The relative populations of the levels may be found by setting the equilibrium equation between the transition into and out of each specific level. However, as in the previous section, a physical reasoning is preferred to easily show the mechanisms involved. In the low density limit ($N_e -> 0$ cm$^{-3}$), every collisional excitation is followed by the emission of a photon, while in the high density limit ($N_e \gtrsim N_c$) collisional de-excitations dominate. Between the two density regimes, the relative intensity of the [S II] emission lines is a function of the electron density:

$$R_{[SII]} = F(\lambda 6716)/F(\lambda 6731) = 1.49\frac{1+3.77x}{1+12.8x}, \tag{A.2}$$

where x= 0.01 $N_e/\sqrt{T_e}$ is the term related to the collisional de-excitation rate, and make explicit a slight dependence on the electron temperature. This dependence is due to the descading from $^2P^0$ level. Therefore, for a fixed temperature the emission line ratio [S II]λ6716/[S II]λ6731 can be used as a tracer of electron density (Osterbrock & Ferland 2006). We use [S II] ratio as a measure of $N_e$ in

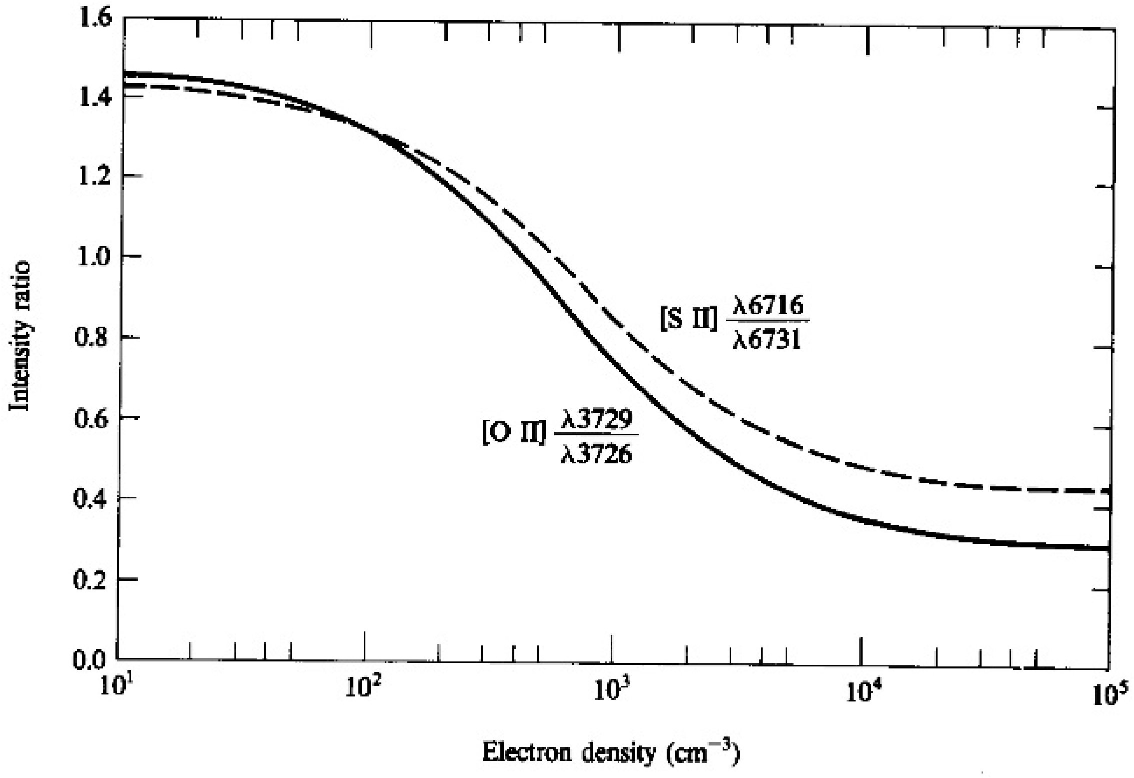

Figure A.4: Few temperature-sensitive ratios as a function of the electron temperature. [NII] ratio is indicated with dashed line for clarity. All the analytic solutions refer to low-density regimes.

Chapters xx and xx. A similar treatment holds for [O II] doublet. In Fig. **??** are shown the variation of [O II] and [S II] ratio as function of the electron density at fixed $T_e$. However, from the observational point of view, [O II] are so close in wavelength that only good wavelength resolutions can be used to derive the relative ratio.

As for the $R_{OIII}$ diagnostic, density-sensitive ratios work at least for the portion of the NLR characterized by densities not greatly in excess of the $N_c$ ($\approx 10^{3.5}$ ;see Table A.1)

## A.4 Balmer decrement and Extinction

H$\alpha$ and H$\beta$ are part of the Balmer emission line series and are referred to recombination lines because are formed by captures of electrons into excited levels that are cascading by downward radiative transitions to the ground level. As the atomic structure of hydrogen is well understood, the strength of the emission line fluxes can be well determined through equilibrium equations. The relative fluxes of the resulting hydrogen emission lines are only weakly dependent on the local conditions (i.e. Ne and Te; Osterbrock and Ferland 2006). In particular, two cases exist for which the Balmer decrement has been determined over a range of temperatures and densities: Case A and Case B. Case A assumes that an ionized region is optically thin to all resonant photons emitted (i.e. escaping without absorption and therefore without causing further transitions), while Case B assumes that the emitting region is optically thick, meaning that these photons are absorbed and can be re-emitted as Balmer lines. These two cases lead to different intrinsic ratios for the Balmer lines. Case B is generally preferred in astrophysical context because is easily associated with dense observed environments. Such predicted intrinsic ratios have been obtained considering both photo-ionization by AGNs or by early-type OB stars: H$\alpha$/H$\beta$ should be $\approx$ 2.86 in star-forming galaxies and $\sim$ 3.1 in regions ionized purely by AGN radiation. In fact, in the latter case, the harder photo-ionizing spectrum results a partly ionized region, in which neutral gas coexists with ions and free electrons (see A.5 for more details). In this region, collisional excitation is able to enhance H$\alpha$ with respect to H$\beta$ w.r.t. the Case B ratio.

The $f(\text{H}\alpha)/f(\text{H}\beta)$ ratio (Case B, Gaskell and Ferland 1984) is mostly used to determine the amount of extinction for low-density gas, such as that of the NLR. The average value of BLR Balmer ratio of 3.06 obtained by Dong et al. 2008 for a large, homogeneous sample of ≈500 low-redshift type 1 AGN with minimal dust extinction effects, suggest that we can assume a ratio of 3.1 also for the BLR. Any deviation to higher flux ratios are interpreted as due to dust extinction, which fade emission lines at lower wavelengths.

## A.5 Line ratio diagnostic diagrams

Separating emission-line galaxies into those that are excited by AGN radiation, those that are excited by early-type stars, and those that show a combination of both, may be particularly challenging when distinctive characteristic of AGN activity are missing. In particular, these difficulties arise from the absence of BLR emission and Fe II features, as well as from the fact that high-ionization lines such as [Fe VII], [Ne V] are not present in all AGN spectra. The segregation between star-forming galaxies and AGNs is done by adopting several diagnostic diagrams (Baldwin et al. 1981; Kewley et al. 2013, 2006, 2001) that combines pairs of emission line flux ratios. Such ratios reflect the differences in the shape of the spectrum of ionizing radiation and in the environment composition among active and inactive galaxies. Before introducing diagnostic diagrams, it is useful to define an important parameter related to the ionization processes, the ionization parameter $U$.

If emission lines are produced by highly ionized gas, the total amount of ionizing photons must be large enough to balance the total number of recombinations in the gas. The flux of photons incident on the gas can be expressed in terms of the ionization parameter

$$U = \frac{\int_{\nu_1}^{\infty} L_\nu/h\nu d\nu}{4\pi r^2 c}\frac{1}{N_H}, \tag{A.3}$$

where $L_\nu$ is the luminosity of the source per unit frequency interval, r is the distance from the source of radiation, $N_H$ is the hydrogen density, and $c$ is the speed of light (which is introduced to make $U$ dimensionless). Physically, $U$ represents the dimensionless ratio of the density of ionizing photons to that of neutral hydrogen. Typical values of ionization parameter for AGN sources are $10^{-3} - 1$. Typical AGN have gas both in high and low states of ionization. The ionization structure depends mainly on the shape of the incident spectrum (and, in particular the X-ray part; see below) and the value of $U$: large ($\sim$ 0.1-1) ionization parameter results in sharply defined hydrogen ionization fronts, while smaller $U$ enables several stages of ionization to coexist over large part of the ionized region (Blandford et al. 1990).

One of the most important line flux ratio in diagnostic diagrams is the $f([\text{O III}]\lambda5007)/f(\text{H}\beta)$, [O III]/H$\beta$ for simplicity. This ratio provides information about the level of ionization of the gas. On the one hand, a strong [O III] line is related with a radiation field characterized by high level of ionization (i.e., large $U$) and large mean ionizing energy ($IP(\text{O}^{2+}) = 35.12$ eV), typical of an AGN. On the other hand, H$\beta$ flux is proportional to the number of recombining hydrogen ions and is hence a measure of the total number of ionizing photons absorbed by the gas. This line ratio is, therefore, large in highly ionized AGN gas. A smaller [O III]/H$\beta$ ratio indicates either an AGN energy spectrum with a low $U$ or soft stellar SED.

Other examples are the $f([\text{N II}])/f(\text{H}\alpha)$, $f([\text{S II}])/f(\text{H}\alpha)$ and $f([\text{O I}]\lambda6300)/f(\text{H}\alpha)$ line ratios. These flux ratios are less sensitive to the level of ionization than the [O III]/H$\beta$ ratio since their ionization potentials are nearly equal to that of hydrogen (i.e., around 13.59 eV, to be compared with 35.1 eV for $\text{O}^{2+}$; see Table A.1). From their ionization potentials, we can infer that the [N II], [O I] and [S II] lines are strong in the outer part of the ionized environment, where partly neutral gas is present. The reason is that the high-energy ionizing photons emitted by AGNs (X-ray photons) can penetrate beyond the $H^+$ ionization front, into the region where most of the oxygen is neutral and the sulphur and nitrogen are singly ionized and excite them. This process is relevant in LINER sources, in which [N II] and [O I] lines dominate the optical spectrum (see Sect. 1.2). Conversely, stellar radiation fields, even those associated with very massive, early-type stars, cannot efficiently penetrate beyond the hydrogen ionization front. Low-ionization emission lines in such sources are weak and their ratios to $f(\mathrm{H}\alpha)$ are much smaller than in most AGNs. Such flux ratios provide therefore a very useful way of dividing soft and hard SEDs. The combination of one of the three low-ionization line to H$\alpha$ flux ratios and the [O III]/H$\beta$ plotted one against the other, allow the division of the plane into regions of low and high $U$, and soft and hard SEDs. The ratio involving [N II], [O I] and [S II] provides therefore similar information and can be used to replace one each other in those cases in which some line is too weak to measure. Another important argument can be exposed for these ratios related to the shape of the ionizing radiation. In fact, these line ratios provide additional information about the gas metallicity ($Z$) in both AGN and stellar environments. Sulphur, nitrogen and oxygen are $\alpha$-elements. Assuming that all the $\alpha$-elements increase together, being proportional to the star formation rate, $O/H \propto N/H$[2]$\propto S/H \propto Z$.

Summarizing, plotting these and other emission-line ratios against each other, for many objects, allows a powerful way to distinguish low- from high-ionization gas, soft from hard ionizing SED, and low from high metallicity. The most popular of these is the Baldwin-Phillips-Terlevich diagram (BPT diagram; Baldwin et al. 1981; also see Veilleux and Osterbrock 1987) which uses the ratios [N II]/H$\alpha$ and [O III]/H$\beta$. The close wavelengths of the pairs of lines in these ratios means that differential dust reddening is minimal. Large samples of emission-line objects, like the SDSS sample, with hundreds of thousands of sources, can be classified into various types of sources by diagnostic diagrams. Figure A.5 shows one such example that has been used to separate star-forming galaxies from AGNs, as well as to distinguish between low- (LINERs) and high-ionization AGNs. The boundaries to isolate AGN on the BPT diagram have been created both from modelling (of the ionization conditions and using stellar population synthesis; e.g., Kewley et al. 2001) and from empirical methods (e.g., Ho et al. 1997a). The line ratios (and the velocity widths) of the forbidden lines in the spectra of type 1 sources are very similar to those observed in type 2 spectra, and indicate that the basic physics in the NLR of both classes is the same. However, diagnostic diagrams are currently the main way to classify type 2 AGNs: type 1 classification is more problematic because of the strong broad Balmer lines that make difficult the estimate of the contribution from the only narrow emission gas.

---

[2] Nitrogen is partially a secondary element, and may show linear or quadratic proportionality to $Z$ depending on the metallicity regime (Blandford et al. 1990).

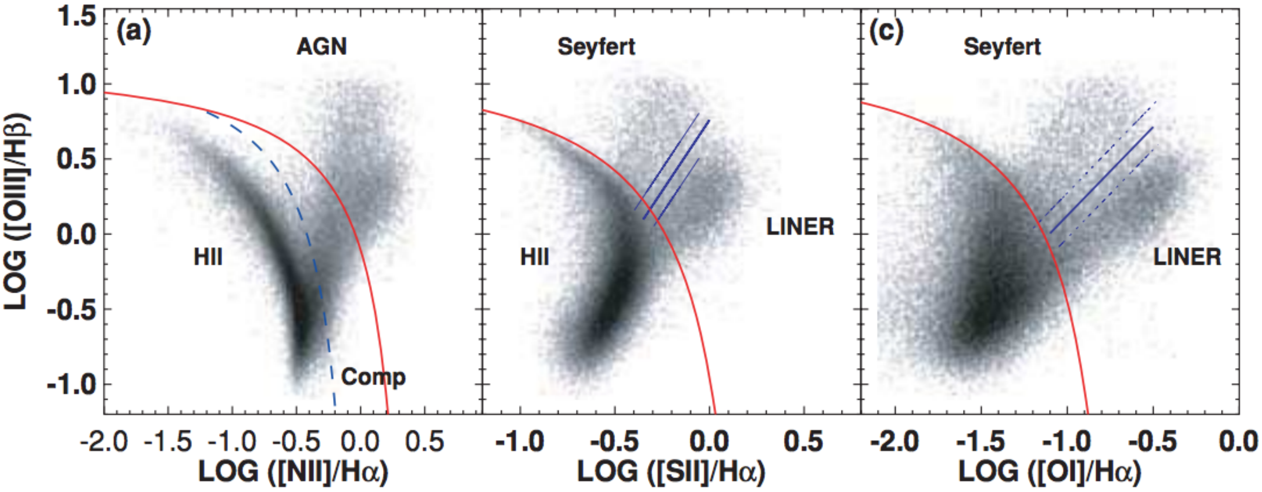

Figure A.5: The [N II]/H$\alpha$ versus [O III]/H$\beta$ diagnostic diagram for SDSS galaxies shown by Kewley et al. 2006. The Kewley et al. 2001 extreme starburst line and the Ka03 classification line are shown as the solid and dashed lines, respectively. (b) The [S II]/H$\alpha$ versus [O III]/H$\beta$ diagnostic diagram; (c) the [O I]/H$\alpha$ versus [O III]/H$\beta$ diagnostic diagram.

## Appendix B

# Ionized gas masses and outflow characterization

We may estimate the mass and the size of the emitting gas starting from the observed luminosities. The luminosity emitted by the recombination line H$\beta$ and by the [OIII]$\lambda$5007 (hereafter [O III]) are generally used to derive such quantities, because they are the strongest lines in the optical spectrum and do not suffer particular blending problems. The [O III] luminosity is given by

$$L_{[OIII]} = \int_V f N_e N(O^{2+}) j_{[OIII]} dV \tag{B.1}$$

where V is the total volume within the line is produced, and $\varepsilon$ is the filling factor, defined as the fraction of the total volume occupied by emitting gas; $N_e$ and $N(O^{2+})$ are the electron and O$^2$+ density, while $j_{[OIII]}$ is the line emissivity, which depends on both electron density and temperature ($T_e$). The doubly ionized oxygen density $N(O^{2+})$ can be written as

$$N(O^{2+}) = \left[\frac{N(O^{2+})}{N(O)}\right] \left[\frac{N(O)}{N(H)}\right] \left[\frac{N(H)}{N_e}\right] N_e$$

that, under the reasonable assumptions that most of the oxygen is in the doubly ionized form, $N(O^{2+}) = N(O)$, can be written as

$$N(O^{2+}) \approx (6.0 \times 10^{-4} \times 10^{[O/H]-[O/H]_\odot}) \times (1.2)^{-1} \times N_e$$

where $[O/H] - [O/H]_\odot$ is the metallicity relative to solar with a solar oxygen abundance of $[O/H] \sim 8.86$ (Centeno and Socas-Navarro 2008). The factor $(1.2)^{-1}$ takes into account a 10% number density of He atoms with respect to hydrogen atoms. Therefore, Eq. B.1 can be rewitten as

$$L_{[OIII]} = 6.0 \times 10^{-4} f 10^{[O/H]-[O/H]_\odot} j_{[OIII]} < N_e^2 > V, \tag{B.2}$$

where $< N_e >$ is the volume-averaged squared density. The ionized gas mass is given by

$$M_{ion} \approx \int_V f \bar{m} N(H) dV \approx f m_p < N_e > V, \tag{B.3}$$

where $\bar{m}$ s the average molecular weight, $m_p$ is the proton mass (assuming 10% number density of He atoms with respect to H atoms). Finally, combining Eq. B.1 with B.3 we get:

$$M_{ion} = 1.7 \times 10^3 \frac{m_p C L_{[OIII]}}{10^{[O/H]-[O/H]_\odot} j_{[OIII]} < N_e >} \tag{B.4}$$

where $C =< N_e >^2 \; / < N_e^2 > \approx 1$ is a 'condensation factor'. Note that the gas mass is sensitive to temperature and density of the clouds, but also to the abundance. However, it is independent of the filling factor of the emitting clouds and the total volume. The total amount of ionized gas into the emitting region can be derived assuming a relative oxygen abundance and its physical plasma properties (i.e., $N_e$ and $T_e$). For $N_e = 10^3$ cm$^{-3}$ and $T_e = 10^4$ K, we obtain a mass of

$$M_{ion} = 5.3 \times 10^7 \frac{C(L_{[OIII]}/10^{44} erg/s)}{10^{[O/H]-[O/H]_\odot} < N_e/1000cm^{-3} >} \; M_\odot \tag{B.5}$$

Similarly, we may derive the gas mass from H$\beta$ (Osterbrock and Ferland 2006):

$$M_{ion} \approx 2.8 \times 10^8 \frac{CL_{H\beta}/10^{43}\; erg/s}{N_e/1000cm^{-3}} \; M_\odot, \tag{B.6}$$

where $L_{H\beta}$ is the H$\beta$ luminosity.

Using this equation, we may visualize the typical extension of the narrow-line emitting region assuming a spherical distribution, $V = 4\pi/3R^3$: for a typical luminous Seyfert 1 galaxy, $L_\beta \approx 10^{41}$ erg/s, and we can obtain $M_{ion} \approx 10^7 M_\odot$ and $R \approx 1kpc$.

These extensions imply that narrow-line gas cannot be under the gravitational influence of the central black hole. This suggests that the narrow line region (NLR) should be considered ad the part of the host galaxy interstellar medium (ISM) whose emission lines are the product of the unobscured ionizing radiation escaping from the central SMBH.

### B.0.1 Outflowing gas component

The amount of ionized outflowing gas can be derived from the [O III] luminosity following the approach described above, assuming if required a specific dust-attenuation correction. This information, added with the geometrical information regarding the extension and the configuration is important to derive the energetics of such phenomena and therefore to infer some constrain on the galaxy-black hole co-evolution models. In fact, outflow energetics allow a direct comparison with theoretical predictions (see e.g., Cicone et al. 2014; A. King and K. Pounds 2015; J. Stern et al. 2016).

Two different morphological configuration for the outflowing clouds are assumed to derive such energetics. In the first scenario, the outflowing material is assumed in a small cloud at a distance R from the central SMBH and a velocity $V_{out}$, and the outflow rate is given by the relation:

$$\dot{M}_{out} = M_{out}/t_{dyn} = V_{out}(M_{out}/R), \tag{B.7}$$

with $t_{dyn}$ being the dynamical time required by the clouds to reach the current distance $R$. This formula provides an appropriate description for an outflow associated with a single explosive event, in which the material is ejected. In the second scenario, the outflowing material uniformly populate a spherical (or bi-conical) region which is continuously refilled with the gas ejected from the central SMBH, as expected in feedback scenarios. In this case, the mass rate changes by a multiplicative factor of 3 (Maiolino et al. 2012). Currently, it is not possible to distinguish between these two possible scenarios and higher angular resolution data are required. However, other factors play a more important role in the computation of outflow energetics, that unfortunately are still affected by high uncertainties ($\gg$ of a factor 3).

Through this thesis we assume that the outflow has a bi-conical geometry and, from the Eq. **??**, we derive the outflow mass rate,

$$\dot{M}_{out} = 164 \frac{CL_{44}([OIII])V_{out,3}}{N_{e,3}R_{kpc}10^{[O/H]-[O/H]_\odot}} \; M_\odot s^{-1}, \tag{B.8}$$

and the kinetic power

$$\dot{K}_{out} = \frac{1}{2}\dot{M}_{out}V_{out}^2 = \frac{1}{2}\frac{M_{out}}{R}V_{out}^3$$

$$= 5.17 \times 10^{43} \frac{C L_{44}([OIII]) V_{out,3}^{3}}{N_{e,3} R_{kpc} 10^{[O/H]-[O/H]_{\odot}}} \; erg\ s^{-1}, \tag{B.9}$$

where $L_{44}([OIII])$ is the [O III] luminosity associated to the outflow component in units of $10^{44}$ erg $s^{-1}$ and corrected for the extinction, $N_{e,3}$ is the electron density in units of 1000 $cm^{-3}$, $V_{out,3}$ is the outflow velocity $V_{out}$ in unit of 1000 km/s, $C$ is the condensation factor ($\approx 1$) introduced in the previous section, $10^{[O/H]-[O/H]_{\odot}}$ is the metallicity in solar units, $R_{kpc}$ is the radius of the outflowing region in units of kpc. In the same manner, we derive the momentum flux, defined as $\dot{P}_{out} = \dot{M}_{out} V_{out}$. All these equations are derived following the prescription introduced by Cano-Díaz et al. (2012), assuming an electron temperature of $10^4$ K and an electron density of $10^3$. The coefficients in the equations change of a multiplicative factor of 1/3 when we assume a higher temperature ($2 \times 10^4$ K), with very weak dependence on the electron density.

## B.1 The black hole mass

It has become common practice to estimate AGN SMBH masses based on single-epoch (SE) spectra. This approach assumes that the BLR is virialized. SE determination is based on an empirical correlation between the radius $R_{BLR}$ and the optical continuum luminosity, $R_{BLR} \propto L^{\gamma}$, that has been calibrated using reverberation-mapped (RM) sample at low redshifts and luminosities ($z < 0.3$ and $\log(\lambda L_{\lambda}(5100\mathring{A}) < 46$; Kaspi2000,2005). There are indications that the extrapolation to high luminosities and redshift could be valid (i.e. $z \approx$ 2-4 and $\log(\lambda L_{\lambda}(5100\mathring{A}) \gtrsim$ 47-48; see Saturni et al. 2016).

Using the continuum luminosity as a proxy for the BLR radius, and the BLR FWHM as a proxy for the virial velocity, the SE mass estimate can be expressed as

$$log(\frac{M_{BH,SE}}{M_{\odot}}) = a + b\ log\frac{\lambda\ L_{\lambda}}{10^{42} erg/s} + 2\ log(\frac{FWHM}{10^{3} km/s}) \tag{B.10}$$

where the coefficients a and b are empirically calibrated against local AGNs with RM masses. H$\alpha$, H$\beta$, MgII and CIV emission lines and their corresponding continuum luminosities (namely, $\lambda L_{\lambda}$ at $5100\mathring{A}$, $3000\mathring{A}$ and $1350\mathring{A}$ respectively) are all frequently adopted in such virial calibrations, although without consensus about the scatter and possible biases between the different estimators, in particular regarding the CIV line (see e.g. Treves14 and references therein). The additional multiple Gaussian/Lorentzian fits for the broad H$\alpha$ and H$\beta$ BLR component provide a better fit to the overall broad line profile. It is unclear, however, which FWHM is a better surrogate for the true virial velocity, that is, the one that yields the smallest scatter in the calibration against RM black hole masses. Following Shen+11, we adopted the FWHM measured from the best-fit model of the BLR profile.

Given that our continuum luminosities at 5100 suffer from host contamination at the low-luminosity end, according to the redshift of the source, we adopted the SE relations calibrated by GreeneHo2005, in which the H$\alpha$ and H$\beta$ luminosities are used instead of the L5100 (see also sect refbolsec): (their Eqs. 6 and 7),

$$(a, b) = \begin{cases} (6.30, 0.55), & \text{with } L(H\alpha) \text{ instead of } \lambda L_{\lambda}, \text{for } z < 0.4 \\ (6.56, 0.56), & \text{with } L(H\beta) \text{ instead of } \lambda L_{\lambda}, \text{for} z > 0.4 \end{cases} \tag{B.11}$$

electron density (BLR, coronal lines region, NLR)

## APPENDIX C

# Simultaneous fit capabilities

## C.1 Fe II emission line template

We use theoretical model templates of Kovačević et al. 2010 to reproduce Fe II emission. The authors constructed a F II template consisting of tens of line components, identified as the strongest within 4000-5500 range. Many of them are sorted into four line groups according to the lower term of their atomic transition (P, F, S and G, see Fig. C.1). Relative intensities of each FeII Gaussian line within a single group have been calculated studying the transition probabilities. A fifth group, whose relative intensities have been obtained on the basis of their best-fit of the well-studied I Zw 1 spectrum, was added to reproduce the overall FeII profile. These templates assumes seven free fitting parameters: the shift relative to the systemic redshift and the FWHM of the FeII lines, which are assumed to be the the same for all the lines of the template, and the intensities of the Fe II lines within the line groups. As noticeable from Fig. C.1, iron emission strongly cover the entire wavelength range of H$\beta$ and [OIII]. As a result, a correct modelling is needed to fully characterize the Balmer profile, and in particular its FWHM, from which crucial information can be derived, and the double ionized oxygen emission. One of the S group line (the central solid red gaussian in the central panel of Fig. C.1) may be responsible for a red excess in the [OIII] line, leading to a wrong determination of the kinematic conditions in the ionized gas. The fact that the amplitude of this line is linked to the intensity of the entire S group (and, in particular, to the nearest line in the red Fe II bump, i.e. the bluer red solid gaussian in the central panel) gives and important contribution to the deconvolution between Fe II and reddest emission from [OIII]. As an example, we show in Fig. **??** the fitting results we obtain for a couple of SDSS sources, in which prominent red wings in the [OIII] line are detected.

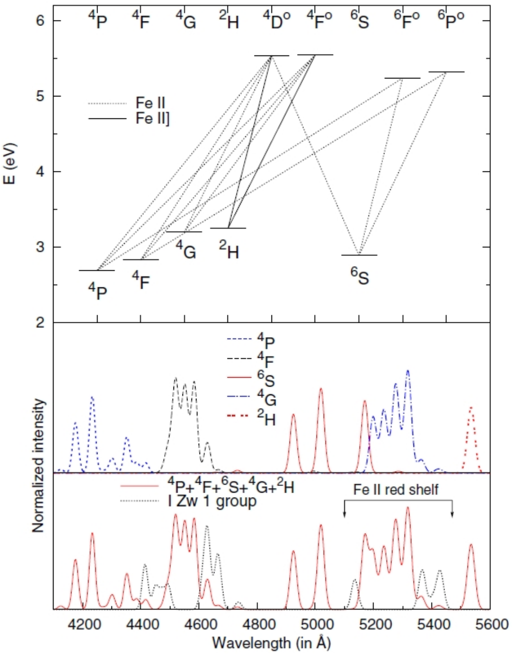

Figure C.1

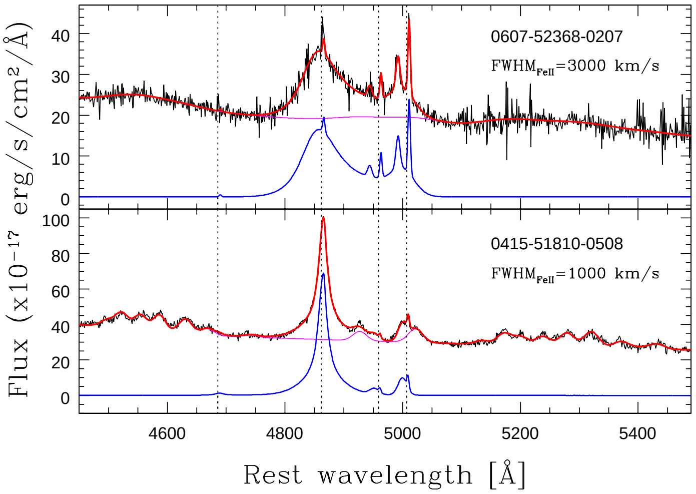

Figure C.2

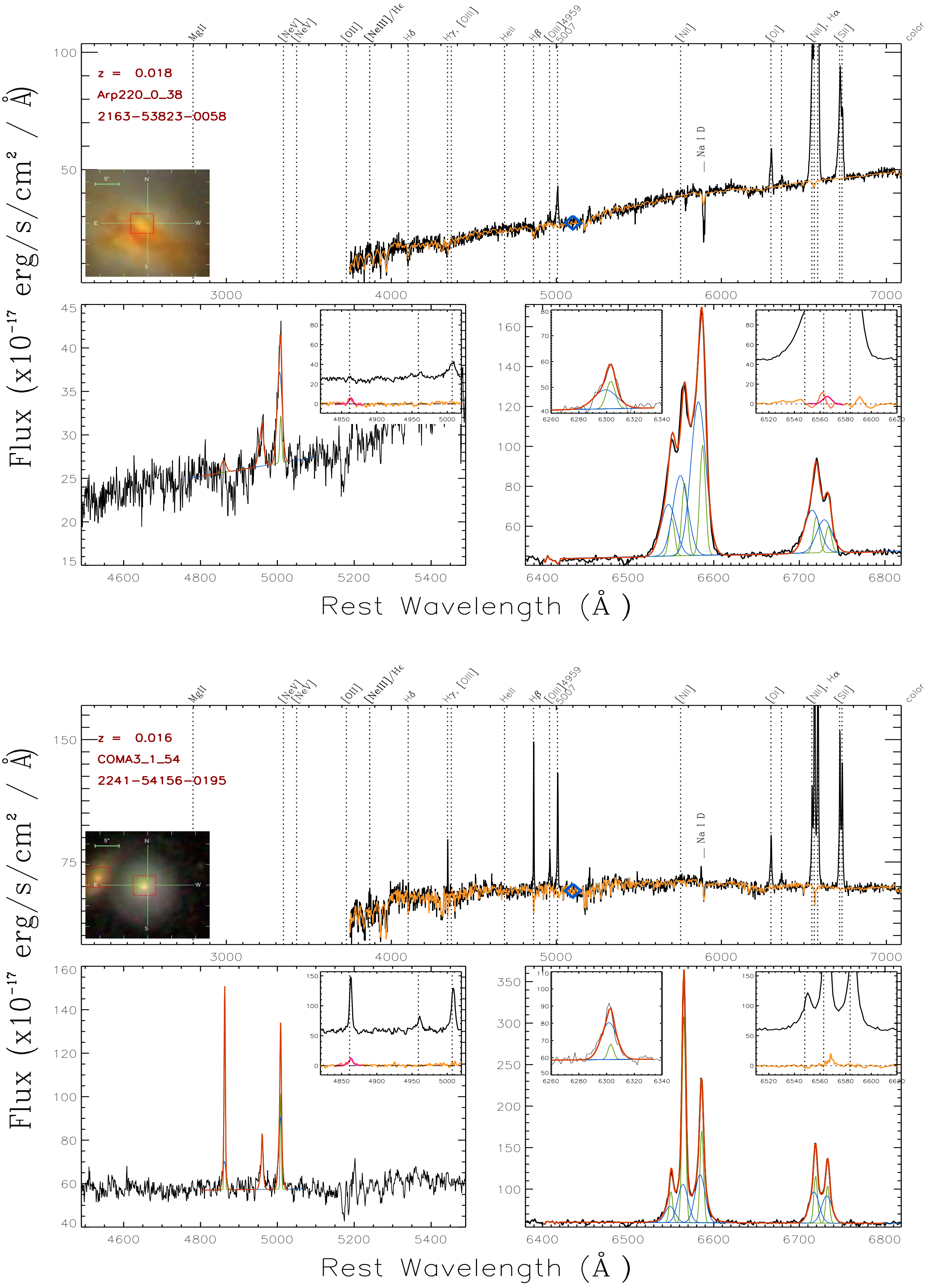
z = 0.018
Arp220_0_38
2163-53823-0058
z = 0.016
COMA3_1_54
2241-54156-0195
MgII
[NeV]
[NeV]
[OII]
[NeIII]/Hε
Hδ
Hγ, [OIII]
HeII
Hβ
[OIII]4959
5007
[NII]
[OI]
[NII], Hα
[SII]
color
Na I D
Flux (x10$^{-17}$ erg/s/cm$^2$ / Å)
Rest Wavelength (Å)

Figure C.3: xx

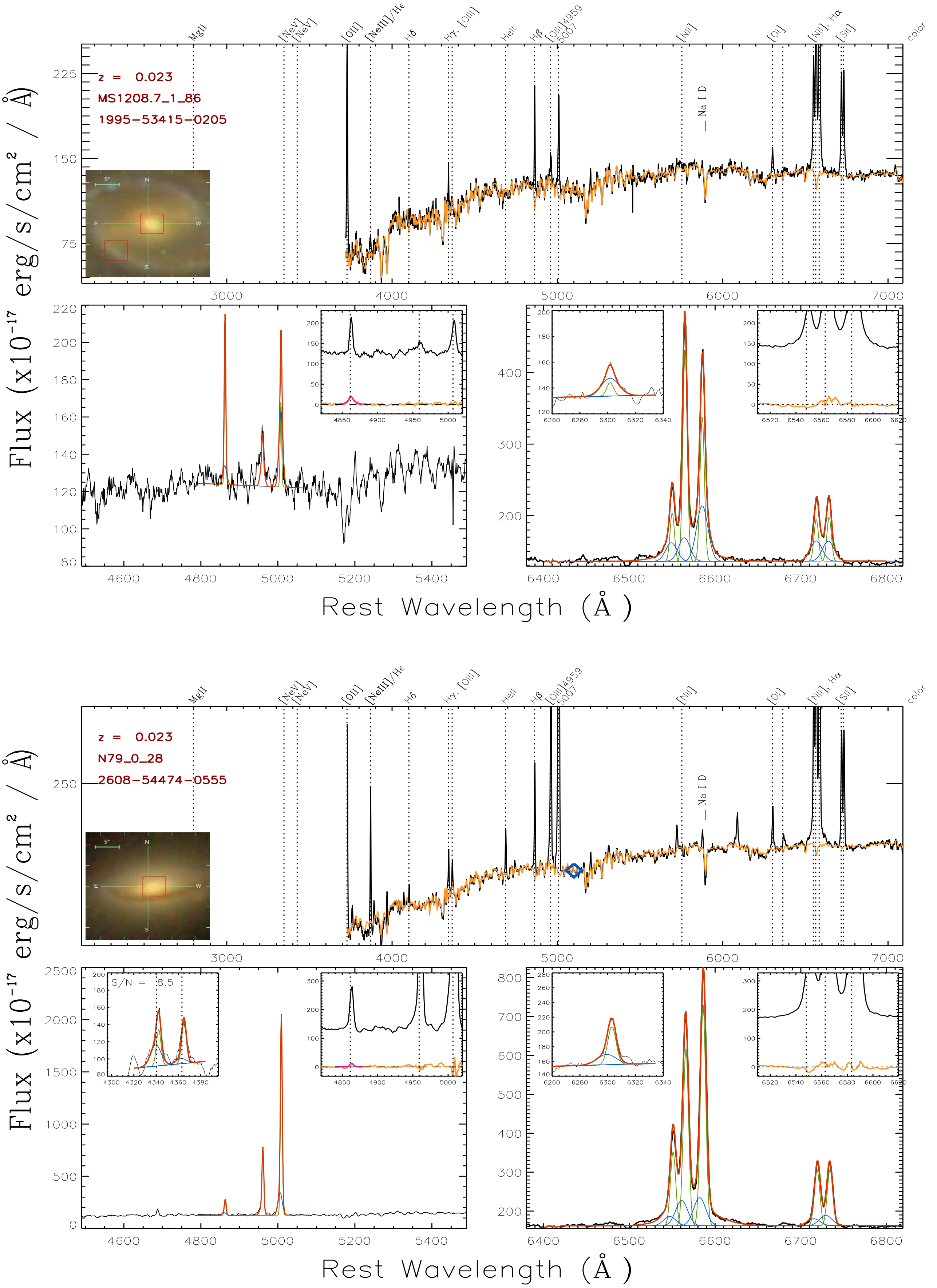
MgII
[NeV]
[NeV]
[OII]
[NeIII]/Hε
Hδ
Hγ, [OIII]
HeII
Hβ
[OIII]4959
5007
[NII]
[OI]
[NII], Hα
[SII]
color
Na I D
z = 0.023
MS1208.7_1_86
1995−53415−0205
N79_0_28
2608−54474−0555
S/N = 8.5
5"
N
E
W
S
Flux (x10$^{-17}$ erg/s/cm$^2$ / Å)
Rest Wavelength (Å )
3000
4000
5000
6000
7000
225
150
75
250
4600
4800
5000
5200
5400
6400
6500
6600
6700
6800
220
200
180
160
140
120
100
80
400
300
200
2500
2000
1500
1000
500
0
800
700
600

Figure C.2: xx

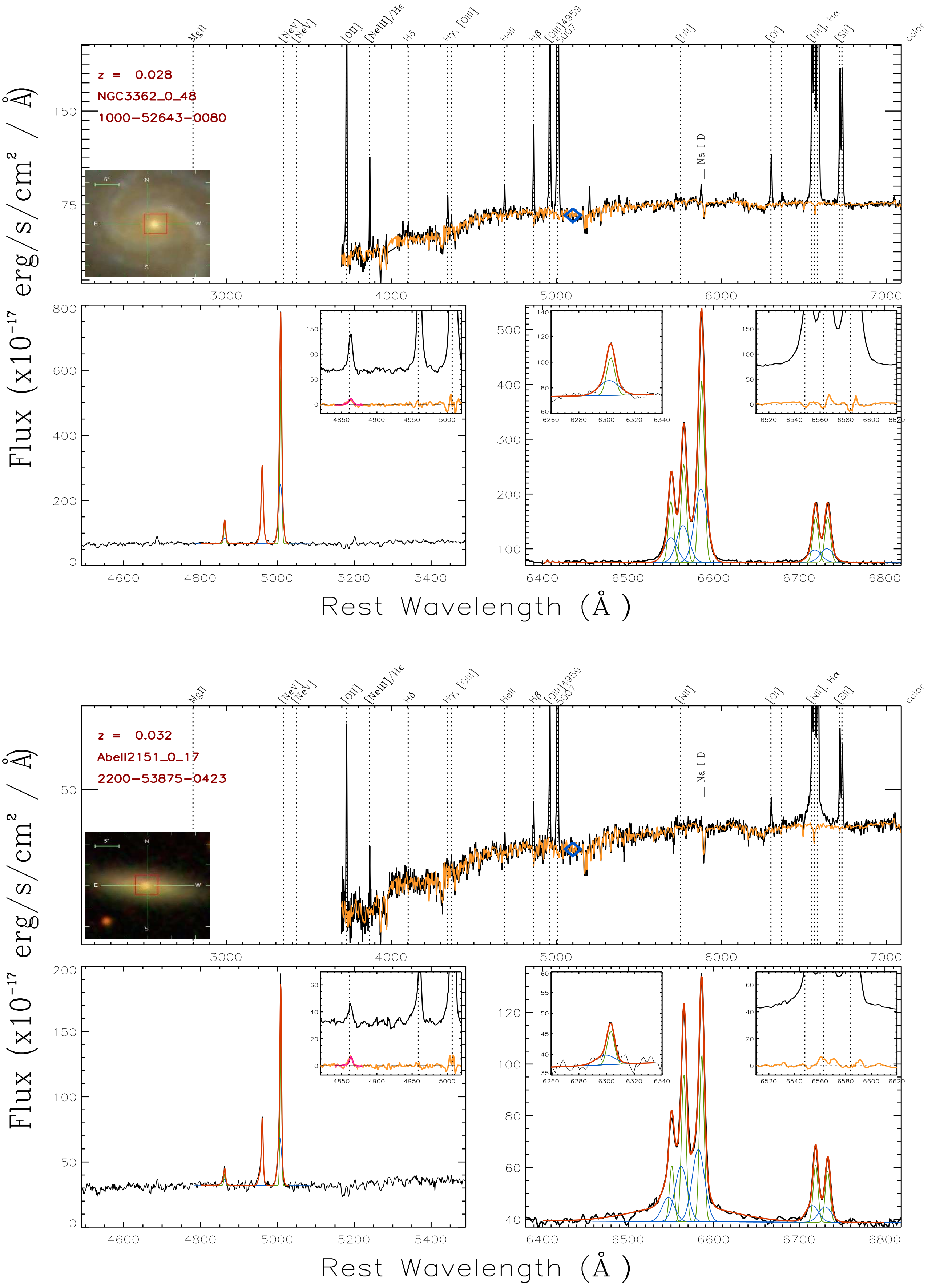
MgII
[NeV]
[NeV]
[OII]
[NeIII]/Hε
Hδ
Hγ, [OIII]
HeII
Hβ
[OIII]4959
5007
[NII]
[OI]
[NII], Hα
[SII]
color
Na I D
z = 0.028
NGC3362_0_48
1000−52643−0080
z = 0.032
Abell2151_0_17
2200−53875−0423
Flux (x10$^{-17}$ erg/s/cm$^2$ / Å)
Rest Wavelength (Å )
3000
4000
5000
6000
7000
4600
4800
5000
5200
5400
6400
6500
6600
6700
6800
N
S
E
W
5"

Figure C.1: xx

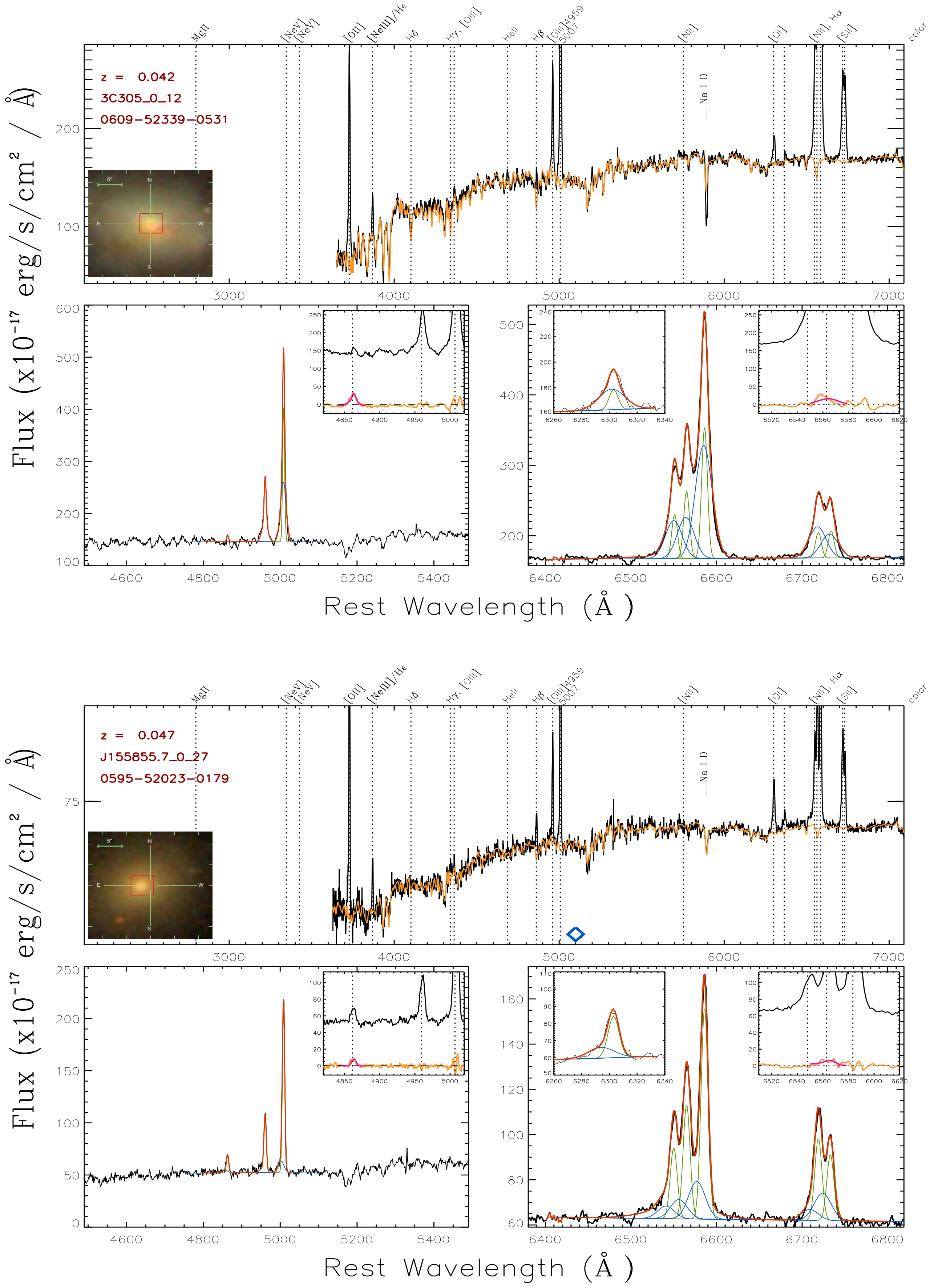
MgII
[NeV]
[NeV]
[OII]
[NeIII]/Hϵ
Hδ
Hγ, [OIII]
HeII
Hβ
[OIII]4959
5007
[NII]
[OI]
[NII], Hα
[SII]
color
Na I D
z = 0.042
3C305_0_12
0609−52339−0531
z = 0.047
J155855.7_0_27
0595−52023−0179
5"
N
E
W
S
Flux (x10⁻¹⁷ erg/s/cm² / Å)
Rest Wavelength (Å)

Figure C.0: xx

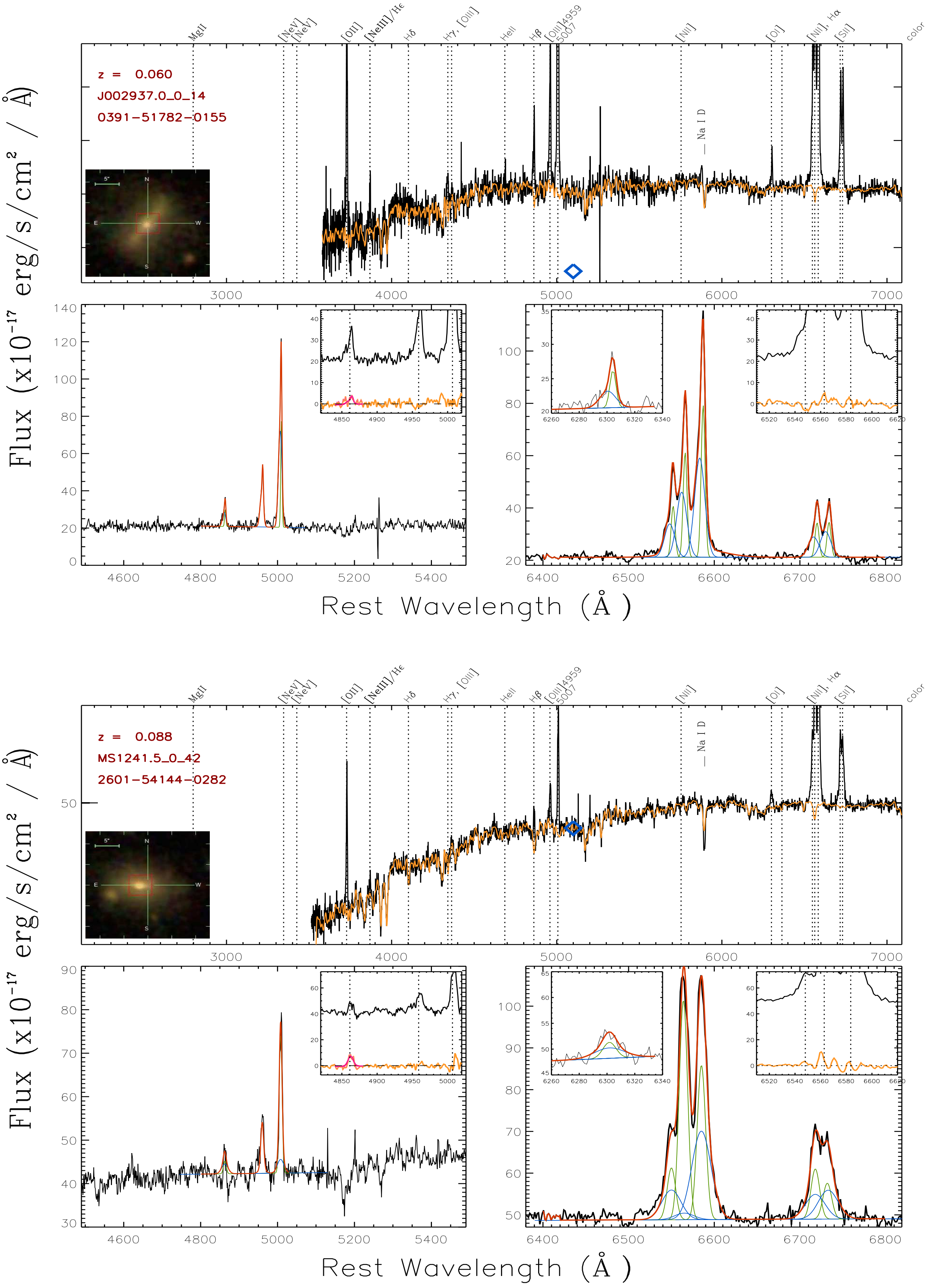
MgII
[NeV]
[NeV]
[OII]
[NeIII]/Hε
Hδ
Hγ, [OIII]
HeII
Hβ
[OIII]4959
5007
[NII]
[OI]
[NII], Hα
[SII]
color
Na I D
z = 0.060
J002937.0_0_14
0391−51782−0155
z = 0.088
MS1241.5_0_42
2601−54144−0282
5"
N
E
W
S
Flux (x10$^{-17}$ erg/s/cm$^2$ / Å)
Rest Wavelength (Å)
3000
4000
5000
6000
7000
4600
4800
5000
5200
5400
6400
6500
6600
6700
6800
4850
4900
4950
5000
6260
6280
6300
6320
6340
6520
6540
6560
6580
6600
6620
0
20
40
60
80
100
120
140
30
50
70
90

Figure C.-1: xx

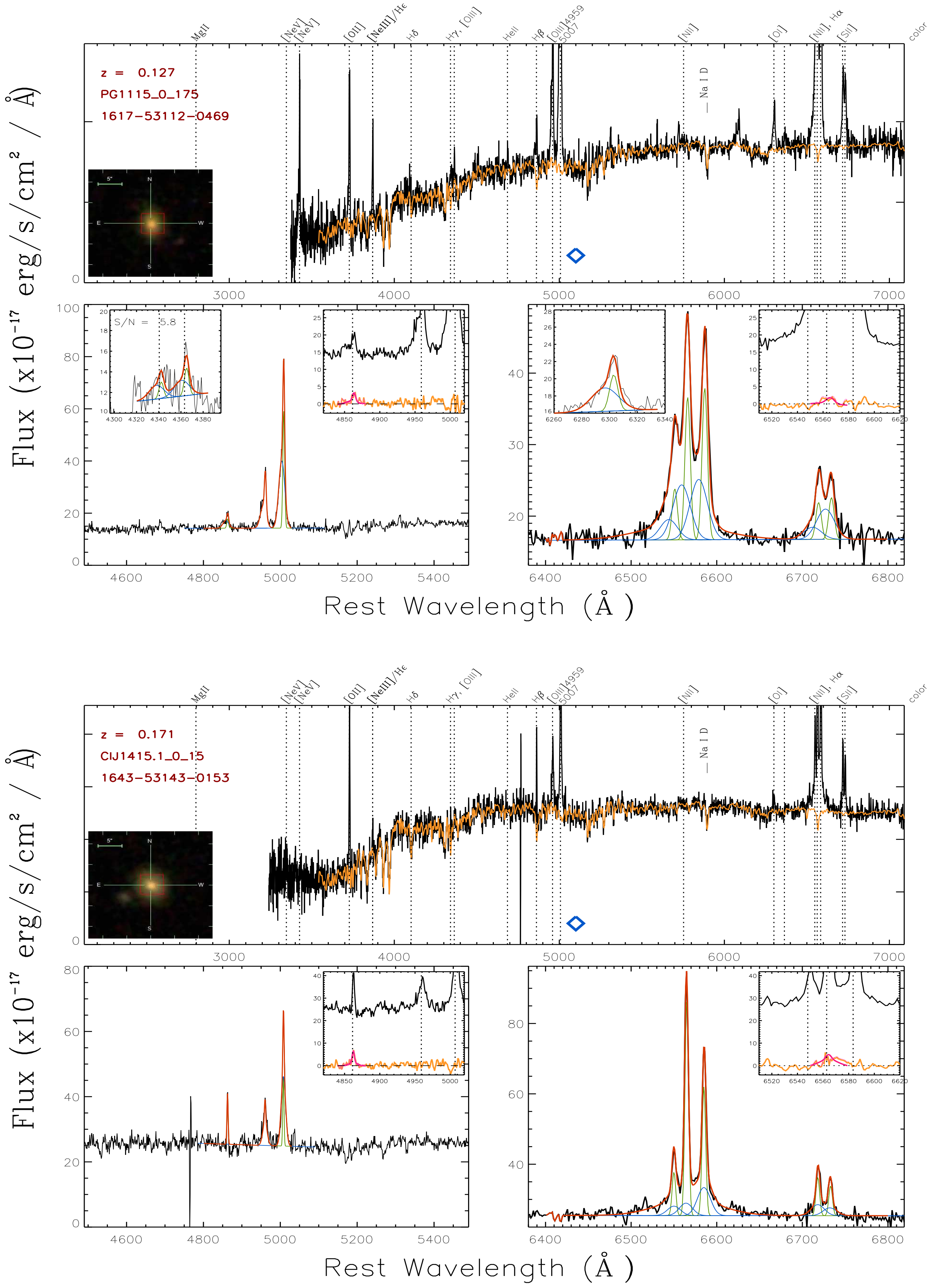
z = 0.127
PG1115_0_175
1617-53112-0469
MgII
[NeV]
[NeV]
[OII]
[NeIII]/Hε
Hδ
Hγ, [OIII]
HeII
Hβ
[OIII]4959
5007
[NII]
Na I D
[OI]
[NII], Hα
[SII]
color
5"
N
E
W
S
S/N = 5.8
Flux (x10$^{-17}$ erg/s/cm$^2$ / Å)
Rest Wavelength (Å)
z = 0.171
ClJ1415.1_0_15
1643-53143-0153

Figure C.-2: xx

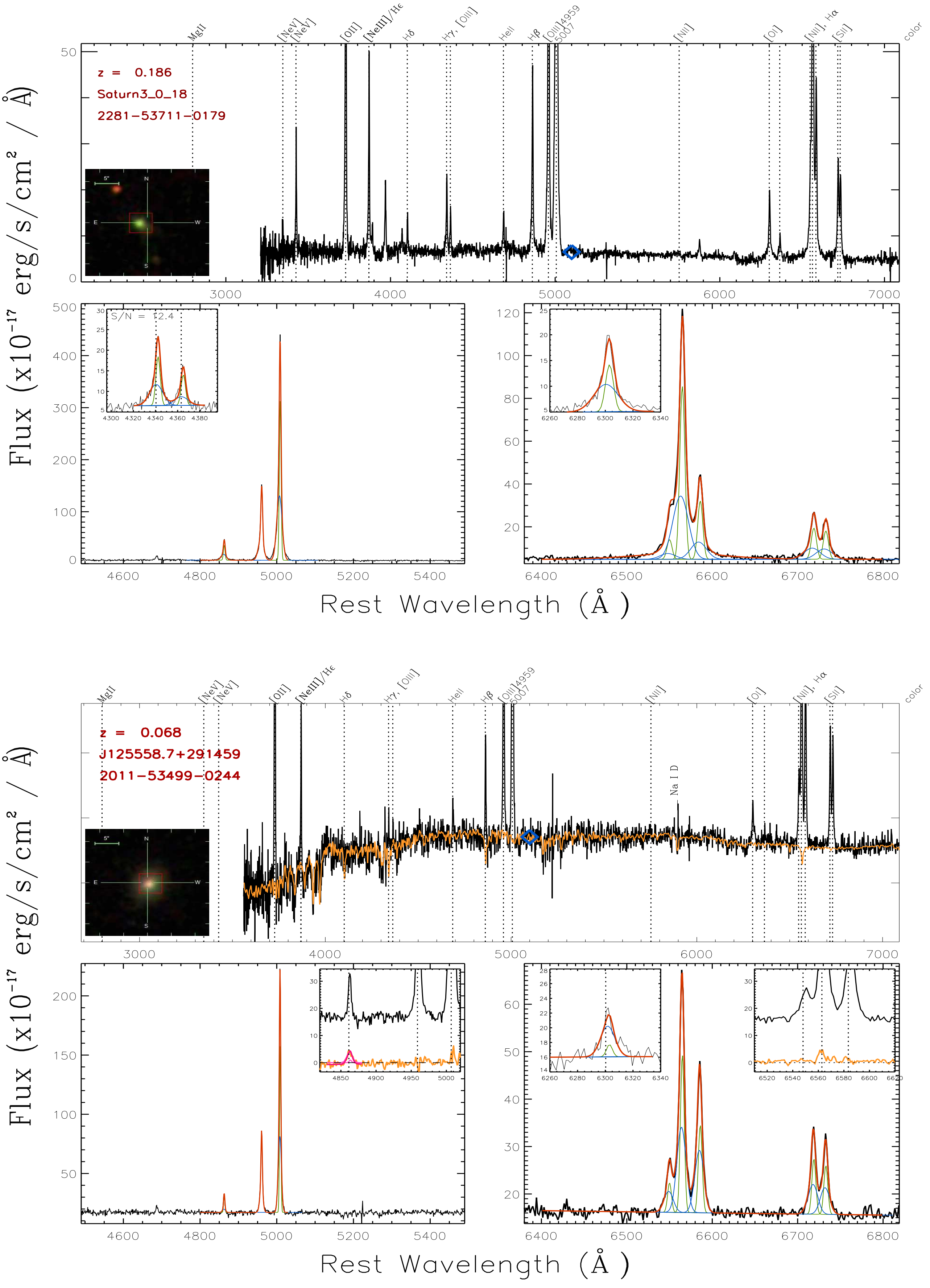
z = 0.186
Saturn3_0_18
2281−53711−0179
MgII
[NeV]
[NeV]
[OII]
[NeIII]/Hϵ
Hδ
Hγ, [OIII]
HeII
Hβ
[OIII]4959
5007
[NII]
[OI]
[NII], Hα
[SII]
color
S/N = 12.4
Flux (x10$^{-17}$ erg/s/cm$^2$ / Å)
Rest Wavelength (Å )
z = 0.068
J125558.7+291459
2011−53499−0244
Na I D
Flux (x10$^{-17}$ erg/s/cm$^2$ / Å)
Rest Wavelength (Å )

Figure C.-3: xx

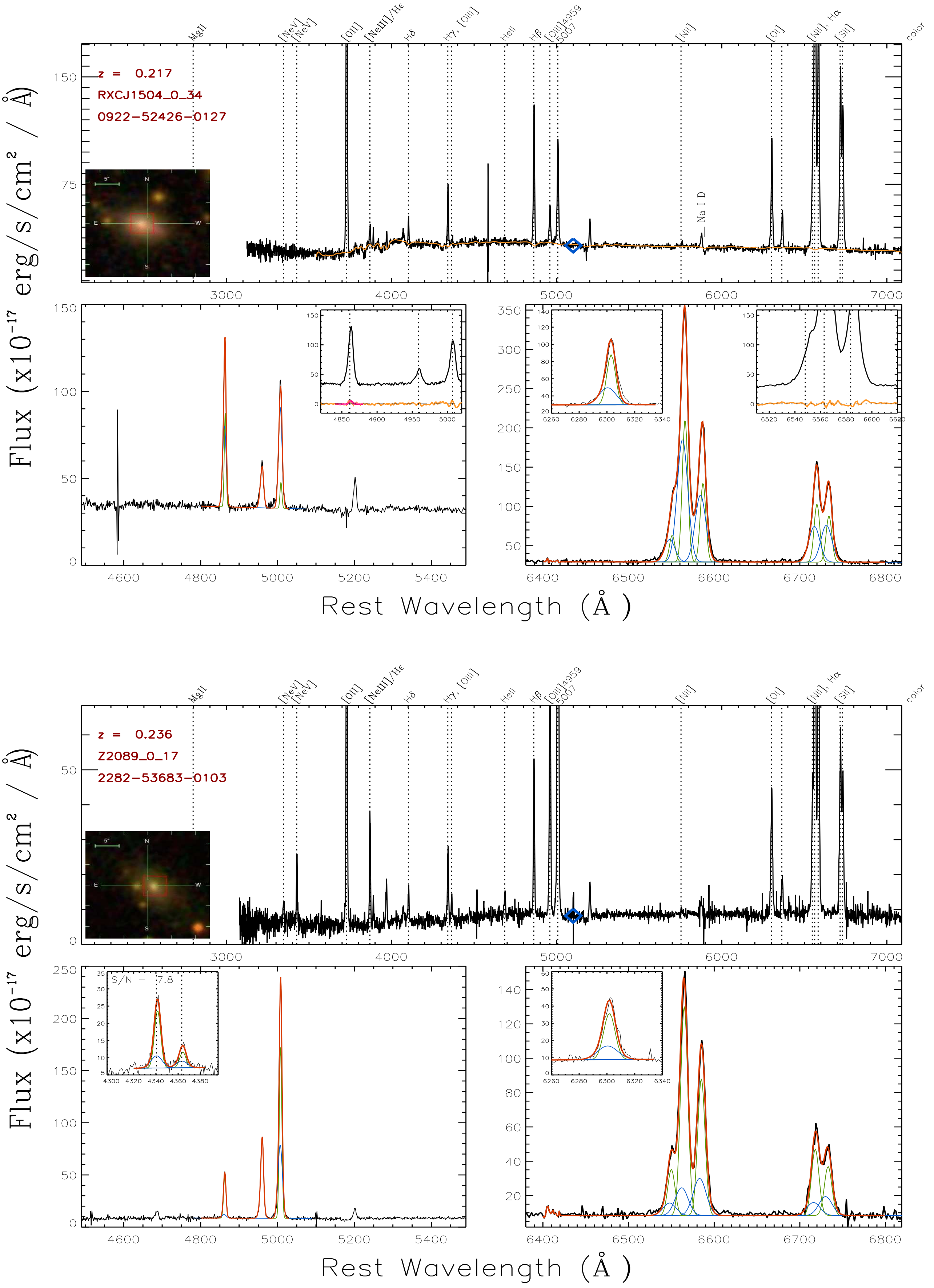
MgII
[NeV]
[NeV]
[OII]
[NeIII]/Hε
Hδ
Hγ, [OIII]
HeII
Hβ
[OIII]4959
5007
[NII]
[OI]
[NII], Hα
[SII]
color
z = 0.217
RXCJ1504_0_34
0922-52426-0127
Na I D
5"
N
E
W
S
150
75
3000
4000
5000
6000
7000
Flux (x10^-17 erg/s/cm² / Å)
4600
4800
5000
5200
5400
6400
6500
6600
6700
6800
Rest Wavelength (Å)
z = 0.236
Z2089_0_17
2282-53683-0103
S/N = 7.8
50
0
Flux (x10^-17 erg/s/cm² / Å)
Rest Wavelength (Å)

Figure C.-4: xx

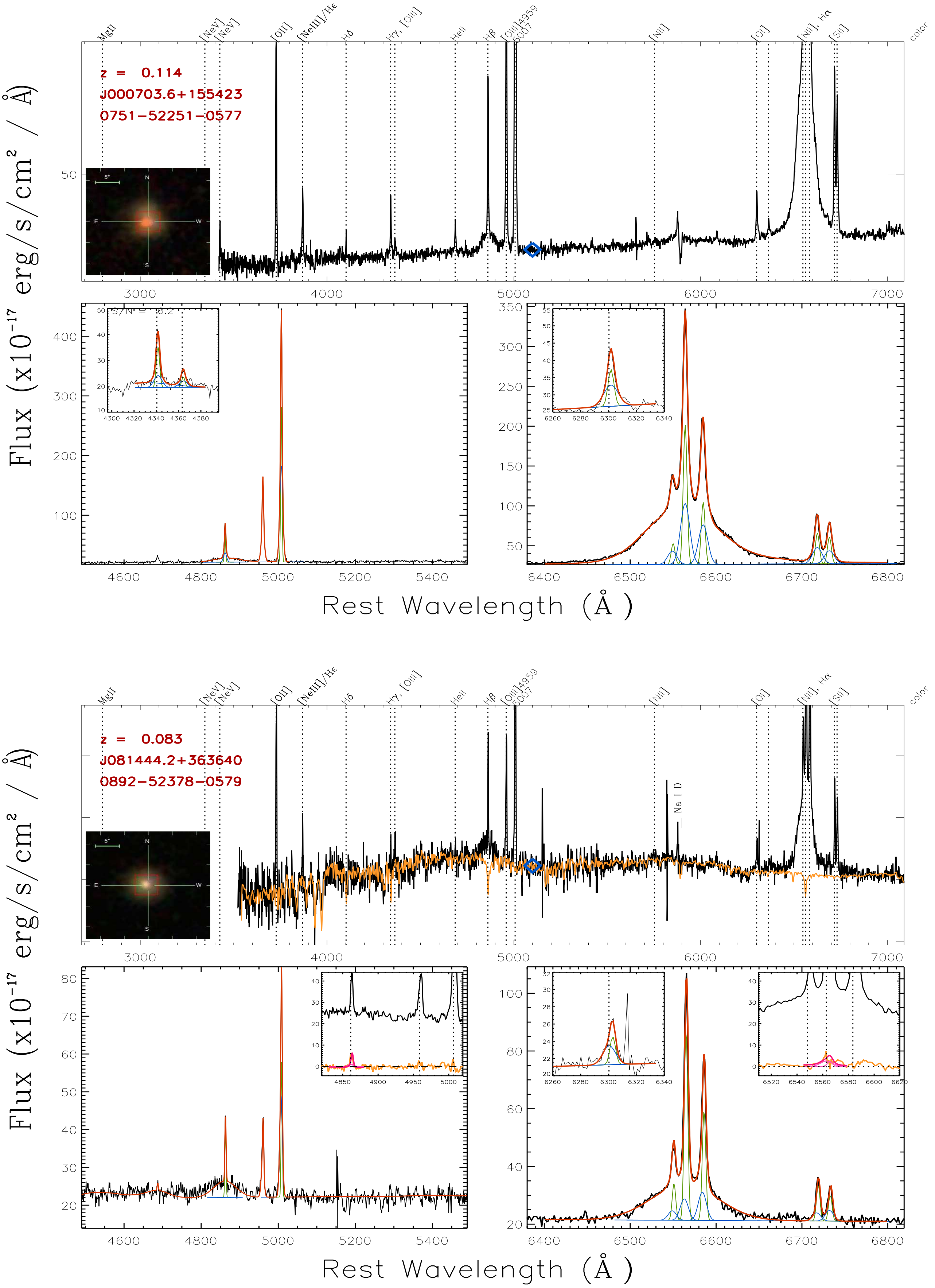
MgII
[NeV]
[NeV]
[OII]
[NeIII]/Hε
Hδ
Hγ, [OIII]
HeII
Hβ
[OIII]4959
5007
[NII]
[OI]
[NII], Hα
[SII]
color
z = 0.114
J000703.6+155423
0751−52251−0577
5"
N
E
W
S
50
3000
4000
5000
6000
7000
S/N = 6.2
4600
4800
5000
5200
5400
6400
6500
6600
6700
6800
Flux (x10$^{-17}$ erg/s/cm$^2$ / Å)
Rest Wavelength (Å )
z = 0.083
J081444.2+363640
0892−52378−0579
Na I D

Figure C.-5: xx

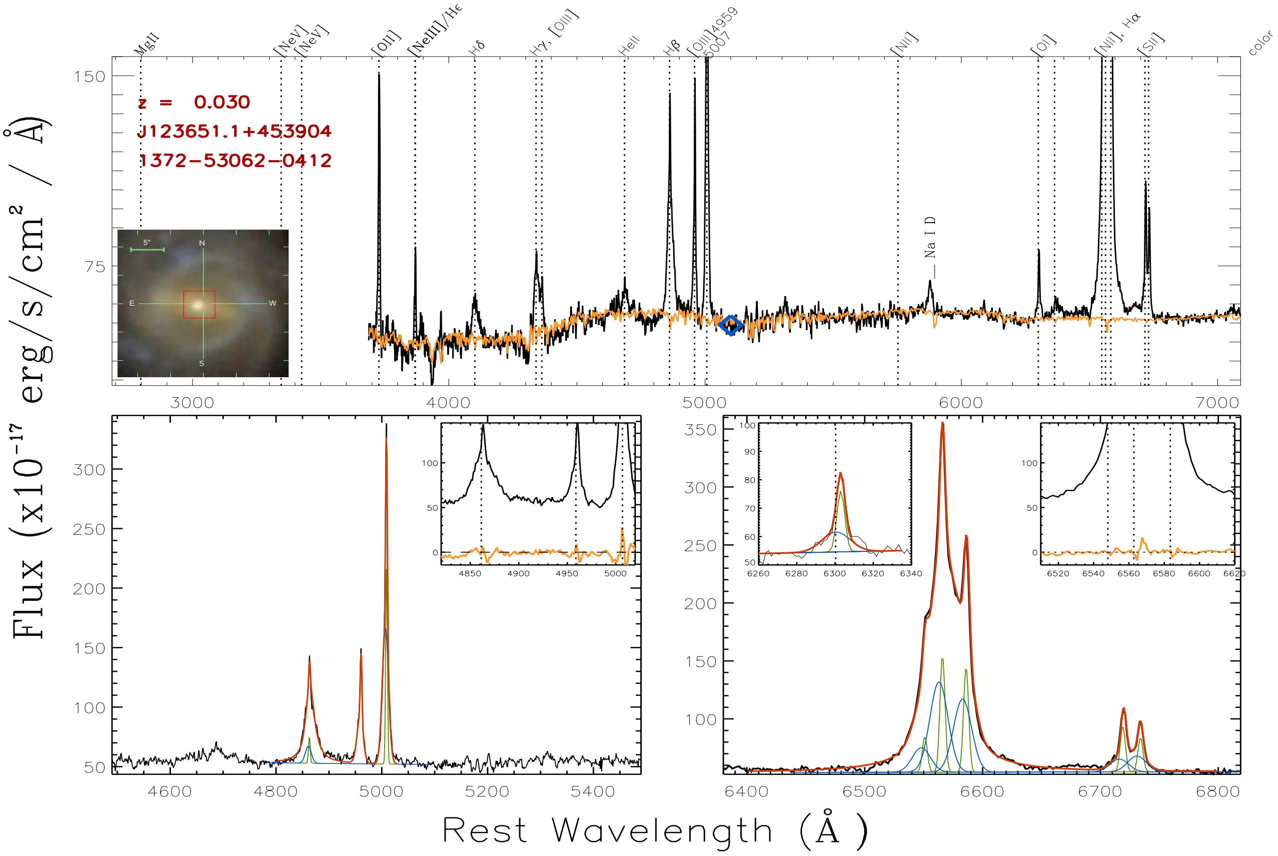
MgII
[NeV]
[NeV]
[OII]
[NeIII]/Hε
Hδ
Hγ, [OIII]
HeII
Hβ
[OIII]4959
5007
[NII]
[OI]
[NII], Hα
[SII]
color
z = 0.030
J123651.1+453904
1372−53062−0412
Na I D
N
S
E
W
5"
150
75
3000
4000
5000
6000
7000
Flux (x10$^{-17}$ erg/s/cm$^2$ / Å)
300
250
200
150
100
50
4600
4800
5000
5200
5400
4850
4900
4950
5000
350
6400
6500
6600
6700
6800
6260
6280
6300
6320
6340
6520
6540
6560
6580
6600
6620
Rest Wavelength (Å )

Figure C.-6: xx

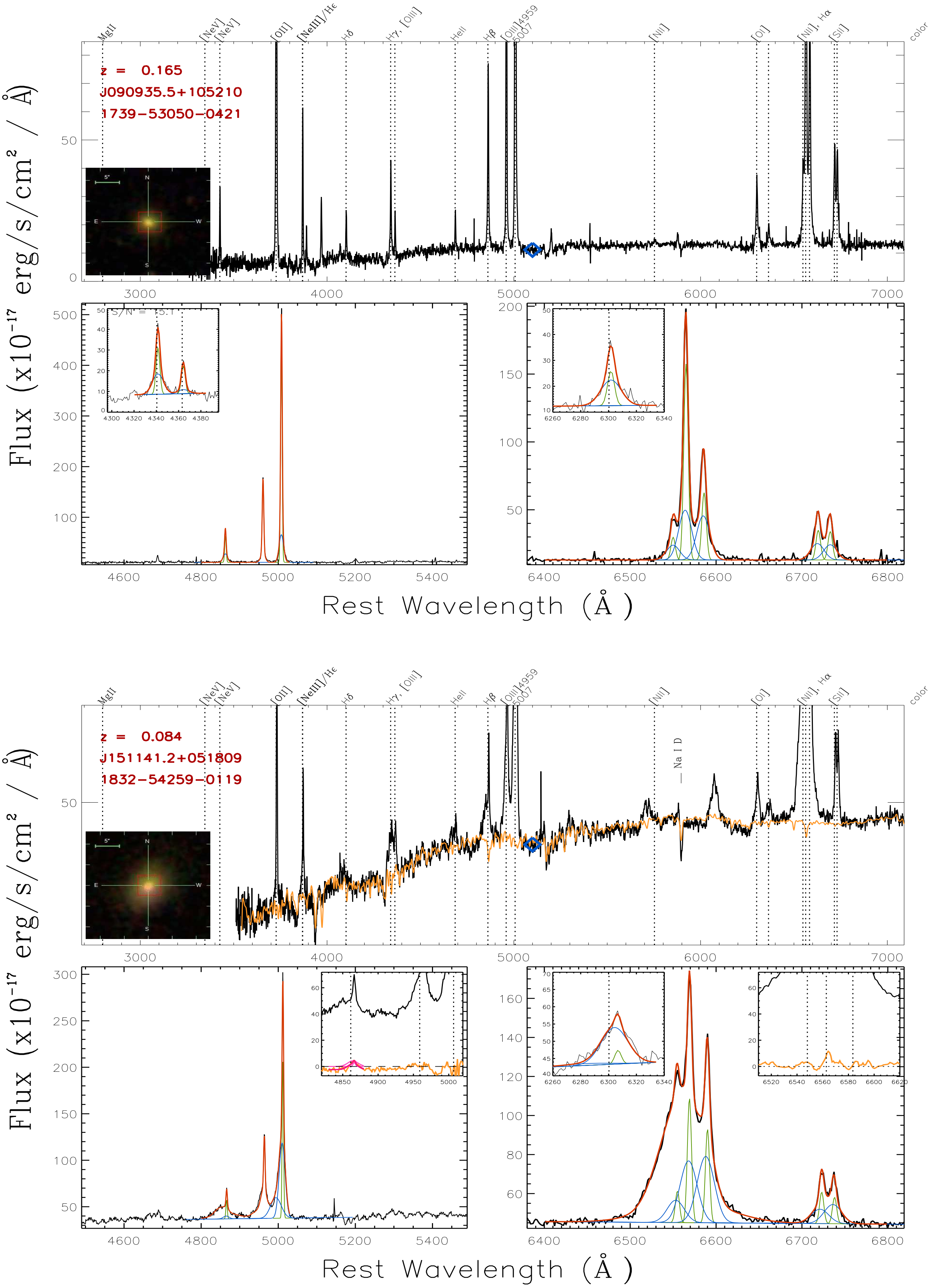
MgII
[NeV]
[NeV]
[OII]
[NeIII]/Hε
Hδ
Hγ, [OIII]
HeII
Hβ
[OIII]4959
5007
[NII]
[OI]
[NII], Hα
[SII]
color
z = 0.165
J090935.5+105210
1739−53050−0421
5"
N
E
W
S
Flux (x10$^{-17}$ erg/s/cm$^2$ / Å)
Rest Wavelength (Å )
S/N = 5.1
z = 0.084
J151141.2+051809
1832−54259−0119
Na I D

Figure C.-7: xx

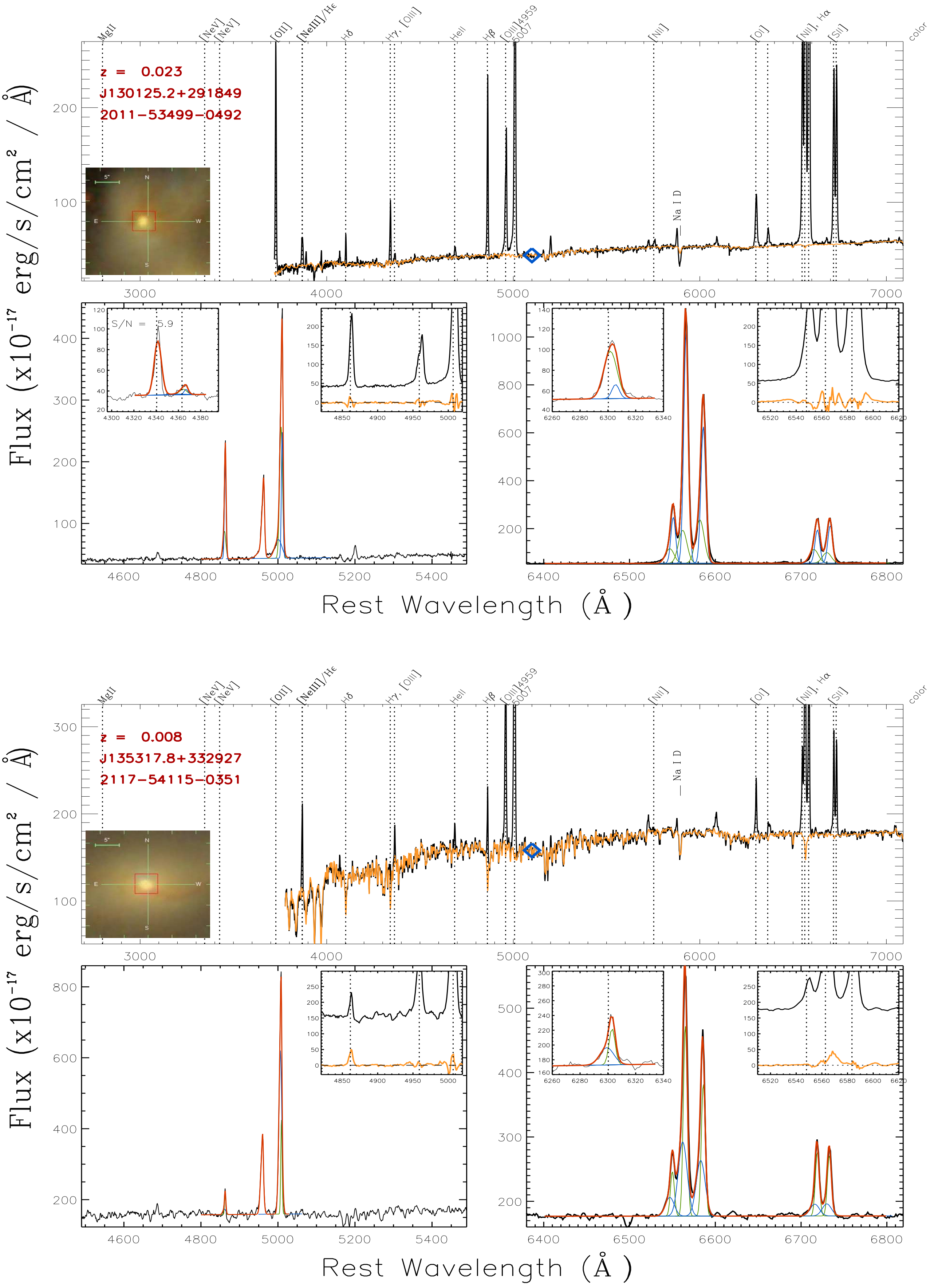
MgII
[NeV]
[NeV]
[OII]
[NeIII]/Hε
Hδ
Hγ, [OIII]
HeII
Hβ
[OIII]4959
5007
[NII]
[OI]
[NII], Hα
[SII]
color
z = 0.023
J130125.2+291849
2011−53499−0492
Na I D
S/N = 5.9
z = 0.008
J135317.8+332927
2117−54115−0351
Flux (x10$^{-17}$ erg/s/cm$^2$ / Å)
Rest Wavelength (Å)
3000
4000
5000
6000
7000
4600
4800
5000
5200
5400
6400
6500
6600
6700
6800

Figure C.-8: xx

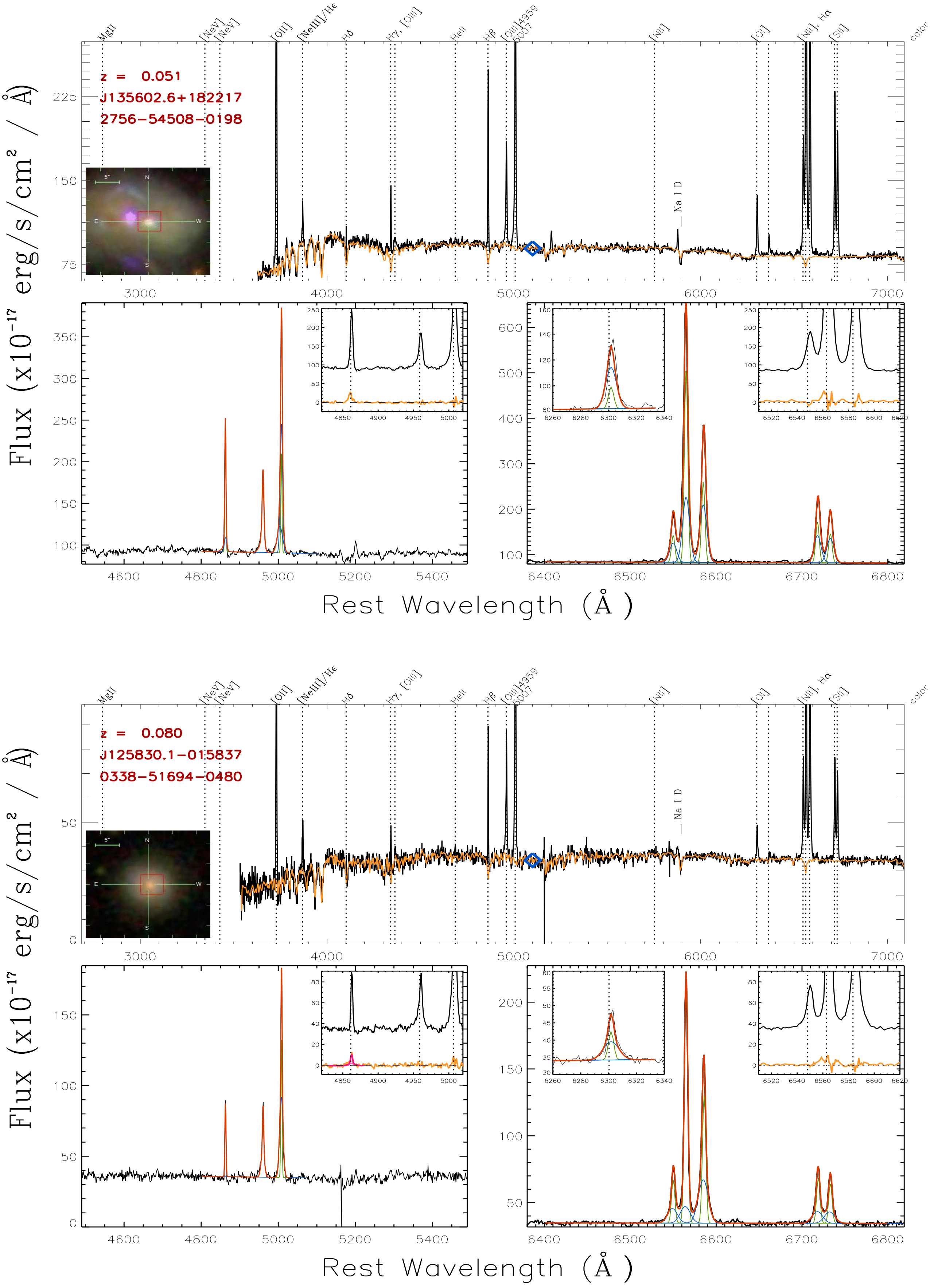
z = 0.051
J135602.6+182217
2756−54508−0198
z = 0.080
J125830.1−015837
0338−51694−0480
MgII
[NeV]
[NeV]
[OII]
[NeIII]/Hε
Hδ
Hγ, [OIII]
HeII
Hβ
[OIII]4959
5007
[NII]
[OI]
[NII], Hα
[SII]
color
Na I D
Flux (x10$^{-17}$ erg/s/cm$^2$ / Å)
Rest Wavelength (Å)
3000
4000
5000
6000
7000
4600
4800
5000
5200
5400
6400
6500
6600
6700
6800

Figure C.-9: xx